Aerothermal Impact of Time-Resolved Inlet Boundary Conditions in High-Pressure Turbine Simulations

Zum aerothermalen Einfluss von zeitaufgelösten Eintrittsrandbedingungen in numerischen Simulationen von Hochdruckturbinen

Zur Erlangung des akademischen Grades Doktor-Ingenieur (Dr.-Ing.)
Genehmigte Dissertation von Jonathan van de Wouw aus Heidelberg
Tag der Einreichung: 10. Juni 2024, Tag der Prüfung: 29. Oktober 2024

1. Gutachten: Prof. Dr.-Ing. Heinz-Peter Schiffer
2. Gutachten: Prof. Dr.-Ing. Christian Hasse
Darmstadt, Technische Universität Darmstadt

TECHNISCHE UNIVERSITÄT DARMSTADT

Mechanical Engineering Department

Institut Gasturbinen, Luft- und Raumfahrtantriebe

Aerothermal Impact of Time-Resolved Inlet Boundary Conditions in High-Pressure Turbine Simulations
Zum aerothermalen Einfluss von zeitaufgelösten Eintrittsrandbedingungen in numerischen Simulationen von Hochdruckturbinen

Accepted doctoral thesis by Jonathan van de Wouw

Date of submission: 10. Juni 2024
Date of thesis defense: 29. Oktober 2024

Darmstadt, Technische Universität Darmstadt

Bitte zitieren Sie dieses Dokument als:
URN: urn:nbn:de:tuda-tuprints-286526
URL: http://tuprints.ulb.tu-darmstadt.de/28652
Jahr der Veröffentlichung auf TUprints: 2024

Dieses Dokument wird bereitgestellt von tuprints,
E-Publishing-Service der TU Darmstadt
http://tuprints.ulb.tu-darmstadt.de
tuprints@ulb.tu-darmstadt.de

Editor's Preface

The series Research Reports from the Institute of Gas Turbines and Aerospace Propulsion accounts for the advances made in turbomachinery research and development at Technische Universität Darmstadt. Because of the strong application oriented focus of the research in this area, the academic problems reflect actual industrial development trends.

The current development foci adapt to the changing political, economic and ecological framework which keeps carrying the turbomachine towards the border of technological feasibility. In consequence, it is not unusual for findings to be transferred to the industrial application directly.

It is within this environment, that the industry and application oriented research works of this series originate. The reports describe current findings of experimental investigations and numerical simulations which were obtained at the Institute of Gas Turbines and Aerospace Propulsion at Technische Universität Darmstadt.

Heinz-Peter Schiffer
Darmstadt, 2024

Authors's Preface

Acknowledgements

I would like to express my sincere gratitude to my supervisor, Prof. Dr.-Ing Heinz-Peter Schiffer, for his valuable support and guidance during my 5-year period at the Institute of Gas Turbines and Aerospace Propulsion. His technical expertise and his knowledge of the industrial and academic environments have been of great benefit to this work. The consistently positive and innovative atmosphere at the institute, coupled with the familiar and motivating working environment, constituted the fundamental basis for the successful completion of this project. Furthermore, I would like to thank Prof. Dr.-Ing Christian Hasse for co-examining this thesis. I would also like to thank Nico Rademeacher, Florian Goertz, Marius Linne and Anton Hilfrich for proofreading this work.

My time at GLR was distinguished by a high level of interaction with all colleagues, as well as a considerable degree of enjoyment derived from both professional and personal pursuits. I would like to express my sincerest gratitude to all of my colleagues, particularly Barbara Löhr, for her valuable assistance with the project administration and for the engaging discussions during our coffee breaks. I would also like to acknowledge the contributions of Marius Schneider, Jonathan Hilgert, Faramarz Bakhtiari, Florian Goertz, Nico Rademacher, and Anton Hilfrich from the CFD team, as well as Manuel Wilhelm, Tom Ostrowki, Johannes Eitenmüller, Dominik Ade, and Marius Linne from the LSTR team, for their insightful and diverse discussions.

Over time, a significant number of students have made valuable contributions to the success of the project. In particular, I would like to express my gratitude to Florian Goertz, Nico Rademacher, Anton Hilfrich, and Lingping Wan for their contributions to the project through their master's theses, and to Anton Hilfrich and Tamara Hinz for their contributions through their bachelor's theses.

This research would not have been possible without the assistance of the industrial partner, Rolls-Royce Deutschland. I would like to express my sincerest gratitude to Roland Wilhelm, Jens Ortmanns, Christoph Lyko, Marcus Meyer, Sebastian Brehmer, Paolo Adami, Ruud Eggels, Max Staufer, Thorsten Voigt, and Axel Gerstenberger. I am most grateful to Knut Lehmann for the extensive and productive discussions we had via telephone and in person,

for his unwavering support and confidence in my work, and for organizing the memorable mountain tours in the Dolomites. Thank you Knut!

Finally, I would like to express my gratefulness to my family, friends, and especially Linda for their unbroken support throughout this endeavor.

Jonathan van de Wouw
Darmstadt, 2024

Research Context and Funding

This thesis is embedded into a series of numerical and experimental investigations on the *combustor-turbine aerothermal interaction* (CTI) at the Rolls-Royce University Technology Centre at TU Darmstadt.

The dissertation is largely based on the findings of the research project *PRESTIGE* funded by the German Luftfahrtforschungsprogramm (LuFo V-3) under grant 20T1716A in close cooperation with *Rolls-Royce Deutschland Ltd & Co KG*. Computational Fluid Dynamics (CFD) calculations were conducted on the *NHR Center NHR4CES at TU Darmstadt*. This is funded by the Federal Ministry of Education and Research, and the state governments participating on the basis of the resolutions of the GWK for national high performance computing at universities (www.nhr-verein.de/unsere-partner). Licensing was kindly provided by ANSYS® via their *Academic Partner Program*.

Abstract

The high-pressure turbine in a jet engine, and in particular the initial stage of it, is significantly influenced by the flow in the combustor upstream. The presence of high temperature nonuniformities, large flow angles, and high levels of turbulence results in a reduction in turbine efficiency and an increased demand for an efficient turbine cooling scheme. To ensure that the turbine is designed to meet lifetime requirements and to achieve optimal efficiency, it is of paramount importance to comprehend the interaction mechanisms between the combustor and turbine and to incorporate all the crucial combustor-related effects into the design of the turbine.

Numerical simulations play a pivotal role in the design of combustor and high-pressure turbine and the analysis of the combustor-turbine aerothermal interaction (CTI), as they offer a cost-effective and efficient means of understanding the complex flow and thermodynamics in both components. Due to the harsh conditions in this part of the engine, measurements and experiments are often limited. In most cases, the combustor and turbine are treated in separate simulations, with 2D mean field data transferred at the interface to be used as inlet boundary conditions in the high-pressure turbine. This approach, however, fails to account for unsteady effects from the combustor, which can significantly impact the design of the turbine. It has long been known that scale-resolving simulation methods can increase the predictive accuracy of CFD simulations. The increasing availability of computational power enables design teams to use unsteady and scale-resolving simulations more frequently. This is also the case for the combustor and turbine component of a jet engine. However, this increased fidelity comes at a cost in terms of both computational resources and time, as well as the production of significantly higher amounts of data, which must be stored and handled. For a standalone turbine simulation, this also means that the demands for the inlet boundary conditions are much higher. For a scale-resolving turbine simulation, combustor unsteadiness and turbulence must be applied at the inlet boundary.

This work presents a method for the efficient storage of unsteady snapshot time series from a combustor simulation, which can then be used as inlet boundary conditions for a subsequent turbine simulation. This is achieved by employing a combination of Proper Orthogonal Decomposition (POD) and Fourier series development in the PODFS method. By considering only that portion of the data which has energetic relevance, a reduced order model of the snapshot data is created that is independent of time. The application of these unsteady inlet boundary conditions to scale-resolving turbine simulations reveals

significant differences in the thermal fields and film cooling effectiveness on the turbine vanes when compared to standard RANS simulations using mean fields as inlet boundary conditions. The aerodynamics of the vanes are minimally influenced by the selection of inlet boundary conditions. The pronounced impact of unsteady inlet boundary conditions on the thermal behavior of the vanes highlights the significance of the choice of inlet boundary conditions that match the scale-resolving character of the simulation scheme when numerically investigating high-pressure turbines.

Zusammenfassung

Die Hochdruckturbine eines Turboflugtriebwerks, insbesondere die erste Stufe, ist in erheblichem Maße von der Strömung in der vorgeschalteten Brennkammer beeinflusst. Das Vorhandensein hoher Temperaturungleichmäßigkeiten, großer Strömungswinkel und starker Turbulenzen führt zu einer Verringerung des Turbinenwirkungsgrads und zu einem erhöhten Bedarf an einem effizienten Turbinenkühlsystem. Um zu gewährleisten, dass die Turbine die Anforderungen an die Lebensdauer erfüllt und einen optimalen Wirkungsgrad erzielt, ist es von größter Bedeutung, die Wechselwirkungsmechanismen zwischen Brennkammer und Turbine zu verstehen und alle entscheidenden Effekte, die mit der Brennkammer zusammenhängen, in die Auslegung der Turbine einzubeziehen.

Numerische Simulationen stellen ein zentrales Instrument bei der Auslegung von Brennkammer und Hochdruckturbine sowie bei der Analyse der aerothermalen Wechselwirkung zwischen beiden Komponenten dar. Sie ermöglichen ein kostengünstiges und effizientes Verständnis der komplexen strömungsmechanischen und thermodynamischen Vorgänge in beiden Komponenten. Aufgrund der harschen Bedingungen in diesem Teil des Triebwerks sind Messungen und Experimente oft begrenzt. In den meisten Fällen werden die Brennkammer und die Turbine in separaten Simulationen behandelt. Dabei werden 2D-Mittelfelddaten an der Schnittstelle übertragen, um sie als Eintrittsrandbedingungen in der Hochdruckturbine zu verwenden. Bei diesem Ansatz bleiben jedoch die instationären Effekte der Brennkammer unberücksichtigt, die sich erheblich auf die Auslegung der Turbine auswirken können. Es ist seit langem bekannt, dass skalenauflösende Simulationsmethoden die Vorhersagegenauigkeit von CFD-Simulationen erhöhen können. Die zunehmende Verfügbarkeit von Rechenleistung erlaubt es Auslegungsteams, instationäre und skalenauflösende Simulationen immer häufiger einzusetzen. Dies gilt ebenfalls für die Brennkammer- und Turbinenkomponenten eines Strahltriebwerks. Die höhere Genauigkeit dieser Simulationen ist jedoch mit einem Preis verbunden, sowohl in Bezug auf die Rechenressourcen und die Simulationszeit als auch in Bezug auf die Erzeugung erheblich größerer Datenmengen, die gespeichert und verarbeitet werden müssen. Für eine eigenständige Turbinensimulation bedeutet dies, dass die Anforderungen an die Eintrittsrandbedingungen deutlich höher sind. Für eine skalenauflösende Turbinensimulation ist die Berücksichtigung von Brennkammerinstabilitäten und Turbulenzen am Eintritt unabdingbar.

In dieser Arbeit wird eine Methode zur effizienten Speicherung von instationären Felddaten aus einer Brennkammersimulation präsentiert, welche anschließend als Eintrittsrandbedin-

gungen für eine nachfolgende Hochdruckturbinensimulation verwendet werden können. Die Kombination von Proper Orthogonal Decomposition (POD) und Fourier-Reihenentwicklung in der PODFS-Methode wird eingesetzt. Die ausschließliche Berücksichtigung des energetisch relevanten Teils der Daten führt zur Erstellung eines zeitunabhängigen Modells reduzierter Ordnung. Dies führt zu einer signifikanten Reduktion der Datengröße. Die Anwendung dieser instationären Eintrittsrandbedingungen in skalenauflösenden Hochdruckturbinensimulationen zeigt signifikante Unterschiede in den thermischen Feldern und der Filmkühleffektivität auf den Turbinenschaufeln im Vergleich zu stationären RANS-Simulationen mit mittleren Feldern als Eintrittsrandbedingungen. Die Aerodynamik der Schaufeln erfährt durch die Wahl der Eintrittsrandbedingung lediglich eine minimale Beeinflussung. Der signifikante Einfluss der instationären Eintrittsrandbedingungen auf das thermische Verhalten der Schaufeln unterstreicht die Relevanz der Wahl von Eintrittsrandbedingungen, die dem skalenauflösenden Charakter des Simulationsschemas entsprechen, wenn Hochdruckturbinen numerisch untersucht werden.

Contents

1. Introduction

1.1. Background and Motivation

Aviation has played a crucial role in driving globalization, serving as the foundation for international trade, tourism, and cultural exchange. The industry has experienced significant growth, with passenger numbers tripling since the 1990s and cargo tonnage doubling in the same period. This surge is attributed to factors such as trade agreements and open markets, which have facilitated global business activity, driving demand for both passenger and cargo transportation. The development of fuel-efficient engines and larger aircraft has enabled airlines to offer affordable tickets and expand their reach. Additionally, rising global living standards mean that more people have the means and funding to travel internationally for leisure and business. Fig. 1.1 illustrates the global passenger numbers in aviation over the past four decades and demonstrates the impact of global crises on the aviation industry.

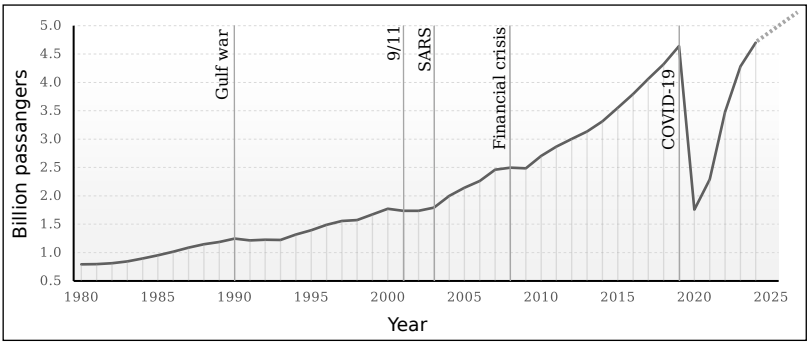

Figure 1.1.: Development of air travel from 1980 till now. Data from IEA [75] and IATA [74]

The COVID-19 pandemic had a significant impact on societies worldwide and halted global travel (German Aviation Association [54]). The aviation industry was particularly affected. However, recent developments indicate a rapid recovery of air travel, with some sectors already surpassing pre-pandemic levels (Dube [45], Sun et al. [177]).

Although aviation undoubtedly carries globalization, its rapid growth comes at an environmental cost. The industry is a significant contributor to global warming and environmental pollution. Air travel is responsible for approximately 2% of global Carbon Dioxide (CO_2) emissions (ACARE [1]), a figure that is expected to increase if left unaddressed. Emissions from aircraft contribute to local air quality problems, particularly in the proximity of airports, which can have an impact on public health. Furthermore, aircraft noise can cause disruption to communities living near airports, affecting the well-being of residents (Masiol and Harrison [110]).

The aviation industry and policymakers are seeking solutions to promote sustainable growth in the face of these challenges. To achieve this, investments in research for electric and hybrid-electric aircraft are necessary to reduce emissions on short distance flights. Nevertheless, at present, there are no viable alternatives to propulsion systems based on carbon-based fuels for medium- and long-haul flights due to the high energy density of liquid fuels. Therefore, improvements in core engine technologies and investments in research for biofuels are necessary. Additionally, programs that compensate for emissions by supporting projects that remove carbon from the atmosphere should be implemented. Technology can also be utilized to streamline flight paths to reduce fuel consumption. The European Union defined the Flightpath 2050 agenda (Kallas et al. [84]), aiming to reduce CO_2 emissions by 75%, Nitrogen Oxides (NO_X) emissions by 90%, and noise emissions by 65% compared to the year 2000.

1.2. Technical Measures to Reduce Emissions

To achieve the set emission goals, improving jet engine technology is crucial. A typical civil aircraft engine is designed as a turbofan engine, as illustrated in Fig. 1.2b. The air stream behind the fan is divided into a core mass flow $\dot{m}_{core}$ and a bypass mass flow $\dot{m}_{bypass}$. The bypass ratio

$$\alpha := \frac{\dot{m}_{bypass}}{\dot{m}_{core}} \tag{1.1}$$

describes the ratio of both mass flows and exceeds 10:1 for modern turbofan engines. Most of the air that enters the engine is directed by the fan through the bypass channel, which contributes to the majority of the thrust of the engine. The engine core operates like a gas turbine and generates the power to drive the fan. The air is compressed by multiple compressor stages (② → ③) after entering the engine core. The air is then mixed with fuel and burned in the combustion chamber (③ → (40)). The turbine ((40) → ⑤) converts the thermal energy of the hot combustor exit gas into mechanical energy by rotating the engine shafts, which in turn drive the compressor and fan that are mechanical coupled with the turbine. Turbofan engines are usually designed with a multi-shaft (spool) configuration,

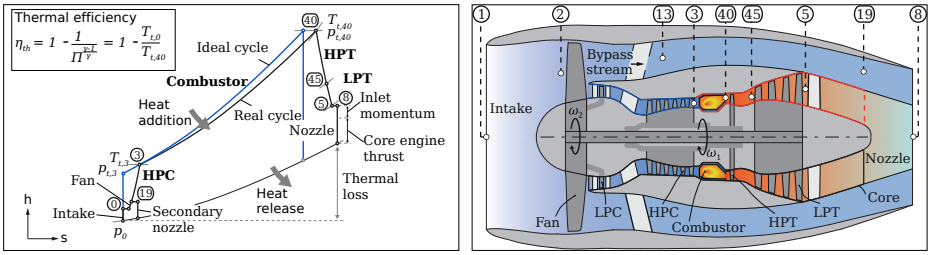

(a) Brayton cycle (red: ideal, black: real) **(b)** Components of a turbofan engine

Figure 1.2.: Components and cycle of a modern turbofan engine (adapted from Schneider [158])

with the low- and high-pressure components of the compressor and turbine mounted on different shafts to run at different rotating speeds ω. This approach reduces aerodynamic losses and minimizes fan noise emissions. In a two-shaft architecture, the fan and Low Pressure Compressor (LPC) are mounted on the same shaft as the Low Pressure Turbine (LPT), while the High Pressure Compressor (HPC) and High Pressure Turbine (HPT) sit on the second shaft. Rolls-Royce has engines in their portfolio that use a third shaft for intermediate pressure components. A recent development is the implementation of a gearbox to further decouple the rotational speed of the fan from the LPT, enabling even larger fan diameters and higher bypass ratios.

There are two ways to reduce aircraft engine pollutant emissions. The first way is to target the location where the emissions are produced, specifically in the combustion chamber. Measures to reduce combustion emissions are diverse and include striving for complete combustion to decrease Carbon Monoxide (CO) and Unburned Hydrocarbons (UHC) emissions (Farokhi [49]), as well as reducing peak temperatures to decrease NO_X generation (Joos [83]). The current combustion technologies are Rich-burn Quick-quench Lean-burn (RQL) and Lean Premixed Prevaporized (LPP) combustion. For a detailed description of both, please refer to Section 2.1.

The emissions of the engine can also be reduced by enhancing the overall efficiency of the engine, resulting in less fuel burned and fewer emissions, while maintaining the same level of thrust. The Specific Fuel Consumption (SFC) is a measure of the efficiency of the engine, calculated by relating the fuel mass flow $\dot{m}_f$ to the generated thrust F_T. The operation of an aircraft engine involves a two-stage energy conversion process. As with all energy conversion processes, these are accompanied by losses. Initially, the chemical power stored in the fuel P_{th} is converted into kinetic power P_{kin} of the air flowing through the engine with the thermal efficiency $\eta_{th} := P_{kin}/P_{th}$. In the second conversion process, the kinetic power P_{kin} is converted into output propulsive power P_{pr} with the propulsive efficiency

$\eta_{pr} := P_{pr}/P_{kin}$. The overall efficiency η_o of an engine is determined by the product of its thermal and propulsive efficiency.

$$\eta_o := \eta_{th}\eta_{pr} = \frac{P_{pr}}{P_{th}} = \frac{F_T V_0}{P_{th}} \equiv \frac{\text{thrust power}}{\text{power stored in the fuel}} \tag{1.2}$$

It describes the ratio of engine thrust as output to the thermal energy of the fuel brought into the system. The efficiency of the engine can be enhanced by improving either its thermal or propulsive efficiency.

To enhance the propulsive efficiency, the net outlet velocity of the engine can be reduced by mixing the high velocity exhaust of the engine core with the slower bypass flow, thereby reducing the losses of the exhaust jet. To maintain high thrust levels, the mass flow needs to increase, resulting in higher bypass ratios and larger engine diameters.

Fig. 1.2a shows the thermodynamic cycle of the turbofan engine plotted in an h-s diagram. The idealized *Brayton* cycle (red) serves as a reference for the real process and sets the upper limits for the state changes of the engine components. Ideally, the compression and expansion processes would be isentropic ($s = 0$), and the combustion process would be isobaric. However, in reality, all components experience losses which are evident through entropy production. To enhance the thermal efficiency of the engine, it is necessary to minimize losses in individual components, or to change the idealized process. According to the efficiency of the ideal Brayton process

$$\eta_{th,ideal} = 1 - \frac{1}{\Pi^{\frac{\gamma-1}{\gamma}}}, \tag{1.3}$$

increasing the compressor pressure ratio $\Pi = p_{t,3}/p_{t,2}$ can also improve efficiency. An increase in compressor pressure ratio always results in a rise in Turbine Entry Temperature (TET) $T_{t,40}$ (Birch [21]). The TET is a crucial design parameter as it determines the amount of work that can be extracted in the turbine (Lechner and Seume [99]) and sets the temperature that the turbine material needs to withstand. In modern engines, the TET exceeds the melting temperatures of the turbine materials, and intensive cooling measures are necessary to protect the vanes and blades. To improve the thermal efficiency of the engine, it is important to reduce losses in every component, increase the overall pressure ratio (which corresponds to a high TET), and use secondary air efficiently for cooling and sealing (Haselbach et al. [67]).

In order to enhance the efficiency of engine components and achieve the ambitious targets for emissions and fuel consumption, it is necessary for the tools used by engineers, developing the next generation of aircraft engines and gas turbines, to evolve too. Numerical simulations, particularly Computational Fluid Dynamics (CFD), have become increasingly important in the turbomachinery development process over the last few decades and is now an integral

part of all R&D programs. Despite their well-known weaknesses, Reynolds-Averaged Navier-Stokes (RANS) turbulence models remain the primary tool in the turbomachinery industry. As margins for improvement become smaller, improved methods outside the RANS toolbox are increasingly being used. With the rise of computational resources, scale-resolving simulation methods, such as Large Eddy Simulation (LES), are becoming increasingly prevalent in various application cases, including turbomachinery development (Tyacke et al. [187]). While the use of high-fidelity simulation of individual components is important in new engine design, rising attention is now being paid to component interaction, which presents new challenges for design tools.

1.2.1. Implications for the High-Pressure Turbine

The pursuit of greater engine efficiency is affecting the HPT in two ways (Schneider [158]). Firstly, the improvements in the thermal efficiency of the engine core are driving the TET far beyond the temperature limits of the turbine materials. This necessitates effective protection and cooling measures. Modern HPT components are cooled both internally and externally, and Thermal Barrier Coatings (TBC) are also employed (cf. Section 2.3). A significant amount of cooler compressor air is used for cooling purposes, but it does not participate in the energy conversion process of the engine. Therefore, the usage of cooling air reduces the efficiency of the engine and should be limited to the necessary minimum (Schmid [151]). Another trend is the downsizing of the engine core to increase the bypass ratio, which enhances the propulsive efficiency of the engine, as explained earlier. The reduction in combustor size results in intensified temperature non-uniformities and residual swirl at the turbine inlet, posing challenges for the aerodynamic and cooling design of the turbine. Both effects present challenging conditions for the turbine. Therefore, it is increasingly important to have precise knowledge of the flow conditions at the interface between the combustor and turbine. This has resulted in a lot of research activities on the topic of the interaction between combustor and turbine. Numerical predictions are heavily relied upon for the development of combustors and HPTs due to their very high temperatures and the limited possibilities to collect measurements. The measurement of Nozzle Guide Vane (NGV) temperatures under real operating conditions is limited and very expensive and relies solely on thermal paint tests (Clemen et al. [36]). Numerical simulations are crucial in the development of improved turbines, and the enhancement of simulation methods is essential to achieving this goal.

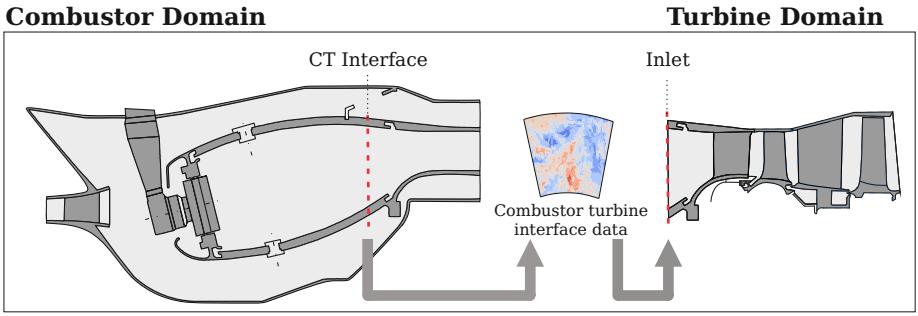

Figure 1.3.: Illustration of the decoupled simulation of a combustor and turbine, which employs data transfer at the interface

1.2.2. Implications for the Interaction between Combustor and Turbine

The interaction between the two components is referred to as Combustor and Turbine aerothermal Interaction (CTI). Numerical prediction of the flow in both components is challenging due to the highly complex flow physics. The flow in the combustor is highly turbulent, and combustion involves chemical reactions, requiring the use of highly specialized solvers. On the turbine side, a different type of flow solver is used to simulate the flow. It is necessary for the turbine solver to be capable of handling high Reynolds numbers and compressibility effects, transonic conditions, and blade row interaction. Fig. 1.3 shows the industry standard, which involves simulating both components separately and exchanging interface data. The time-averaged data from the extraction plane of the combustor simulation is used as the inlet boundary conditions for the subsequent turbine simulation. By using mean field data, temporal information is lost in the exchange process. For steady-state RANS simulations, this approach is reasonable. However, when using scale-resolving simulation methods, a more sophisticated set of data exchange is required. To initialize the turbulent motion in the freestream, time-accurate inlet boundary conditions must be prescribed for scale-resolving turbine simulations. In the past, this was achieved either by coupling two separate simulations and exchanging data at the interface on the fly (Vagnoli and Verstraete [188], Miki et al. [121]) or by simulating both the combustor and turbine in one domain (Klapdor et al. [86], Raynaud et al. [141]). As explained in Section 2.4, these approaches have their difficulties and limitations. Recent developments trend towards the decoupled approach, which involves exchanging time-accurate data between two separate simulations (Martin et al. [109], Tomasello et al. [182], Verma et al. [190]). This work pursues this approach and develops a method to use transient boundary conditions in a turbine simulation.

1.3. Placement of this Work and Research Objectives

This thesis addresses the interaction between the combustor and the turbine. Research on this topic has been conducted at the *Institute of Gas Turbines and Aerospace Propulsion* (GLR) at the *Technical University Darmstadt* since 2006 in collaboration with *Rolls-Royce* as part of the University Technology Centre (UTC). This strategic partnership between science and industry aims to develop new technologies for aircraft engines that meet future economic and ecological goals.

Work has already been carried out at the UTC focusing on the experimental measurement of turbine flow under realistic inlet boundary conditions (Werschnik [192], Wilhelm [197], Ostrowski [129]).

Numerical investigations on the effect of combustor exit flow on the HPT heat transfer were conducted by Schmid [151]. Hilgert [71] developed a pragmatic method for matching Conjugate Heat Transfer (CHT) predictions of HPT blades with thermal paint tests. Schneider [158] developed a method to manipulate and construct turbine inlet conditions based on a parameter model. This tool was used to investigate the robustness of the HPT against variations in the inlet conditions. Bakhtiari [10] investigated the effect of pulsating pressure inlet boundary conditions on the aerothermal behavior of the HPT. These inlet conditions may be encountered with novel combustion concepts, such as rotating detonation combustion.

All previous numerical investigations of CTI in the context of UTC Darmstadt have been based on steady or unsteady RANS simulations. This work is novel because it includes unsteady effects on the level of turbulent fluctuations at the Combustor-Turbine (CT) interface and scale-resolving turbine simulations are conducted. The research objectives of this work are the following:

1. Review of unsteady effects at the combustor outlet
2. Development of a method to efficiently collect and store unsteady field data at the interface between the combustor and turbine
3. Integration of unsteady boundary condition reading routines into turbine CFD solvers
4. Validation of the entire workflow for collecting, compressing and reusing of the interface data, to demonstrate the capability of the method to reproduce the turbulent, time-accurate flow fields at the interface
5. Application of the method on a engine representative CT case by using the snapshot data of an RQL combustor LES and application of the compressed form as inlet boundary conditions of a turbine vane simulation

6. Investigation of the impact of combustor unsteadiness and turbulence on the aerodynamics of turbine vanes: The investigation includes analysis of vane loading and turning, secondary flows, loss development and turbine capacity
7. Investigation of the impact of combustor unsteadiness and turbulence on the thermal loading and cooling of the turbine vanes by analyzing the temperature distribution, Heat Transfer Coefficient (HTC) and film cooling effectiveness
8. Seperation of effects caused by scale resolving turbulence models and scale resolving inlet boundary conditions
9. What are the most relevant turbulent scales? Is an Unsteady Reynolds-Averaged Navier-Stokes (URANS) simulation capable to resolve the relevant transient effects?

1.4. Thesis Outline

This Thesis is structured as follows: Chapter 1 introduces the topic of reducing aircraft engine emissions and explains how this work contributes to it. Chapter 2 presents the state of the art of combustion and turbines, with a focus on the HPT aerothermal behavior and the interaction mechanisms of the combustor and turbine. Chapter 3 describes the CFD methods used, with an emphasis on turbulence modelling. The validation of the CFD setup against measurement data is performed using a research turbine. The last section of this chapter presents methods for generating unsteady inlet boundary conditions and explains the basis for the methods developed in this work

Chapter 4 outlines the methodologies employed to collect and compress unsteady interface data, along with their validation on a generic test case and the research turbine. The capacity of the method to reproduce the turbulent flow state at the interface between two simulations is demonstrated, and various turbulence models and compression ratios are compared.

Chapter 5 presents the application of the developed method on an engine representative combustor-turbine test case. The chapter mainly focuses on the simulation results of an RQL combustor- turbine test case, which is split into two sections. The first section discusses the impact of combustor unsteadiness on the aerodynamics of the turbine vanes, while the second section discusses its impact on the thermal behavior of the vanes.

Chapter 6 summarizes the results and findings of this work and provides implications for future research.

2. State of the Art

This chapter provides an overview of the current state of combustion chamber and turbine development. It outlines the theoretical foundation relevant to the work within the context of CTI. After establishing the fundamentals of combustion technology, it then describes the basic principles of turbine aerodynamics, turbine losses, and thermal topics such as heat transfer and cooling. Finally, it describes the most important features of the interaction between the combustor and the turbine and gives an insight into past and current studies on the topic.

2.1. Combustion and Emission

The purpose of the combustion chamber is to efficiently convert the chemical energy of the fuel into thermal energy of the flow through the machine by burning the fuel. Thus the combustion chamber is a critical part for the operation of the engine and underlies very strict requirements (Bräunling [28] and Rick [143]).

- In all operating points, the aim is to achieve a high burnout, also known as combustion efficiency, of over 99%. This ensures the maximum utilization of chemical energy.
- To comply with regulations, the emissions of pollutants and noise must be kept low.
- The flame needs to remain stable across a broad range of chamber pressures and air-fuel ratios.
- Reliable ignition and re-ignition can be achieved in all conditions, such as after a flame out in high altitude.
- Low total pressure loss across the combustion chamber is necessary to ensure high overall efficiency.
- The design is both compact and lightweight, while still maintaining thermal and mechanical integrity.
- Optimal temperature distribution at the outlet to ensure efficient and secure turbine operation.

- Long service life, ease of maintenance and cost efficiency.

The main development goals of new combustion technologies are to secure efficient and safe operation while reducing emissions. The combustion process of hydrocarbons is a complex chemical reaction. A detailed explanation of the chemical reaction kinetics can be found in the work by Oates [126]. Hydrocarbon fuels produce water vapor and CO_2 emissions, which can only be reduced by decreasing the overall fuel burn of the engine. Other pollutants, such as CO, UHC, Nitrogen Oxide (NO) and Nitrogen Dioxide (NO_2) (summarized as NO_X), Sulfur Dioxide (SO_2), Sulfur Trioxide (SO_3), and soot, can be influenced by the combustion process.

CO and UHC are primarily formed during taxi and idle operation of the engine, when temperatures and fuel-air ratios are low. Sulfur oxides SO_2 and SO_3 are a result of fuel contamination with sulfur and can be reduced during the refinery process. Soot and NO_X are generated during high temperature and high fuel-air ratio operation conditions, such as take-off and climb.

NO_X is generated in three different ways (Joos [83]). At temperatures above 1800 K and with an equivalence ratio close to one, nitrogen can react with oxygen in the *Zeldovich* mechanism to produce *thermal* NO_X, which is the majority of the total NO_X emitted by aircraft engines. In addition to temperature and fuel-air ratio, the residence time of the reaction products in the combustion zone has a significant impact on the generation of thermal NO_X. In areas with an excess of fuel, the *Fenimore* mechanism creates NO_X from nitrogen and hydrocarbon radicals. This is known as *Prompt* NO_X. Additionally, hydrocarbon fuels contain nitrogen which oxidizes during the combustion process to form *Fuel* NO_X.

In aviation, NO_X emissions are considered the most problematic contribution to global warming, alongside unavoidable CO_2 and water vapor emissions (Faber [48]). The impact of NO_X depends on the altitude and climate conditions of the area. At ground level, NO_X deteriorates air quality (ACARE [1]). In the troposphere ($<$18 km), which is the typical altitude of subsonic aircraft, NO_X emissions contribute to the formation of ozone, a greenhouse gas that warms the atmosphere (Lee et al. [100]). However, at higher altitudes in the stratosphere, NO_X reduces ozone and depletes the crucial ozone layer. This is especially critical for supersonic flights. The relationship between NO_X and ozone is complex due to finely balanced chemical equilibrium states. However, it is important to note that NO_X has negative effects on both people and the environment in all atmospheric layers.

2.1.1. RQL Combustion

The main approach to reducing aviation emissions is to decrease the use of fossil fuels. This will reduce all emissions including the main contributor to global warming, CO_2. Improving

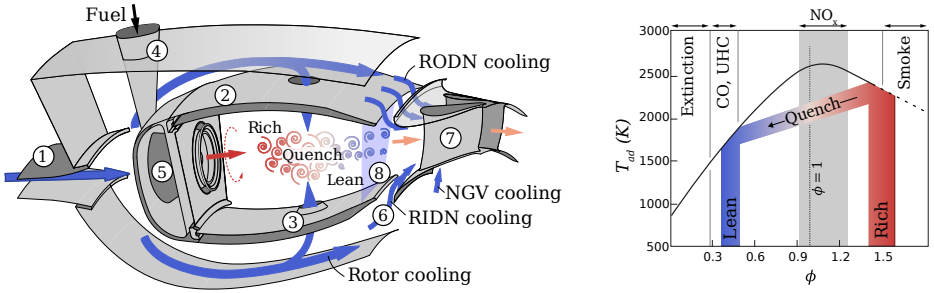

Figure 2.1.: Schematic illustration of modern RQL combustion chamber (left) and adiabatic flame temperature T_{ad} over equivalence ratio ϕ (right) adapted from Schneider [158]

the overall efficiency of the aircraft, including its engines, is one way to achieve this. On a component level, optimizing the combustion process can help reduce other emissions, particularly NO_X. Thermal NO_X is the primary source of NO_X emissions and is formed at very high temperatures. The RQL combustion concept, introduced by Mosier and Pierce [124], aims to reduce the formation of NO_X by decreasing the time that combustion gases spend at high temperatures and stoichiometric fuel-air ratios (McGuirk [112]). The equivalence ratio ϕ (Eq. (2.1)) describes the fuel-oxidizer ratio referred to the stoichiometric[1] ratio. ϕ>1 represents fuel-rich combustion, ϕ<1 represents fuel-lean combustion, and ϕ=1 represents stoichiometric conditions.

$$\phi = \frac{\dot{m}_f / \dot{m}_{ox}}{(\dot{m}_f / \dot{m}_{ox})_{stoic}} \tag{2.1}$$

The adiabatic flame temperature T_{ad} is determined by the equivalence ratio ϕ, as shown in Fig. 2.1 (right). The operating range of a modern RQL combustor is illustrated, starting with fuel-rich combustion in the primary zone, followed by rapid quenching of the mixture by introducing a high amount of air, and ending with fuel-lean combustion in the secondary zone. Fig. 2.1 (left) shows a schematic representation of the geometry and flow path of a contemporary RQL combustion chamber.

The air from the compressor enters the combustor module through a pre-diffuser ①. This reduces the velocity of the fluid, which in turn reduces pressure losses in the chamber and prevents the risk of flame blowout. The liner ② divides the combustion chamber into the flame tube and an inner and outer annulus. Approximately 80-85% of the air entering the combustion chamber is directed through the inner and outer annuli surrounding the flame tube, with the objective of cooling the flame tube. Part of this air is then introduced

[1]The stoichiometric fuel-oxidizer ratio is the ideal mass ratio of fuel and oxidizer required for complete combustion (Joos [83]).

into the secondary combustion zone through multiple holes in the liner, known as dilution ports ③ to lean out the combustion gas mixture. The other 15-20% of the air is mixed with fuel from the fuel injector ④ and the fuel rich mixture enters the flame tube through the swirler ⑤. The function of the swirler is to create a recirculation zone that stabilizes the flame and redirect unburned fuel back to the flame. In the secondary combustion zone, dilution air is used to create a lean mixture, reducing the flame temperature. It is also used to condition the combustor outlet traverse to meet requirements by the downstream following turbine. The remaining air from the inner and outer annuli is used for cooling in Rear Inner Discharge Nozzle (RIDN), Rear Outer Discharge Nozzle (RODN), NGV, and the turbine rotor. The combustor and turbine are phenomenologically separated at the CT interface ⑧.

2.1.2. Lean-Burn Combustion

The RQL combustion concept is widely used in modern jet engines. However, the LPP concept is identified as the key technology to further reduce NO_X emissions. The RQL combustion will continue to be relevant, especially in small engines for regional and business jets due to limited installation space. The LPP combustion concept, which is currently used in stationary gas turbines (Lechner and Seume [99]) and a few aircraft engines [2], shows promise in reducing emissions further but also presents several new challenges.

In the lean burn concept, combustion occurs at a lean fuel-oxidizer mixture, which helps to avoid high temperatures and thermal NO_X generation. In lean burn, the injector is fed with a much higher amount of air (70% of the total mass flow). This means that there is less air available in the inner and outer annuli for flame tube cooling and combustor exit traverse manipulation. This poses challenges for turbine design. The injector is required to atomize and mix the fuel with the air, as well as lean out the mixture (Lazik et al. [98]). It is unnecessary to further quench the mixture through the dilution ports. Achieving stable operation of the lean flame close to the extinction limit is challenging, and relight capabilities are limited, particularly in low power output operating conditions (McGuirk [112]). In order to minimize NO_X emissions, it is necessary to ensure that the residence times of the combustibles are as short as possible. However, this is contrary to the requirement for a high burnout rate. The larger injector increases the geometry of the combustor in the radial direction, resulting in higher pressure loss (McGuirk [112]). The small droplet size and good mixing with air in the injector pose a danger of self-ignition and flame flashbacks (Rick [143]). Additionally, lean-burn combustion chambers are more prone to thermo-acoustic oscillations. A coupling between heat release, chamber acoustics, and pressure in the fuel

[2] The Twin Annular Premixing Swirler (TAPS) is a lean burn combustion system developed by GE aviation. It is used in the GEnx engine (Boeing 787 Dreamliner) and CFM56 DAC (Boeing 737, Airbus A220 families) (Stickles [174])

lines can lead to positive feedback and high pressure fluctuations, which can ultimately damage or destroy the component. Lazik et al. [98] presented the design of a single annular combustor that uses fuel staging to ensure operational stability in all conditions. This design addresses the aforementioned challenges.

2.1.3. Combustor Exit Conditions

The interface between the combustor and turbine components is crucial in the development process of new engines as it facilitates the exchange of important information between the design teams of combustor and turbine. The flow in the combustor upstream significantly impacts the high-pressure turbine, particularly its first stage. Povey and Qureshi [135] note that obtaining reliable experimental data at the CT interface under real engine conditions is rare due to the harsh environment. Although the interaction between the combustor and turbine is of great importance, it is primarily investigated numerically, which places significant demands on the tools used.

Numerical prediction of the flow in both components is challenging due to the highly complex flow physics. The turbulent, swirled flow and chemical reactions in combustion require the use of highly specialized combustion solvers. On the turbine side, a different type of flow solver is used to simulate the flow. The turbine solver needs to be specialized in handling high Reynolds numbers, transonic conditions, and blade row interaction. The industry standard involves simulating both components separately and exchanging interface data.

When assessing the impact on the high-pressure turbine, the most relevant characteristics in the combustor outlet plane are residual swirl, temperature non-uniformities caused by discrete burners around the circumference, and unsteadiness, which contributes to high levels of turbulence intensity (Schneider [158]).

Differences in combustor outlet characteristics exist between RQL and lean-burn combustors. In the exit traverse of an RQL combustor, the velocity field is dominated by entrainment flows, which are the imprint of the dilution ports. These cross flows interact with the swirl flow from the primary combustion zone and reduce the residual injector swirl in the outlet plane. On the other hand, in lean-burn combustors, the dominant flow feature at the CT interface is the injector swirl. The swirl in the interface plane is characterized by a yaw (circumferential) and a pitch (radial) angle. Experimental studies of lean-burn combustor simulators (Qureshi et al. [139], Bacci et al. [7], Giller and Schiffer [56], Jacobi and Rosic [78] and Wilhelm et al. [198]) have reported a maximal yaw angle ϕ to lie between 30° and 50°.

The temperature traverse at the CT interface is characterized by temperature non-uniformity (Cha et al. [32]). The discrete burners create a circumferentially varying pattern of hot zones, also called hot streaks. The cooling and quenching air, which is introduced through the combustor liner, creates high temperature gradients towards the endwalls. There are differences in radial and circumferential temperature distribution between RQL and lean-burn combustors. In RQL combustors, dilution air is used for mixture quenching and conditioning the temperature field towards the outlet of the combustor. The high mixing of the hot core flow with the dilution air flattens out circumferential non-uniformities, while the input of large amounts of cooling air creates a steep radial temperature profile towards the walls. The temperature profile at the combustor outlet is flattened out in the radial staged lean-burn combustion chamber, where the main flame is located at the inner and outer flame tube walls and secondary air is not extensively used for liner cooling. This results in lower peak temperatures but higher temperatures at the inner and outer endwalls. The higher temperature at the inner endwall is particularly critical for the rotor as it increases the thermal load on the blade root (Joos [83]).

According to Povey and Qureshi [135], temperature non-uniformities in the CT interface can be quantified using temperature distortion factors.

$$\text{(L)OTDF} := \frac{T_{t,40(max)} - \overline{T_{t,40}}}{\overline{T_{t,40}} - \overline{T_{t,30}}}, \qquad \text{(L)RTDF} := \frac{\overline{T_{t,40_{(max)}}}^{circ} - \overline{T_{t,40}}}{\overline{T_{t,40}} - \overline{T_{t,30}}}. \tag{2.2}$$

The Overal Temperature Distortion Factor (OTDF) and Radial Temperature Distortion Factor (RTDF) are two temperature non-uniformity descriptors that are important for the NGV and rotor heat load, respectively. The OTDF relates the maximum overall temperature $T_{t,40(max)}$ to the mean temperature, while the *pattern factor* or local (L)OTDF is described by using the Two-Dimensional (2D) distribution of $T_{t,40}$ instead of its maximum. The RTDF, on the other hand, describes the radial non-uniformity of the temperature traverse. It uses the maximum of the circumferential averaged temperature $\overline{T_{t,40_{(max)}}}^{circ}$. The local (L)RTDF or *profile factor* is given when the radial profile of the circumferential average is used instead of its maximum value.

Combustion relies on turbulence to achieve a high heat release in a small space. Turbulent conditions promote faster reactive mixing processes, which are essential for an efficient combustion and for reducing NO_X emissions. (Joos [83]) Both the highly swirled flow in the primary zone and the jet-in-crossflow effect of the dilution port flow generate high turbulent fluctuations in the combustion chamber. Consequently, the flow conditions at the CT interface are highly turbulent, which has a massive impact on the turbine.

Flow field measurements in actual combustion chambers are limited and rare. Typically, information about turbulence at the combustor outlet is derived from isothermal experiments on combustor simulators or numerical simulations. Schroll et al. [160] present an example of

rare measurements under realistic combustion conditions using laser-optical measurement techniques to characterize the outlet flow field of a single-sector lean-burn combustor. Regarding turbulence, the researchers recorded levels of turbulent intensity I of up to 15% with only the pilot and up to 20% with both the pilot and main flame. It is important to note that these measurements were not taken under full power of the combustor, where even higher levels of turbulence intensity may be expected.

Several experimental setups of non-reactive lean-burn combustor simulators were used to evaluate the turbulence intensity at the combustor outlet. Bacci et al. [7] reported a maximum turbulent intensity I of 28%, Beard et al. [17] reported a mean value of 11%, and Wilhelm et al. [198] reported an average of 25% with peak values of 45%. Recent investigations have mainly focused on the effects of lean-burn combustion on the flow conditions at the combustion-turbine interface. The mechanisms that create turbulence in RQL differ significantly from those in lean burn combustors, where turbulence is primarily generated by fluctuating heat release and highly swirled flow. In RQL combustion, however, turbulence is created by the mixing of secondary air with the main flow through the dilution ports, resulting in a jet in cross-flow type of flow. This leads to different length scales and distribution of turbulence. Cha et al. [33] conducted isothermal experiments on real engine hardware of an RQL combustor and the first NGV of the high-pressure turbine. They found peak levels of turbulence intensity to be 35% (Cha et al. [34]). Additionally, they noted that the length scales were similar to the size of the dilution port diameter, which is 25% of the NGV chord length for the given case.

2.2. Turbine Aerodynamics

2.2.1. Turbine Functionality and Work Extraction

The turbine is positioned downstream of the combustion chamber and converts flow energy into mechanical work that drives the compressor and fan. This energy exchange occurs via a shaft connecting the turbine and compressor. Axial turbines are typically used in aircraft engines due to their ability to handle higher air mass flows compared to radial turbines. Modern engines typically use a two or three-shaft configuration for the turbine, allowing the low and high-speed components to operate at different speeds, resulting in improved component efficiencies. The LPT can be operated at a reduced speed, leading to a notable reduction in noise emissions and shock losses in the fan. The HPT operates at a significantly higher speed to increase power density and save installation space (Bräunling [28]).

HPTs are usually designed with one or two stages, each comprising a stationary row of vanes and a rotating row of blades. The function of the stator is to accelerate the flow and induce swirl. It is commonly referred to as a NGV due to its accelerating properties. The

deflection of the stator induces a circumferential velocity component $C_{u,1}$ at the outlet of the stator. The energy change in the turbine is due to a change in momentum in the circumferential direction in the rotor blades. The *Euler turbine equation* (Eq. (2.3)) is based on the axiomatic assumption of conservation of angular momentum. It describes the specific power output of a turbine as proportional to the speed of rotation U and the deflection in the rotor ΔC_u.

$$\frac{P}{\dot{m}} = \Delta h_t = (U_2 C_{u,2} - U_1 C_{u,1}) = U \Delta C_u \tag{2.3}$$

The equation is typically applied at the midspan of the turbine, assuming stationary operation, a constant deflection distribution across the entire blade height, and a flow that follows the blade angles without deviation (incidence). It can be used in an early design stage of the turbine for a first estimation of the turbine's power output. The velocity triangles in Fig. 2.2 (right) illustrate the flow conditions in a turbine stage.

The Degree of Reaction (DoR) r is an indicator of the distribution of static pressure drop between the rotor and stator in a turbine stage.

$$r := \frac{\Delta \overline{h}''}{\Delta \overline{h}'' + \Delta \overline{h}'} \tag{2.4}$$

It relates the static isentropic enthalpy change in the rotor $\Delta \overline{h}''$ to the total static isentropic enthalpy change of the stage $\Delta \overline{h}'' + \Delta \overline{h}'$. Modern HPT are designed as reaction turbines ($r \approx 0.5$), which means that the acceleration of the flow is equally distributed over the stator and rotor. This design is optimal for reducing turbine losses (Rick [143]).

2.2.2. Turbine Efficiency

The isentropic efficiency $\overline{\eta}$ is a crucial metric for describing the capability of the turbine stage. It is defined as the ratio of the power actually generated by the turbine P to the power of the idealized isentropic process $\overline{P}$. Fig. 2.2 (left) presents the thermodynamic states and the different power definitions of a turbine stage in an h-s diagram. For an adiabatic change of state the first law of thermodynamics describes the power output of the turbine as the change in total enthalpy $P = \dot{m} \Delta h_t$. For a constant heat capacity c_p the isentropic efficiency can be expressed with the help of the temperature differences.

$$\overline{\eta} = \frac{P}{\overline{P}} = \frac{\dot{m} \Delta h_t}{\dot{m} \Delta \overline{h}_t} = \frac{T_{t,0} - T_{t,2}}{T_{t,0} \left[1 - \left(\frac{p_{t,2}}{p_{t,0}} \right)^{\frac{\gamma - 1}{\gamma}} \right]} \tag{2.5}$$

The isentropic exit temperature $\overline{T}_{t,2}$ is hereby expressed by the pressure ratio over the turbine stage using the isentropic relation. This definition of efficiency is only applicable to

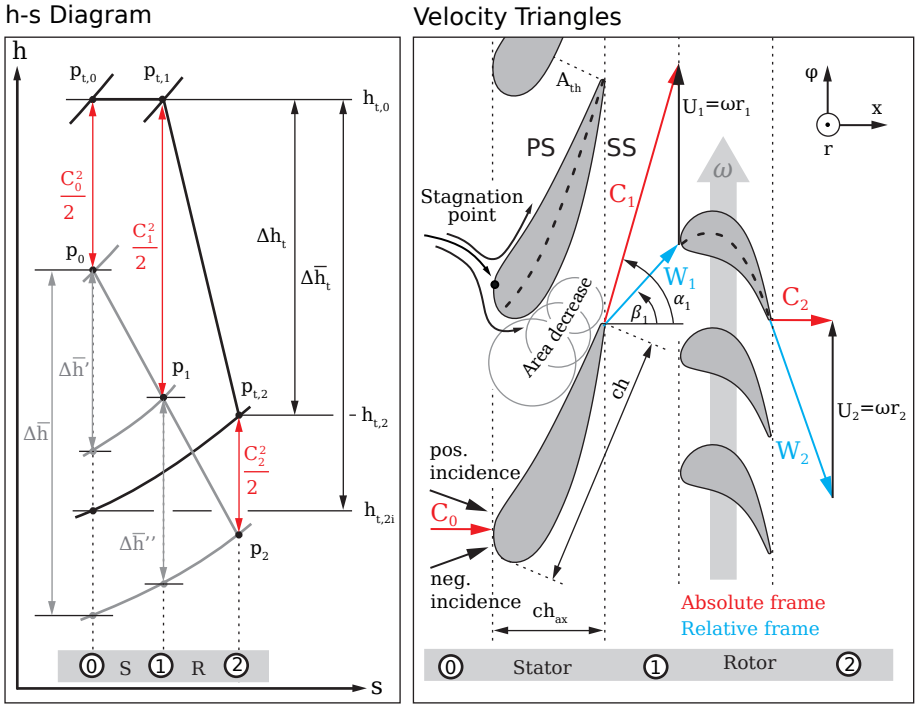

Figure 2.2.: Turbine velocity triangles (right) and h-s diagram of the change of state in a one stage HPT (left)

uncooled geometries. However, HPTs are typically cooled and have cavities from which sealing air exits, resulting in a mixture of cooling and sealing air in the hot gas path. The additional mass flows introduced must be considered when calculating the efficiency, as mixing losses and cooling air volume can significantly impact stage efficiency. The literature discusses various approaches to calculating the ideal power $\overline{P}$ in the cooled case (Young and Horlock [201], Suresh et al. [178]). The definition by Hartsel [66] is commonly used. All mass flows entering the system are considered separately so that each case expands isentropically to a common outlet pressure $p_{t,2}$. Fluid properties such as c_p or the isentropic exponent γ are strongly temperature dependent, so the values for the hot gas and the cooling air are very different. Therefore, individual fluid properties c_{pi} and γ_i are determined for each mass flow entering the system. These are calculated by averaging between the respective inlet of the different mass flows and the common outlet.

2.2.3. Turbine Loss Mechanisms

The following section provides an explanation of the loss mechanisms that occur in high-pressure turbines, which are relevant to an understanding of the present work. The discussion is centered on flow losses due to friction and secondary flow phenomena. A comprehensive explanation of the losses in turbomachinery is available in Lakshminarayana [95] and Denton [41]. Numerous loss mechanisms are involved in turbomachinery operations. According to Denton [41], losses are always accompanied by an increase in entropy, i.e. they are irreversible processes in which energy is dissipated. For ideal gases, the rise in entropy can be expressed by the change in total pressure and total temperature between inlet and outlet, following

$$\Delta s = c_p \cdot ln\left(\frac{T_{t,out}}{T_{t,in}}\right) - R \cdot ln\left(\frac{p_{t,out}}{p_{t,in}}\right). \tag{2.6}$$

Hereby c_p denotes the specific heat capacity under constant pressure and R the specific gas constant of the fluid. In the flow through an adiabatic, stationary vane passage, the total temperature is constant and the increase in entropy caused by friction losses is only accompanied by a reduction in total pressure. In this case, the total pressure loss coefficient Y (Eq. (2.7)) can be used to quantify the losses in the vane row. It reflects the total pressure loss in relation to the dynamic pressure at the outlet of the vane passage. The total pressure loss coefficient includes the losses of all kind and does not differentiate between the different loss mechanisms. In Eq. (2.7), $\bar{p}_{t,in}$ represents the mass flow-averaged total pressure on the inlet of the vane row, while p_t denotes the local total pressure. The dynamic component of the outlet pressure is defined as the difference between the total pressure $\bar{p}_{t,out}$ and the static pressure $\bar{p}_{out}$ at the outlet boundary of the domain. In case of a cooled vane, the change in total temperature due to the cooling is neglected.

$$Y := \frac{\bar{p}_{t,in} - p_t}{\bar{p}_{t,out} - \bar{p}_{out}} \tag{2.7}$$

It is worth noting that the various individual losses often interact and, therefore, can hardly be fully separated from each other. However, losses are typically classified into four categories.

- Friction losses
- Secondary flow losses
- Leakage losses
- Cooling losses

Denton [41] states that, for an uncooled turbine, the total losses are equally contributed to by friction losses, secondary flow losses, and leakage losses.

Friction Losses

The no-slip condition is applicable to viscous flows around walls, wherein boundary layers develop between the wall and the free flow around it. These layers cause velocity and pressure gradients with increasing flow length along the wall. The shear processes accompanying these gradients cause friction losses, which result in total pressure losses at each wetted surface. In a turbine stage, these surfaces comprise the aerofoils, as well as the hub and shroud endwalls. The friction losses at the profiles surfaces are called *profile losses*. The boundary layers on the pressure and suction side of the vanes converge at the trailing edge, forming the wake. The wake of a profile is characterized by a velocity and total pressure deficit, which leads to gradients and sheer processes and thus is source of further losses. These losses are called *wake losses* or *mixing losses* but are often attributed to the *profile losses* (Bräunling [28]). The losses originating from the boundary layers at the hub and shroud endwalls are called *endwall losses*. An additional loss mechanism falls under the category of friction losses. Even in absence of solid walls, losses are generated by turbulent redistribution and mixing processes. In a turbulent flow, part of the kinetic energy of the mean-flow is converted into Turbulent Kinetic Energy (TKE) and later dissipated into heat. The velocity gradients in the vortices lead to shear and thus friction losses. These losses are called *freestream losses*.

Secondary Flow Losses

Secondary flows refer to flows that deviate from the main flow direction and often results in losses. The extensively utilized theory of inviscid secondary flows is founded on the theory by Hawthorne [68] and extensively explicated by Sieverding [167]. It is grounded in the concept of inviscid, incompressible flow through a linear cascade. Fig. 2.3 provides an illustration of the development mechanisms of secondary flows. These are generated due to the interaction between incoming boundary layer profiles at the inner and outer endwall, curvature, and pressure gradient in the passage. There exists a pressure gradient $\frac{\partial p}{\partial y}$ between pressure and suction sides of the adjacent vanes, which is assumed to be constant over the entire passage height. As fluid particles move through the passage, they follow a curved trajectory creating centrifugal forces. The pressure and centrifugal forces are balanced along the streamline of the particle.

$$\frac{\partial p}{\partial y} = \frac{\rho u^2}{R} \tag{2.8}$$

In the undisturbed part of the passage, a fluid particle travels at a velocity of u_A and follows streamline A-A-A. However, in the velocity deficit of the boundary layer (B), a second particle experiences reduced velocity ($u_B < u_A$), but both particles are subjected to

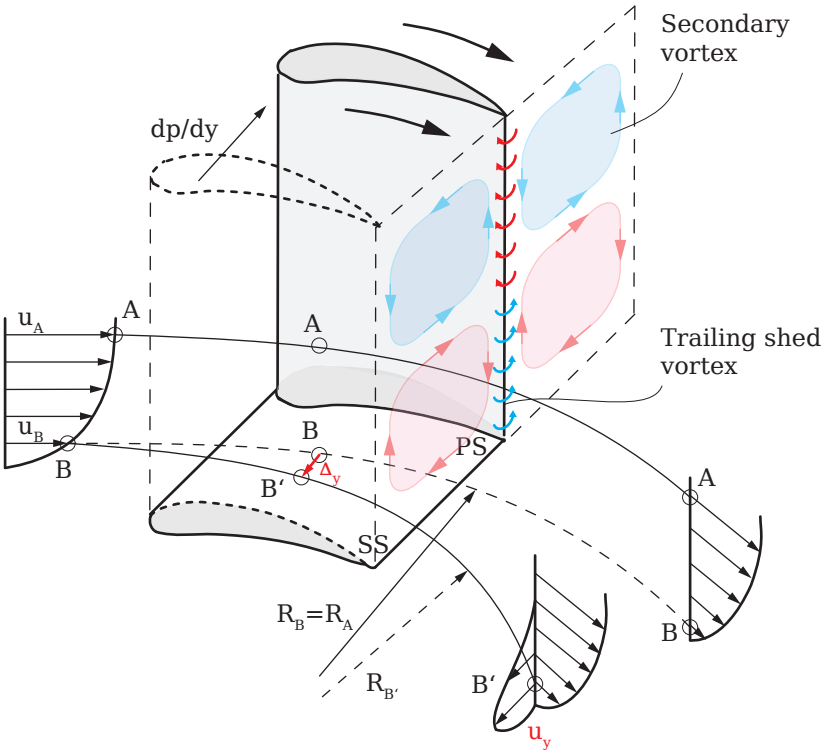

Figure 2.3.: Schematic illustration of classical inviscid secondary flow phenomena in vane passage (based on Hawthorne [68], according to Lakshminarayana [95] and Sieverding [167])

identical pressure force. To establish a state of equilibrium between pressure and centrifugal forces (Eq. (2.8)), the trajectory radius B-B'-B' needs to be smaller than that of A-A-A ($R_{B'} < R_A$). This generates a deflection Δy and a velocity component u_y perpendicular to the main flow direction. This phenomenon arises at both end walls, creating a pair of large, counter-rotating secondary circulations known as secondary or *passage vortices*.

At the trailing edge of the vane profile, the passage vortices from neighboring vane passages meet, locally with opposite flow directions. This results in the formation of an additional vortex system, also known as *trailing edge vortex* which counterbalances these opposing secondary flows. Following the theory of Hawthorne [68], these secondary vortices are

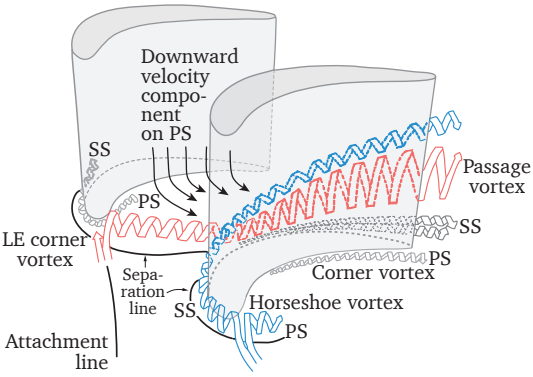

Figure 2.4.: Schematic illustration of viscous secondary flow phenomena in vane passage according to Goldstein and Spores [57], adapted from Schneider [158]

reinforced by the *trailing shed circulation* and the *trailing filament circulation*.

In addition to inviscid secondary flows, viscous effects produce noticeable secondary flow characteristics. When the boundary layers of the hub and shroud endwalls encounters the profiles of the vanes at their leading edges, it rolls up on both the pressure and suction sides to develop the horseshoe vortex system (Fig. 2.4). The leg on the suction side follows the surface of the vane (Sieverding [167]). Due to the pressure gradient in the passage the pressure side leg of the horse shoe vortex shifts towards the suction side of the neighboring vane when moving downstream through the passage. Here it merges into the *passage vortices*. Additional vortices form in the corners of the vanes and the endwalls. These are called *corner vortex* and are difficult to detect due to their weak characteristics.

The schematic illustrations in Fig. 2.3 and Fig. 2.4 are very simplified. In reality, the depicted secondary flow systems are interacting with each other to form a very complicated Three-Dimensional (3D) flow field. 3D formed profiles and endwalls can help to reduce the negative impact of secondary flows, but they cannot be completely eliminated. The implementation of fillet radii at the junction between profile and end walls can help to reduce the development of the horseshoe vortex (Zess and Thole [202], Mank et al. [107]). Additionally, the lean and bow of the profiles and the non-axisymmetric endwall contouring can help to reduce secondary flow losses by reducing the strength or location of the aforementioned secondary flow features (Poehler et al. [133]).

Leakage Flow Losses

The third significant cause of loss in turbomachinery is leakage flows, which commonly arise at various locations in a turbomachine, predominantly between fixed and moving elements, such as the blade tip of a rotor and the surrounding casing. The tip leakage flow usually generates a vortex system when it interacts with the primary passage flow, which leads to energy losses and diminishes the power input/output of the blade row by decreasing the masses contributing to the power generation. In this study, the focus is on stationary vane rows where leakage flows do not have a significant impact. Detailed descriptions of the associated phenomena will not be provided but can be found in relevant literature (Lakshminarayana [95], Bräunling [28]).

Cooling Losses

In cooled turbines, additional losses are incurred as a consequence of the thermal equalization of fluids of disparate temperatures and the shear stress associated with the mixing of coolant and main flow air (Farokhi [49]).

2.2.4. Turbine Capacity

The maximum mass flow through the engine core is dictated by the smallest cross section of the core. This is typically in the high pressure turbine either in the first NGV or rotor. A common design philosophy is to operate the HPT in a choked condition. This means that the turbine operates at $Ma = 1$ in the smallest cross section, also called the throat area. The advantage of this operation is a constant reduced mass flow over a wide range of operating points. The maximum corrected mass flow in the smallest cross section, also called the *capacity* (Eq. (2.9)), is invariant to a reduction in outlet pressure.

$$\Gamma := \frac{\dot{m}_{40}\sqrt{T_{t,40}R}}{A_{40}p_{t,40}} \tag{2.9}$$

This makes the capacity a very important design parameter as it links the operating point of the turbine with that of the compressor.

2.3. Turbine Heat Transfer and Cooling

2.3.1. Heat Transfer

The first stage of the high-pressure turbine is one of the most thermally stressed parts of the engine. The turbine materials face significant demands due to the hot combustion gases that heat them up. INCONEL 100, an advanced nickel-based alloy, is commonly used to withstand these demands (Bräunling [28]). The life of the components is directly impacted by the material temperature. The primary threats to the life of the turbine are thermal fatigue, corrosion or sulfidation, and creep. The rotating blades of the turbine rotor are particularly susceptible to creep damage due to the high thermal and mechanical loads they experience. Creep is exponentially dependent on temperature (Larson and Miller [96]), and a 10K increase in blade temperature leads to a halving of creep lifetime (Bräunling [28]). Determining the precise metal temperature is crucial but often challenging, introducing uncertainties into the design process of high-pressure turbines. Montomoli et al. [123] presents the translation of these uncertainties into lifetime uncertainties.

Heat transport is achieved through heat conduction, heat convection, and radiation, as explained by Stephan et al. [173]. Fourier's law

$$\dot{q} = -\lambda \frac{\partial T}{\partial y} \tag{2.10}$$

describes heat conduction in solid materials and stagnant fluids, where $\dot{q}$ is the specific heat flux and λ is the material-specific thermal conductivity. Heat conduction always occurs from high to low temperature, as indicated by the negative sign. Similar to the velocity field, the temperature profile also develops a boundary layer when approaching solid walls (refer to Fig. 2.5).

Heat transfer from the fluid to the solid at the profile walls is a complex process that involves heat conduction and convection. It depends not only on the material properties and temperature difference between the fluid and solid wall, but also on the flow conditions close to the wall, such as turbulence intensity, velocity and temperature boundary layer, and wall roughness (Bons [24]). All these effects serve as a thermal resistance for the heat flux from the hot gas into the turbine blade material.

The no-slip condition results in zero velocity at the wall, which reduces heat transfer directly at the wall to heat conduction. The wall heat flux $\dot{q}_W$ can be described using:

$$\dot{q}_W = -\lambda \left(\frac{\partial T}{\partial y} \right)_{y=0}. \tag{2.11}$$

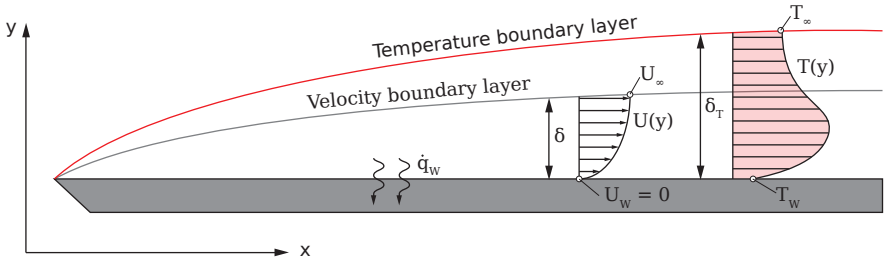

Figure 2.5.: Thermal boundary layer and heat transfer in a boundary layer flow over a flat plate

The temperature gradient at the wall is usually unknown because it depends on the local flow conditions near the wall. Therefore, the common approach is to apply Newton's law (Eq. (2.12)), which correlates the wall heat flux with the temperature difference between the main flow and the wall using the HTC h. The HTC includes all the unknown boundary layer effects together with the material properties. It is important to note that this approach assumes a linear relationship between the wall heat flux and the temperature difference and is based on empirical observations.

$$\dot{q}_W = h(T_\infty - T_W) \tag{2.12}$$

In Eq. (2.12), T_∞ represents the bulk temperature of the main flow, while T_W represents the wall temperature. Determining both values accurately can be challenging. In situations where there are local temperature differences, it may be more appropriate to use the adiabatic wall temperature $T_{W,ad}$ as the reference temperature (Moffat [122]). As a consequence of viscous dissipation in the boundary layer, the temperature of lossy deceleration $T_{W,ad}$ differs from the ideal temperature $T_{t,\infty}$. The Prandtl number $Pr = \nu/\lambda$ is the determining factor as to whether $T_{W,ad}$ is above or below the ideal temperature $T_{t,\infty}$. For $Pr > 1$, the viscous effects are larger than the heat conduction, resulting in $T_{W,ad}$ being larger than $T_{t,\infty}$. The *recovery factor* r describes the ratio of temperature rise between adiabatic and lossy deceleration (Schlichting and Gersten [150]).

$$r =: \frac{T_{W,ad} - T_\infty}{T_{t,\infty} - T_\infty} \tag{2.13}$$

To determine the actual wall temperature and the heat flux through the wall, CFD must be considered for the external flow and Finite Element Analysis (FEA) for the internal heat conduction in a one-way or two-way coupled iterative process (CHT). In numerical studies, the focus is often on the effect of aerodynamics on heat conductivity at the wall (HTC). The HTC can be described as the gradient of heat flux per change of wall temperature

($h = \partial\dot{q}/\partial T_W$). When assuming a linear relation between wall heat flux and the driving temperature difference, the HTC can be approximated linearly by using central differencing (Metzger et al. [120]). Two simulations with different fixed wall temperatures are conducted to calculate the HTC using:

$$h = \frac{\dot{q}_{W,1} - \dot{q}_{W,2}}{T_{W,1} - T_{W,2}}. \tag{2.14}$$

However, upon closer examination of the relationship between heat flow and wall temperature, it was discovered that the linear assumption is not always valid. Maffulli and He [106] proposed a quadratic approach to approximate the HTC. This approach requires three simulations using different wall temperatures. The first simulation sets the heat flow through the wall to zero and uses the adiabatic wall temperature. The other two simulations use fixed wall temperatures, one slightly below the cooling temperature and the other slightly above the farfield temperature. Fig. 2.6 presents a schematic representation of this process to calculate the HTC. The relationship between wall heat flux $\dot{q}_W$ and wall temperature T_W is described by a quadratic function.

$$\dot{q}_W = C_1 + C_2 T_W + C_3 T_W^2 \tag{2.15}$$

The coefficients C1, C2, and C3 are determined by solving the linear system of equations obtained by describing Eq. (2.15) for all three simulations. Finally, by replacing T_∞ with $T_{W,ad}$ in Eq. (2.12), the HTC h can be calculated using the same equation.

$$h = C_2 + 2C_3 T_{W,ad} \tag{2.16}$$

The quadratic approximation is used to calculate all HTC values presented in this work.

The *Nusselt* number (Eq. (2.17)) represents the dimensionless form of the HTC, using the chord-length of the NGV as reference length and the thermal conductivity of the fluid λ. It can be interpreted as the ratio of the characteristic length of the problem to the thickness of the thermal boundary layer (Lakshminarayana [95]).

$$Nu = \frac{hL_{ref}}{\lambda} \tag{2.17}$$

On the surface of an HPT vane, the highest HTC is typically found at the leading edge where the hot gas impinges on the vanes and the thermal barrier effect of the boundary layer is low due to its thinness. The transition between laminar and turbulent boundary layers plays a significant role in the distribution of HTC. The higher energy transfer towards the wall in a turbulent boundary layer results in increased HTC values. For this reason, the HTC is typically higher on the suction side than on the pressure side of a profile (Lakshminarayana [95]). The highest HTC values on the endwalls are located towards the throat in the rear of the passage. This is due to the strong acceleration and high levels of secondary flow in that area (Werschnik et al. [195], Qureshi et al. [137]).

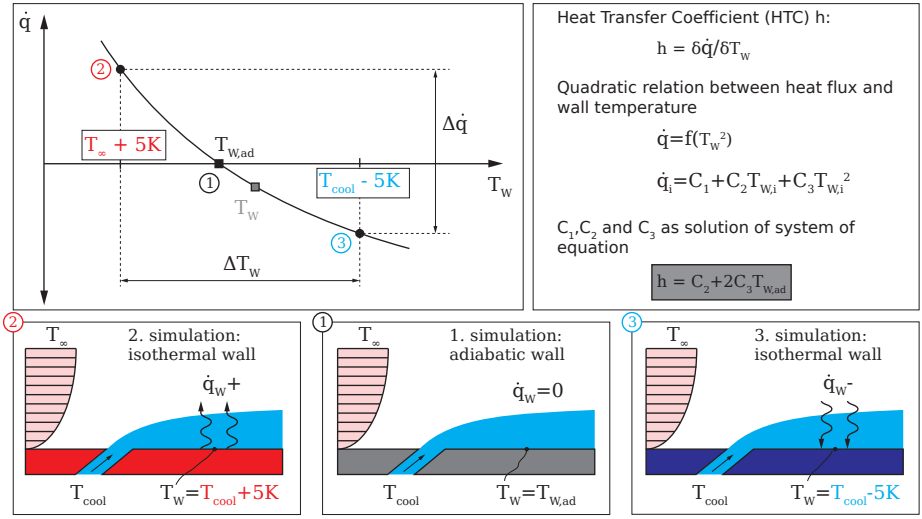

Figure 2.6.: Calculation of HTC using the cubic approximation (adapted from Bakhtiari [10])

2.3.2. Turbine Cooling

The temperatures of the hot gas in the high-pressure turbine are well above the melting point of the turbine materials. To prevent severe damage to the vanes and blades, they are actively and passively cooled (Bräunling [28]). Passive cooling is achieved by applying thermal barrier coatings to the surface of the profiles, which reduces heat conduction into the metal.

Active cooling measures can be further divided into internal and external cooling. Internal cooling involves the flow of cool air through channels within the vanes and blades to remove heat from the metal. The mechanism described in Section 2.3.1 is reversed, with the hot metal transferring heat to the colder fluid. To achieve a high HTC, turbulence can be increased or impingement cooling can be used. Additionally, introducing cooling ribs to the channels maximizes the area for heat transfer.

In the first stage of HPT, the thermal load is so high that internal cooling is not sufficient. Therefore, the turbine material is also externally cooled by blowing cool air along the surface of the profiles to create a protective cooling layer. In most cases, discrete film cooling holes are distributed over areas of the highest thermal load. The holes are cylindrical or fan-shaped. Fan-shaped holes act as a diffuser by expanding the cross-section towards the

surface of the profile. This reduces the momentum ratio of the cooling jet and the main flow, which in turn reduces the penetration depth of the cooling jet and keeps it close to the wall where cooling is required. Han et al. [65] provides a collection of studies on these different cooling concepts.

Turbine cooling is crucial for enabling the engine to operate at higher turbine inlet temperatures, which enhances overall efficiency (Bräunling [28]). However, the air used for cooling is drawn from the compressor, directed around the combustion chamber, and therefore not utilized for power generation in the turbine, resulting in a reduction of efficiency. An effective turbine cooling design is crucial to balance the need for turbine material protection and safe engine operation with high efficiency and optimal power generation in the turbine.

Film Cooling Effectiveness

To evaluate the effectiveness of film cooling, the adiabatic film effectiveness η_{fc} is often considered (Bogard [23]). It measures the effectiveness of film cooling to reduce the adiabatic wall temperature.

$$\eta_{fc} = \frac{T_{t,ref} - T_t}{T_{t,ref} - T_{t,30}} \tag{2.18}$$

In Eq. (2.18), T_t is the adiabatic wall temperature in the cooled configuration, $T_{t,30}$ the coolant temperature and $T_{t,ref}$ the adiabatic wall temperature of the uncooled reference case. Two simulations are used to calculate the different temperatures. The first one determines the uncooled reference temperature by simulating a setup where all cooling mass flows are turned off. The second simulation has all cooling features enabled. Both simulations use the same inlet Boundary Conditions (BC), run for the same simulation time, and collect the values for averaging over the same period. Low values of η_{fc} mean the wall temperature in the cooled and the uncooled case are close to identical, and the film cooling has no effect in this region. A high value implies a wall temperature close to the cooling temperature and, thus an optimal cooling effect.

2.4. Combustor Turbine Interaction

In recent years, numerous numerical and experimental studies have contributed to the fundamental understanding of the effects at the CT interface and the impact of combustor-related flow features on the operation of the high-pressure turbine. As outlined in Section 2.1.3, the turbine is most affected by combustor swirl, temperature non-uniformities (hot streaks), and turbulence. Schneider [158] provides a comprehensive literature review of studies on these features.

Dedicated rigs are available to investigate the impact of combustor related flow features on turbine performance and thermal load. In Europe, the following rigs exist to investigate the interaction between the combustor and turbine. These are among others: The Large Scale Turbine Rig (LSTR) facility at TU Darmstadt is an isothermal, low Mach number test rig. It consists of a 1.5-stage scaled-up turbine stage that is dedicated to investigating the influence of inlet swirl on the aerodynamics and cooling of the high-pressure turbine (Krichbaum et al. [93]). Due to its scaled up geometry it allows for excellent measurement access, enabling detailed flow measurements. The Oxford Turbine Research Facility (OTRF) is a short-duration blowdown rig that houses the MT1 turbine. Its purpose is to investigate various cooled and uncooled turbine configurations under realistic inlet BC (Povey and Qureshi [135], Chana et al. [35]). The NG-Turb test facility, operated by the DLR in Göttingen (Rehder et al. [142]), can accommodate up to 2.5 stages of high-pressure turbine and operates in a continuous loop. The facility allows for testing of various turbine configurations, including the INTER-Turb rig (Wolf et al. [199]), which is designed to investigate the interaction between combustor and turbine using a combustor simulator in front of the HPT, and the Trisector rig (Koupper et al. [90]). The latter enables the flow in a novel lean burn combustor and its effect on the downstream HPT to be investigated. The Turbomachinery Laboratory at ETH Zurich operates the LISA test rig, a 1.5-stage turbine test facility used to investigate unsteady phenomena in turbines (Behr et al. [20]).

Intensive research on this topic has been conducted in the United States of America. Early experiments were conducted by NASA at the Combustor Exit Radial Temperature Simulator (CERTS) (Dorney and Schwab [44]). The Large Scale Rotating Rig (LSRR) is a rotating rig for investigating inlet temperature distortions at the United Technology research Centre (Butler et al. [29]). The Air Force Research Laboratory runs the Turbine Research Facility (TRF) to investigate the effect of combustor exit profiles on the aerodynamics and heat transfer of the vanes (Barringer et al. [11], [12], [13]). The Gas Turbine Laboratory of the Ohio State University is running tests on hot streak migration (Mathison et al. [111]). In addition to the availability of experimental test data, numerical analyses play an important role in the investigation of CTI.

The section below outlines the key findings of CTI-related research over the past few decades.

Hot Streaks

The investigation of the effect of temperature distortions, also known as hot streaks, on the high-pressure turbine yields the following key takeaways:

- The rotor blades experience high thermal loads in the presence of temperature non-uniformity, particularly on the pressure side, which is subject to hot streak induced secondary flow, also called preferential heating (Butler et al. [29], Shang and Epstein

[163] and Salvadori et al. [147]). The hub and tip of the rotor can experience high thermal loads due to the interaction between vane secondary flow and the migration of hot streaks in the rotor (Ong and Miller [127] and Basol et al. [14]).

- The thermal load of the rotor is particularly affected by the clocking and circumferential extent of the hot streak (He et al. [69] and He et al. [70]). It can be reduced when clocking the hot streak to the Leading Edge (LE) or pressure side of the of the preceding vane (Gundy-Burlet and Dorney [62], Jenkins and Bogard [81] and Basol et al. [14]).
- The presence of hot streaks reduces the turbine efficiency by up to 0.8% (Beard et al. [16], Salvadori et al. [147] and Qureshi et al. [138])
- Peak temperatures of hot streaks decrease as they pass through the HPT, especially when encountering high levels of free stream turbulence and highly cooled vanes and blades (Jenkins et al. [80], Jenkins and Bogard [81]).

Swirl

Residual swirl from the combustor is effecting the flow in the high pressure turbine. As noted by Beard et al. [17] and Schmid [151], this effect is primarily limited to the first NGV. The investigations conducted on this topic in recent years have highlighted the following:

- The turbine efficiency is reduced by 1-3.1% due to the presence of inlet swirl (Schmid et al. [153], Beard et al. [15], Beard et al. [17] and Pyliouras et al. [136]). This is due to not ideal inflow, resulting in incidence and higher losses in the turbine (Werschnik et al. [195]).
- It is widely reported that the swirl of the combustor has an impact on the thermal load and cooling of the NGV. The swirling inflow is inducing up and down wash on the surfaces of the vanes which is changing the HTC distribution on the vanes (Qureshi et al. [139]), inner end wall (Werschnik et al. [193], Werschnik et al. [194] and Schmid and Schiffer [152]), outer endwall, rotor casing (Qureshi et al. [137]) and rotor tip (Wilhelm [197]). The film cooling effectiveness is also affected by the swirling inflow (Giller and Schiffer [56], Insinna et al. [77]).
- According to reports by Jacobi and Rosic [78] and Shaikh and Rosic [162], the interaction between the leading edge of the vanes and the residual combustor swirl is causing unsteady secondary flow features which alter the HTC on the vanes.
- To counteract these penalties, several optimizations of the vane geometry have been conducted to improve its operation under heavy swirling inflow (Shih and Lin [164]).

At least some of the aerodynamic penalties could be recovered (Shahpar and Caloni [161])

Swirl and Hot Streaks

In addition to individually analysing the effects of hot streaks and swirl on the high-pressure turbine, both phenomena are also studied together as they interact with each other (Khanal et al. [85]). Dedicated rigs are utilized to investigate the combined effect of swirl and temperature non-uniformities on the HPT (Hall et al. [64], Hall and Povey [63], Koupper et al. [90], Andreini et al. [4], Andreini et al. [5] and Beard et al. [18]).

- The presence of swirl at the inlet of the turbine is leading to an up- or down wash of the hot streak on the vanes surfaces (Khanal et al. [85], Bacci et al. [9]).
- The stagnation line is shifted due to the swirling inflow (Insinna et al. [76] and Bacci et al. [8]). This leads to a change in vane loading
- The combination of hot streaks and swirl alters the film cooling effectiveness (Bacci et al. [8] and Insinna et al. [77]).
- The positioning of the hot streak and swirl in relation to the leading edges of the vanes (clocking) is affecting the thermal load on the vanes. The highest temperatures on the vanes occur when the hotspot is aligned with the LE (Griffini et al. [58], Bacci et al. [8], Koupper et al. [91]).

Turbulence

As stated in Section 2.1.3, the turbulence levels are high in the combustion chamber and consequently also at the turbine inlet. The investigation into the effects of high turbulence at the turbine inlet yielded the following results:

- High levels of inlet turbulence is affecting the losses in the turbine (Folk et al. [51]). As per the research, the presence of combustor turbulence results in a 50% increase in turbine losses. Furthermore, the research determined the percentage contribution of each loss mechanism to the total losses.
- The heat transfer on the vane surfaces is affected by the level of free stream turbulence. Higher levels of free stream turbulence lead to an augmentation of the heat transfer on the vanes (Ames et al. [2], Nasir et al. [125]). This is due to changes in the vanes boundary layers (Radomsky and Thole [140]).

- The migration of the hot streak downstream is influenced by the level of turbulence in the free stream (Ong et al. [128]). A higher level of turbulence leads to greater mixing of the hot gas with the colder surrounding air, resulting in reduced peak temperatures as it moves through the vane passage (Jenkins et al. [80]). The positioning of the hot streaks relative to the LE of the vanes does not affect this trend (Jenkins and Bogard [81]).

Uncertainties

The flow conditions at the interface between the combustor and turbine are subject to uncertainties due to the challenging conditions, such as high temperatures, which make it difficult to measure or numerically predict the exact flow conditions. The typical uncertainty in temperature predictions at the CT interface is around $\pm$ 2% of $T_{t,40}$, as reported by Montomoli et al. [123]. Schneider [158] reported mean temperature differences of up to 3.5% due to sector-to-sector variations in the combustor. Uncertainty Quantification (UQ) frameworks are utilized to determine the propagation of uncertainties arising from the inlet condition in the turbine. Schneider et al. [159] combined a parametrized combustor exit flow model with a polynomial chaos UQ method and highlighted that uncertainties in predicting the swirl position relative to the NGVs leading edge are critical, as they determine the strength of swirl-induced secondary flows in the turbine.

CFD Analysis of Combustor-Turbine Interaction

Experimental data at the CT interface is limited due to the harsh conditions in the combustion chamber. Rig tests are typically conducted under isothermal conditions, without taking into account the chemical reactions that occur during the combustion process. Test rigs are designed to mimic realistic interface conditions using combustor simulators. However, to account for the real combustion effects at the CT interface, numerical simulations are the only tool to deliver the full data set. As previously stated, the industry standard involves simulating each component separately and exchanging interface data. Most design tools still use steady-state RANS simulations. However, due to the increasing computational capacity, transient and scale-resolving simulations are also becoming more important (Tyacke et al. [187]).

LES methods are commonly used in the design of combustion chambers. Recent publications have shown that Scale-Resolving Simulation (SRS) methods can improve the prediction of correct combustor exit conditions. Boudier et al. [26] conducted LES and RANS simulations

of an inverted-flux combustor operating according to the RQL combustion concept. The comparison with measurement data highlighted the improved prediction of RTDF distribution in LES compared to RANS.

Cubeda et al. [38] found similar results when comparing the data at the outlet of a combustor simulator between RANS simulation and a scale-resolving Scale-Adaptive-Simulation (SAS). The SAS results showed much better agreement with experimental data, whereas the RANS simulation predicted exaggerated temperature peaks.

When considering swirl and flow angles at the combustor outlet, SAS results match experimental data better than RANS results. This was demonstrated by Hilgert et al. [72] through simulating the combustor simulator of the LSTR and comparing the results of SAS and RANS to experimental data.

When conducting turbine CFD simulations, the use of unsteady methods such as URANS or even SRS has been shown to be beneficial, particularly for off-design operation (Dombard et al. [43]) and for resolving the interaction of multiple stages (Tallman [180]). Cottier et al. [37] demonstrated the improved ability to predict temperature mixing in SAS compared to RANS by means of RTDF distributions upstream and downstream the first NGV of the HPT. This was achieved through simulation of the Trisector rig, which consists of a combustor simulator and a 1.5 stage HPT.

The SRS of the HPT shows promise in improving the thermal predictive accuracy of turbine CFD simulations. However, it requires higher computational resources and more sophisticated inlet BC. To accurately simulate combustor-related turbulence in the turbine, these fluctuations must be prescribed at the inlet of the simulation. Cubeda et al. [38] highlighted this by comparing HPT simulation results using different inlet BC. The current industrial standard involves using the mean field of a combustor simulation as inlet BC for the steady state RANS simulation of the turbine. The aerothermal results of this baseline NGV simulation were compared to the integrated combustor-NGV simulation using SAS turbulence modelling. The scale resolving character of the NGV inflow affected both the thermal load and film cooling on the NGV, resulting in temperature differences of up to 150K compared to the RANS results. Tomasello et al. [181] conducted similar investigations on a real combustor-turbine geometry and also concluded that prescribing realistic combustor turbulence is necessary for accurately predicting the film cooling effectiveness on the HPT vanes. Verma et al. [190] compared the integrated scale-resolving simulation of the combustor and NGV with the RANS simulation of the NGV using mean values as inlet BC. Differences in the NGV results were noted.

Duchaine et al. [46] emphasizes the importance of defining realistic inlet BC, which requires spatial and temporal coherence of the fluctuations. To accurately transfer combustor-related unsteadiness into the turbine, it is best to simulate both components in one domain (Klapdor et al. [86]; Raynaud et al. [141]). However, this approach is often challenging due to the

differing requirements on the CFD solver in both components. Most of the time, it is only used on isothermal rig geometries or only taking combustor and first NGV into account.

When using different CFD solvers for the combustor and turbine, it is necessary to couple both solvers within a co-simulation (Vagnoli and Verstraete [188], Miki et al. [121]) or transfer unsteady interface data between the two simulations. Tomasello et al. [182] compared the integrated simulation of the combustor and NGV with different NGV-only simulations. The first NGV-only simulation used time-averaged mean field data as inlet BC. The second simulation of the NGV uses time-resolving interface data from a combustor-only simulation as inlet BC. Comparing these three simulations showed an improvement in predicting film cooling effectiveness on the NGV vanes when using the unsteady inlet BC compared to the steady RANS. However, even the unsteady inlet BC simulation could not perfectly match the integrated simulation results. This could be due to the absence of the NGV in the combustor-only simulation.

In a recent study, Martin et al. [108], Martin et al. [109] introduced the Spectral Proper Orthogonal Decomposition (SPOD) method to recycle and compress data at the combustor-turbine interface of the integrated simulation. The study used a lean-burn combustor simulator and the first film-cooled NGV of the HPT. Several stand-alone NGV simulations were performed with different inlet BC. A strong agreement was found between the SPOD boundary condition simulations and the integrated simulation and measurement data when comparing the aerothermal results.

3. Methods Review - CFD and Unsteady Inlet Boundary Conditions

This chapter provides an overview of the theoretical basis of the CFD methods employed. It describes the conservation equations used to describe the state of the flow, the numerical discretisation schemes and the different turbulence models. It also evaluates the capability of the CFD solver to predict the flow in a combustor-turbine case by comparing the simulation results to experimental data of a research turbine. Finally, it presents the most commonly used methods for creating unsteady inlet boundary conditions.

3.1. Computational Fluid Dynamics

This section provides an overview of the fundamental principles of fluid mechanics that underpin the flow simulations presented in this thesis. In the following, the central terms and their mathematical formulations of the conservation principles required to describe the fluid flow are discussed, before the numerical methods for solving these equations are explained. Finally, the key concepts of turbulence modelling are discussed. The existing literature provides comprehensive information on the subject areas of fluid mechanics, including Bird et al. [22] and Spurk and Aksel [172], on the topic of CFD, including Ferziger and Perić [50], Hirsch [73] and Schäfer [149] and on turbulence modelling Pope [134], Wilcox [196] and Davidson [40]. Most of the basics in this section are based on these sources and for further details please refer to them.

3.1.1. Conservation Equations

Technical flows can be described by the conservation equations for mass, impulse, energy and species. The general differential form of the conservation equation for the quantity Φ

$$\underbrace{\frac{\partial(\rho\Phi)}{\partial t}}_{\text{temporal change}} + \underbrace{\frac{\partial(\rho u_i \Phi)}{\partial x_i}}_{\text{convection}} = \underbrace{\frac{\partial}{\partial x_i}\left(\alpha_\Phi \frac{\partial \Phi}{\partial x_i}\right)}_{\text{diffusion}} + \underbrace{S_\Phi}_{\text{Source}} \tag{3.1}$$

balances the surface fluxes of Φ and source terms. The resulting equation can be broken down into a temporal change term, a convection term, a diffusion term and source terms. A simplified representation often used is the material derivative $\frac{D\Phi}{Dt}$, which summarizes the temporal and convective changes.

Mass Conservation

For Φ=1, the equation describes the conservation of mass. There is no creation and destruction of mass, which eliminates the source term S_Φ from the equation. This simplifies Eq. (3.1) to the continuum equation

$$\frac{\partial \rho}{\partial t} + \frac{\partial (\rho u_i)}{\partial x_i} = 0. \tag{3.2}$$

Momentum Conservation

According to the law of conservation of momentum, the sum of all forces acting on a body is equal to the change in momentum over time. In Eq. (3.3), f_i describes the specific volume forces.

$$\rho \frac{Du_i}{Dt} = \frac{\partial \tau_{ij}}{\partial x_j} + \rho f_i \tag{3.3}$$

The stress tensor τ_{ij} describes the forces resulting from local deformations, which is crucial for the diffusive momentum flow. The material equation of *Newtonian* fluids relates the stress tensor τ_{ij} linearly to the strain rate tensor S_{ij}.

$$\tau_{ij} = -p\delta_{ij} + \lambda^* S_{kk}\delta_{ij} + 2\mu S_{ij} \tag{3.4}$$

In Eq. (3.4) the two material properties λ^* and μ are dependant on the thermodynamic state of the fluid. Taking Stokes' hypothesis $\lambda^* + \frac{2}{3}\mu = 0$, with μ being the dynamic viscosity of the fluid and substituting Eq. (3.4) into Eq. (3.3) gives the *Navier-Stokes* Equation

$$\rho \frac{Du_i}{Dt} = -\frac{\partial p}{\partial x_i} + \frac{\partial}{\partial x_i}\left[\mu\left(\frac{\partial u_i}{\partial x_j} + \frac{\partial u_j}{\partial x_i}\right) - \frac{2}{3}\mu \frac{\partial u_k}{\partial x_k}\delta_{ij}\right] + \rho f_i. \tag{3.5}$$

For a multi-dimensional flow problem, a separate conservation equation is solved for each velocity component u_i. This results in a set of three coupled differential equations in 3D. It is therefore common to use the plural form of the *Navier-Stokes* equations.

Energy Conservation

The first law of thermodynamics states that the change of energy in a system over time is caused by the work of external forces and the energy introduced into the system. The conservation of energy of a system, which is the internal energy e plus the kinetic energy $k = \frac{\rho}{2} u_i u_i$, is given by the following equation. The internal energy can be expressed by the enthalpy: $h = e + \frac{p}{\rho}$ and the commonly used form of the energy equation can be derived.

$$\rho \frac{D}{Dt}\left[\frac{u_i u_i}{2} + h\right] = \frac{\partial p}{\partial t} + \rho f_i u_i + \frac{\partial}{\partial x_j}(P_{ij} u_i) - \frac{\partial \dot{q}_i}{\partial x_i} \tag{3.6}$$

In Eq. (3.6), $\rho f_i u_i$ is the change of energy due to the volume forces, P_{ij} a tensor of friction forces and $\dot{q}_i$ the specific heat flux, which can be described by *Fourier's* law:

$$\dot{q}_i = -\lambda \frac{\partial T}{x_i} \tag{3.7}$$

with λ being the thermal conductivity of the fluid.

Equation of State

Eq. (3.2), Eq. (3.3) and Eq. (3.6) are coupled for a compressible flow as found in a turbine. A thermal and a caloric equation of state are required to close the system of equations. For this purpose, the fluid is often assumed to be an ideal gas. In this case, the thermal equation of state is

$$\frac{p}{\rho} = RT \tag{3.8}$$

and the caloric equation of state is

$$h = c_p T. \tag{3.9}$$

R denotes the specific gas constant and c_p the specific heat capacity under constant pressure. For wide temperature ranges, the material properties as c_p are defined depending on the temperature. The two equations of state, together with the equations for the conservation of mass and energy and the three conservation of momentum equations, give seven coupled equations which can be used to calculate the seven unknown variables, pressure p, density ρ, temperature T, energy e and the velocity components u_i, with $i = 1, 2, 3$.

3.1.2. Numerical Solution of Conservation Equations

The equations described in Section 3.1.1, together with a full set of boundary conditions, provide a complete mathematical model of the flow in turbomachinery. As they are partial differential equations, there is no analytical solution except in special cases where simplifications and assumptions are made. In CFD, an approximation to the solution of these equations for a given flow problem can be derived using discretisation methods. The numerical solution is subject to errors of various kinds, which are described later in this chapter.

Numerical Grid

After defining the mathematical model of the problem, the continuous model is converted into a discrete representation of the problem. This is done by dividing the geometry of the flow path into small grid elements on which the flow quantities are calculated. Numerical grids can be distinguished by the logical arrangement of the cells into *structured* and *unstructured* grids (Schäfer [149]). Structured grids have the advantage that the mesh generation effort and the resulting grid size are small. However, complicated geometries cannot be meshed in a structured manner, so unstructured grids are used in such cases. This grid type is suitable for complex geometries and adaptive mesh refinement and has a high degree of flexibility. When meshing, there is always a trade-off between the highest possible resolution of the geometry, good mesh quality and a low total number of cells to reduce the computational effort.

High mesh quality is necessary for good convergence of the numerical solution. The main quality gates are orthogonality, aspect ratio of mesh elements and volume ratio between neighboring cells. The latter is particularly important for LES.

Finite Volume Method

A discretisation method is needed to transform the continuous conservation equations into a discrete form. The Finite Volume Method (FVM) is the most commonly used form of spatial discretisation in CFD. A numerical grid (see previous section) is used to subdivide the flow problem into small volumes. To apply the conservation equations, Control Volume (CV) are defined with the element nodes as the centroid. The mesh nodes thus coincide with the centres of the control volumes. All flow variables are stored at this location. For each of the CV, the conservation equations from Section 3.1.1 are formulated in integral form. Eq. (3.10) represents the integral form of the conservation equation of the variable Φ.

The volume integrals of the convective and diffusive terms are converted to integrals over the CV surfaces using the *Gauß* integral theorem.

$$\int_V \frac{\partial(\rho\Phi)}{\partial t} dV + \int_S \rho u_i \Phi \cdot n_i dS = \int_S \alpha_\Phi \frac{\partial \Phi}{\partial x_i} \cdot n_i dS + \int_V S_\Phi dV \tag{3.10}$$

The subsequent step involves approximating the surface and volume integrals in Eq. (3.10). Procedures of varying degrees of accuracy can be used. The simplest method is the *midpoint* rule. For surface and volume integrals, the integral value is approximated by the product of the value at the surface/volume centre and the surface/volume. Other rules for the approximation of the integrals can be found in the work of Ferziger and Perić [50].

The values of Φ and the gradients of Φ are not known on the surfaces and must be interpolated with respect to the values at the CV centres. Several interpolation schemes are available, which differ in the degree of accuracy. In CFD, a commonly used interpolation scheme is the second order Central Differencing Scheme (CDS). It calculates the surface values of Φ and its gradients by linear interpolation of the adjacent centre values. As the order of the method rises, the accuracy of the numerical approximation increases. At the same time, however, the computational complexity increases and the methods become less stable. This is also true for the CDS, where oscillating solutions can occur. First-order methods, such as Upwind Differencing Scheme (UDS), do not suffer from these oscillations and are much more stable. On the other hand, the accuracy is lower and UDS introduces artificial diffusion due to the diffusive nature of the truncation error. In the UDS, the value of the upstream cell centre is used at the CV surface. For the RANS simulations in this work, a blending between CDS and UDS is used. For running LES a bounded version of the CDS is used to reduce the oscillation of the solution.

The temporal derivatives of the conservation equations must also be discretized. Explicit and implicit methods of different order are used. Explicitly the next time step $\Phi(t + \Delta t)$ is calculated based on the solution of the current time step $\Phi(t)$. In an implicit scheme the next time step is calculated based on the current time step and the next time step.

Numerical Errors

Numerical solutions always contain three types of systematic error. According to Ferziger and Perić [50] these are the following: The *modelling error*, which is the difference between the exact solution of the mathematical model and the real flow. The fluid material properties, turbulence modelling, geometric deviations, boundary conditions and periodicity assumptions affect this error.

The *discretisation error*, defined as the deviation between the exact solution of the discretized equations and the exact solution of the mathematical model. It is directly related to the

spatial and temporal resolution of the discretized model (Δ and Δt) and the order of the discretisation scheme n and decreases with the refinement of the grid.

The last type of error is the *iteration error*, which describes the difference between the iterative and the exact solution of the discretized equations. This error is closely related to the *residual* of the simulation solution and decreases with successive iterations.
It is not possible to precisely determine the errors that occur during a simulation. However, it is possible to estimate them and they should be taken into account to ensure the quality of the simulation.

3.2. Turbulence

Most technical flows are turbulent. This also applies to the flow conditions in turbomachinery. Turbulent flow is characterized by chaotic fluctuations in all flow quantities. In contrast to laminar flows, where the fluid particles move on smooth streamlines, in turbulent conditions the fluid particles follow an arbitrary trajectory. The transition from a laminar to a turbulent flow regime is determined by the ratio of inertial and viscous forces in the fluid. This ratio describes the Reynolds number

$$Re := \frac{\rho u L_{ref}}{\mu}. \tag{3.11}$$

Despite the stochastic nature of turbulence, it is also characterized by coherent vortex structures, often referred to as eddies. These turbulent structures have a characteristic length scale $\mathcal{L}$ and move on a characteristic time scales $\mathcal{T}$.

3.2.1. Turbulent Scales and Energy cascade

A very important mechanism in turbulence is the decay of turbulent eddies into smaller eddies. This process is described by the *energy cascade*, Fig. 3.1. In the *production range*, the kinetic energy of the mean flow is converted into TKE by shear processes and forms the largest turbulent eddies. These typically have the size $\mathcal{L}_0$ of the dominant geometric features of the flow. In the *inertial range* the large eddies decay into ever smaller eddies, ranging over multiple scales in size. This process takes place in energetic equilibrium. Turbulent production and dissipation balance each other out. At the end of the *energy cascade*, the size of the eddies reaches the *Kolmogorov* scale η. There the viscous forces dominate the inertial forces and the eddies dissipate into heat. According to Kolmogorov [88], the smallest scales depend only on the kinematic viscosity ν and the dissipation rate ϵ in the flow. Furthermore, the turbulence in the *dissipation range* can be assumed to be locally isotropic, homogeneous and universal. The latter means that the turbulence on the

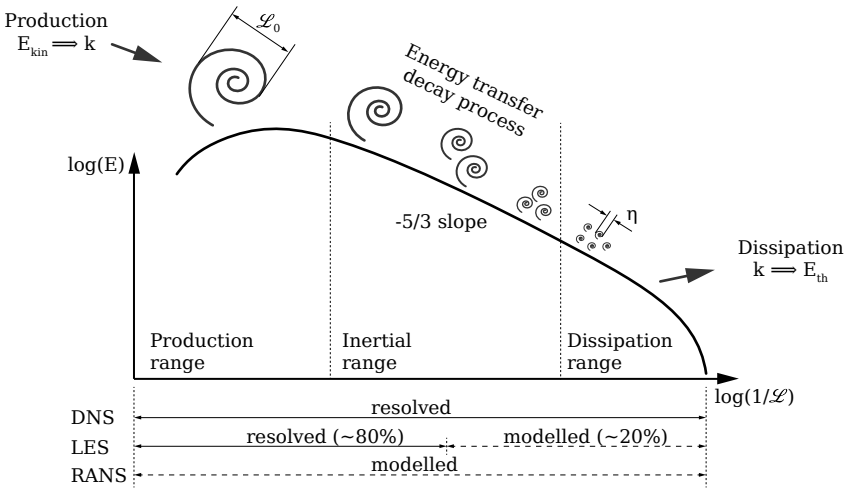

Figure 3.1.: Energy spectrum of turbulent motion, illustrating the turbulent energy cascade and the areas of application of the different turbulence treatments in CFD simulations

smallest scales behaves in the same way, regardless of the flow on the larger scales. On the basis of the degree of resolution of the energy cascade, a distinction can be made between the most common types of turbulence treatments. In the Direct Numerical Simulation (DNS), the turbulent structures are resolved on all scales and no modelling is required. This is the most accurate way of describing a turbulent flow but demands for an enormous amount of computational power. The ratio of the largest and the smallest turbulent scales rises when the *Reynolds* number of the flow increases.

$$\frac{\eta}{\mathcal{L}_0} = Re^{-\frac{3}{4}} \tag{3.12}$$

This requires a very high spatial and temporal resolution of the simulation setup. For this reason DNS is unsuitable for most engineering applications. One way to reduce the computational effort compared to DNS is to use LES. This method originates from weather modelling but is now widely used in other technical flow applications. In LES a filter is applied to the flow field. Only turbulent structures larger than the filter width are resolved. Smaller vortices are modelled using *sub-grid scale* models. Typically, about 80% of the TKE is resolved and 20% is modelled. The determination of the exact location of the filter cut off is not trivial and depends of the characteristic of the flow. It is supposed to lie between the

largest and the *Kolmogorov* scales, somewhere in the inertial range (Cuxart [39]). Although the LES shows a significant saving in computational resources in contrast to DNS, the effort is still to high for most technical applications, especially in rapid design passes. That is why the most commonly used approach to turbulence is the RANS procedure. There 100% of the turbulent spectrum is modelled. This reduces the requirements for mesh and time resolution dramatically and makes the approach applicable to all technical flow cases.

Two key quantities can be used to describe the turbulent state of a flow: The TKE k or turbulence intensity I (in dimensionless form) are measures of the strength of turbulence and the turbulent length scale describes the characteristic size of the turbulent motion. The turbulence intensity I (Eq. (3.13)) relates turbulent fluctuating velocity to the underlying mean velocity magnitude $\overline{U_{mag}}$.

$$I = \frac{\sqrt{1/3(u'^2 + v'^2 + w'^2)}}{\overline{U_{mag}}} = \frac{\sqrt{2/3k}}{\overline{U_{mag}}} \tag{3.13}$$

Information about the spatial extend of the turbulent eddies is given by the integral length scale. The in-plane length scale can be calculated by using the two-point correlation of the velocity fluctuations:

$$R_{ij}(\mathbf{x}, \mathbf{r}, t) = \overline{u_i'(\mathbf{x}, t) u_j'(\mathbf{x} + \mathbf{r}, t)} \tag{3.14}$$

This relationship measures the correlation between the velocity fluctuation components of two points in space. Hereby is $\mathbf{r}$ the spatial distance between two points and for its limit $\mathbf{r} = 0$, the aforementioned Reynolds stress tensor is obtained. The integral length scale at a specific point can be determined by calculating the two-point correlation between that point and every other point in the flow field, integrating the results, and normalising it with the Reynolds stress value of the point, according to

$$\mathcal{L}(\mathbf{x}, t) = \frac{1}{R_{ii}(\mathbf{x}, \mathbf{r} = 0, t)} \int_{r=0}^{\infty} R_{ii}(\mathbf{x}, \mathbf{e}_i r, t) dr. \tag{3.15}$$

This length scale is a characteristic measure for the largest turbulent eddies.

3.2.2. RANS Turbulence Modelling

In this section, the RANS method and its most important turbulence models are described. Then the theory of SRS methods like LES and hybrid RANS/LES modelling is introduced.

Reynolds-Average Navier-Stokes Equations

For most engineering applications, the time-averaged flow variables are of most interest. The changes with time, especially at the small scales of turbulent motion, are usually of secondary importance. Therefore, in the context of RANS turbulence modelling the conservation equations are solved for the time averages. In a first step, the *Reynolds decomposition* is used, in which the flow quantities $\Phi(x,t)$ are represented as the sum of the mean $\overline{\Phi}(x)$ and the fluctuation $\Phi'(x,t)$

$$\Phi(x,t) = \overline{\Phi}(x) + \Phi'(x,t). \tag{3.16}$$

For compressible flows, the *Favre average* is used, with $\overline{\Phi}(x) = \overline{\rho\Phi}/\overline{\rho}$ and $\overline{\Phi'}(x,t) \neq 0$ but $\overline{\rho\Phi'}(x,t) = 0$. This mass-weighted average accounts for density fluctuations. Inserting the *Reynolds decomposed* quantities into the conservation equations Eq. (3.2), Eq. (3.5) and Eq. (3.6) and then averaging over time gives the *Reynolds-averaged* transport equations. Additional terms arise when *Reynolds- averaging* a product of two variables (Eq. (3.17)).

$$\overline{\Phi_1\Phi_2} = \overline{(\overline{\Phi}_1 + \Phi'_1)(\overline{\Phi}_2 + \Phi'_2)} = \overline{\Phi}_1\overline{\Phi}_2 + \overline{\Phi'_1\Phi'_2} \tag{3.17}$$

This leads to new, unknown terms such as the *Reynolds stress* $\overline{u'_i u'_j}$ from averaging the momentum equation. Further transport equations for these unknown terms lead to additional unknown terms which creates an infinite hierarchy of transport equations. This is known as the *Closure Problem* of turbulence (Wilcox [196]). To achieve closure and obtain a solution to the system of equations, a modelling approach must be applied at some point in the hierarchy.

Eddy Viscosity Approach

The most commonly used class of RANS turbulence models is applied directly at the first level by modelling the unknown *Reynolds stresses*. These are called *eddy viscosity models*. As the name suggests, the turbulent stresses are modelled by introducing a *turbulent viscosity* μ_t which relates the turbulent stresses to the mean velocity gradients, analogous to molecular stresses. It follows, that in *eddy viscosity models* the effect of turbulent mixing, caused by convective transport in turbulent structures is modelled by an artificial increase of diffusivity. This leads to an effective viscosity μ_{eff} which is the combination of molecular μ and turbulent viscosity μ_t:

$$\mu_{eff} = \mu + \mu_t \tag{3.18}$$

Following Boussinesq [27]

$$\rho\overline{u'_i u'_j} = -\mu_t S_{ij} + \frac{2}{3}\rho\delta_{ij}k, \tag{3.19}$$

the *Reynolds stresses* $\overline{u_i' u_j'}$ are modelled linear proportional to the mean shear rate $S_{ij} = \frac{1}{2}\left(\frac{\partial \overline{u}_i}{\partial x_j} + \frac{\partial \overline{u}_j}{\partial x_i}\right)$. Thereby is

$$k = \frac{1}{2}\overline{u_i' u_i'} \tag{3.20}$$

the specific TKE.

In analogy to the *Reynolds stresses*, the averaging of the energy equation (Eq. (3.6)) produces an additional term $\overline{u_i' T'}$, which can be interpreted as turbulent heat flux. This term is directly modelled using the Gradient Diffusion Hyphothesis (GDH):

$$c_p \rho \overline{u_i' T'} = -\lambda_t \frac{\partial T}{\partial x_i} \tag{3.21}$$

with the turbulent heat conductivity λ_t calculated according to Eq. (3.22),

$$\lambda_t = \mu_t \frac{c_p}{Pr_t} \tag{3.22}$$

where the turbulent *Prandtl* number Pr_t describes the ratio of temperature and velocity boundary layer thickness. It can also be interpreted as the ratio of momentum exchange due to friction and the heat exchange due to heat conduction. In most RANS models, it is set to constant. Although the analogy between viscous and turbulent stresses, on which the *Boussinesq hypothesis* is based on, poorly reflects the reality of turbulent flows (Schmitt [157], Pope [134]) and only gives valid results for simple flow cases, it is still the central part of most turbulence models used today. Following from dimensional analysis $\mu_t \propto \mathcal{L}^2 \mathcal{T}^{-1}$, the turbulent viscosity can be expressed by a time-scale $\mathcal{T}$ and a length-scale $\mathcal{L}$. The different *eddy viscosity* turbulence models are distinguished by the way in which the two scales and thus the turbulent viscosity are calculated. This can be done by using algebraic modelling approaches or by solving additional conservation equations.

One-Equation Model

The Spalart Allmaras (SA) model by Spalart and Allmaras [169] is a widely utilized one-equation model. One additional transport equation is solved for the turbulent viscosity μ_t. Despite its simplicity, it produces reasonable results for aerodynamics of air foils and turbomachinery components.

Two-Equation Model

More complex modelling approaches are used with 2-equation models. Two additional transport equations are solved to calculate the turbulent viscosity. In the k-ϵ model by Launder and Sharma [97], a transport equation for the TKE k and the turbulent dissipation ϵ are solved to calculate the turbulent viscosity μ_t as following:

$$\mu_t = C_\mu \rho \frac{k^2}{\epsilon} \tag{3.23}$$

C_μ is a constant model parameter that requires determination through empirical studies. The k-ϵ model performs well in free flow conditions but shows weaknesses when approaching solid walls.

A second widely used two-equation turbulence model is the k-ω model of Wilcox [196]. Here the dissipation ϵ is replaced by the specific dissipation rate $\omega = \epsilon/k$ for which a transport equation is solved. The k-ω is designed to work throughout the boundary layer, but has a higher sensitivity to inlet boundary conditions and is therefore disadvantaged in free flow conditions compared to the k-ϵ model.

Shear-Stress-Transport Model

In order to combine the strengths of the k-ϵ and k-ω models, while avoiding their weaknesses, a combination of both models is used in the Shear-Stress-Transport (SST) model of Menter [115]. Here the model operates in a k-ω mode in regions close to the wall but switches to its k-ϵ representation away from the walls. The model is based on solving the modified transport equation for the TKE k and the the turbulent dissipation rate ω. The following modification to the transport equations is used, compared to the original formulation: To account for the k-ϵ character of the model in regions away from solid walls, the transport equations of the k-ϵ model are reformulated by replacing ϵ by ω. In a second step, a blending between these newly obtained equations and the original k-ω equations is used, depending on the wall distance. Finally the turbulent viscosity is defined by:

$$\mu_t = \frac{k}{\omega} f(S_{ij}, k, \omega, \mu, \rho, y) \tag{3.24}$$

This corresponds to the normal k-ω representation of μ_t with a modification to prevent the overestimation of the turbulent viscosity and to predict flow separation more precise. This is done by using Bradshaw's assumption (Menter [113]) that the turbulent shear stresses are proportional to the TKE in regions close to the walls. A detailed description of the model equations is not given here. These and all model coefficients can be found in the original publications (Menter [115], Menter [113]). Within this work, the SST model is used for all steady and unsteady RANS simulations.

3.2.3. Scale-Resolving Turbulence Modelling

Scale-Adaptive-Simulation

Most two-equation RANS turbulence models use the transport equation for the TKE k. To calculate the turbulent viscosity μ_t, a second transport equation is needed to determine a turbulent scale (scale-determining equation). As explained in Section 3.2.2, either the turbulent dissipation ϵ or the specific dissipation rate ω is used. The standard turbulence models, even in URANS, do not predict a spectrum of turbulent scales because the modelled maximum length scale in a shear layer is always proportional to the thickness of the respective turbulent boundary layer. This dampens the formation of resolved scales in unsteady flows. The basic idea behind SAS models is to solve a transport equation for a turbulent length scale to adjust the scales in favour of resolving a turbulent spectrum. The use of a transport equation of the product of the turbulent length scale $\mathcal{L}$ and the TKE k was first introduced by Rotta [144] and later changed to $\Phi = \sqrt{k}\mathcal{L}$ by Menter and Egorov [117]. Two transport equations are solved in the k-$\sqrt{k}\mathcal{L}$ model. The first is solved, as in most models, for the TKE

$$\frac{\partial(\rho k)}{\partial t} + \frac{\partial(\rho \overline{u}_j k)}{\partial x_j} = \mathcal{P}_k - {C_\mu}^{3/4}\rho\frac{k^2}{\Phi} + \frac{\partial}{\partial x_j}\left(\frac{\mu_t}{\sigma_k}\frac{\partial k}{\partial x_j}\right), \tag{3.25}$$

where $\mathcal{P}_k$ is the production term and C_μ and σ_k are model constants. The second transport equation is solved for Φ.

$$\frac{\partial(\rho\Phi)}{\partial t} + \frac{\partial(\rho \overline{u}_j \Phi)}{\partial x_j} = \frac{\Phi}{k}\mathcal{P}_k\left(\zeta_1 - \zeta_2\left(\frac{\mathcal{L}}{\mathcal{L}_{vK}}\right)^2\right) - \zeta_3\rho k + \frac{\partial}{\partial x_j}\left(\frac{\mu_t}{\sigma_k}\frac{\partial\Phi}{\partial x_j}\right) \tag{3.26}$$

Here, ζ_1 to ζ_3 are other model constants and $\mathcal{L}_{vK}$ is the *von Karman* length scale

$$\mathcal{L}_{vK} = \kappa\left|\frac{U'}{U''}\right|. \tag{3.27}$$

This plays a central role in SAS models. It is calculated by the *von Karman* constant $\kappa = 0.41$ and the ratio of the absolute value of the strain rate tensor

$$U' = \sqrt{2S_{ij}S_{ij}} \tag{3.28}$$

to the curvature of the velocity field

$$U'' = \sqrt{\frac{\partial^2\overline{u}_j}{\partial x_k^2}\frac{\partial^2\overline{u}_j}{\partial x_j^2}}. \tag{3.29}$$

By using the second derivative of the velocity and including the *von Karman* length for modelling the production term of the scale-determining equation, the ability to adjust the

turbulent length scale is added to the model. It is able to accurately resolve the turbulent structures of the unstable flow regions, while treating the stable regions as a RANS model. It switches seamlessly between LES-like and RANS mode without being dependent on the grid resolution. Since it is still a two-equation RANS model, the turbulent viscosity μ_t is calculated as follows:

$$\mu_t = {C_\mu}^{1/4} \rho \Phi \tag{3.30}$$

The original k-$\sqrt{k}\mathcal{L}$ model can be transformed to other variables. This was done by Menter and Egorov [118] to bring the SAS functionality to the widely used SST model. The resulting model is called the SST-SAS model and is used in this thesis. A detailed description of the model and a list of all model constants can be found in the work by Menter and Egorov [118].

Large-Eddy-Simulation

In the LES, a part (about 80%) of the turbulent spectrum is resolved and the remaining part is modelled. To separate the large scale turbulent fluctuations from the small scales, the conservation equations are filtered. This can be seen as a low-pass filtering process. The large-scale structures, which represent the scale-determining turbulent eddies, are completely resolved in this way. The filtering process produces correlation terms containing velocity fluctuations whose characteristic length is smaller than the filter width. These terms represent the small scale structures and cannot be calculated directly. They are described by so-called *subgrid scale* models, usually based on the eddy viscosity approach, similar to RANS models. The theory behind LES can be found in more detail in the work by Sagaut [145]. In the following, the key points of the LES model used in this work will be explained.

The filtered flow variable $\widehat{\Phi}(x)$ is described by

$$\widehat{\Phi}(x) = \int_V \Phi(x') G(x; x') dx', \tag{3.31}$$

as the convolution of the variable with the filter function G. The spatial discretisation of the computational domain into finite control volumes implicitly provides the filter through the numerical grid. In the solver applied in this work (CFX [31]), an implicit box filter by means of the control volume V

$$G(x; x') = \begin{cases} 1/V, & x' \in V \\ 0, & \text{otherwise} \end{cases} \tag{3.32}$$

is used. The filtering of the conservation equations (Eq. (3.2) and Eq. (3.5) and Eq. (3.6)) leads to additional unknown terms. The filtered impulse equation becomes:

$$\widehat{\rho} \frac{D\widehat{u}_i}{Dt} = -\frac{\partial \widehat{p}}{\partial x_i} + \frac{\partial}{\partial x_i} \left[\mu \left(\frac{\partial \widehat{u}_i}{\partial x_j} + \frac{\partial \widehat{u}_j}{\partial x_i} \right) \right] + \frac{\partial \tau_{sgs}}{\partial x_j}, \tag{3.33}$$

with the unknown subgrid-scale stresses

$$\tau_{sgs} = -\widehat{\rho u_i u_j} + \widehat{\rho}\widehat{u}_i\widehat{u}_j. \tag{3.34}$$

Analogous to the procedure in the RANS context, the subgrid-scale stresses are modelled using the eddy viscosity approach

$$\tau_{sgs} = 2\mu_{sgs}\widehat{S}_{ij} + \frac{1}{3}\delta_{ij}\tau_{kk} \tag{3.35}$$

Several models are available to describe the subgrid-scale viscosity μ_{sgs}. The one used for this work is the Wall-Adapted Local Eddy-viscosity (WALE) model from Ducros et al. [47].

$$\mu_{sgs} = \widehat{\rho}(C_W\Delta)^2 f(\widehat{S}_{ij}, \widehat{\Omega}_{ij}), \tag{3.36}$$

with $C_W = 0.5$ and Δ being the grid spacing. To account for the correct prediction of the laminar-turbulent transition and to give the correct wall asymptotic behavior of the subgrid-scale viscosity, a combination of the filtered strain rate tensor $\widehat{S}_{ij}$ and the filtered vorticity tensor $\widehat{\Omega}_{ij}$ is used.

Hybrid LES/RANS models

RANS calculations are notable for being very cheap and giving relatively good results when the flow around solid bodies is attached. As soon as detachment, shedding and vortex formation occur, the usual RANS turbulence models fail to make accurate predictions. For these types of flow conditions, LES approaches have been shown to perform much better by resolving part of the turbulent spectrum. However, this higher fidelity comes at a cost and the computational effort increases dramatically. Not only do the spatial resolution requirements of the numerical grids increase, but the temporal resolution of the simulation also rises dramatically. As a result, the resolution of the entire boundary layer with LES for high Reynolds numbers, such as those typically found in turbomachinery, is still rarely achievable with the available computing power. In widespread use, this will remain the exception. Through the use of wall models or hybrid LES/RANS approaches, SRS in turbomachinery is increasingly becoming an alternative to the current RANS standard.

A hybrid LES/RANS approach was first presented by Spalart et al. [171]. This led to a new class of turbulence models, the Detached-Eddy Simulation (DES). The basic idea behind this approach is to use a single turbulence model which operates as a subgrid-scale model in the LES part of the flow and as a RANS model in the other regions of the flow. Switching between the two modes is automatic according to the grid spacing. In regions where the turbulent length scale is smaller than the grid spacing, for example in the boundary layer near solid walls, the RANS mode is active. Away from the walls and in regions of high

separation and larger turbulent length scales, the model operates in LES mode. In the original formulation by Spalart et al. [171], the one-equation SA model was used. In the DES form of the model, the turbulent viscosity μ_t shows following proportionality:

$$\mu_t \propto S\tilde{d}^2, \tag{3.37}$$

where S is the strain rate tensor and

$$\tilde{d} = \min(\delta_y, C_{DES}\Delta). \tag{3.38}$$

C_{DES} is a model constant and δ_y is the wall distance. Δ is the grid spacing and for three dimensional grids, the maximum value of the three directions is used. In areas where the wall distance is smaller than the local grid spacing ($\delta_y << \Delta$), the model works as the original SA turbulence model (RANS). When $\delta_y >> \Delta$, the model switches to the *Smagorinsky* Subgrid-Scale (SGS) model for LES.
To improve the prediction accuracy of the RANS part of the DES approach, Strelets [175] integrated the SST model by Menter [115] into DES. To do so, a turbulent length scale

$$\tilde{\mathcal{L}} = \min(\mathcal{L}_{k\omega}, C_{DES}\Delta) \tag{3.39}$$

is added to the dissipative term of the k-equation of the SST model

$$\mathcal{D}^k_{DES} = \rho k^{3/2}/\tilde{\mathcal{L}}, \tag{3.40}$$

with $\mathcal{L}_{k\omega} = \sqrt{k}/C_\mu\omega$ being the turbulent length scale of the k-ω model. For $C_{DES}\Delta < \mathcal{L}_{k\omega}$, the grid spacing is smaller than the RANS length scale and the model operates in LES mode. The RANS mode of the model is active for $C_{DES}\Delta > \mathcal{L}_{k\omega}$.
Both the SA and SST versions of the basic DES model have problems with boundary layer flows. Unintentional switching to LES mode can lead to *mesh-induced separation*. To prevent this, a protective *shielding* function is introduced into the model. These models are called Delayed Detached-Eddy Simulation (DDES) models. A detailed description of the shielding mechanisms can be found in the works of Menter and Kuntz [119] and Gritskevich et al. [59].

So far, DES models rely on the LES capability of the DES version of RANS turbulence models. This leads to a slow transition from RANS to LES mode under certain flow conditions. Grid-induced separation can still be a problem even when using the DDES approach. Another disadvantage of DES is the unclear distinction between RANS and LES in the flow domain. All these drawbacks limit the usability of DES models. A relatively new concept is the Stress-Blended Eddy Simulation (SBES) of Menter [114]. In contrast to the DES approach, where the LES- and RANS version of a single set of equations is used, the SBES model combines a separate RANS model with a seperate LES model. The blending mechanism of

both models is adapted by the shielding in DES models but happens on the level of turbulent stresses,

$$\tau_{ij} = \tau_{ij}^{RANS} f_S + \tau_{ij}^{LES}(1 - f_S) \tag{3.41}$$

or if both models use the eddy-viscosity on the level of turbulent viscosity

$$\mu_t = \mu_t^{RANS} f_S + \mu_t^{LES}(1 - f_S). \tag{3.42}$$

The definition of the blending function f_S is crucial to the success of the model. In the SBES model, the shielding function provides a high level of shielding, allows rapid switching between RANS and LES, and proves to be very robust to mesh related variability. In addition, the single value of f_S provides a clear indication of the demarcation between RANS and LES. It could be demonstrated, that the SBES model is superior to the other DES turbulence models and that it presents a versatile hybrid RANS/LES model (Menter [114], Menter [116]). In this work, it will be used as the favourable model for SRS.

SRS quality assessment

Besides the standard quality criteria in CFD, with SRS there are additional points to consider. An important measure of the quality of a LES is the ratio of resolved to unresolved TKE. When using implicit filter methods, the grid is used as the filter and determines the filter width. Therefore, the amount of resolved turbulence is directly related to the grid resolution and can be used as a measure of the quality of the LES grid. Celik et al. [30] present different ways of describing an *index of resolution quality for LES*. The basic idea follows the suggestion of Pope [134] that 80% of the TKE is resolved in LES.

$$\frac{k_{res}}{k_t} > 0.8 \tag{3.43}$$

To increase the amount of resolved TKE, the mesh resolution needs to be refined. In addition to an appropriate spatial resolution, LES also necessitates a sufficient resolution in the temporal domain. Turbulent scale separation represents one of the main challenges in SRS. The range of turbulent length scales goes from the size of the relevant geometric flow features to the smallest eddies located at the end of the turbulent spectrum. According to Eq. (3.12), the ratio of the largest scales to the smallest scales depends on the Reynolds number. In a engine representative CT case, the typical Reynolds number is of the order of 10^6, and the largest and smallest scales are separated by multiple orders of magnitude. For spatially resolving the relevant part of the smaller eddies, a fine mesh resolution is necessary. The length scales of turbulent eddies are directly linked to the time scales of the turbulent motion. Significant separation of length-scales automatically results in the same

level of separation for the most significant and minor time-scales in the flow. To temporarily resolve small eddies and meet the Courant-Friedrichs-Lewy (CFL) condition

$$\Delta t < \frac{\Delta}{u}, \tag{3.44}$$

the time step width of the simulation should be set small enough. However, the total simulation time must allow for a sufficient amount of time to average large time scales. The convergence of the Root Mean Square (RMS) of monitor points placed at significant locations within the CFD domain is utilized to evaluate the averaging duration. The need for high-quality mesh resolution, along with the requirement of fine temporal resolution and long averaging times is what necessitates significantly greater computational resources for SRS when compared to RANS simulations.

3.3. Solver

For the simulations in this work the solver ANSYS® CFX®2021.2 is utilized. It is an element-based FVM solver. The advective fluxes are discretized with a blend between first- and second order schemes for steady and unsteady RANS simulations and by using a bounded CDS for SRS. A second order implicit time stepping scheme is used for transient simulations. The coupled system of discretized equations is solved numerically using the Incomplete Lower-Upper (ILU) and a coupled algebraic multi-grid method. Further information on the solver theory can be found in the documentation of CFX [31].

3.3.1. Evaluation of the Flow Solver

In this section, numerical simulation results are compared with experimental data to demonstrate the ability of the solver to predict flow in a combustor-turbine problem. The solver ANSYS® CFX®is a commonly utilized tool for turbomachinery simulations, having been demonstrated to be an effective and reliable simulation instrument for this specific application on numerous occasions (Schneider [158], Hilgert [71] and Bakhtiari [10]). The LSTR is used as a test vehicle to evaluate the flow solver in this work. This is a low Mach number test rig located at the Institute of *Gas Turbines and Aerospace Propulsion* (GLR) at the Technical University of Darmstadt (Fig. 3.2). The 1.5-stage HPT is scaled 3:1 to a real engine and operates in a closed loop. A combustor module is located upstream of the turbine section to simulate the flow of a modern low emission combustor. The unit is operated under isothermal conditions, so no combustion reaction is taken into account. The swirl, which is characteristic of a combustor, is generated by swirl generators comprising three rings with vanes arranged circumferentially. This gives a nominal swirl number of

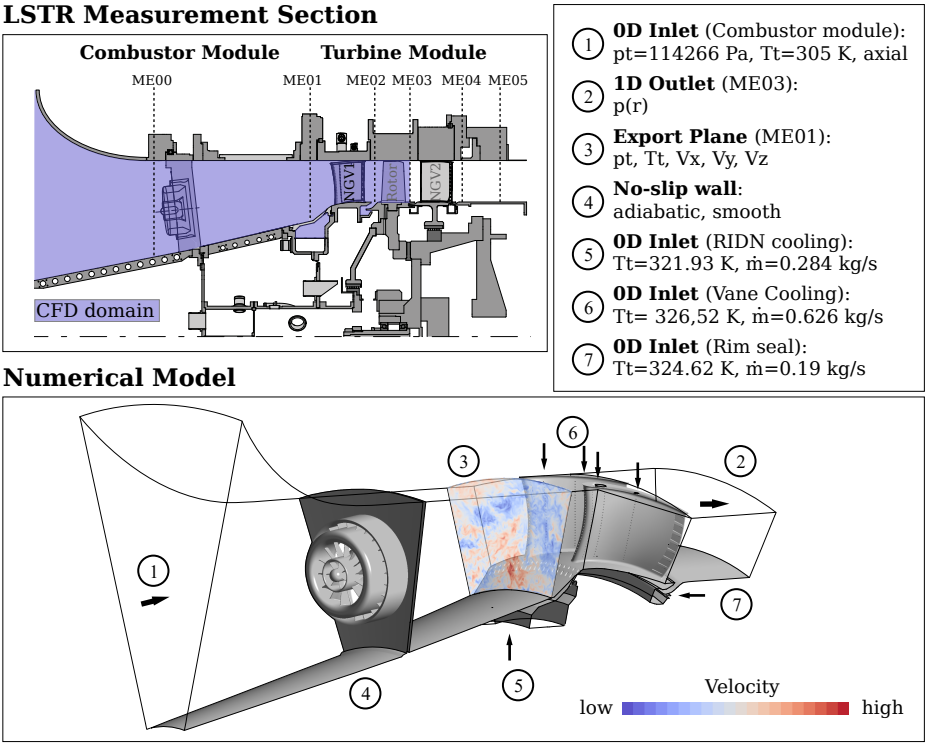

Figure 3.2.: Top: Cut through the measurement section of the LSTR, adapted by Schneider [158]; bottom: Numerical setup of integrated combustor and turbine simulation of the LSTR

$S = 0.6$. There are a total of 12 swirl generators around the circumference. The relative position of the swirlers to the downstream NGVs can be adjusted. The rig is mostly operated with two swirl settings. In the Swirl Leading edge clocking (SWL) configuration, the centre of the swirler is aiming at the leading edge of a NGV, while in the Swirl Passage clocking (SWP) configuration the swirler is pointing at the passage between two NGVs. The turbine section consists of 24 vanes in the first NGV row, 36 rotor blades and 34 vanes in the second NGV row. The operating conditions are adapted according to the geometric scaling of the geometry to obtain a similar *Reynolds* number compared to the real engine. Following Eq. (3.11) and using the NGV cord length and the NGV1 exit velocity, $Re \approx 1 \times 10^6$. At $Ma_{01} = 0.045$, the *Mach* number at the interface between combustor and turbine is well

Table 3.1.: Mesh Statistics and Numerical setup for Simulations of the LSTR Combustor-Turbine Case

Numerical Mesh			**Set-up and Convergence**	
Domain	Combustor	Turbine	Solver	ANSYS® CFX® v2021.2,
Cells (Mio.)	96.8	111.2		unsteady
Min. cell angle (°)	2.4	1.9	Gas model	ideal compressible
Avg. cell angle (°)	70	50	Turbulence	SBES
Max. EVR*	247.8	263	Δt	8.335×10^{-6}s
Avg. EVR*	1.5	2.7	sub iter.	7
Max. EAR†	641	2872	Advection	CDS††
Avg. EAR†	2.1	2.2	Transient	2$^{\text{nd}}$ order backward Euler
Max. y^+	5.5	6.1	Residuals	$< 7.6 \times 10^{-4}$
Avg. y^+	0.8	1.9	Imbalances	$< 0.0025\%$ (for u,p)
$\Delta^{\star\star}$	0.8 mm	0.5 mm		$< 0.028\%$ (for H)

* Element volume ratio † Element aspect ratio ** Grid spacing †† Central differencing scheme

below that of a real engine. The main annulus mass flow at the turbine inlet $\dot{m}$ is $9.2kg/s$. A secondary air system is available to provide cooling and sealing air. Each vane of the first NGV is equipped with 6 film cooling rows and trailing edge slots. 6.8% of the main mass flow enters through these features. A further 3% of the main mass flow enters through two rows of RIDN holes. These are located at the hub of the turbine, just ahead of the vanes. The seal between the stationary NGV1 hub and the rotating platform of the rotor stage is provided by the rim seal, which accounts for 2% of the main mass flow. A detailed description of the rig setup can be found in Krichbaum et al. [93].

The scaled geometry allows for the application of detailed measurement techniques. The aerodynamics of the turbine have been evaluated in several measurement campaigns. The experiments to obtain the measurement data by means of pneumatic Five-Hole Probe (5HP) and Hot-Wire Anemometry (HWA) were conducted by Wilhelm et al. [198] and Werschnik et al. [194]. Infrared thermography was used to conduct measurements of heat transfer and film cooling effectiveness using the auxiliary wall method (Werschnik et al. [195]). A sectional view of the LSTR is shown in Fig. 3.2. The position of the measurement planes and the extent of the numerical domain are illustrated. Within this work, the focus lies on the interaction between the combustor module and the first NGV of the turbine. Therefore the measurement planes *ME01* (at the interface between combustor and turbine) and *ME02* (behind the first NGV) are relevant.

For the integrated combustor-turbine simulation, the computational domain starts in front

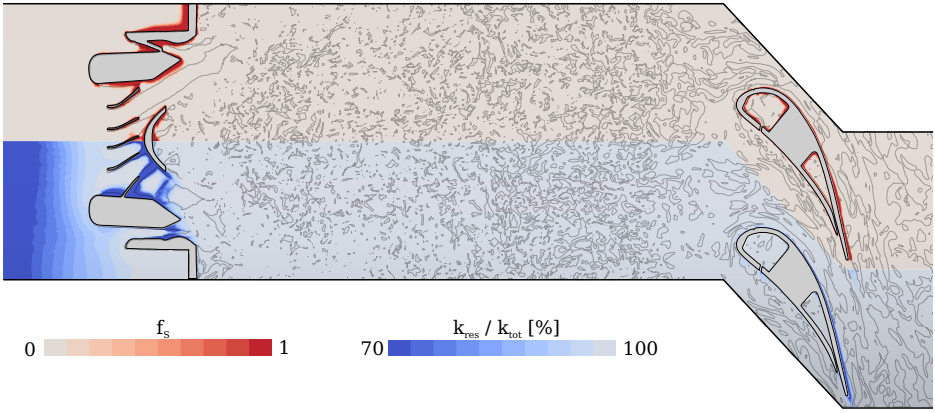

Figure 3.3.: Upper half: ratio of resolved TKE and total TKE; Lower half: operation mode of SBES turbulence model by means of shielding function f_S; Visualization of vortex structures with black contour lines ($\lambda_2 = 0$)

of the swirler of the combustor module and ends at the measurement plane *ME03*, which is located just behind the rotor. To reduce the mesh size of the simulation, the rotor blade is omitted and only the rotating hub is simulated. Also shown in Fig. 3.2 is the numerical model and boundary conditions of the combustor-turbine simulation. A single sector of the annular rig geometry is simulated, with a single swirler module and two NGVs modelled. The mesh statistics and the solver settings are listed in Table 3.1. The following section evaluates the quality criteria mentioned in Section 3.2.3.

The numerical mesh is designed for SRS using the SBES turbulence model. Areas close to solid walls are treated with RANS and everywhere else LES is used. The corresponding mesh is characterized by a fine mesh resolution in the core of the mesh and a stack of prism layers at the walls to resolve the boundary layer. In Fig. 3.3 the mode of operation of the SBES is illustrated. The upper half of the contour is coloured using the blending function f_S and the lower half using the percentage of resolved TKE k_{res}/k_{tot}. Additionally, contour lines of vorticity are plotted to visualize the resolved vortex structures. The SBES works in LES mode for $f_S = 0$, which is the case for most of the domain. For $f_S = 1$ the simulation uses the RANS turbulence model. This is the case in regions close to the walls. The LES quality criterion of resolving at least 80 % of the TKE (Eq. (3.43)) is satisfied in most part of the LES region ($f_S = 0$) of the domain. In areas where the model operates in RANS mode, lower values are visible as expected. The mesh upstream of the swirler module is coarsened because the inlet flow into the combustor module is laminar. Here, the ratio

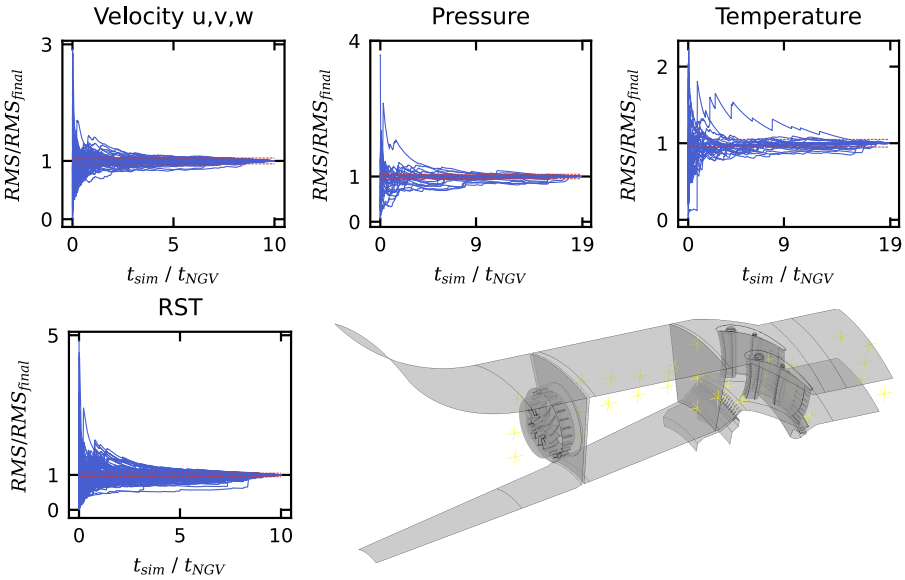

Figure 3.4.: Cumulative RMS for each monitor point for pressure, temperature, velocity components and Reynolds Stress Tensor (RST) components, normalized by the respective final value as a function of the number of NGV flow-through time t_{sim}/t_{NGV}. The red dashed lines indicate upper and lower thresholds, set at $\pm 5\%$ to the final value. Lower right: position of monitor points in the NGV domain

between resolved and total TKE provides unrealistic values because the turbulence level in the free stream is close to zero.

In addition to adequate spatial resolution, LES also requires sufficient resolution in the temporal domain. The CFL condition (Eq. (3.44)) is fulfilled in most of the domain. Only in small areas in the cooling holes, where the flow contracts, higher values are present.

The second important parameter in the temporal context is the time which is used to collect the values for the time average. The transient simulation is averaged for a satisfactory duration to achieve convergence of the time average. The RMS magnitude of relevant flow variables is monitored at various points distributed across the entire fluid domain. In addition to the monitor point locations, Fig. 3.4 displays the convergence envelope of the cumulative RMS for each monitor point and for relevant flow variables. The graphs in Fig. 3.4 feature upper and lower thresholds, set at $\pm 5\%$, to the final value. These lines are standardized throughout all graphs presented. The RMS values of the three velocity

components are presented in a single graph, indicating values that fall within the $\pm 5\%$ range during the averaging period. A similar convergence pattern is noted for the temperature and pressure levels. Furthermore, the convergence behavior of the six independent components of the RST is displayed. As higher order moments, the convergence of Reynolds stresses is slower compared to their average counterparts. This trend is displayed in Fig. 3.4. The RMS values solely attain the $\pm 5\%$ threshold within the averaging time.

To assess the ability of the solver to provide accurate results in combustor-turbine simulations, CFD simulation results are compared to experimental data using circumferentially-averaged radial profiles. The work by Schneider [158] provides a comprehensive validation of RANS results against measurements. It includes an in-depth review of different RANS turbulence models and their sensitivity to variations in mesh resolution. Please refer to that work for further information. This work expands the evaluation of the flow solver by incorporating the results of SRS and highlighting differences from the RANS simulation results. Fig. 3.5 shows the results at two evaluation planes: one in front of the NGV (ME01) and one behind the NGV (ME02). In addition to the experimental data, this presentation includes the results of a RANS simulation and a scale resolving SBES simulation of the integrated combustor module-NGV domain. Both simulation results demonstrate good agreement with the experimental data. The RANS and SRS simulations produce comparable results with some differences. In ME01, the RANS simulation overestimates the swirl, resulting in a higher predicted circumferential angle ϕ and a stronger deficit in Mach number in the swirl centre. The SRS predicts these aspects more accurately but also exhibits slight deviations from the experimental data at the inner and outer endwalls. The distribution of Mach number suggests a mass redistribution from the inner endwall towards the centre of the passage. This trend is also evident in the total pressure distribution. The radial distribution of turbulence intensity shows significant differences between RANS and SRS. The RANS simulation over-predicts intensity values in the centre and under-predicts them at the end walls of the domain, while the SRS matches the experimental data well. As anticipated, the SRS outperforms the RANS in highly swirled and turbulent flow conditions, such as those found in the combustor simulator. However, the RANS simulation is capable of predicting the general flow trends with significantly less computational effort.

Moving downstream to ME02, which is situated behind the first NGV, there is a good agreement between simulation results and measurement data. Differences between RANS and SBES can be observed in the hub region, where the main flow interacts with the rim seal air. The SBES predicts a slightly higher turbulence intensity, resulting in higher losses and a reduction in total pressure and Mach number in that region. The CFD simulations closely match the aerodynamic trends, with some improvements observed when using a scale-resolving turbulence model instead of RANS.

Although the LSTR is an isothermal test rig, it is possible to determine the film effectiveness η_{fc} and evaluate the ability of the CFD to predict it. This is achieved by heating up the

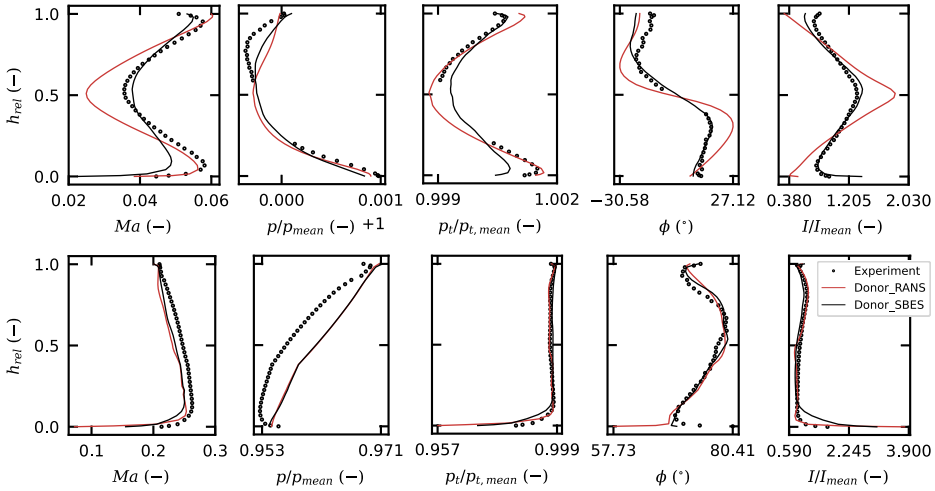

Figure 3.5.: Comparison of Experimental and Simulation data. Upper row: ME01 (NGV Inlet), lower row: ME02 (NGV Outlet). Experimental values for pressure and total pressure are 5HP data. All other values are HWA data

cooling air of the RIDN. Eq. (2.18) can then be used to determine the adiabatic film cooling effectiveness. Fig. 3.6 shows the film cooling effectiveness η_{fc} on the inner platform for the experiment and the two CFD simulations. The cooling films from the first row of cooling holes are detached and not visible on the platform. The films from the second row of cooling holes leave a pattern of high and low film cooling effectiveness on the end wall. The pair of kidney vortices transport cooling air away from the wall and leave stripes of low effectiveness between the holes. The RANS results exhibit distinct stripes of high and low effectiveness, while the experimental data shows a more homogenous cooling pattern. This is also evident in the SRS simulation, which demonstrates the enhanced predictive capabilities of scale-resolving simulations for thermal mixing processes. The SBES in the front area of the film cooling matches the experimental results accurately. However, larger deviations are observed in the rear part of the platform. Both CFD results show higher values of η_{fc} than the experiment in this area. Nevertheless, the general trend is matched, and the imprint of secondary flow can be seen along the corner of the pressure side of the vane and the hub. Here, the cooling air accumulates, especially from the first row of film cooling holes, leaving an imprint of high cooling effectiveness (Werschnik et al. [195]). Table 3.2 shows the area average of the film cooling effectiveness on the evaluation plane. Comparing the RANS results with the experimental average, the RANS simulation shows almost twice the average effectiveness than the experiment. Using the scale resolving

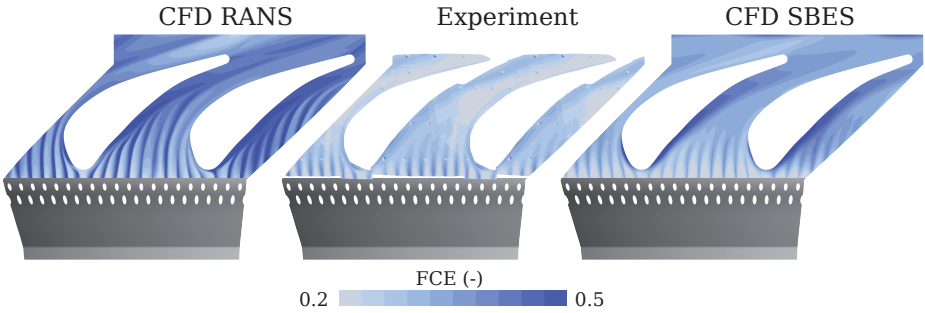

Figure 3.6.: Comparison of film cooling effectiveness on inner platform between experiment and simulation

simulation method, the difference between simulation and experiment can be reduced to 7% (see Table 3.2).

Table 3.2.: Average film cooling effectiveness of RANS, Experiment and SRS

	RANS	Experiment	SRS
avg(η_{fc})	0.4	0.26	0.33

In summary, both CFD simulations match the aerodynamic measurements well. However, certain aspects, such as circumferential angles and turbulence values, are better predicted using SRS. Despite this, the overall trends are well matched by the RANS simulation. When considering cooling-related aspects, such as the prediction of film cooling effectiveness, there are larger gaps between simulation results and experimental data. This discrepancy can be significantly reduced by using scale-resolving simulation methods such as the SBES turbulence model. Overall, the used CFD solver provides valid results and is capable of simulating combustor-turbine related problems.

3.4. Unsteady Inlet Boundary Conditions

Scale resolving turbulence models have been shown to improve the accuracy of CFD calculations compared to the simpler RANS approach, particularly in highly unsteady flow conditions where turbulent mixing processes are dominant. However, this increased fidelity

comes at the cost of a significant increase in simulation time and required resources. The increasing demand for computational resources is matched by the availability of greater computational power. It is now possible to perform simulations with higher resolution across a wider range of applications. As demonstrated in the previous section, this is also true for combustor and turbine simulations. In addition to the requirement for significant computational resources, these simulations necessitate more complex boundary conditions than RANS simulations. The simulation resolves a significant portion of the turbulent fluctuations, which must be provided at the inlet boundaries. For the decoupled development process of the combustor and turbine, relevant information is exchanged at the interface between the two components. In most cases, mean values of the combustor outlet data are used as turbine inlet conditions. The combustor unsteadiness is not transferred, and the turbulent information is only exchanged in the form of model parameters of the RANS formulation. In order to perform scale-resolving simulations in the context of turbines, it is crucial to establish a suitable set of time-accurate inlet boundary conditions. The challenge here is to provide boundary condition data that creates both the randomness and coherence of turbulent eddies at the inlet of the simulation domain (Wu [200]).

A thorough examination of the most commonly used methods for applying inlet boundary conditions in scale-resolving simulations can be found in Tabor and Baba-Ahmadi [179] and Wu [200]. To generate turbulent inlet boundary conditions, two main categories are distinguished: recycling methods and synthetic turbulence methods. Recycling methods use a separate precursor simulation to create turbulent data for use as inlet boundary conditions. In Synthetic Turbulence Methods, turbulent inlet boundary conditions are synthesized using modelling approaches while fulfilling certain constraints. This section presents the most commonly used examples of both categories.

Synthetic Turbulence

The recycling methods presuppose the availability of time-resolved field data. This can either be obtained by temporally and spatially resolving measurement techniques like Particle Image Velocimetry (PIV) or unsteady, scale resolving numerical simulations. However, both methods are expensive and, in many cases, data is not available in this form. In this instance, the utilization of synthetic turbulence methodologies enables the superimposition of artificial fluctuations upon the mean field data. This generates time-accurate inlet boundary conditions for scale-resolving simulations.

At the lowest level of synthesizing turbulent fluctuations, white noise is superimposed on the inlet velocity components. However, as pointed out by Tabor and Baba-Ahmadi [179], this approach has been proven to be ineffective multiple times as it lacks the required

spatio-temporal coherence, and any fluctuations are destroyed by the Navier-Stokes solver a few cells downstream of the inlet.

Fourier Methods: A more advanced method of synthesising turbulent inlet boundary conditions is to utilize a superposition of harmonic functions in the form of a Fourier series. The turbulent velocity fluctuations $\mathbf{u}'(\mathbf{x}, t)$ can be written as the sum of N Fourier modes as

$$\mathbf{u}'(\mathbf{x}, t) = 2\sum_{i=1}^{N} \hat{u}_i(t) cos(\mathbf{k}_i \cdot \mathbf{x} + \psi_i)\mathbf{n}_i, \tag{3.45}$$

where $\hat{u}_i$ is the amplitude, $\mathbf{k}_i$ is the wave number and ψ_i the phase angle. By linking the amplitude $\hat{u}_i$ to the turbulent energy spectrum $E(k_i)$

$$\hat{u}_i(t) = \sqrt{E(k_i)\Delta k_i} \tag{3.46}$$

the synthesized signal follows a prescribed turbulent spectrum and with

$$E_t = \sum_{i=1}^{N} \hat{u}_i^2 = \int_0^{\infty} E(k)dk, \tag{3.47}$$

it contains a certain total TKE E_t. An early version of this method was presented by Kraichnan [92] and later adapted by Lee et al. [101] and Bechara et al. [19]. Temporal correlation is created by applying a digital filter as explained in the following section. The early versions of this method where limited on creating isotropic turbulence. Auerswald et al. [6] added the possibility of creating anisotropic turbulence. Sandham et al. [148] introduced a zonal approach, to distinguish between the inner and outer region of a boundary layer and to account for differences in turbulent characteristics.

Digital Filter Methods: The digital filter method by Klein et al. [87] uses a random noise signal rather than harmonic functions as a starting point, and imposes temporal and spatial coherence through digital filtering. Firstly, a three-dimensional random field r_i is generated for each velocity component. The inlet plane is on the y-z plane and the x direction corresponds to the temporal coordinate. The dimensions of the random fields are $(2 \times N_{F,x} + 1, N_y + 2 \times N_{F,y} + 1, N_z + 2 \times N_{F,z} + 1)$. Hereby, N_y and N_z represent the number of grid points on the inlet plane in the two in-plane directions, while $N_{F,x}$,$N_{F,y}$ and $N_{F,z}$ represent the half filter width in terms of grid points in all three directions. This means that the random fields are sized to match the inlet plane, with an additional overhang of one filter width in the y and z directions, and one filter size in the x direction, also with an overhang of one filter width. The random fields are characterized by an average of zero and a variance of one filter width.

The filtering process runs in a loop for a predetermined number of time steps. For each time step, the three-dimensional filter is applied to the random data.

$$\tilde{\mathbf{u}}_{m,n,l} = \sum_{k=-N}^{N} \sum_{j=-N}^{N} \sum_{i=-N}^{N} b_{ijk} \mathbf{r}_{m+i,n+j,l+k} \tag{3.48}$$

Where N is the discrete filter size and b_{ijk} the three dimensional filter coefficients. These are the product of three one dimensional filter coefficients:

$$b_{ijk} = b_i \cdot b_j \cdot b_k \tag{3.49}$$

Then, the random fields are shifted forward in the x-direction, neglecting the first field. The empty space at the end of the series is then filled with a new random field. By doing this, a progressive signal is generated over time, ensuring coherence between multiple time steps.

The one dimensional filter coefficients can be approximated by the two point correlation function, which for homogeneous turbulence can be written as:

$$R_{uu}(r) = exp\left(-\frac{\pi r^2}{4L^2}\right) \tag{3.50}$$

Where r is the distance between the two points and L the characteristic length scale of the turbulent eddies. The filter coefficient follow as:

$$b_k \approx \tilde{b}_k / \left(\sum_{j=-N}^{N} \tilde{b_j}^2 \right)^{1/2} \tag{3.51}$$

$$\tilde{b}_k = exp\left(-\frac{\pi k^2}{2n_F^2}\right) \tag{3.52}$$

In Eq. (3.52), n_F is the length scale in terms of grid spacing. To minimize the numerical error of the filter process, the filter size should be twice the size of the length scale (Klein et al. [87]).

After the filter operation, the fluctuations are of the right size but not yet correlated. This is done in the last step. Lund et al. [105] proposed the usage of the *Cholesky* decomposition a_{ij} of the Reynolds stress tensor R_{ij}, to correlate the fluctuations of the different velocity components and to adapt them to fulfill the demands of the final signals turbulent statistics:

$$a_{ij} = \begin{pmatrix} (R_{11}^{1/2}) & 0 & 0 \\ R_{21}/a_{11} & (R_{22} - a_{21}^2)^{1/2} & 0 \\ R_{31}/a_{11} & (R_{32} - a_{21}a_{31})/a_{22} & (R_{33} - a_{31}^2 - a_{32}^2)^{1/2} \end{pmatrix} \tag{3.53}$$

Finally, the three dimensional velocity field u_i is obtained by multiplying the filtered field $\tilde{u}_i$ with a_{ij}. This product is then added to the mean fields $\bar{u_i}$:

$$u_i = \bar{u_i} + a_{ij}\tilde{u}_i \tag{3.54}$$

These three steps are repeated for every time step.

Di Mare et al. [42] extended the original formulation of the digital filter by Klein et al. [87] to more precisely link the filter coefficients to the full Reynolds stresses and incorporate a spatial distribution of length scale to the filter process. This improves the prediction capabilities of LES in wall-bounded flows compared to the standard filter approach.

The convolution process in the Digital Filter Method can be time-consuming, particularly for a spatially varying filter width. To address this issue, Veloudis et al. [189] introduced two improvements to the method. Firstly, the convolution is performed in the frequency domain. Secondly, an interpolation in time is implemented. The generation of transient inlet boundary conditions could be significantly speeded up.

In a recent publication, Schmidt and Breuer [156] describes the integration of the digital filter into a LES solver. Turbulent fluctuations are modelled directly using source terms in the simulation, allowing for generation at any location. This reduces the need for a finely resolved inlet section and simplifies the storage and reading of transient boundary conditions. The external flow around an airfoil has been used to demonstrate the operation and capability of this method.

Synthetic Eddy Method: The methods described thus far are based on a statistical view of turbulence and according to Wu [200] these are effective in areas far from the wall and with isotropic turbulence. However, close to solid walls, turbulence is highly anisotropic. In such cases, the Coherent Eddy Method has shown promising results. This method is based on a structural approach to turbulence and uses shape functions to create turbulent spots. Jarrin et al. [79] provide a comprehensive description of the method. The calculation of velocity fluctuation at a single point involves superimposing N turbulent spots

$$u'(\mathbf{x}, t) = \frac{1}{\sqrt{N}} \sum_{i=1}^{N} \epsilon_{ij} f_j(\mathbf{x} - \mathbf{x}_i(t)), \tag{3.55}$$

represented by Gaussian shape functions f_j and the sign of vortex i on component j. The convection of eddies through the inlet plane is achieved using *Taylor's* frozen turbulence hypothesis [1]. Cross-correlations between different velocity components are ensured by the *Cholesky* decomposition of the Reynolds-stress tensor (Eq. (3.53)). More realistic

[1] *Taylor's* frozen turbulence hypothesis postulates that turbulent structures are not changing over time and that they flow with the average velocity through each respective point (Pope [134])

distribution of turbulence can be achieved by zonally and directionally using different kind of shape functions, as shown by Pamiès et al. [130].

Subbareddy et al. [176] presents a slightly different approach. The Attached Eddy Method constructs an eddy box by filling a three-dimensional space with hairpin vorticities. The solenoidal velocity field is then calculated using the *Biot-Savart* law and transported into the inlet of the scale-resolving simulation.

One weakness of the early synthetic eddy methods was that continuity was only fulfilled in special cases, such as near-isotropic turbulence. However, with the introduction of coordinate stretching, Kröger and Kornev [94] were able to fulfill continuity under all kinds of anisotropic conditions.

AI Methods: The recent Artificial Intelligence (AI) boom has led to the increased use of Machine Learning (ML) applications in various fields. This includes the generation of turbulent, time-resolved inlet boundary conditions, where AI methods are also being employed. Fukami et al. [52] propose a machine-learned turbulence generator that uses an autoencoder-type Convolutional Neural Network (CNN) and Multilayer Perceptron (MLP) to generate turbulent inlet boundary conditions. The model was trained using DNS data from a channel flow and is capable of accurately reproducing the turbulent statistics and spatio-temporal correlations on a cross-section. However, the benefits of the method are limited because full DNS data is required for training. Pan et al. [131] presents the Neural Implicit Flow (NIF) framework, which enables a mesh-agnostic, low-rank representation of large-scale spatial-temporal data by employing two MLPs: one for the spatial and one for the temporal part of the signal. The ability of the method to learn and replicate turbulent flow has been demonstrated across multiple flow types.

The above-mentioned applications of ML for inlet data creation are just a few examples. In general, these methods show great promise for data reduction. However, they all require the full spatio-temporal information of precursor simulations for training. The development of networks capable of generating fully turbulent inlet data using only lower order data as input, as is done in synthetic turbulence methods such as the digital filter, would be a significant advancement. This subject is currently being researched.

The artificial synthesis of turbulence for use as unsteady inlet boundary conditions is an attractive option due to its flexibility and lack of need for an expensive precursor simulation. However, because of the complex nature of turbine inlet conditions, these methods are not applicable to CT cases. The interface between the combustor and turbine is characterized by fluctuations in velocity, pressure, and temperature, which are coupled by the conservation equations. Standard turbulence generating methods only account for velocity fluctuations and are insufficient for constructing the complex set of inlet boundary conditions required at the turbine inlet. The generation of realistic unsteady inlet boundary conditions for turbine simulations is commonly achieved through the use of an integrated simulation,

where the combustor module is simulated together with the turbine, or through the use of transient snapshot data of the outlet plane of a dedicated combustor simulation by employing recycling methods.

Recycling Methods

Recycling methods involve using transient field data from a precursor simulation (or measurements) as inlet boundary conditions for the main simulation. These approaches have the advantage that the generated inflow data is the solution of a simulation, fulfilling conservation laws and providing realistic turbulent statistics. In self-similar flows, such as the fully developed channel or flat plate flow, the data from the same simulation downstream of the inlet can be used instead of precursor simulations. Most recycling methods are based on the proposal of Spalart and Leonard [170] and further improved by Lund et al. [105]. The velocity profiles remain invariant in the streamwise direction, and scaled version of the downstream data can be applied as inlet boundary conditions. Examples and modifications of the recycling method can be found in the works of Sagaut et al. [146], Tabor and Baba-Ahmadi [179], Jiang et al. [82] and Boudet and Giauque [25]. The basic version of the method assumes self-similarity, which is not met in more complex technical applications. Recently, Garai et al. [53] introduced an adjoint optimization process to the recycling method, making it applicable to more general flow problems.

In the context of CTI, the recycling method involves using a scale-resolving simulation of the combustion chamber as a precursor simulation for the turbine simulation. Due to the high level of anisotropic and inhomogeneous pressure, temperature and velocity fluctuations in the combustor exit flow, similarity approaches are not suitable. The use of snapshot data from a precursor simulation is called *strong recycling*.

The turbulent flow at the interface between combustor and turbine is characterized by a wide range of turbulent motion with a broad spectrum of length scales and frequencies. To achieve a high temporal resolution and accommodate long simulation times, a significant amount of interface data is generated. This data must be stored on disk and loaded as inlet boundary conditions for the turbine solver. Furthermore, there is a difference in the time step width between the two simulations. The flow acceleration towards the rear of the first NGV passages necessitates a time step that is one order of magnitude smaller than that of the combustor simulation. Due to the significant difference in time step width, an interpolation is required to directly map the transient data from the combustor onto the turbine simulation. To address these challenges, some form of data compression must be employed.

Various methods exist for reducing the degree of freedom of interface data by isolating relevant motion structures. One such method is the Dynamic Mode Decomposition (DMD)

by Schmid [154], which extracts the dynamic characteristics of the flow field by calculating a set of modes associated with a specific oscillating frequency. Another popular method is Proper Orthogonal Decomposition (POD), also known as Principle Component Analysis (PCA) or *Karhunen-Loève* decomposition (eg. Sirovich [168], Lumley [104]). It is commonly used to visualize flow structures, both in measurement data and simulation results. (e.g. Kostas et al. [89], Weiss [191]). In POD, the flow is described by energy-ranked orthogonal structures with a separation of spatial and temporal shares by solving the Eigenvalue problem of the correlation matrix of the spatio-temporal snapshots. Treleaven et al. [185] suggests that the POD formulation is better than DMD for flow states with multiple frequencies because it is capable of capturing the greatest amount of energy with the fewest possible modes. Treleaven et al. [185] introduced the Proper Orthogonal Decomposition and Fourier Series (PODFS) method, which combines POD and Fourier Series (FS) to compress time-resolved inlet data for thermo-acoustic combustor simulations. Using a FS for the temporal part of the decomposition provides several benefits. The temporal signal is periodic and independent of the time step between snapshots. Furthermore, it ensures that the reduced order representation remains bounded, even for poorly converged POD modes. The combination of a digital filter for artificially creating turbulent fluctuations and this method has proven to be a powerful tool for providing realistic turbulent inlet boundary conditions (Treleaven et al. [184]).

To combine the benefits of energy-ranked POD and frequency-ranked DMD, two approaches were introduced, both named SPOD. Although they share the same name, the methods are clearly distinct, and it is important to distinguish between them. Both methods use different kernels to calculate the POD modes. The standard POD method uses the correlation matrix of the snapshots as a basis. Sieber et al. [166] introduced a filter to the correlation matrix of the standard POD formulation. By adjusting the filter strength and size, the method can smoothly transition from POD with a low filter strength and a wide filter size to DMD with a distinct and strong filter. The spectral constraints aid in separating flow structures and reducing the sensitivity of the method to signal noise compared to the standard POD method by finding an optimal filter size for the given flow problem.

The second approach, known as SPOD, is described by Towne et al. [183] and Schmidt and Colonius [155]. It is based on the idea of Picard and Delville [132], to use the cross-spectral density as the kernel for the POD. The eigenvalue problem is solved for each frequency, and the resulting modes are orthogonal under the time-space product. This is beneficial for the analysis of spatio-temporal coherent structures as found in turbulent flows. The SPOD method has been used multiple times to generate transient inlet boundary conditions for scale-resolving simulations. Ghate et al. [55] extended the basic SPOD method by adding the option to model the small turbulent scales in the inertial subrange using physics-based Gabor modes, while isolating the larger scales using the SPOD. This combined approach accurately reproduced wake turbulence and could be prescribed as inlet boundary conditions

for subsequent simulations. In the context of combustor-turbine interaction, the SPOD method is used too. Martin et al. [108] used the SPOD representation of snapshot data from a combustor-simulator simulation as inlet boundary conditions for a subsequent turbine NGV simulation. More details on this work can be found in Chapter 2.

The techniques outlined above for compressing spatially and temporally resolved field data are all founded on fundamental vector algebra and share many similarities. Each method has its own advantages and disadvantages and is more or less suitable for certain applications. For instance, the DMD is advantageous when distinct frequencies are present in the data, while POD is optimal for data compression due to its energy-ranked character. The combination of POD and FS provides temporal flexibility in the PODFS method. The SPOD combines the benefits of DMD and POD, presenting a sophisticated solution for visualising and analysing flow characteristics. Due to the availability of previous work, the PODFS method was chosen as the compression tool for the data at the CT interface in this study.

3.4.1. PODFS

This section will describe the original PODFS method. Chapter 4 outlines the adaptations made to the method and its implementation for use in CT cases. The POD decomposes the vector field of turbulent flow into a set of deterministic modes. The basic functionality of POD is described based on the 2-dimensional, time-dependent velocity vector $\mathbf{u}(\mathbf{x},t)$. For a more detailed description of the POD method, please refer to the work of Weiss [191]. The first step involves calculating the velocity fluctuations $\mathbf{u}'(\mathbf{x},t)$ by subtracting the time mean $\bar{\mathbf{u}}(\mathbf{x})$ from the instantaneous velocity field.

$$\mathbf{u}'(\mathbf{x},t) = \mathbf{u}(\mathbf{x},t) - \bar{\mathbf{u}}(\mathbf{x}) \tag{3.56}$$

The vector field of fluctuating velocity components can be described as a set of spatial modes $\Phi_i(\mathbf{x})$ and temporal coefficients $a_i(t)$.

$$\mathbf{u}'(\mathbf{x},t) = \sum_{i=1}^{N_S} a_i(t)\Phi_i(\mathbf{x}) \tag{3.57}$$

In Eq. (3.57), N_S is the number of time snapshots. To transform 2-dimensional snapshot data into the POD formulation, the *snapshot POD* method by Sirovich [168] is used, which is a modified form of the standard POD method. Eq. (3.57) is symmetric in t and $\mathbf{x}$, allowing for interchangeability between spatial modes and temporal coefficients. This method is more efficient than the standard POD method for datasets with a larger product of points and variables than time steps. The following provides an overview of the basic steps involved in *snapshot POD*:

1. collect all snapshot data in the *snapshot matrix* **U**
2. build correlation matrix $C_S = \frac{1}{N_S}\mathbf{U}\mathbf{U}^T$
3. solve Eigenvalue problem of C_S and obtain the temporal coefficients $A_i(t)$ as the Eigenvectors and the corresponding energy λ_i as the Eigenvalues
4. scale temporal coefficients with energy $a_i(t) = A_i(t)\sqrt{\frac{\lambda_i}{a_{i,mag}(t)}}$, with $a_{i,mag}(t) = \frac{1}{N_S}\sum_{i=0}^{N_S} A_i(t)^2$
5. calculate spatial modes: $\phi_i(\mathbf{x}) = \mathbf{U}a_i(t)$
6. scale spatial modes with energy $\Phi_i(\mathbf{x}) = \frac{1}{N_S}\phi_i(\mathbf{x})diag(\frac{1}{\lambda_i})$

The POD formulation has an important property where the first N_P modes represent the majority of the total energy in the data set. The ratio of the energy of the first N_P POD modes to the energy of the original data is denoted by E_λ, which determines the number of POD modes used for data compression.

$$E_\lambda(N_P) = \frac{\sum_{i=1}^{N_P}\lambda_i}{\sum_{i=1}^{N_S}\lambda_i} \tag{3.58}$$

In Eq. (3.58), λ_i represents the energy of the i^{th} POD mode. By reducing the number of modes, the data size can be significantly decreased while still preserving the essential information of the original data. To address the issue of the time step difference between the precursor and the main simulation and to further compress the data, the temporal coefficients $a_i(t)$ are approximated using Fourier Series:

$$\tilde{a}_i(t) \approx \sum_{j=0}^{N_{F_i}-1} b_{il(j)} e^{2\pi l(j)t/\Delta t N_S}, \tag{3.59}$$

where $l(j)$ is a ranking function that sorts the Fourier coefficients according to their magnitude. The Fourier coefficients are calculated using Eq. (3.60) with $j = -N_S/2, ..., N_S/2-1$.

$$b_{ij} = \frac{1}{N_S}\sum_{k=0}^{N_S-1} a_i(t) e^{-2\pi ijt/\Delta t N_S} \tag{3.60}$$

Similar to Eq. (3.58), the number of Fourier coefficients per mode can be reduced without losing the important temporal information. The energy criteria for the Fourier coefficients can be expressed as follows:

$$E_b(N_{F_i}, i) = \frac{\sum_{j=0}^{N_{F_i}} |b_{il(j)}|}{\sum_{j=0}^{N_S-1} |b_{il(j)}|} \tag{3.61}$$

The number of Fourier coefficients per mode N_{F_i} is determined by E_b. It represents the ratio of Fourier-approximated mode energy to total mode energy. Finally, the snapshot data can be reconstructed using:

$$\tilde{\mathbf{u}}(\mathbf{x}, t, E_\lambda, E_b) = \bar{\mathbf{u}} + \sum_{i=1}^{N_P} \Phi_i(\mathbf{x}) \sum_{j=0}^{N_{F_i}-1} b_{il(j)} e^{l(j)t/\Delta t N_S}. \tag{3.62}$$

By truncating the modes and Fourier coefficients, this formulation greatly reduces the amount of data that needs to be stored and loaded at the interface between two simulations. The Fourier formulation of the temporal part allows for the signal to be reconstructed at any necessary time value for the main simulation, making the PODFS method highly efficient and superior to the strong recycling method.

4. Methods Development - Unsteady Inlet BC

The initial section of this chapter outlines the implementation of the PODFS method in the context of CTI. Additionally, it presents the supplementary modules that facilitate the reading of transient PODFS BC with the CFD solver ANSYS® CFX®. The second section of this chapter illustrates the potential of the method to recreate the temporal and spatially resolved fields at the interface between two simulations, using a generic test case and the research turbine case.

4.1. PODFS Implementation

The aim of this work is to enhance the predictive capabilities of CFD simulations of HPT. To achieve this, a method is developed to use transient snapshot data from a combustor simulation as inlet boundary condition for a subsequent turbine simulation. The PODFS method introduced in Section 3.4.1 is implemented in a *PYTHON* routine to perform the task of collecting the snapshot data, creating a reduced order model from it and providing it in a form suitable for use in turbine CFD.

Fig. 4.1 shows the schematic illustration of the program sequence. The transient snapshot fields of pressure, temperature, and velocity serve as input for the method. In addition, parameters are used to control the PODFS process. The PODFS routine runs in a three-step scheme, starting with the *data reader*.

In a loop over all snapshots, the fields are read in, and in the first step derived values are calculated. These values are the BC required for a turbine simulation. CFX as the turbine solver requires total pressure, total temperature, and the cylindrical components of velocity directions. Meanwhile, the Rolls-Royce in-house solver HYDRA requires flow angles in the radial and circumferential directions instead of the velocity vector components. In the second step, all fields are interpolated onto a regular grid with a user-defined resolution, *res*, for further processing. To avoid loss of information during interpolation, it is important to choose a resolution similar to that of the original data. To obtain the mean turbulence values, the turbulence intensity and the turbulent length scale are calculated in the next step following the procedures described in Section 3.2.1. The total pressure fields are normalized to the mean value at the interface plane and the total temperature fields are normalized

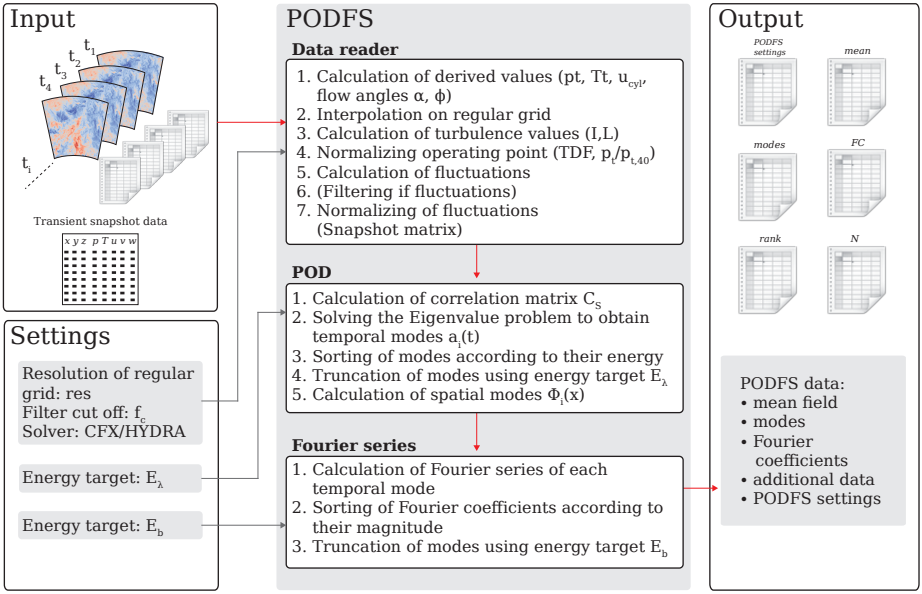

Figure 4.1.: Methods Development: schematic representation of PODFS with input and output

using the formulation of the local OTDF (cf. Section 2.1.3) to allow for operating point scaling. The next step is to calculate the fluctuations of all components by subtracting the time mean from the instantaneous snapshots. If necessary, these fluctuations can be filtered to account for low-frequency movements or operating point drifts. More information on this subject can be found in Section 5.1.2. The POD is performed on the snapshot matrix of all fluctuating components together. In the final step of the data reader, the fluctuations of all components are scaled to the interval of -1 to 1 and then saved in the snapshot matrix, ensuring equal balance of fluctuations among all components, which is important for the energy criterium to determine the amount of POD modes used. The second step in the PODFS method involves performing a POD of the snapshot matrix. This requires following the steps outlined in Section 3.4.1 for snapshot POD. In the last step the approximation of the temporal modes using Fourier series is done.

The PODFS method generates files that contain a reduced order model of the snapshot data at the interface between two simulations. These files include a settings and statistics file for the PODFS. This file is crucial for the turbine solver as it contains information about the operating point and the size and format of the PODFS data. When scaling the

operating point, the desired values for total pressure and temperature must be adjusted there. Additionally, files containing coordinate information for the data points, mean fields, spatial POD modes, and Fourier coefficients exist and contain the actual PODFS data. The dataset is supplemented with information on the number and ranking of the Fourier coefficients, which is necessary to reconstruct the actual BC fields from the PODFS data.

4.2. PODFS Reader in CFD Solver

To use the PODFS data as unsteady inlet BC in a turbine simulation, it was necessary to add PODFS reading capabilities to the turbine CFD solvers, namely ANSYS® CFX® and the Rolls-Royce in-house solver HYDRA.

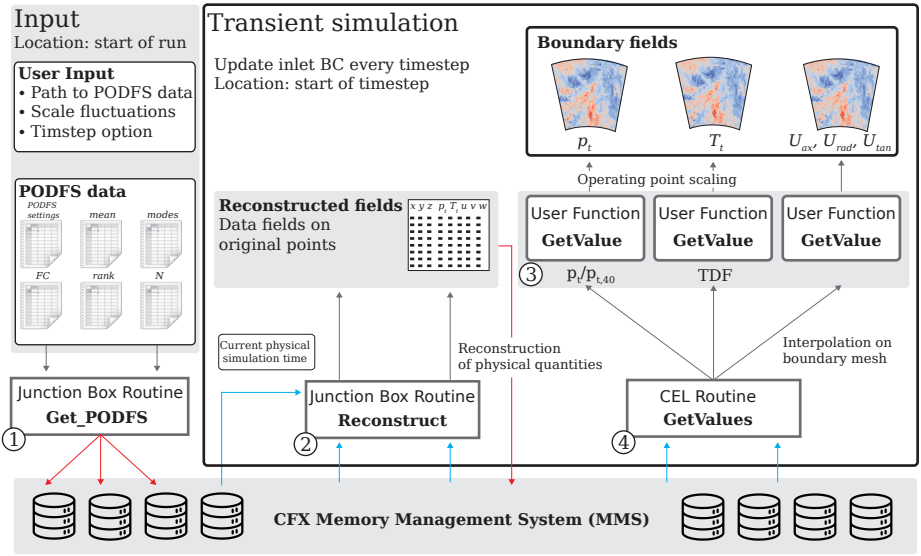

Figure 4.2.: Methods Development: schematic representation of PODFS reader in CFX

In ANSYS® CFX® this is done via Fortran subroutines whithin the framework of *user Fortran*. They allow the user to add features and models to CFX which are not available in the solver. These user routines are called by the solver via junction box routines or CEL functions/routines.

Fig. 4.2 shows a schematic illustration of the Fortran framework used to read unsteady inlet BC in CFX. In the user input section of CFX the path to the PODFS data and other options are set. At the start of the simulation, the first user subroutine *GetPODFS* ① is called via a Junction Box Routine to read in the PODFS data. The POD modes, Fourier coefficients, and other data from the PODFS files are loaded into the CFX Memory Management System (MMS) to make them available for the solver process. Before every time step in the loop of the transient simulation, a series of routines are called to update the inlet BC. The *Reconstruct* subroutine ② called by another Junction Box Routine utilises the PODFS data in the MMS and the current simulation time to reconstruct the physical values of the boundary fields using Eq. (3.62). The resulting fields are then stored in the MMS for future use. The boundary condition is defined through user functions *GetValue* ③ for each boundary variable. These functions call the CEL routine *GetValues* ④, which reads the corresponding field from the MMS and interpolates it to the boundary mesh. At this stage, the scaling of the operating point for total pressure and total temperature is performed using the averaged turbine inlet values (40) provided in the PODFS settings file.

4.3. Validation of PODFS on a Generic Test Case

To test the ability of the PODFS method to replicate the inlet boundary condition for scale-resolving simulations, a generic test case is used. This test case is designed to provide results with little computational effort compared to actual CT test cases. This allows many simulations to be run to investigate the effect of different PODFS parameter settings. Despite its simplicity and small mesh size, the test case is intended to map the mechanisms relevant to CTI. These are: high velocity, pressure and temperature fluctuations and strong temperature non-uniformity at the interface between two simulations. A portion of the results has already been published in Gründler et al. [60].

The validation process of the PODFS method involves two simulations sets. In the first simulation, the entire domain, consisting of an inlet section and the section of interest is simulated in integrated form. In analogy to a CT case, the inlet part represents the combustion chamber and the section of interest the HPT. In the second simulation the computational domain is reduced to the section of interest only and the flow at the interface between the inlet section and the section of interest is modelled via inlet BC. For transient SRS the inlet BC are provided by the PODFS representation of transient snapshot data. In this approach, the first simulation serves two purposes: it provides snapshots for the PODFS method to use as inlet BC for the second simulation with a truncated domain and acts as a baseline for comparison with the PODFS solution.

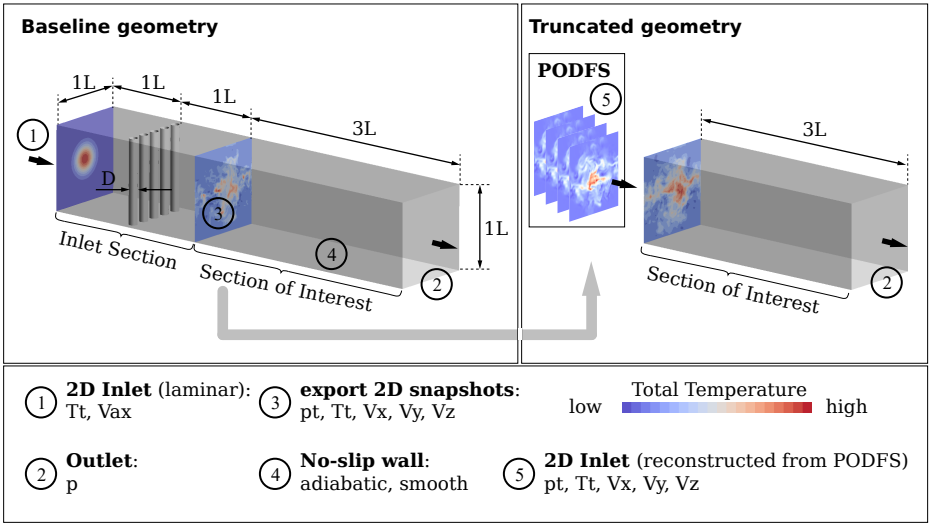

Figure 4.3.: Numerical setup of baseline channel geometry (left) and truncated channel geometry (right)

4.3.1. Numerical Setup

The geometry and the numerical setup of the channel test case is shown in Fig. 4.3. The baseline geometry (left) consist of a rectangular channel with an edge length of $L = 0.01\text{m}$. The snapshot extraction plane, located $2L$ downstream of the inlet, marks the end of the inlet section. At this location, the 2D fields are extracted as snapshots to be used as input in the PODFS method. The section of interest extends over $3L$. Five turbulence-generating structures are located halfway through the inlet section. These are cylindrical rods that extend the full height of the channel, have a diameter of $D = L/10$ and are evenly distributed across the channel width. At the inlet of the baseline geometry a 2D distribution of total Temperature and boundary-normal velocity are prescribed. The velocity profile is used to specify a fully developed boundary layer profile. A hotspot is located in the middle of the inlet plane. This creates temperature inhomogeneities that allow thermal mixing to be studied. The truncated geometry (right) only consists of the section of interest. The inlet section is neglected and the flow at the interface is modelled by using the PODFS data as inlet boundary condition.

The hybrid structured/unstructured meshes of the channel are created using the commercial

software CENTAUR®v15.0[1]. The first 15 layers near the walls are prismatic to resolve the boundary layer. The area around the turbulence generating structures is filled with tetrahedral cells. To reduce the overall mesh size, the sections from the inlet to just upstream of the turbulators and from just downstream of the turbulence generators to the outlet are meshed with structured hexahedrons. The mesh size is chosen to be in the range of the Taylor length scale (cf. Section 3.2). To ensure the position of the first element at the walls in the viscous sublayer, y^+ is kept below one throughout the domain. ANSYS® CFX®2021.2 (cf. Section 3.3) is used for the simulations. The main mesh statistics and solver settings are listed in Table 4.1.

Table 4.1.: Mesh statistics and numerical setup for simulations of the channel test case

Numerical mesh			**Setup and convergence**	
Domain	Baseline	Truncated	Solver	ANSYS® CFX® v2021.2,
Cells (Mio.)	10.7	4.4		unsteady
Min. cell angle (°)	21	46.3	Gas model	ideal compressible
Max. EVR*	102.3	9.1	Turbulence	LES WALE
Avg. EVR*	1.5	1.5	Δt	2×10^{-6}s, 7 sub iterations
Max. EAR†	72	67.3	Advection	CDS††
Avg. EAR†	2	1.6	Transient	2$^{\text{nd}}$ order backward Euler
Max. y^+	0.8	0.3	Residuals	$< 2 \times 10^{-4}$
Avg. y^+	0.41	0.08	Imbalances	$< 0.015\%$ (for u,p)
$\Delta^{\star\star}$	9×10^{-5}m			$< 0.15\%$ (for H)

* Element volume ratio † Element aspect ratio ** Grid spacing †† Central differencing scheme

4.3.2. Baseline Geometry and Variation of Turbulence Model

In this preliminary investigation, the baseline geometry is utilized to compare commonly used turbulence modelling approaches for predicting turbulent mixing processes in the channel flow behind the turbulence generating rods. The models used for the comparison are: RANS, URANS, both using the $k-\omega$ SST model, and three SRS methods: SAS, SBES, and LES. The same mesh is used for all simulations and the same time step settings, simulation duration and averaging interval in all unsteady simulations. Fig. 4.4 (top left) shows the evaluation objects for the channel case. Data is evaluated along the centerline and five lateral lines in both directions at different streamwise locations x/L. In addition,

[1] https://www.centaursoft.com/

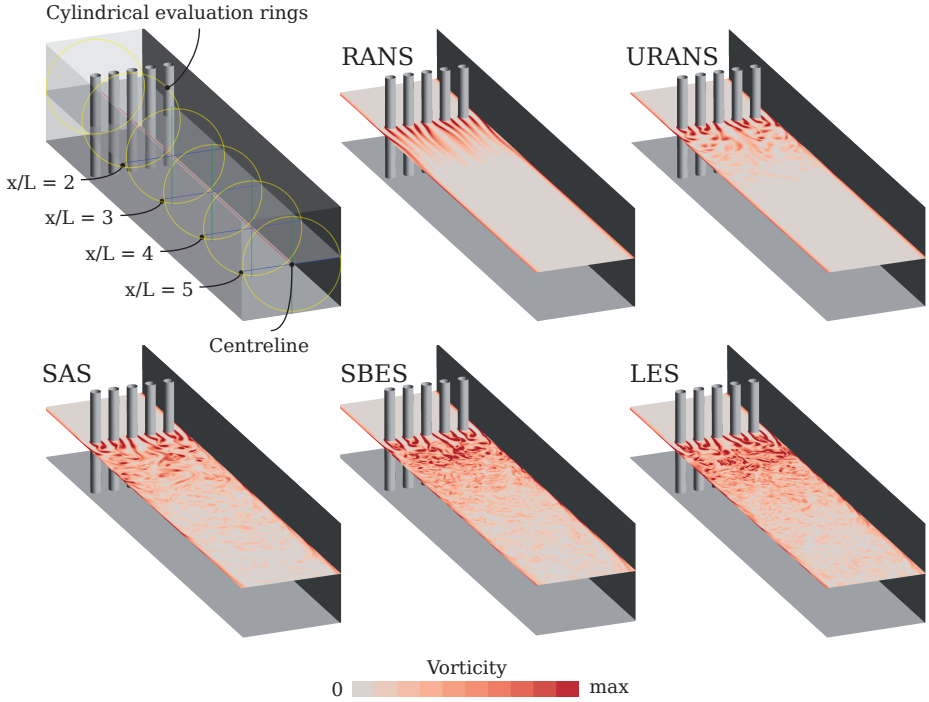

Figure 4.4.: Evaluation locations and vorticity contours for different turbulence models

the temperature is evaluated on cylindrical ring surfaces along the channel to assess the transport of hot fluid towards the channel walls.

In addition, Fig. 4.4 displays the instantaneous vorticity contours on a plane in the middle of the channel for the various simulations, highlighting their scale-resolving characteristics. As anticipated, the RANS simulation displays only the vorticity streaks of the wakes without any lateral fluctuations as it does not resolve any unsteadiness. The URANS method permits unsteady motion but only resolves very large vortices behind the rods. The three SRS reveal vortex structures that are significantly smaller than those in the URANS simulation. Notable differences, however, can be observed between SAS and the other two SRS. In the SAS, the resolved turbulent structures are not as small as in the LES or SBES. The SAS lies between the URANS and the LES. The SBES and LES show turbulent structures of comparable size. The SBES model utilises LES in most regions of the domain, with the model switching to

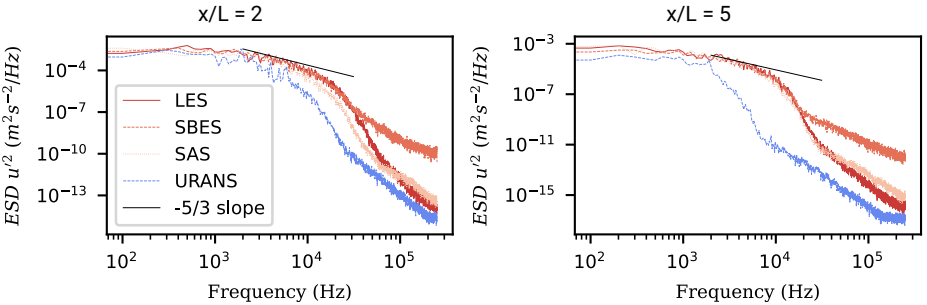

Figure 4.5.: Energy Spectral Density (ESD) of two monitor points, one at the inlet/interface and one at the outlet of the channel for different turbulence models

RANS only in proximity to solid walls. This is why both models produce very similar results.

The differences mentioned above are also reflected in the ESD, as shown in Fig. 4.5 at two monitor points. The first one is located at the snapshot extraction plane $x/L = 2$ and the second one at the outlet $x/L = 5$, both in the centre of the channel. At both monitoring locations, the spectrum of the URANS is lower than that of the other simulations and bends downwards earlier. The LES and SBES follow the $-5/3$ slope for the longest and the SAS drops off earlier, especially in the front part of the channel.

The differences in partially resolving the turbulent motion is effecting the flow field in the channel. Although there are local variations in the velocity field, particularly within the first two length units (L) behind the bars, the overall velocity distribution is comparable in all simulations (refer to Appendix A, Fig. A.1). The simulation using the RANS model under-predicts turbulent mixing, and the wakes of the rods are visible at $x/L = 2$. In the other simulations, the imprints of the wakes are mixed out. Towards the outlet of the domain, the results of the RANS simulation approach the other results, and the velocity field is similar there.

Significant temperature differences are apparent when examining the temperature field. The test case is designed with a hot spot located in the middle of the inlet plane to investigate turbulent thermal mixing in the region behind the turbulence generating rods. Turbulence redistributes hot fluid from the central part of the channel towards the outer regions, resulting in a decrease in temperature along the centerline and an increase in temperature in the outer regions of the channel. The varying treatment of turbulence in the simulations is directly affecting the mixing of temperature.

Fig. 4.6 displays the total temperature on a plane at mid-channel height for the different

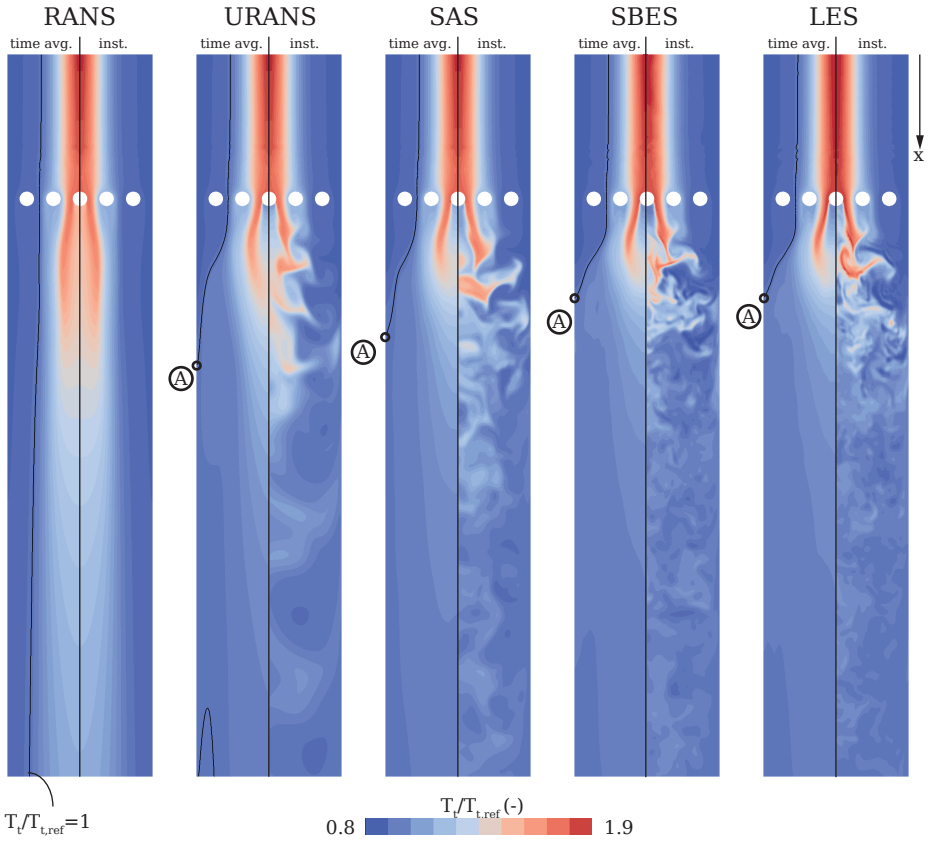

Figure 4.6.: Total temperature contours on the mid-plane for different turbulence models. Time average on the left and instantaneous value on the right

simulation types. The contours are divided in half, with the right-hand side showing the instantaneous temperature field at a fixed time step and the left-hand side presenting the time-averaged temperature field. The instantaneous temperature fields reveal the imprint of turbulence, highlighting differences between turbulence modelling approaches. Finer temperature filaments become visible when transitioning from URANS to LES. As is typical in technical applications, mean quantities are of great importance here as well.

Comparing the time-averaged temperature fields between the different simulations reveals differences in temperature mixing. The strongest thermal mixing is observed in the LES and SBES simulations, followed by the SAS and URANS simulations. As indicator for this, the iso-line of $T_t/T_{t,ref} = 1$ and the location Ⓐ, where the temperature at the channel wall is reaching the reference temperature for the first time are taken into account. The stationary RANS simulation underestimates the thermal mixing, leaving the temperature hot spot behind the rods intact. There is a noticeable trend of increasing thermal mixing when the capability of the turbulence model to resolve turbulent fluctuations is increased. The temperature curves in Fig. 4.7 show that the centerline temperature decreases and the temperature on the cylindrical surface at the channel walls, downstream of the turbulence generating rods, increases as the resolved turbulence of the modelling approach rises. The lateral temperature distributions at different streamwise locations indicate that the higher turbulent fluctuations in the scale-resolving simulations mix out the temperature hot spot in the centre of the channel with the surrounding colder fluid. As one progresses downstream through the channel, a decrease in temperature is observed in the center, while an increase is noted towards the channel walls. Table 4.2 displays the total temperature difference of the simulations that used various turbulence models in comparison to the LES result. The two scale-resolving simulations, SBES and SAS, match the LES results with small deviations. The URANS simulation is capable of resolving the largest vortex structures, modelling a large portion of thermal mixing. The difference in total temperature to the LES is relatively small, with 0.91% on the centerline and 0.22% at the walls. The stationary RANS simulation is unable to accurately replicate turbulent thermal mixing and is underestimating wall temperatures by 14.5% when compared to the LES.

Table 4.2.: ΔT variation of turbulence model on baseline geometry

	ΔT_t [†]centerline	ΔT_t [†]channel walls
SBES	-0.12%	-0.02%
SAS	0.14%	-0.08%
URANS	0.91%	-0.22%
RANS	14.5%	-3.72%

[†] $\Delta T_t = \frac{T_t - T_{t,LES}}{T_{t,ref}} \cdot 100$

From the variation of the turbulence modelling approach follows:

- The ability to resolve temporal fluctuations is the most crucial factor in predicting turbulent thermal mixing in a simulation approach. As a result, the stationary RANS simulation fails to accurately predict turbulent temperature mixing.
- Switching to URANS is significantly increasing the turbulent thermal mixing compared

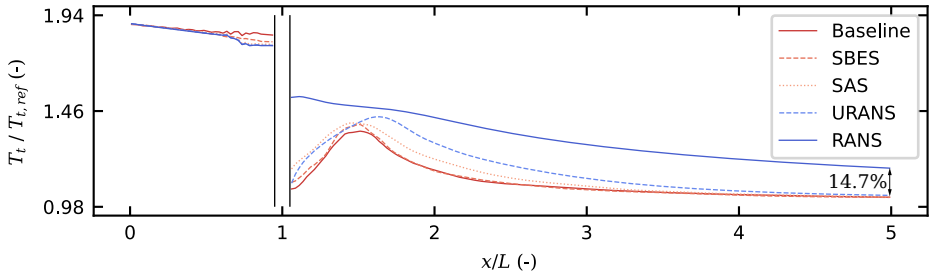

(a) Centerline total temperature

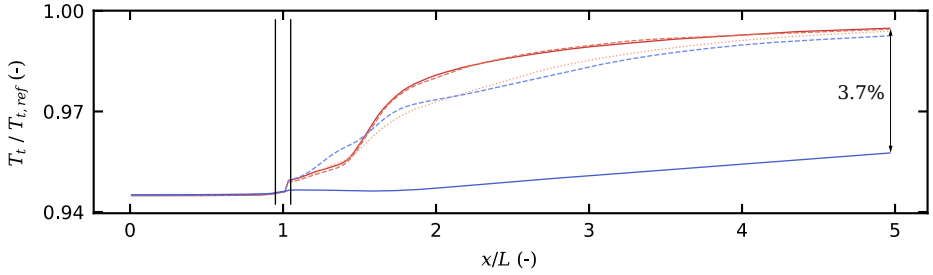

(b) Averaged total temperature on cylindrical surface at channel walls

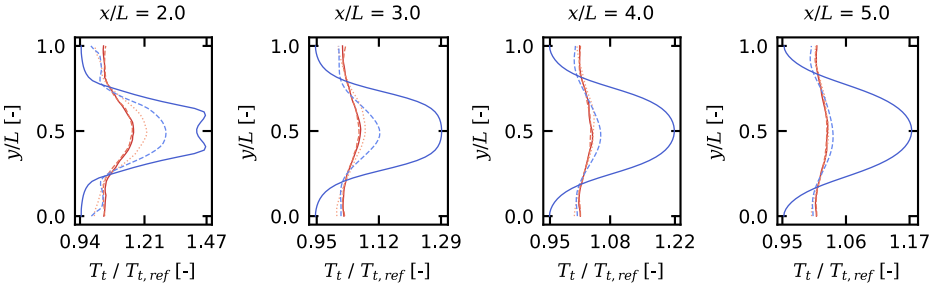

(c) Lateral total temperature distribution at different streamwise positions

Figure 4.7.: Total temperature distribution in baseline channel for different turbulence models

to the steady RANS simulation because the largest turbulent structures are resolved.

- SRS methods are capable of predicting an even higher thermal mixing, while the LES and SBES predict slightly higher thermal mixing than the SAS.

- In this test case, the SBES model performs similarly to the LES. In cases of high *Reynolds* number flow conditions, such as those found in CT cases, the mesh resolution at solid walls may not be fine enough for LES. The SBES model is expected to perform better and should be selected (Menter [114]).

4.3.3. Truncated Domain and Unsteady Inlet Boundary Conditions

The primary objective of this test case is to demonstrate the capability of the PODFS method to replicate turbulent flow conditions at the inlet of the truncated channel domain. The following section compares a simulation using the PODFS data as inlet BC to the baseline simulation. To separate two components, interface data must be transferred from the upstream to the downstream component. Introducing a discontinuity at the interface by splitting the domain in two leads to modelling errors (Schneider [158]). To differentiate these modelling errors from the errors introduced by the PODFS method, the *strong recycling* method is used to directly apply the transient snapshot data as inlet BC. The results of this simulation is then compared to the results of a simulation using the PODFS method to compress the interface data before using it as inlet BC.

Fig. 4.8 displays the vorticity contours, which reveal vortex structures of comparable size for the baseline simulation and the two truncated domain simulations. The instantaneous and mean temperature fields also demonstrate a high level of agreement among all three simulations. The agreement between the baseline simulation and the two truncated simulations is evident in the centerline and lateral mean velocity profiles in Appendix A Fig. A.2, which show an almost perfect match. Small deviations are visible in the temperature distribution in Fig. 4.9. Table 4.3 presents the differences in total temperature at the outlet of the channel between the truncated domain simulations and the baseline simulation. It is important to note that the deviations between the baseline and the simulations with the truncated domain are small.

Table 4.3.: ΔT_t truncated domain using inlet BC vs. baseline case

	ΔT_t [†]centerline	ΔT_t [†]channel walls
strong recycling	0.37%	-0.11%
PODFS	-0.39%	0.04%

[†] $\Delta T_t = \frac{T_t - T_{t,BSL}}{T_{t,ref}} \cdot 100$

The ESD on the inlet plane $x/L = 2$ in Fig. 4.10c displays similar curves in the lower frequency range for all three simulations. This implies that the largest turbulent structures

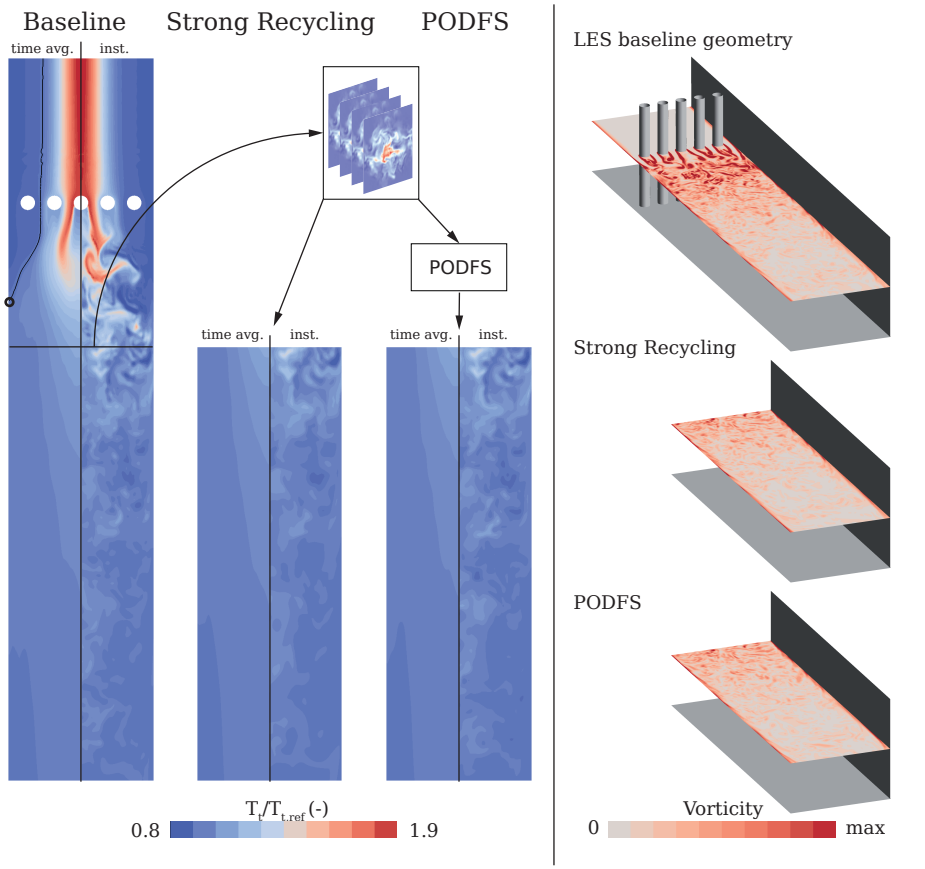

Figure 4.8.: Baseline domain versus truncated domain simulation using unsteady inlet BC: Vorticity contours and total temperature contours on the mid-plane.

are correctly applied by both inlet boundary methods. In the inertial subrange, at around 1×10^4 Hz, the PODFS simulation deviates from the $-5/3$ slope slightly earlier than the other two simulations and drops off at a higher rate. This is due to the compression in the PODFS method where low energetic modes are neglected. The most significant differences in the turbulent spectrum between the simulations occur at very high frequencies ($> 5 \times 10^4$ Hz). Here, the two simulations with the truncated domain exhibit higher energy levels

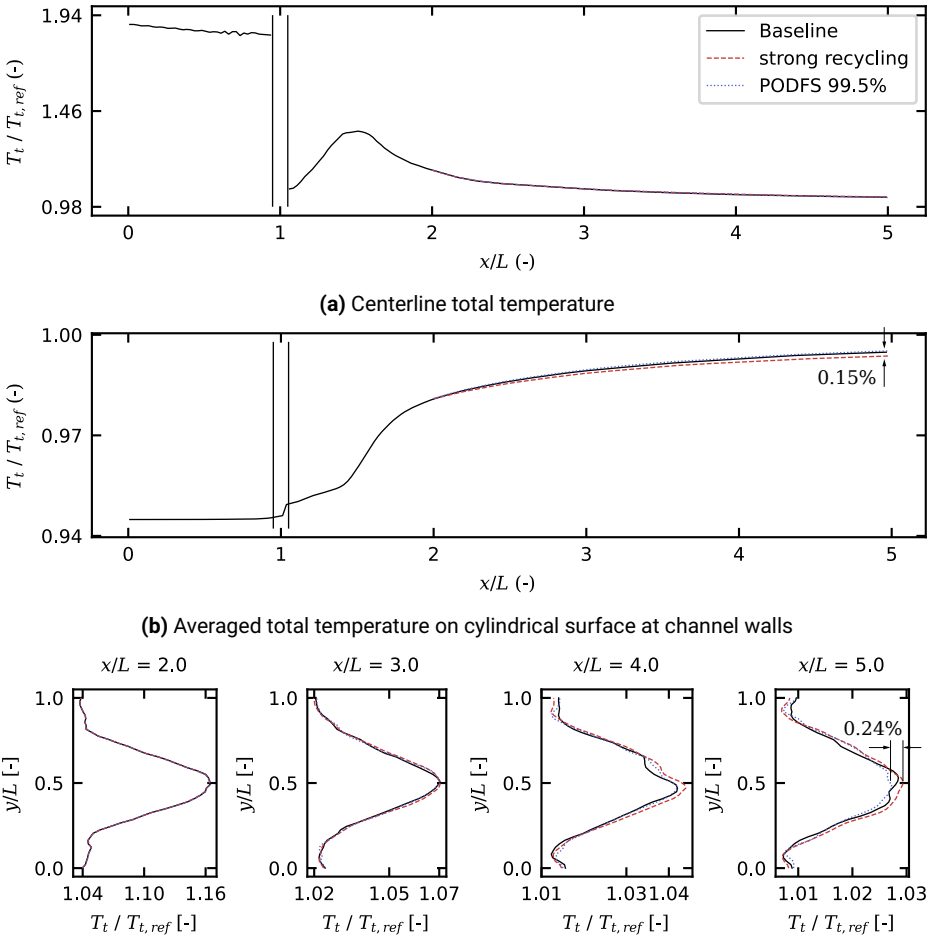

(a) Centerline total temperature

(b) Averaged total temperature on cylindrical surface at channel walls

(c) Lateral total temperature distribution at different streamwise positions

Figure 4.9.: Comparison of total temperature distribution between baseline channel and truncated channel with different inlet BC

than the baseline simulation. These differences in simulation results are attributed to the separation of the domain and the prescription of inlet BC and not to the PODFS method, as

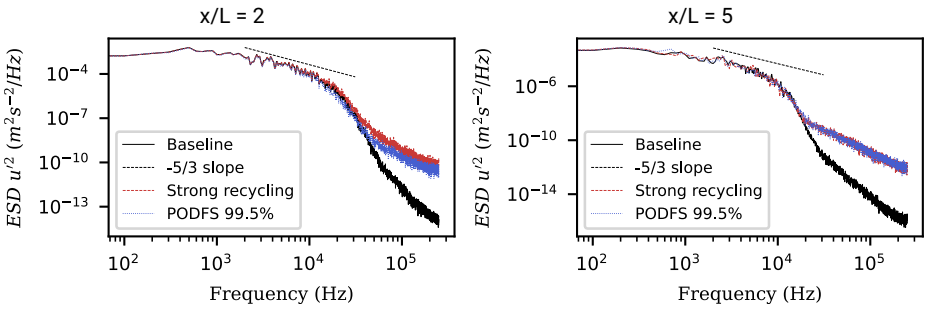

(c) ESD of two monitor points, one at the inlet/interface and one at the outlet of the channel

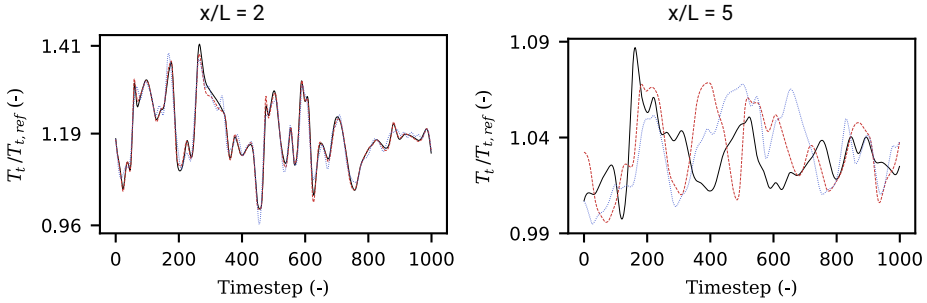

(f) Time trace of total temperature of two monitor points, one at the inlet/interface and one at the outlet of the channel

Figure 4.10.: Temporal and spectral signal of monitor points in channel for baseline and truncated simulations

they occur in both simulations with the truncated domain. It is worth noting that these differences are minor in nature, occurring at the smallest scales and very low energy levels. This is also evident in the time course of the total temperature at the monitoring points shown in Fig. 4.10f, which are very similar for all three simulations in the inlet plane ($x/L = 2$). Even the slightest difference at the inlet of the channel can cause a significant drift in the local temperature values towards the outlet. As a result, the time traces in the outlet plane exhibit greater differences. (The average RMS error in all monitor points for the strong recycling simulation and the PODFS simulation, compared to the baseline simulation, is 1.18% and 1.56%, respectively.) From a frequency perspective, however, all three simulations exhibit a similar ESD in the lower frequency range, with differences only at very high frequencies. These differences arise from the separation of domains and are

already apparent at the channel inlet.

The comparison of simulation results between the baseline simulation and the two simulations using the truncated domain and unsteady inlet BC shows an excellent match. This demonstrates the capability of both the strong recycling and the PODFS method to reproduce turbulent conditions at an interface. Both methods are suitable for the use case of unsteady coupling of two scale resolving simulations.

4.3.4. Variation of Turbulence model in Combination with PODFS boundary conditions

Section 4.3.2 presented the differences between various turbulence modelling approaches in simulating the flow in the baseline channel geometry. The stationary RANS simulation cannot model the highly turbulent flow behind the rods and the corresponding turbulent thermal mixing. The predicted mixing of fluids with disparate temperatures is more pronounced when the turbulence model's capacity to resolve turbulence structures is enhanced. The LES predicts the highest level of mixing, but already the URANS simulation forecasts significantly higher rates of turbulent mixing processes than in the stationary RANS simulation. Section 4.3.3 demonstrated the ability of the PODFS method to replicate turbulent flow at the interface. In this section, the use of different turbulence models in combination with the PODFS boundary condition on the truncated domain is investigated. It is anticipated that the same trend as in the baseline case will be observed, with turbulent thermal mixing increasing as the fidelity of the turbulence model used increases. The question remains whether the URANS simulation can capture sufficient transient fluctuations to simulate adequate turbulent mixing.

Table 4.4.: ΔT_t truncated domain under variation of the turbulence model

	ΔT_t †centerline	ΔT_t †channel walls
SBES	0.04%	0.04%
SAS	0.11%	0.04%
URANS	0.87%	-0.26%

† $\Delta T_t = \frac{T_t - T_{t,LES}}{T_{t,ref}} \cdot 100$

The ESD and time trace of the monitor point in Fig. 4.11 indicate that the URANS simulation matches well with the other scale-resolving simulations at the inlet, as expected due to the same inlet boundary condition. However, differences arise towards the outlet where the spectrum lies below the other simulations in all frequencies and the characteristic $-5/3$

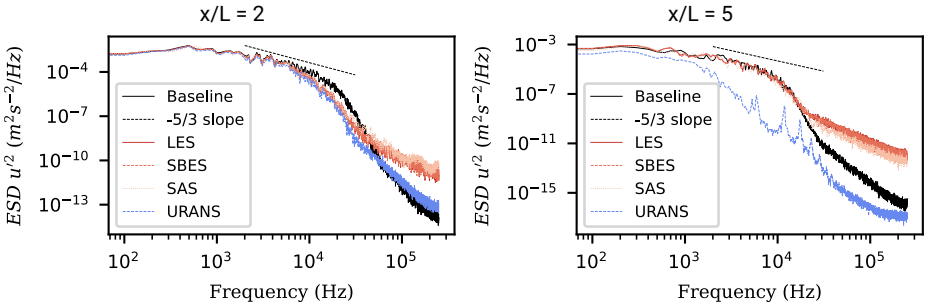

(c) ESD of two monitor points, one at the inlet/interface and one at the outlet of the channel

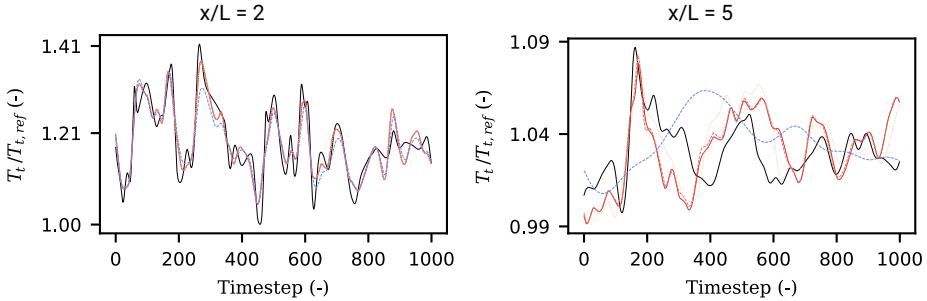

(f) Time trace of total temperature of two monitor points, one at the inlet/interface and one at the outlet of the channel

Figure 4.11.: Temporal and spectral signal of monitor points in channel for truncated simulations under variation of turbulence model

slope is not visible. The URANS method is capable of resolving large unsteady structures, but it is not suitable for modelling the decay process of eddies into smaller ones.

The turbulence model variation in the baseline geometry (refer to Section 4.3.2) revealed a discrepancy of 0.91% in centerline temperature and -0.22% in channel wall temperature at the outlet of the channel between URANS simulation and LES. The temperature differences between the URANS and LES cases can be observed to be similar for the truncated geometry when using PODFS BC. Specifically, Table 4.4 shows a total temperature difference of 0.87% at the centerline and -0.26% at the channel walls. The three scale-resolving turbulence models, LES, SBES, and SAS, produce almost identical results, with only minor differences. The lack of turbulent motion in the URANS simulation results in an under-prediction

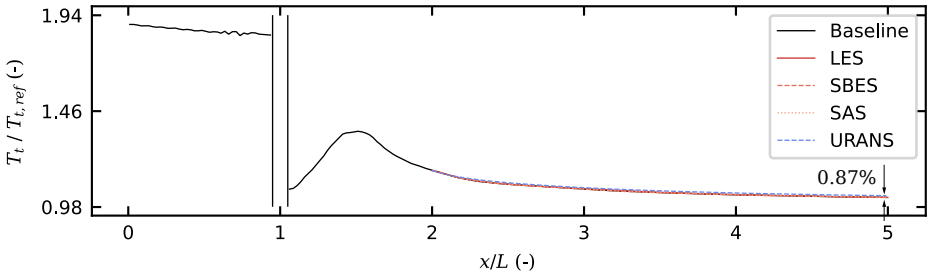

(a) Centerline total temperature

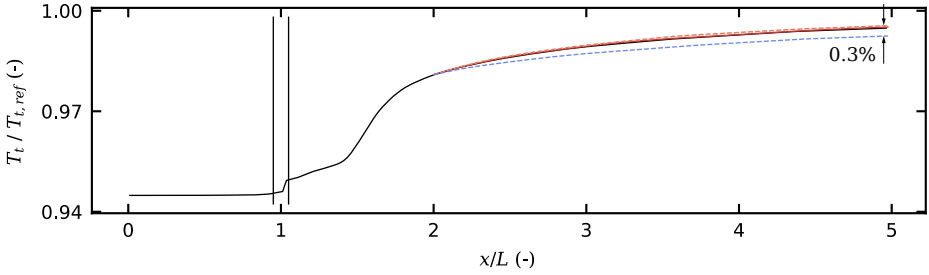

(b) Averaged total temperature on cylindrical surface at channel walls

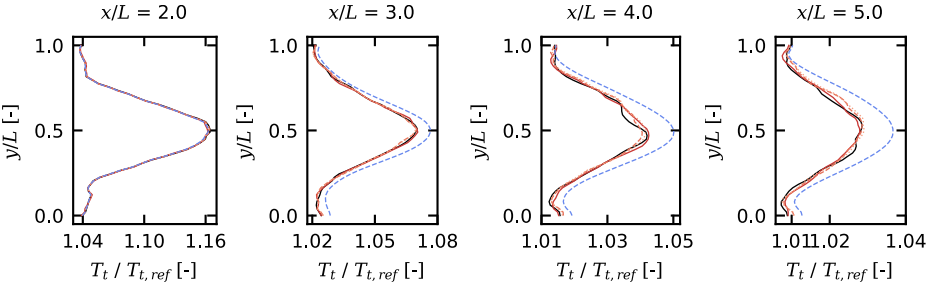

(c) Lateral total temperature distribution at different streamwise positions

Figure 4.12.: Total temperature distribution in truncated channel under variation of turbulence model

of turbulent heat flux from the center towards the walls of the channel. However, the URANS method can still determine the temperature distribution to a certain extent, and the differences to scale resolving simulations are small (Fig. 4.12). These findings support

the thesis that the largest turbulent structures are mainly responsible for turbulent thermal mixing. In a subsequent chapter, it will be determined whether these findings are applicable to an actual CT case.

4.3.5. Variation of PODFS Compression Rate

The PODFS method has a compression capability, achieved by using only the most energetic modes and Fourier Coefficient (FC), resulting in a two-level compression of the data. In this section, both the number of POD modes and the number of FC are varied to determine the compression rate and its effect on the results of the truncated channel simulation. In two series of simulations, either the number of POD modes or the number of FC are changed while keeping the other parameter constant. Table 4.5 presents the PODFS parameters, their corresponding compression ratios, and the temperature deltas to the reference simulation for each PODFS simulation. In the first simulation series, the number of POD modes is

Table 4.5.: ΔT_t truncated domain under variation of the turbulence model

	$N_{POD}(E_\lambda)$	$N_{FC}(E_b)$	$\mathrm{CR}^{\star}_{rel}$	$\mathrm{CR}^{\star}_{abs}$	$\Delta T_t{}^{\dagger}\mathrm{CL}^{\star\star}$	$\Delta T_t{}^{\dagger}\mathrm{CW}^{\S}$
PODFS_{ref}	1050 (99.5%)	18845 (99.5%)	-	2.3	-	-
POD_99.5%	1050 (99.5%)	4153 (90%)	-	7.2	-	-
POD_98%	601 (98%)	4153 (90%)	1.21	8.8	0.02%	0.03%
POD_90%	161 (90%)	4153 (90%)	1.53	11.1	-0.08%	0.12%
POD_80%	37 (80%)	4153 (90%)	1.65	12	0.06%	0.34%
POD_70%	3 (70%)	4153 (90%)	1.69	12.2	2.27%	-0.45%
FC_99.5%	601 (98%)	18845 (99.5%)	-	2.4	-	-
FC_98%	601 (98%)	15505 (98%)	1.2	2.9	-0.002%	-0.0002%
FC_90%	601 (98%)	4153 (90%)	3.6	8.8	0.12%	0.006%
FC_70%	601 (98%)	874 (70%)	8.6	21	0.2%	0.023%

* compression ratio ** centerline § channel wall $^{\dagger}\,\Delta T_t = \frac{T_t - T_{t,PODFS,ref}}{T_{t,ref}} \cdot 100$

varied to resolve between 99.5% and 70% of the energy of the signal, while the number of FC is kept constant to resolve 90% of the amplitude of the time signal. In the second set of simulations, the number of FC is varied in the same range while keeping the number of POD modes constant at resolving 98% of the POD energy.

The absolute compression ratio is the size of the PODFS data on disk compared to the full set of snapshot data used in the strong recycling method. To break down the total

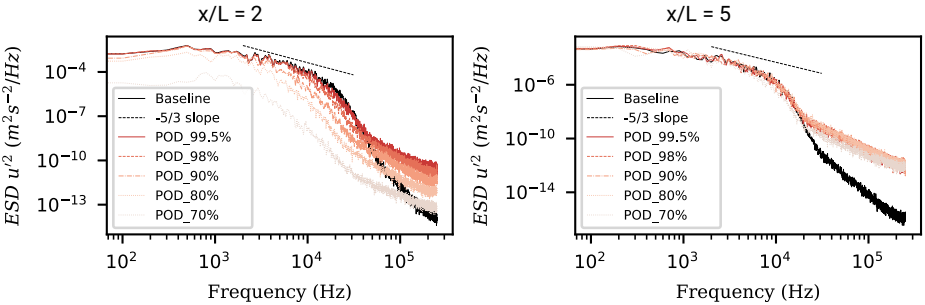

(c) ESD of two monitor points, one at the inlet/interface and one at the outlet of the channel

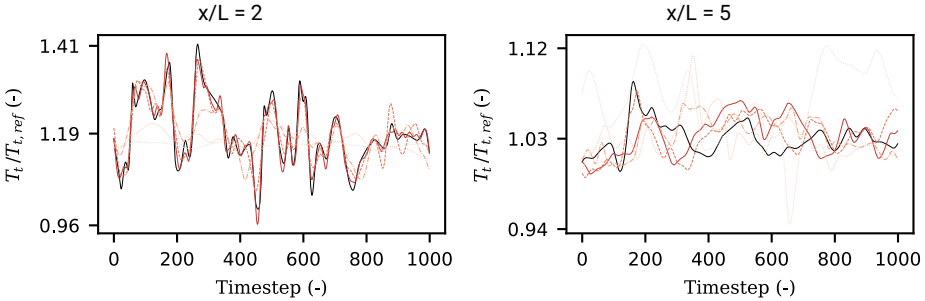

(f) Time trace of total temperature of two monitor points, one at the inlet/interface and one at the outlet of the channel

Figure 4.13.: Temporal and spectral signal of monitor points in channel for truncated simulations under variation of number of POD modes

compression ratio into the share of the POD modes and the FC, a relative compression ratio is calculated. The relative compression ratio for the variation of POD mode energy is determined by relating the required storage size on disc of the different simulations with reduced POD mode energy to the simulation with the highest mode energy (99.5%). The portion of the variation in FC energy is calculated similarly, but with reference to the 99.5% FC energy simulation.

Section 4.3.3 compares the baseline simulation with the PODFS reference simulation, demonstrating excellent agreement between the two. The PODFS boundary condition for that case utilized very high levels of mode energy and FC energy (both 99.5%). The first row in Table 4.5 presents the PODFS parameters of the reference case, with $N_{POD} = 1050$

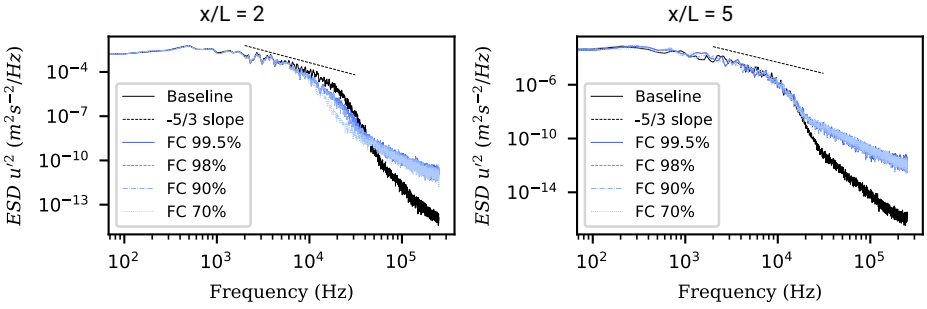

(c) ESD of two monitor points, one at the inlet/interface and one at the outlet of the channel

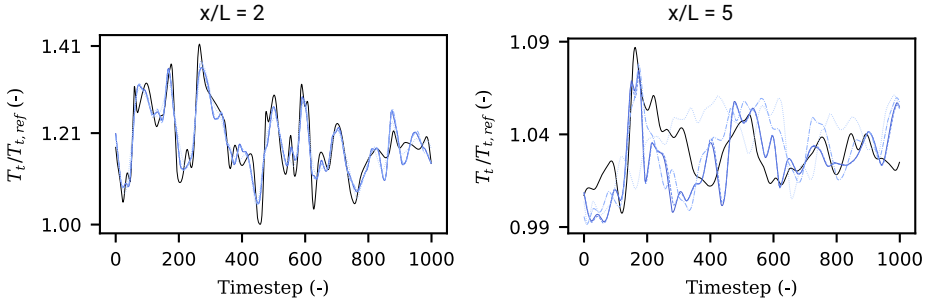

(f) Time trace of total temperature of two monitor points, one at the inlet/interface and one at the outlet of the channel

Figure 4.14.: Temporal and spectral signal of monitor points in channel for truncated simulations under variation of number of Fourier coefficients

replicating 99.5% of the total energy of the data. For the same energy percentage in the Fourier series, $N_{FC} = 18845$ is required.

By resolving 99.5% of both, the POD mode energy and the Fourier series amplitude, the data size can be reduced by a factor of 2.3. This is because the first 1050 of 20000 modes contain most of the relevant information. In the Fourier series, a much higher number of coefficients is necessary to reach the same target. This uneven distribution is the reason why the further reduction in FC shows a much higher potential in increasing the compression ratio than the reduction in POD modes. The relative compression ratio is greater for the variation of the number of FC, indicating this relationship. When considering the percentage changes in temperature in Table 4.5, as well as the centerline and lateral temperature distributions,

and the temperature development at the walls in Fig. A.5 and Fig. A.8, it is evident that the variation of POD modes has a greater potential to affect the flow than the variation of FC. The plots of the temperature distribution in the channel under variation of POD modes can be found in Appendix A.

A good compromise between accuracy and data compression is achieved by combining the resolution of 98% of the POD mode energy and 90% of the Fourier amplitude. In this setting, a compression ratio of 8.8 can be achieved. The ESD and time trace of the monitor point in the inlet plane in Fig. 4.13 and Fig. 4.14 show good agreement with the baseline case for 98% POD mode energy and 90% FC energy. The decrease in POD modes is significantly reducing the TKE of the inlet BC across all frequency ranges. However, the reduction of FC does not have a fundamental effect on the ESD (refer to Fig. 4.14).

The investigations in the channel test case reveal the following key takeaways:

- resolving at least the largest turbulent structures of the flow behind the turbulence generator is crucial for predicting adequate turbulent thermal mixing. The URANS simulation is already capable of doing so, and switching to scale-resolving turbulence models only slightly increases the mixing.
- The simulation of the truncated domain using the PODFS boundary condition demonstrates an excellent match with the baseline case simulation, providing proof of the capability of the PODFS BC to accurately replicate the turbulent conditions at the interface between two components.
- The accuracy of the PODFS boundary condition is more sensitive to the number of used POD modes than to a reduction in FC.
- An adequate set of PODFS parameters can resolve 98% of mode energy and 90% of FC energy. This allows for a compression factor of 8.8 without losing relevant information.

4.4. Validation of PODFS on the Large Scale Turbine Rig

Section 3.3.1 demonstrated the capability of the solver ANSYS® CFX® and the scale-resolving turbulence model SBES to accurately predict the flow in the combustor simulator and the first NGV of the LSTR. This section demonstrates the capabilities of PODFS in prescribing unsteady inlet BC within a turbine case by using the LSTR geometry. The PODFS method is used to create the reduced order model of the interface data by extracting transient snapshot data from the CT interface plane ③ (Fig. 3.2) from the integrated combustor-turbine simulation. A total number of 20,000 timesteps are used. The resulting PODFS statistics are listed in Table 4.6. A compression ratio of 29 can be achieved by using 98%

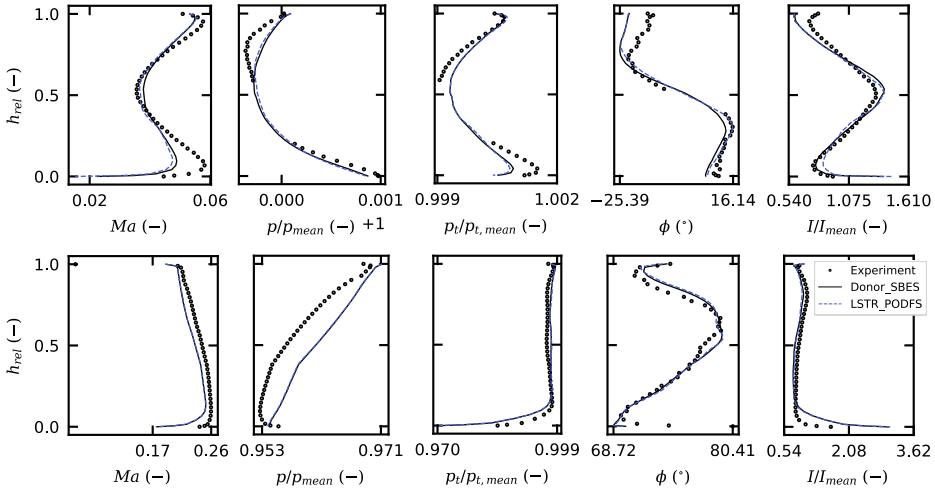

Figure 4.15.: Comparison of circumferential averages of integrated and NGV-only Simulation. Upper row: ME01 (NGV Inlet), lower row: ME02 (NGV Outlet)

of the POD mode energy and 90% of the FC energy. In the turbine-only simulation, the computational domain is reduced to the NGV. The inlet of the simulation is located at the interface plane between combustor simulator and NGV. Here the PODFS data is prescribed as unsteady inlet BC. The other BC and numerical settings are set as presented in Fig. 3.2.

Table 4.6.: PODFS statistics

$N_{POD}(E_\lambda)$	$N_{FC}(E_b)$	CR*
380 (98%)	6862 (90%)	29

* compression ratio

Fig. 4.15 shows the results at two evaluation planes: one in front of the NGV (ME01) and one behind the NGV (ME02). In addition to the experimental data, this presentation includes the results of the scale resolving SBES simulation of the integrated combustor-NGV domain and the NGV-only simulation, denoted with *LSTR_PODFS*. Section 3.3.1 discusses the differences between the integrated simulation and the measurement results. This section will focus on the differences between the two simulations. In ME01, both simulations exhibit

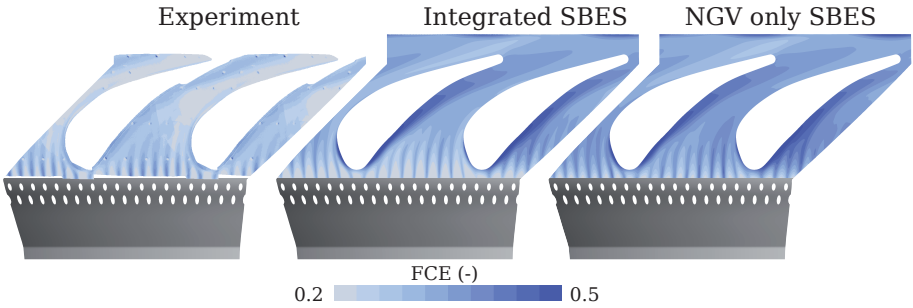

Figure 4.16.: Comparison of Film Cooling Effectiveness (FCE) on inner platform between integrated and NGV only Simulation

similar radial distributions of the different flow variables. Despite some minor deviations, the PODFS BC are able to create the same inlet conditions as in the integrated simulation when considering the time mean. A comparison of the turbulent fluctuations between the integrated and NGV-only simulations reveals a lower turbulence level in the NGV-only simulation. The absolute turbulence intensity in the NGV-only simulation is 3% lower than in the integrated simulation. The decrease in turbulence level can be attributed to the snapshot data being interpolated on a coarser mesh during the PODFS process (step 2 in Data reader, Fig. 4.1). Although the turbulence level at the inlet of the NGV-only simulation is slightly lower, the circumferential averages in ME02 (behind the NGV) show almost identical radial distributions in both simulations. The turbulence level at the inlet determines the mixing of the film cooling with the mean flow. In the NGV-only simulation it is slightly lower compared to the integrated simulation. This difference is illustrated in Fig. 4.16 by small variations in FCE. The cooling films are slightly more noticeable in the NGV-only simulation than in the integrated simulation. These differences are small compared to those observed to the RANS simulation and can be reduced by increasing the resolution of the PODFS data. It is recommended that the resolution of the PODFS data be the same as the grid of the original data points to avoid any loss of information. In the case of LSTR, this was not feasible due to the fine resolution of the interface and the resulting memory limitations when performing the PODFS. In the channel test case in Section 4.3 and the subsequent CT case (see Chapter 5), the resolution of the PODFS data is identical to that of the original data, and the interpolation does not result in any loss of information.

5. Results and Discussion - Impact of Unsteady Inlet Boundary Conditions

This chapter presents the results of simulations of an engine representative CT case. It analyzes the impact of unsteady inlet boundary conditions on the aerothermal behavior of the HPT. The first section of the chapter presents the exit plane data of the precursor combustor LES, which is used in the PODFS method to create the unsteady inlet BC for the turbine simulations. The following section on the HPT simulation results is divided into three parts. The initial section of the chapter examines the impact of mesh resolution and turbulence modeling on the results of the SRS. Subsequently, the impact of unsteady inlet boundary conditions on the vane aerodynamics is analyzed, followed by a thermal analysis.

5.1. Engine Representative Combustor-Turbine Case

The present section showcases the use of the PODFS method on a combustor-turbine case. The simulation setup features a state-of-the-art RQL combustor and the corresponding first NGV of a modern two-shaft engine of medium thrust class under take-off conditions. The industrial partner Rolls-Royce Deutschland Ltd & Co KG conducted the LES of the combustor and kindly provided the snapshot data from the CT interface. Details on the combustor simulation are given in Section 5.1.1 and the presentation and analysis of the interface data is given in Section 5.1.2. The snapshot data is used in the PODFS method to generate unsteady inlet boundary conditions for subsequent turbine simulations. Fig. 5.1 shows the schematic combustor domain and the location of the data extraction plane on the left and the corresponding turbine domain on the right. The NGV is not included in the domain of the combustor simulation. The turbine domain for the simulations in this work is reduced to the first NGV. A detailed description of the numerical setup of the NGV simulations follows in Section 5.2.1.

5.1.1. Combustor Simulation

The general purpose combustion CFD code *PRECISE-UNS* was used to perform the LES of the combustor. The pressure-based solver is capable of processing unstructured meshes and

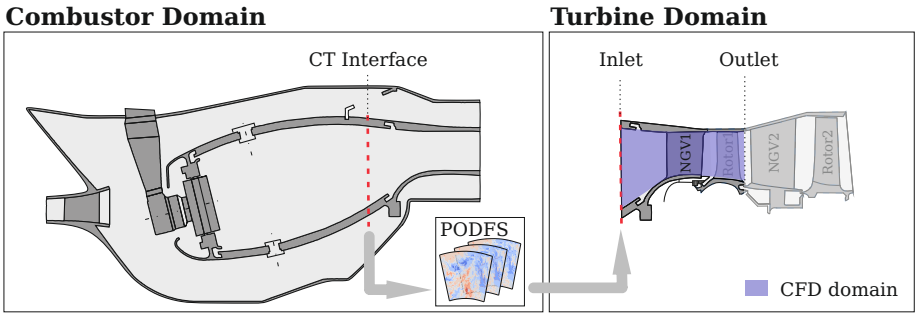

Figure 5.1.: Schematic representation of the combustor (left) and the HPT (right) of engine representative hardware with snapshot extraction plane in combustor simulation and PODFS pipeline for the application of unsteady inlet BC in transient HPT simulations

applying either RANS or LES turbulence modelling approaches. Combustion chemistry is modelled using a Flamlet Generated Manifold (FGM) model, and combustion-turbulence interaction is modelled using Propability Density Function (PDF). NO_X and soot models are employed to calculate combustion emissions. A Lagrangian approach is used to simulate fuel spray and droplet dynamics. The solver has been validated on various academic and industrial test cases and is the standard tool for combustion simulation and combustor development at Rolls-Royce. Additional information about the solver and a detailed presentation of the validation case can be found in the work by Anand et al. [3].

After attaining a settled state in the combustor LES, snapshots of the flow field at the interface plane were exported. A total of 10,000 snapshots were collected over a simulation time of 0.1 seconds, which contain the spatial distribution and temporal evolution of the fields for temperature, pressure, and velocity.

5.1.2. Combustor Outlet Data / Turbine Inlet Conditions

In order to characterize the inlet BC fields for the subsequent turbine simulation the temporal arithmetic average of these fields is plotted in the top row of Fig. 5.2. The consequence of the strong crossflow from the dilution ports and the residual combustor swirl is the formation of an alternating pattern of high and low values within the field of total pressure. This imprint of the dilution port flows is also evident in the distributions of the flow angles. The positive values of pitch angle α at the hub indicate a radial outwards flow, while the negative values at the shroud indicate a radial inwards-oriented component. The ports are arranged in an alternating pattern inside and outside, resulting in a wavy pattern of positive and

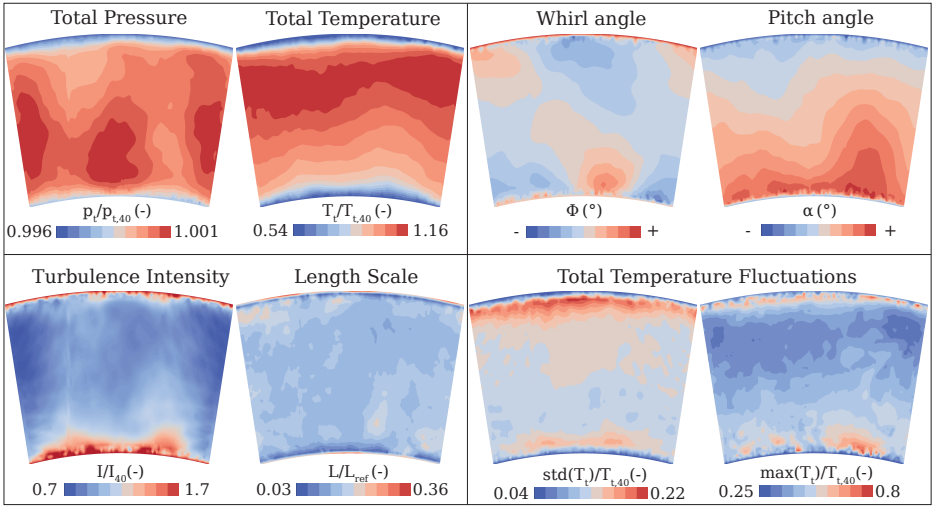

Figure 5.2.: Top row: Time mean of flow field data at CT interface. p_t, T_t and I are normalized with the mean values at the plane 40. Velocity vector is represented by pitch (radial) and whirl (circumferential) angel. Bottom row: Turbulent statistics represented by the turbulence intensity (Eq. (3.13)) and turbulent length scale. Temperature fluctuations are represented by the standard deviation and the maximal fluctuation values

negative radial flow angles α. The positive and negative radial velocity components induce the formation of circumferential velocity components, which can be observed through the formation of a pattern of positive and negative circumferential angles ϕ. The temperature field is defined by a band of elevated temperatures situated in the central region of the traverse, exhibiting a slight displacement towards the outer anulus. This phenomenon can be attributed to the positioning of the primary combustion zone in the center of the flame tube. In the secondary combustion zone, the dilution air exerts a squeezing effect on the hot gases, directing them towards the centre. At the endwalls, the cooling of the combustor liner results in a reduction in temperature.

The turbulence intensity I and turbulent length scale $\mathcal{L}$ distributions are shown in the bottom left of Fig. 5.2. The local turbulence intensity is distributed with the highest values near the walls. This is attributed to the low velocity magnitude in the boundary layer, which results in a small denominator in Eq. (3.13). The average of the turbulence intensity lies between 25% and 35%, which falls within the range of other reported values (refer to Section 2.1.3). The calculation of TKE and turbulence intensity from snapshot data is a relatively straightforward process, which can be achieved by deriving the Reynolds

stresses from the velocity fluctuations. However, determining turbulent length scales is significantly more challenging. The in-plane length scale can be calculated by integrating the two point correlation of the velocity fluctuations using Eq. (3.15). However, integrating to infinity presents practical challenges, so a threshold value of $1/e$ (Tropea et al. [186]) is used instead. The length scale is determined by the distance at which the normalized two-point correlation reaches the value of $1/e$.

$$R_{ii}(\mathbf{x}, \mathcal{L}, t) = \frac{1}{e} \tag{5.1}$$

As the data is presented on a 2D plane, it is not possible to calculate the length scale in the direction perpendicular to the plane using the method mentioned above. However, since the temporal evolution of the flow in the plane is resolved, the Taylor hypothesis of *frozen turbulence* (Pope [134]) can be used to calculate a length scale perpendicular to the plane. The velocity fluctuations at any point in time are correlated with the velocity fluctuation in all other timesteps by using the auto-covariance.

$$R_{ii}(\mathbf{x}, \tau) = \frac{\overline{u_i'(\mathbf{x}, t) u_i'(\mathbf{x}, t+\tau)}}{\overline{u_i'(\mathbf{x}, t) u_i'(\mathbf{x}, t)}}, \tag{5.2}$$

The turbulent time scale $\mathcal{T}$ can be calculated at every point of the interface plane by using the same threshold as before.

$$R_{ii}(\mathbf{x}, \mathcal{T}) = \frac{1}{e} \tag{5.3}$$

According to the Taylor hypothesis, turbulent structures remain constant over time and flow with the average velocity $\overline{u}$ at each respective point. This means that the plane-normal length scale can be calculated using

$$\mathcal{L}(\mathbf{x}) = \mathcal{T}(\mathbf{x}) \overline{u}(\mathbf{x}). \tag{5.4}$$

The calculation of in-plane length scales results in six length scale values, one for each velocity component in both coordinates of the plane. Additional three length scale values are obtained from the normal to plane calculation of all three velocity components. These nine values are then averaged to obtain a single value, which is plotted in Fig. 5.2 normalized with the chord length of the NGV as reference length. The velocity fluctuations near the walls tend towards zero, and the two-point correlations exhibit very high length scales in these regions, which are not physically valid. The length scale at the interface between combustor and turbine is on average 15% of the NGV chord length.

The turbulence intensity and turbulent length scale provide information about the magnitude and size of velocity fluctuations. However, temperature fluctuations are equally important for the turbine. In Fig. 5.2, the distribution of standard deviation and maximal fluctuating amplitude indicate the level of temperature fluctuations. Both values are normalized with

the mean temperature in plane 40 and exhibit the highest values in bands close to the inner and outer endwalls. In this area, the cooling flow of the combustor tiles interacts with the hot flow from the primary combustion zone, resulting in high temperature fluctuations. The standard deviation is approximately 22% of the mean temperature, and peak fluctuations reach 80%. Section 5.3 of this work demonstrates the significance of incorporating velocity and temperature fluctuations in the inlet boundary conditions of the HPT simulation in order to investigate the aerothermal behavior of the HPT.

The reduced order model of the snapshot data is created using the PODFS method. Table 5.1 lists the PODFS statistics. A compression ratio of 9 can be achieved by considering 98% of the POD mode energy and 90% of the Fourier amplitude.

Table 5.1.: Engine representative HPT: PODFS statistics

$N_{POD}(E_\lambda)$	$N_{FC}(E_b)$	CR*
709 (98%)	3952 (90%)	9

* compression ratio

5.1.3. Challenges to High Pressure Turbine Simulations

One of the main challenges in scale-resolving simulations is turbulent scale separation. Turbulent length scales range from the size of relevant geometric features of the flow, denoted as $\mathcal{L}_0$, down to the smallest eddies at the end of the turbulent spectrum η (known as Kolmogorov scales). In the case of flow in a combustion chamber, $\mathcal{L}_0$ is typically on the order of magnitude of the swirling structures and mixing ports (Cha et al. [33]). The ratio of the largest to the smallest scales depends on the Reynolds number of the flow and is particularly high for flows in turbomachinery (Eq. (3.12) Pope [134]).

The Reynolds number of the given NGV case, calculated using the cord-length of the vanes and the velocity at the exit of the domain, is $2.8x10^6$. There are multiple orders of magnitude separating the largest and smallest scales, making it necessary to have a fine mesh resolution in order to spatially resolve the relevant scales of the smaller eddies. The length scales of turbulent eddies correspond directly with the time scales of the turbulent motion. Significant length-scale separation results in a corresponding separation of the most significant and minor time scales in the flow. The time step width of the simulation must be small enough to resolve small eddies temporarily and meet the required CFL criteria for the used time-stepping scheme. However, the total simulation time must allow for enough time to average the large time scales. This leads to the requirement of a very fine temporal

resolution and long simulation times. Besides the need for excellent mesh resolution, this is why scale-resolving simulations require significantly more computational resources than RANS simulations.

The time step size of the NGV simulation is determined by the highly accelerated flow in the back part of the NGV passage, resulting in high flow velocities and small time scales. The time step size required can be determined by using the CFL stability condition, which is based on the local velocity and grid width, and should be close to one for implicit time-stepping schemes in LES (Menter [116]). The total simulation time required is determined by low frequency temporal events. When simulating multiple turbine stages, the simulation setup includes stationary vane rows and rotating blade rows. In this case, the total simulation time is determined by the blade passing frequency, as multiple rotor-stator passes are simulated to reach a converged solution. This study focuses on the first NGV row of the high-pressure turbine, with no investigation into rotor-stator interaction. The total simulation time is dictated by the low-frequency fluctuations in the inlet boundary conditions.

The operating point of the turbine is significantly influenced by the inlet pressure and temperature. Low-frequency drifts in the mean inlet temperature and pressure cause changes in the operating point and delay the convergence of the solution. To obtain a stable converged solution, the simulation must run for a sufficient amount of time. Fig. 5.3a displays the spectral density of the mean temperature in the interface plane, which shows motions in the mean field down to 10 Hz. The simulation of the turbine faces significant challenges due to the low frequency motion in the mean inlet boundary conditions. This is apparent when examining the cumulative average of the total temperature on the interface plane which is displayed in Fig. 5.3b. The cumulative average of the total temperature is plotted for the data collected at a monitor point located in the center of the combustor exit plane (solid line) and for area mean of the entire exit plane (dashed line). The plotted values are the percentage difference of the cumulative average from the final average across all snapshots. The blue lines represent the original data. In the initial timesteps, the monitor point shows a difference of over 8% from the final average, while the mean value shows a difference of around 3%. Both values slowly decrease as more timesteps are accumulated in the average, but remain relatively high for half of the entire simulation period. To ensure good convergence of the turbine simulation statistics, the simulation time should be selected in such a way that the time average of the variables on the inlet boundary condition remains as constant as possible. However, since the time step of the turbine simulation is significantly smaller than that of the inlet boundary condition, achieving a steady state time mean would require the simulation to run for an extended period, which would exceed the available computational resources.

To eliminate low frequency drifts in the mean inlet field, a high pass filter with a cutoff frequency of 200 Hz is applied to the snapshot data. The resulting dataset is then cumulatively averaged and added to Fig. 5.3b. The monitor point is represented by a solid

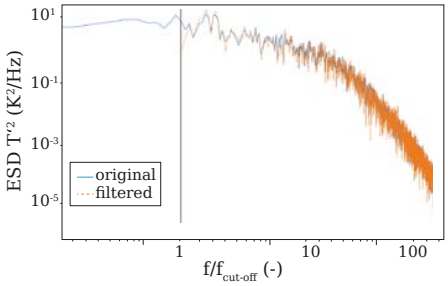

(a) Energy Spectral Density of mean total temperature in CT plane; original and filtered, cut-off frequency 200Hz

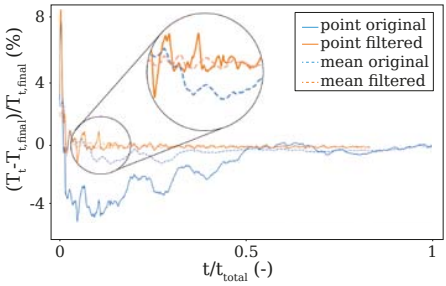

(b) Cumulative average of total temperature, original and filtered compared for one point and the average over the total interface plane

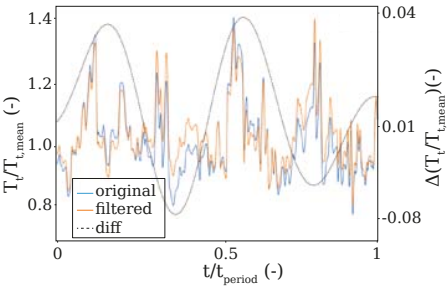

(c) Time trace of total temperature in one point; original, filtered and difference original-filtered

Figure 5.3.: Analysis of temporal evolution of temperature on interface plane. Demonstration of the effect of the filter on the temperature field

orange line, while the mean value is represented by a dashed orange line. The filter ensures that any deviations in the average are smaller and decay much faster than in the original data. To demonstrate the impact of filtering on flow fields, the time histories of the original and filtered total temperature data, both related to the mean, are plotted in Fig. 5.3c for a small sample of time steps. The course of the high-frequency fluctuations is identical for both the original and filtered data. The only difference between the two curves are the low-frequency structures, which are removed from the original data. The discrepancy between the original and filtered data is illustrated with the black dashed line. The impact of the filtering can also be observed by comparing the power spectral density of the original

and filtered signals in Fig. 5.3a. The spectra of the original and filtered data follow a similar pattern in the higher frequency range. The cutoff frequency of 200 Hz is indicated by the black line. The filtering of the data does not alter the time-averaged distribution of the flow fields. However, the filtering process is affecting the fluctuations of the flow quantities, which in turn affects the turbulence intensity. The application of a 200 Hz high-pass filter resulted in a 4% reduction in turbulence intensity within the turbine inlet traverse.

5.2. High Pressure Turbine Vane Simulations

This section presents the results of the HPT vane simulation, which were obtained using different types of inlet boundary conditions and turbulence modelling approaches. A detailed comparison of the simulation results reveals the impact of unsteady inlet boundary conditions on the aerothermal behavior of the NGV. A portion of the results has already been published in Gründler et al. [61].

5.2.1. Numerical Setup and Simulation Overview

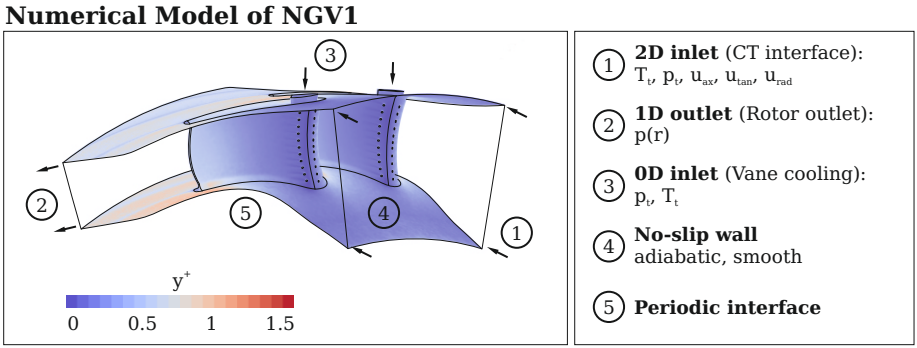

Figure 5.4.: Numerical domain and boundary setup of engine representative HPT simulation. Distribution of y^+ on NGV surface

The computational domain and the numerical setup of the first NGV of the engine representative HPT is shown in Fig. 5.4. The numerical model comprises two nozzle guide vanes of the first stage of the HPT. To reduce the complexity of the simulation, the level of geometry detail is reduced. Endwalls and airfoils are modelled along with two rows of film cooling

holes per vane. The pressure and suction side cooling rows are located near the leading edge of each vane and are fed by separate plenums. Endwall cooling such as RIDN and RODN is neglected, as are purge flows behind the NGV. The inlet of the domain is located at the CT interface. The outlet of the domain is extended to the location of the rotor outlet, but the rotor blades are not included. The inlet conditions are determined by total pressure p_t, total temperature T_t and the velocity directions in cylindrical coordinates: u_{ax}, u_{tan} and u_{rad}. While the time average is used for steady BC, the PODFS representation of the transient field data (Section 5.1.2) is used as unsteady BC. For the steady-state case, the 2D turbulence intensity and length scale distributions computed from the snapshot data are used at the inlet to initialize the RANS turbulence model equations. As outlet BC, a radial profile of static pressure is used, which also regulates the mass flow through the NGV passage by adjusting the total-to-static pressure drop from inlet to outlet of the domain. The total pressure at the inlets of the plenums controls the film cooling mass flow. The vane-to-burner ratio in a periodic sector is two, and a pair of NGVs is included in the model with periodic boundary conditions at the sector borders. All metal surfaces are modelled as no-slip and adiabatic walls. The ANSYS® CFX®solver, outlined in Section 3.3.1, is employed for problem simulation.

Subsequent sections present and compare results from various simulations, to highlight the effect of combustor unsteadiness on the first NGV. Table 5.2 presents an overview of the conducted simulations, categorising them as either steady-state or unsteady time-accurate. The inlet boundary conditions are similarly grouped. The two types of turbulence treatment are either RANS/URANS or SRS, where the SST turbulence model is used for RANS/URANS simulations. For SRS simulations, the two models compared are SBES and SAS. In a preliminary study, the effect of mesh resolution on the forecasts made by SRS is examined using four different meshes (Section 5.2.3). To explore the thermal effects such as film cooling and HTC (Section 5.3.5 and Section 5.3.6), further simulations were carried out without activating any cooling features or with setting a fixed isothermal wall temperature. Finally, the core hours used for each simulation are listed in Table 5.2. In total, fourteen SRS simulations and ten RANS/URANS simulations were conducted, utilizing over 1.5 million Central Processing Unit (CPU) hours.

5.2.2. Convergence of Simulation Statistics

All transient simulations are averaged for a satisfactory duration to achieve convergence of the time average. The RMS magnitude of relevant flow variables is monitored at various points distributed across the entire fluid domain. In addition to the monitor point locations, Fig. 5.5 displays the convergence envelope of the cumulative RMS for each monitor point and for relevant flow variables. The graphs in Fig. 5.5 feature upper and lower thresholds, set at $\pm 5\%$, to the final value. These lines are standardized throughout all graphs presented.

Table 5.2.: Simulation types and settings of the simulations of the engine representative NGV test case

	type	turbulence		BC	cooling	mesh	core h
coarse SBES	u*	SRS	SBES	u*	on	coarse	30000
BSL SBES	u*	SRS	SBES	u*	on	BSL	68000
medium SBES	u*	SRS	SBES	u*	on	medium	120000
fine SBES	u*	SRS	SBES	u*	on	fine	250000
coarse SAS	u*	SRS	SAS	u*	on	coarse	30000
BSL SAS	u*	SRS	SAS	u*	on	BSL	68000
medium SAS	u*	SRS	SAS	u*	on	medium	120000
fine SAS	u*	SRS	SAS	u*	on	fine	250000
RANS	s†	RANS	SST	s†	on	coarse	96
RANS	s†	RANS	SST	s†	on	medium	288
URANS uns BC	u*	RANS	SST	u*	on	coarse	28800
URANS uns BC	u*	RANS	SST	u*	on	medium	120000
SRS steady BC	u*	SRS	SBES	s†	on	medium	24000
SRS uns BC	u*	SRS	SBES	u*	on	medium	120000
no cool RANS	s†	RANS	SST	s†	off	coarse	80
no cool URANS	u*	RANS	SST	u*	off	coarse	24000
no cool SRS steady BC	u*	SRS	SBES	s†	off	medium	20000
no cool SRS uns BC	u*	SRS	SBES	u*	off	medium	105000
RANS $T_{t,cool} - 5K$	s†	RANS	SST	s†	on	coarse	96
RANS $T_{t,40} + 5K$	s†	RANS	SST	s†	on	coarse	96
URANS $T_{t,cool} - 5K$	u*	RANS	SST	u*	on	coarse	28800
URANS $T_{t,40} + 5K$	u*	RANS	SST	u*	on	coarse	28800
SRS $T_{t,cool} - 5K$	u*	SRS	SBES	u*	on	medium	120000
SRS $T_{t,40} + 5K$	u*	SRS	SBES	u*	on	medium	120000

* unsteady † steady

The RMS values of the three velocity components are presented in a single graph, indicating values that fall within the $\pm 5\%$ range during the averaging period. A similar convergence pattern is noted for the temperature and pressure levels. Furthermore, the convergence behavior of all six components of the RST is displayed. As higher order moments, the convergence of Reynolds stresses is slower compared to their average counterparts. This trend is displayed in Fig. 5.5. The RMS values solely attain the $\pm 5\%$ threshold within the averaging time.

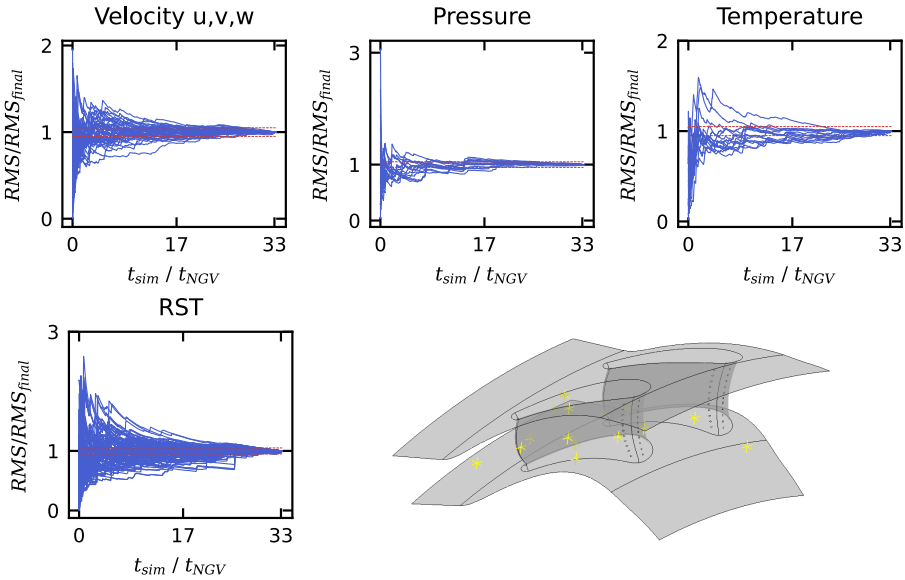

Figure 5.5.: Convergence of averages in SRS: Cumulative RMS for each monitor point for pressure p, temperature T, velocity components u, v, w and RST components, normalized by the respective final value as a function of the number of NGV flow-through time t_{sim}/t_{NGV}. The red dashed lines indicate upper and lower thresholds, set at $\pm 5\%$ to the final value. Lower right: position of monitor points in the NGV domain

5.2.3. Influence of Mesh Resolution and Scale-Resolving Turbulence model

In RANS simulations, a mesh-independent solution can be found. This implies that the further refinement of the mesh does not alter the solution. In "LES-like" SRS, however, this is not necessarily the case. A spatial filter is implicitly implemented by the mesh, which means that the resolution of the grid determines the ratio between resolved and modelled turbulence. Refining the mesh will result in resolving smaller eddies, which may change the solution. However, beyond a certain resolution, further refinement only results in negligible changes to the relevant flow characteristics. For hybrid LES/RANS models such as the SBES model, a RANS turbulence model is used to solve a portion of the flow. In this work, a traditional mesh study aimed at determining the offset to the grid-independent solution is not employed in the context of the SRS. Nevertheless, the subsequent section will showcase simulation results utilizing four distinct meshes to ascertain the effect of mesh resolution on important flow characteristics in the turbine NGV. Table 5.3 lists the settings and statistics

of the used meshes. Starting from a Baseline (BSL) mesh, one coarser mesh and two finer meshes are used.

Table 5.3.: Mesh quality parameters, mesh and numerical settings for simulations of the NGV test case

	coarse	BSL	medium	fine
Cells (Mio.)	13	23	53	112
Min. cell angle (°)	2.18	2.52	3.62	1.81
Avg. cell angle (°)	56.94	58.27	57.61	57.89
Max. EVR*	42.44	102.6	62.84	106.57
Avg. EVR*	1.87	2.66	1.63	1.56
Max. EAR†	16072	17250	17760	20372
Avg. EAR†	3.44	2.52	2.11	1.96
Max. y^+	1.37	1.39	1.42	1.49
Avg. y^+	0.47	0.46	0.46	0.44
$\Delta^{\star\star}$	1 mm	0.5 mm	0.3 mm	0.2 mm
Δt	2.5×10^{-6}s	1.25×10^{-6}s	7.5×10^{-7}s	5×10^{-7}s

* Element volume ratio † Element aspect ratio ** Grid spacing

The meshes required for the hybrid LES/RANS simulations must be suitable for the hybrid nature of the simulation. The model predominantly functions in LES mode for most of the domain. A high mesh resolution is essential for resolving as much of the turbulent spectrum as possible. In the used meshes the grid spacing ranges from 1 mm in the coarse mesh down to 0.2 mm in the fine mesh. Additionally, a low Element Volume Ratio (EVR) is necessary for operating in the LES mode to ensure a similar filter size in all areas. However, in areas proximate to the walls where the model operates in RANS mode, these conditions are not mandatory. Instead, achieving a fine resolution in wall normal direction is essential to accurately capture the boundary layer. For RANS meshes, it is customary to use highly stretched prism-layers. The mesh statistics outlined in Table 5.3 reflect the hybrid nature of the used meshes. Notably, the maximum values for EVR and Element Aspect Ratio (EAR) are high. However, it should be noted that these values are only present in the boundary layer regions and fall within the acceptable limits for RANS models. The time step width Δt on the different meshes is set to have a similar CFL number in all simulations. A different number of time steps are simulated to keep the total simulation time equal in all the simulations to ensure a fair comparison of the results. The non-dimensional distance of the initial cell to the walls y^+ is maintained at values below five in all meshes, facilitating

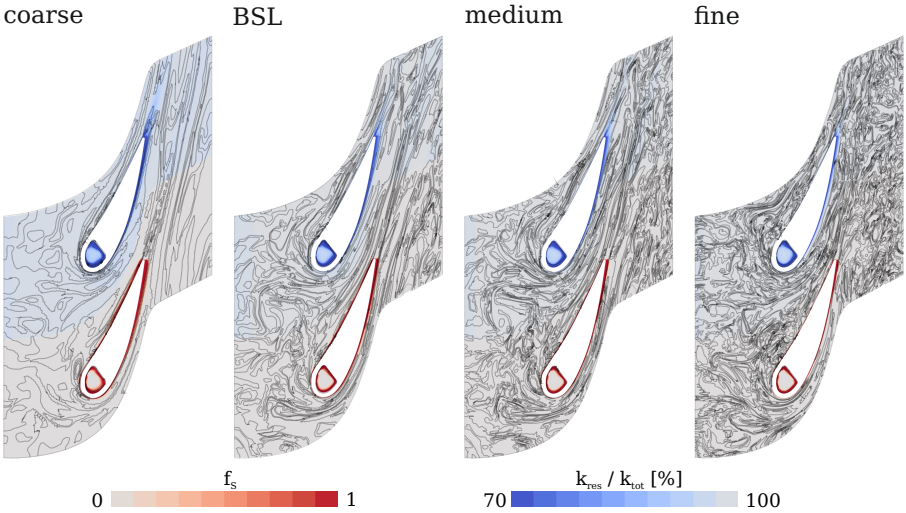

Figure 5.6.: Influence of mesh resolution on SRS results. Plane at 50% span height. Upper half: ratio of resolved TKE k_{res} and total TKE k_{tot}. Lower half: operation mode of SBES turbulence model by means of shielding function f_S. Visualisation of vortex structures with black contour lines ($\lambda_2 = 0$)

the utilization of the RANS model in low-Reynolds mode. Accordingly, the equations are solved down to the walls without employing wall functions.

Refining mesh resolution alters the amount of resolved TKE in the simulation, as demonstrated in Fig. 5.6 by the fraction of resolved TKE. The resolved TKE constitutes over 80% of the total TKE on the midspan plane in all four meshes in the regions, where the model functions in LES mode. These areas have a shielding function value of zero. Only near the walls, the model operates in RANS mode ($f_S = 1$). Here, the resolved TKE is considerably low. By comparing the resolved TKE in the LES part of the domain for all four meshes, an increase in percentage with mesh size refinement can bee observed. The RANS portion around the vanes is becoming thinner, and the wake behind the NGVs exhibits amplified levels of resolved TKE. The contour lines of λ_2 additionally demonstrate how mesh resolution impacts the resolved turbulent structures. The simulation resolves smaller vortex structures when a finer mesh is implemented. This observation is substantiated when average curves are taken into account.

In Fig. 5.7, the normalized resolved TKE is displayed as the mass flow average from the inlet

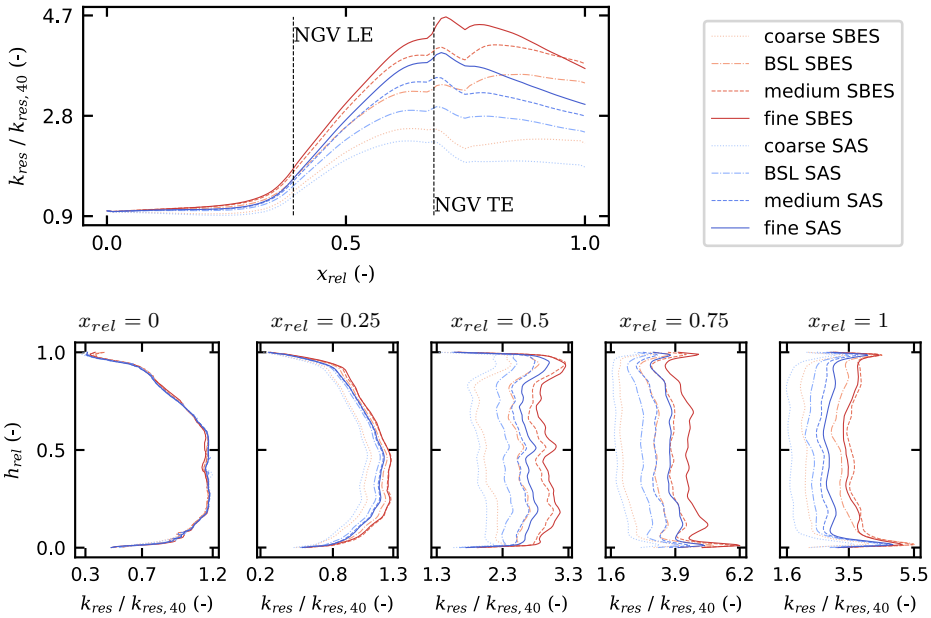

Figure 5.7.: Resolved TKE under variation of mesh resolution and turbulence model. Mass-flow average on surfaces of constant streamwise coordinate as a function of the relative streamwise coordinate (upper left). Circumferential average at different relative streamwise locations x_{rel} (lower row)

to the outlet of the NGV domain at the top and as circumferential averaged radial profiles at different streamwise locations at the bottom. Both turbulence models SBES and SAS and four meshes are taken into account. The same PODFS data set is consistently employed as the inlet boundary conditions throughout all simulations. Nonetheless, the inlet boundary mesh varies along with the rest of the mesh, resulting in a change in resolved turbulence on the inlet surface. This leads to minor variations in turbulence levels at the inlet among different meshes, and the data is normalized by referring to the mean value at the inlet location.

As outlined in Section 3.2, the lower range of the turbulent spectrum involves the transfer of mean flow kinetic energy into TKE, a phenomenon known as turbulent production. Shear processes brought on by velocity field gradients are responsible for turbulent production. On the other end of the spectrum, the smallest turbulent motion dissipates into heat. The NGV flow features both, turbulent production and dissipation. The proportion of both influences

whether the TKE rises or falls. The flow in the NGV simulation, with unsteady inlet BC, starts with a certain baseline of TKE that arises from the upstream located combustor. Traversing the NGV Domain, the only way to increase TKE is through turbulent production mechanisms. Between the inlet and the leading edge of the vanes, the flow undergoes moderate acceleration, while the velocity gradients in the boundary layer profiles at hub and shroud contribute modestly to the production of TKE. Furthermore, gradients in the inlet flow field also contribute to turbulent production. As a result, a minor rise in TKE is discernible from the inlet to the LE of the vanes. As the flow approaches the near field of the vanes, directly ahead of the leading edge, it experiences significant deceleration followed by rapid acceleration along the vanes surfaces. The presence of the vane boundary layers further adds to the turbulent production, resulting in a strong rise in the level of TKE. At the trailing edge of the vanes, the acceleration ceases and the absence of boundary layer effects of the flow around the airfoils further decreases turbulent production. The TKE levels out and in some cases even decreases as it approaches the outlet of the domain. The radial plots in Fig. 5.7 indicate that the highest values of TKE can be found in the area behind the vanes ($x_{rel} = 0.75$ and $x_{rel} = 1$), particularly in areas close to the hub and shroud endwall. The interaction of the endwall boundary layers with the passage vortex is responsible for the high production of turbulent kinetic energy in this region.

The resolved TKE varies with different mesh resolutions when moving downstream through the passage. The finer the mesh, the more turbulent structures are resolved, resulting in higher TKE values. When comparing the SAS and SBES turbulence models, it is apparent that the SBES model resolves a greater amount of TKE than the SAS model. This is despite the fact that both models are applied on identical meshes. When considering the modelled TKE, it is found to be slightly higher in the SAS than in the SBES. However, it does not compensate for the differences in resolved TKE. The SBES exhibits higher levels of total TKE. This phenomena was already discussed in Section 4.3.2.

The previous section has demonstrated that the mesh resolution and choice of turbulence model impact the resolved turbulence in simulations. Nevertheless, the precise impact of this on the aerothermal characteristics of the vanes remains unclear. Therefore, the ensuing part examines the effect of mesh resolution and turbulence model on the performance parameters of the NGV.

In Fig. 5.8d, the vane loading is plotted for all four meshes and the two turbulence models at various span heights. The aerodynamic load of a turbine vane can be expressed using the isentropic Mach number Ma_{is} distribution along the pressure and suction sides of the profiles. The calculation of Mach number requires the application of the isentropic relation between the total to static pressure ratio. In Eq. (5.5), the heat capacity ratio of the fluid is denoted by γ, while p represents the static pressure on the surface of the profiles, and p_t

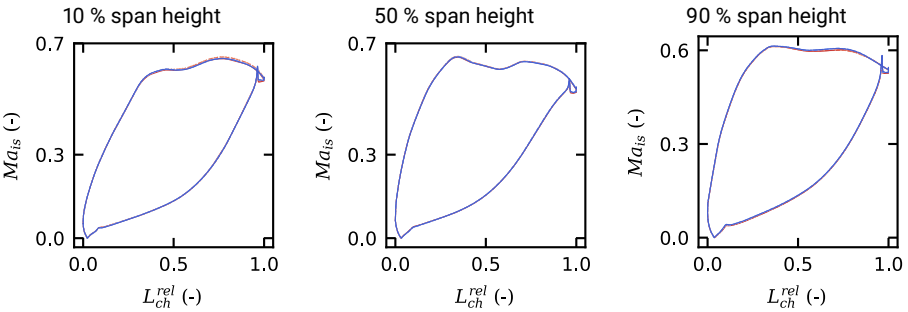

(d) Isentropic Mach number Ma_{is} (Eq. (5.5)) distribution as a function of relative chord length L_{ch}^{rel}

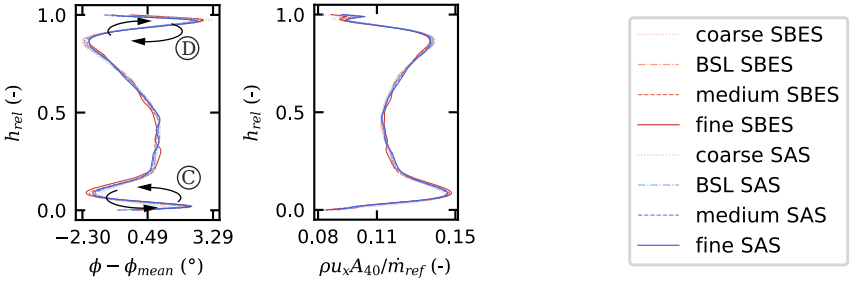

(e) Whirl angle **(f)** Mass flux

Figure 5.8.: Aerodynamic parameters under variation of mesh resolution and turbulence model

represents the total pressure at the airfoil stagnation point.

$$Ma_{is}^2 := \frac{2}{\gamma - 1}\left(\frac{p_t}{p}\right)^{\frac{\gamma-1}{\gamma}} - 1 \tag{5.5}$$

The Mach number distribution at 50% span height is nearly identical in all simulations, whilst slightly larger differences can be seen at the other two span heights 10% and 90%. The most noticeable differences are observed in the aft part of the vanes suction side. Here, secondary flows affect the flow conditions around the profiles. In this area, the mesh resolution and the choice of turbulence model has the greatest impact. While there are minor differences between simulations, the affect of mesh resolution and turbulence model can be considered insignificant with regard to vane loading.

The creation of high circumferential velocity (whirl) is one of the primary objective of

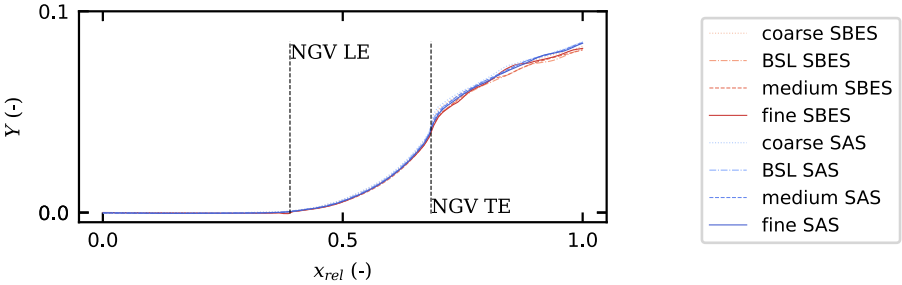

Figure 5.9.: Total pressure loss coefficient under variation of mesh resolution and turbulence model: mass-flow average on surfaces of constant streamwise coordinate as a function of the relative streamwise coordinate

the turbine vanes. Therefore, the impact of mesh resolution and turbulence model on the turning of the vanes is presented in Fig. 5.8e. The deviation of the circumferential flow angle ϕ behind the NGV ($x_{rel} = 0.75$), measured against the mean value, is plotted as a circumferential average over the relative span height h_{rel}. Small discrepancies are discernible between the SBES and SAS turbulence model in the lower third of the channel height. The radial mass distribution behind the NGV is of similar importance to the inflow of the rotor as the turning of the NGV itself. To illustrate the impact of mesh resolution and turbulence model on the mass distribution behind the NGV, Fig. 5.8f shows the radial distribution of the mass flux ρu_x normalized with the specific mass flow at the inlet of the NGV $\dot{m}_{ref}/A_{40}$. Hereby $\dot{m}_{ref}$ is the exit mass flow of the combustor simulation. It also shows only small sensitivity against the variation of mesh resolution and turbulence modelling. Both the circumferential flow angle and mass distribution exhibit the imprint of secondary flows. Within the inner and outer 20% of the channel height, local minima and maxima in flow angles are visible. This change in flow angle is caused by the strong rotation of the passage vortex (Ⓒ and Ⓓ in Fig. 5.17) present in this area. The vortices create a flow component that counteracts the turning of the vanes, which leads to minima in the distribution of ϕ. In this areas, the reduced circumferential velocity component leads to an increase in axial mass transport. This explains the peaks in the mass distribution plot in Fig. 5.8f.

The effect of varying mesh resolution and turbulence model on predicting losses in the NGV passage is demonstrated in Fig. 5.9. The mass flow averaged total pressure loss coefficient Y (Eq. (2.7)) is charted as a function of the relative streamwise position for each of the four meshes and two turbulence models. A more detailed examination of the vane losses will follow in Section 5.3.2. At this stage only the effect of mesh resolution and turbulence model on the total losses will be reviewed.

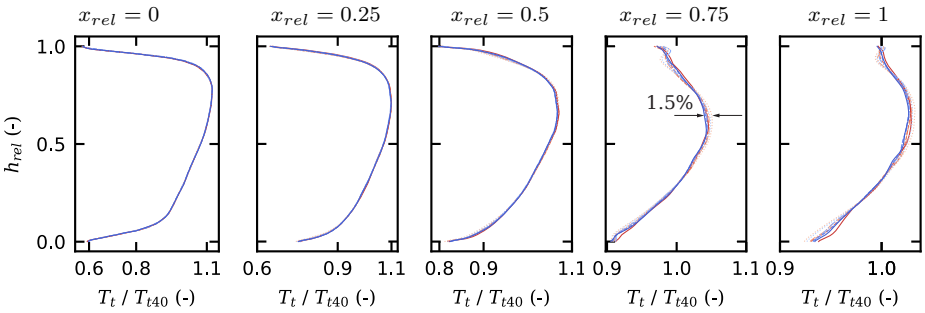

Figure 5.10.: Radial temperature distribution under variation of mesh resolution and turbulence model at multiple relative streamwise locations

From the inlet to the LE of the vane, the pressure loss and the differences between the simulations is negligible. The flow around the vanes and at the endwalls creates a boundary layer that causes shear processes. These processes are amplified by the strong acceleration of the flow, resulting in losses that increase the pressure loss coefficient from the LE to the Trailing Edge (TE). Throughout the passage, the pressure loss coefficient increases in all simulations. Minor differences exist between the various simulations in this flow portion. Loss generation continues downstream of the vanes, but at a lower rate due to the mixing processes of vane wakes and the passage flow. This flow region exhibits noteworthy contrasts between the different simulations, with the mesh resolution having a greater impact here than in other areas of the domain. Towards the outlet of the domain the simulations using the SAS turbulence model show slightly higher pressure losses than the SBES simulations. At the outlet of the domain, the total pressure loss variation is 0.4% due to variations in mesh resolution and turbulence model. Section 5.3.4 demonstrates that the losses in the NGV are primarily driven by the boundary layer. The SBES and SAS models operate in RANS mode near the wall, and since all meshes are sufficiently fine in the wall-normal direction, refining the LES part of the mesh does not significantly alter the loss development in the vane passage.

It can be summarized that the variation of mesh resolution does not significantly affect the aerodynamics and losses in the NGV passage. Additionally, the choice of SAS or SBES as a turbulence model does not have a noticeable effect on both.

Following the assessment of how mesh resolution and the choice of scale-resolving turbulence model affects the aerodynamics of the vane, the following section demonstrates the impact of both on the thermal conditions in the NGV simulation. Doing so, Fig. 5.10 illustrates the progression of radial temperature profiles across the domain. The total temperature

T_t is normalized to the mean inlet total temperature T_{t40} and plotted as a function of the relative span height h_{rel}. Five distinct positions along the stream direction are identified for comparative values. The temperature distribution is comparable across all four meshes and the two turbulence models at $x_{rel} = 0$ (inlet) and $x_{rel} = 0.25$ (just in front of the leading edge of the NGV). Distinctions between the used meshes emerge when going further downstream. At point $x_{rel} = 0.5$, situated halfway along the profiles of the NGV, refining the mesh results in a pattern of increased temperatures near the hub and shroud endwalls and slightly reduced values in the centre. This tendency persists on moving towards the trailing edge and the section behind the vanes ($x_{rel} = 0.75$ and $x_{rel} = 1$), where the distinctions between the four meshes and the two turbulence models are more evident. As the mesh resolution becomes finer, the temperature in the outer regions of the flow path rises while the temperature in the centre decreases. The increase in turbulent thermal mixing is responsible for this effect when refining the mesh to resolve a higher level of turbulence. The radial total temperature distribution behind the NGV ($x_{rel} = 0.75$) varies by a maximum of 1.5% of T_{t40} when changing the mesh resolution and the turbulence model.

Furthermore the wall temperature is analysed separately on the pressure and suction sides of each vane by evaluating the area average adiabatic total wall temperature on ten equally spaced patches over the span height of the vane. The results of SBES and SAS are presented here, varying the mesh resolution. The location and arrangement of the averaging patches is shown in Fig. 5.11 alongside with the normalized temperature distribution of the vanes as a function of the relative span height. This is shown individually for vane 1 and vane 2, and for the pressure and suction sides, respectively. The footprint of the inlet temperature profile is reflected on the vane surfaces. Similarly to the inlet profile, the maximum temperature on the surfaces of the vanes lies at midspan while temperatures decrease towards the outer and inner endwalls. It is noteworthy that on the pressure side of vane 2, the elevated temperature area is shifted towards the outer endwall. This can be attributed to the slightly twisted combustor outlet temperature profile. A similar trend on all four sides cannot be identified. However, redistribution of temperature between suction side and pressure side and between the central part and the outer regions of the passage is visible when refining the mesh. The maximum variation that can result from choosing a specific mesh resolution and turbulence model is 2% of the turbine inlet temperature T_{t40}.

In conclusion, it can be stated that aerodynamic parameters like the Mach number distribution and the turning of the vanes are barely sensitive to a variation in grid resolution. When varying the mesh resolution, more evident deviations in temperature distributions can be observed. This needs to be considered when analysing the thermal behavior of the the turbine components. The SBES turbulence model resolves slightly higher TKE than the SAS model. This has no effect on the aerodynamics but needs to be considered, when analysing thermal effects. In general, the SBES model is superior to the SAS model as it

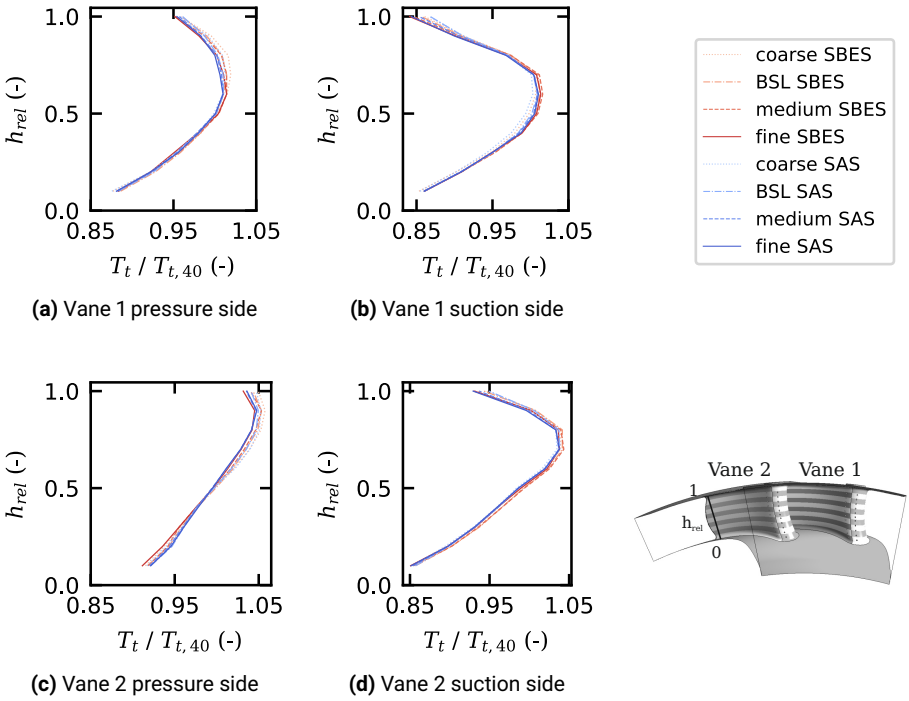

(a) Vane 1 pressure side

(b) Vane 1 suction side

(c) Vane 2 pressure side

(d) Vane 2 suction side

Figure 5.11.: Total temperature (normalized with T_{t40}) distribution on vane 1 and vane 2, pressure and suction side under variation of mesh resolution and turbulence model. Area average on ten equally spaced patches

resolves more TKE for a similar computational effort and should be used if available.

5.3. The Effect of Unsteady Inlet Boundary Conditions on High Pressure Turbine simulations

Four simulation types with different kinds of inlet boundary conditions and turbulence models are assessed to examine the impact of fully unsteady inlet boundary conditions on the aero-thermal predictions of high-pressure turbine simulations. The first simulation type is the state-of-the-art steady-state RANS simulation, employing the time-averaged outlet fields of the combustor LES as inlet boundary conditions (*"RANS steady BC"*). The

second simulation type adopts the same steady-state inlet boundary condition but uses a transient scheme and a scale-resolving turbulence model. This simulation is titled *"SRS steady BC"*. The third simulation type can be considered an intermediate step towards a fully resolved simulation. It is a URANS simulation that uses unsteady PODFS boundary conditions (*"URANS unsteady BC"*). In the fourth simulation type, again the unsteady boundary condition by means of PODFS is utilized. This simulation uses a scale-resolving turbulence model and transient scheme and is referred to as *"SRS unsteady BC"*. The impact of scale-resolving turbulence modelling and boundary conditions type can be studied separately by comparing these four simulation methods. It is noted that in the subsequent diagrams, the variability of the results of the SRS with unsteady BC against variation of mesh resolution and choice of turbulence model is represented by grey bands. Results from simulations performed on both coarse and medium meshes are additionally presented to demonstrate the effect of mesh resolution on RANS and URANS simulations.

5.3.1. Turbulent Kinetic Energy

The evolution of the total TKE through the NGV passage is plotted for the four simulations in Fig. 5.12a. Similar to Fig. 5.7, the total TKE k_{tot} is averaged on slices of constant streamwise location. The total TKE k_{tot} is the sum of the resolved TKE and the subgrid scale TKE for the SRS and the modeled TKE for the RANS simulation. The TKE at the inlet is similar for all three simulations. In downstream direction, the SRS and URANS simulation with unsteady inlet boundary conditions shows the highest increase of k_{tot} when entering the vane passage. Considering the URANS simulation, it is evident that it "resolves" the largest scales of turbulent motion originating from the combustor when using the medium mesh. On the coarse mesh, the total turbulent kinetic energy is lower, but still sufficient to come close to the SRS results on the coarsest mesh. This is noteworthy because URANS, by definition, cannot resolve the decay of turbulence. However, the unsteady nature of the simulation allows for the resolution of the large motion structures, which are the most significant contributors to the total turbulent kinetic energy. In the RANS simulation the increase in TKE is less pronounced. This means that the RANS model underpredicts the turbulent production in the passage of the vane compared to the simulations with unsteady bounday conditions. The SRS with steady inlet boundary conditions is initialized with the same TKE at the inlet as the RANS simulation. However, due to its "LES character" in most part of the flow, it cannot maintain the TKE in form of the RANS values and it drops significantly after the first few cells. It recovers some of the TKE later in the passage and especially in the wake region, but completely under predicts k_{tot}. This effect is also reflected in Fig. 5.12b by means of the total TKE on the 50% span plane. Both URANS and SRS simulations with unsteady boundary conditions exhibit similar contours of TKE, with an increase throughout the second half of the passage. In contrast, the simulations with

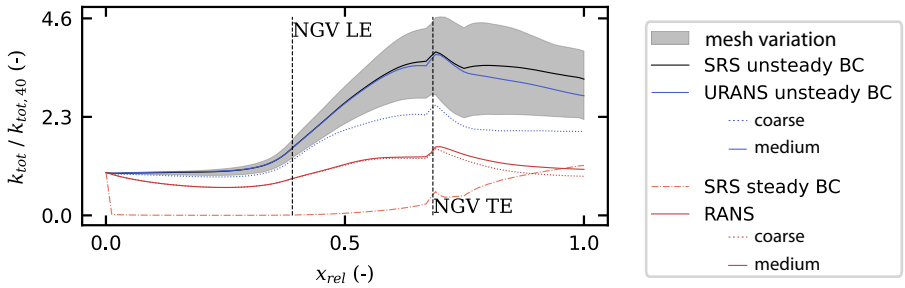

(a) Total TKE: mass-flow average on surfaces of constant streamwise coordinate as a function of the relative streamwise coordinate.

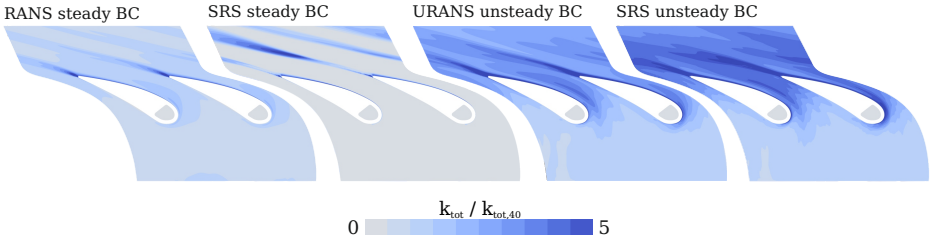

(b) TKE contours on 50% span height for simulations with different types of inlet boundary conditions. RANS with steady state inlet BC (left), SRS with steady state inlet BC (centre left), URANS with unsteady inlet BC (centre right) SRS with unsteady inlet BC (right)

Figure 5.12.: Total TKE k_{tot} referenced to the average value at NGV inlet $k_{tot,40}$

steady inlet boundary conditions only show a significant increase in TKE in the wake region of the vanes. In RANS simulations, the turbulent motion effect on the fluid is modelled by the turbulent viscosity. High turbulence levels increase the effective viscosity of the fluid. When resolving the turbulent fluctuations, there is no artificial increase in viscosity, and the turbulence effect is directly calculated by an exchange of momentum between the eddies and the mean flow. To highlight the impact of this on the aerodynamics of the vanes, losses, secondary flows and performance parameters of the NGV will be compared in the following sections.

5.3.2. Vane Losses

The dominant loss mechanisms in the vane passage are described in Section 2.2.3 and will be analysed for the different simulations. First the total loss will be analysed by means of the pressure loss coefficient. By comparing the development of the pressure loss coefficient Y through the NGV domain, the effect of the unsteady inlet boundary conditions on the loss development in the vane simulation is shown. The coefficient is defined by Eq. (2.7) and describes the total pressure loss due to entropy production. As described in section Section 2.2.3, multiple loss mechanisms contribute to the overall pressure loss. Fig. 5.13a shows the pressure loss coefficient plotted as the mass flow average on slices with constant streamwise position through the passage and Fig. 5.13e as radial plots of the circumferentially averaged values at different streamwise positions. Again, the curves for the RANS and URANS simulation and the two SRS with different inlet boundary conditions are compared. From the inlet to the leading edge of the vanes, the pressure loss is close to zero for all simulations. In this region of the passage flow, only endwall and freestream losses occur at a very low level due to the relatively low flow velocity and velocity gradients.

Loss generation begins in the passage around the vanes. The total loss in this part of the flow is contributed by the endwall and freestream losses, as well as the profile and secondary flow losses of the vanes. The flow channel contracts between the vanes, resulting in a strong acceleration of the flow. This causes the boundary layer to thicken at the endwalls and profiles, leading to an increase in friction losses. This is reflected in an increase in the pressure loss coefficient. For all four simulations, the pressure loss coefficient rises throughout the passage. The RANS and URANS simulation show slightly higher values than the SRS around the vanes. At the trailing edge of the vanes, the SRS steady BC case shows the lowest total pressure loss coefficient. From the radial distribution of Y in Fig. 5.13e it follows that the losses primarily arise from the boundary layers of the endwall and vanes. In the central part of the channel, between 10% and 90% span height the loss distribution is very homogenous in the RANS, URANS unsteady BC and SRS unsteady BC case. This indicates that the profile losses dominate and secondary flows play a minor role in the overall loss development. This is especially the case for the relative streamwise location of $x_{rel} = 0.75$ which is located directly behind the trailing edge of the vanes. Here, the effects of the film cooling, which can be seen with steady inlet BC in the front part of the vane by means of an oscillating radial distribution of the SRS, have little effect any more as the cooling films are mixed out with the main flow. The impact of film cooling on loss development is clearly evident in the simulation results when using steady inlet boundary conditions. Section 5.3.5 will demonstrate that the absence of freestream turbulence in this simulation enables the formation of strong cooling vortices. At the domain outlet, the total pressure loss varies by 1.8% among the different simulations. The total pressure loss contours at the exit of the NGV exhibit similar distributions for RANS, URANS unsteady BC,

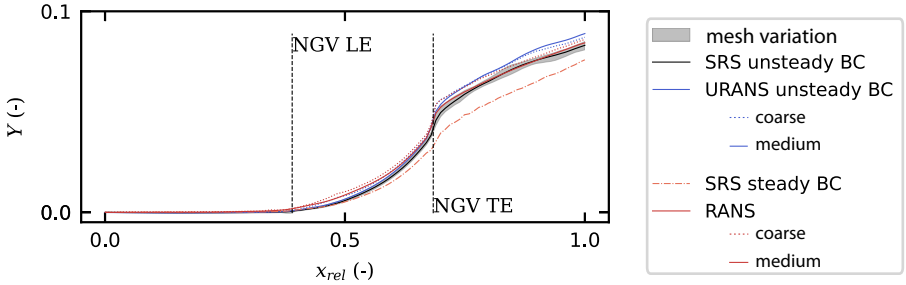

(a) mass-flow average on surfaces of constant streamwise coordinate as a function of the relative streamwise coordinate

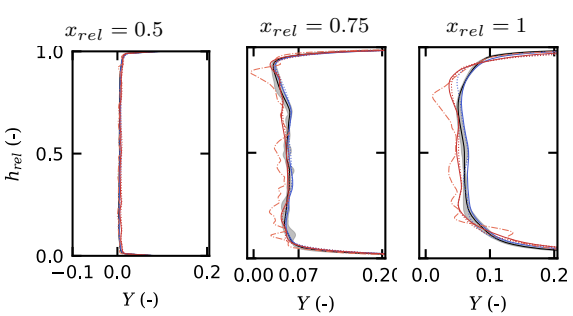

(e) Radial profiles at different streamwise locations

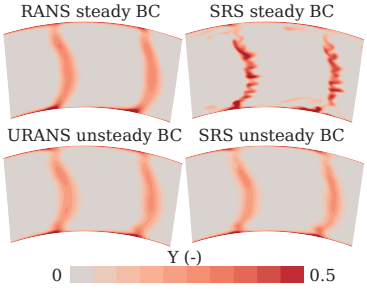

(f) Total pressure loss contour at NGV outlet ($x_{rel} = 1$)

Figure 5.13.: Total pressure loss coefficient under variation of inlet boundary condition

and SRS unsteady BC. The highest values are observed at the hub and shroud endwalls, as well as in the wake regions. In the SRS steady BC case, the pressure loss in the wakes displays higher local values, and the imprint of the film cooling vortices is still visible. This can be attributed to the absence of freestream turbulence.

To elaborate the differences in friction losses resulting from shear in the wall boundary layers of the vanes, Fig. 5.14 shows the boundary layer profiles at six positions on the surfaces of the vanes and in the wake of the profile. There are three locations on the pressure side of the vanes and three locations on the suction side, all at 50% span height. The locations are marked in the sketch in the centre of Fig. 5.14. The shape and thickness of the boundary layer determines the magnitude of the frictional losses. To determine the effect of combustor turbulence on the profile losses, the four simulations with different inlet BC are considered in the comparison of boundary layer profiles. In the top row of Fig. 5.14,

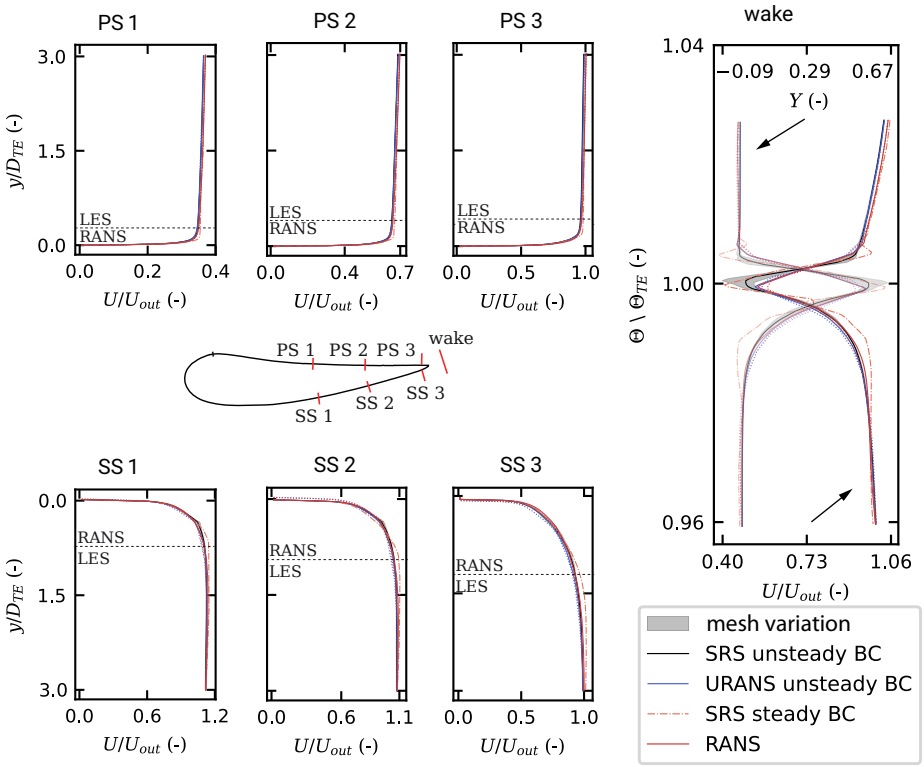

Figure 5.14.: Boundary layer profile at different locations on vane pressure and suction side for different inlet boundary conditions

the boundary layer profiles on the pressure side of the vanes are shown and in the bottom row the profiles on the suction side. The boundary layer profiles are visualized using the velocity magnitude U_{mag} normalized with the free stream velocity U_{out} over the relative wall distance y_{rel}, which is the wall distance y normalized with the diameter of the trailing edge D_{TE}. Furthermore, the demarcation line between the LES and the RANS mode in the SBES model is identified.

The boundary layer on the Pressure Side (PS) of the vanes is relatively thin, and there are only minor differences between the simulations. On the Suction Side (SS), the boundary layer is thicker due to the high acceleration leading to increased speeds. Apart from small

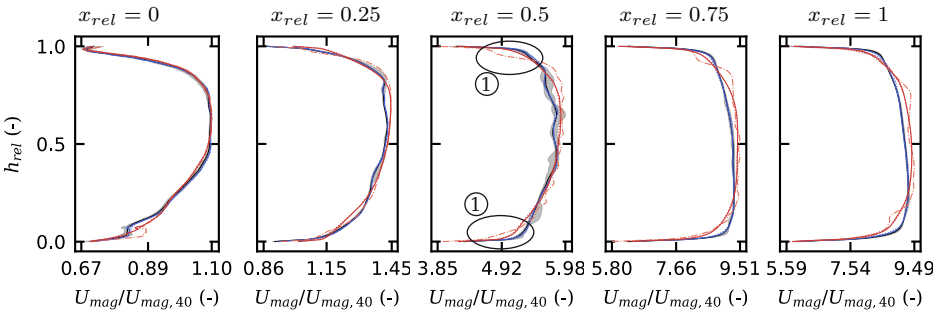

Figure 5.15.: Radial velocity distribution under variation of inlet boundary condition at multiple relative streamwise locations

differences between the SRS steady BC case and the other simulations, the boundary profile on the suction side is very similar for all four simulations. Therefore, the main differences in the development of losses in the passage between the vanes do not occur on the profiles. Upon examining the radial profiles of velocity presented in Fig. 5.15, it is evident that the variances can be attributed to the boundary layers of the hub and casing. At relative streamwise positions $x_{rel} = 0.5$, the SRS steady BC case lacks freestream turbulence and displays a less bulky velocity profile (① in Fig. 5.15) at the hub and shroud endwall, resulting in lower pressure loss compared to the other simulations.

Moving downstream of the trailing edge, the two boundary layer profiles converge in the wakes of the profile. This region of the flow is dominated by mixing processes between the wake flow and the main passage flow. These mixing processes are accompanied by losses that contribute to the total pressure loss. On the right hand side in Fig. 5.14 both, the velocity and total pressure loss coefficient is plotted over the stagger angle Θ normalized with the angle of the trailing edge Θ_{TE}. The wake of the vanes is dominated by a strong velocity deficit which corresponds to high velocity gradients and shear layers which produce losses. In Fig. 5.14 this is visible by a peak in total pressure loss coefficient. Upon comparing the wakes of all four simulations, noticeable differences are visible between the SRS steady BC case and the other simulations. This simulation exhibits a steeper velocity gradient on the suction side flank of the wake, which corresponds to less mixing of wake and passage flow. As a result, there is a smaller total pressure loss in this region, as can also be seen in Fig. 5.13a.

To elaborate on the differences in wake mixing, the streamwise vorticity (Eq. (5.7)) is plotted on a 50% span plane in Fig. 5.16. For the three unsteady cases the plot is split in half. The right side presents instantaneous vorticity contours at a single time step and the

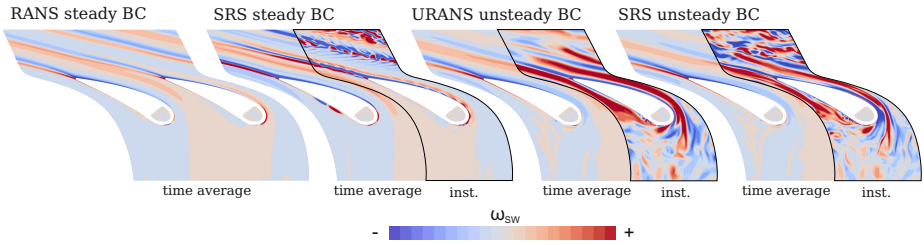

Figure 5.16.: Vorticity contours on 50% span height for simulations with different types of inlet boundary conditions. RANS with steady state inlet BC (left), SRS with steady state inlet BC (centre) and SRS with unsteady inlet BC (right)

left side presents the time average vorticity.

The velocity gradients in the boundary layers at the pressure and suction sides lead to high vorticity values. At the trailing edge, both boundary layers meet and form the wake. In the vorticity contours in Fig. 5.16, this becomes visible by two adjacent streaks of high positive and negative values. In the RANS simulation, the turbulence-induced viscosity dampens the wake shortly after the trailing edge. The turbulent viscosity in the SRS with steady boundary conditions is much smaller (see Fig. 5.12b), and the wake structures remain more substantial for a longer distance. In the wake region, the SRS operates in LES mode, and the turbulent mixing of the wake requires turbulent structures in the flow. Without imposing turbulent structures on the inlet, none in the downstream passage can interact with the wake flow. Instabilities at the edge of the wakes cause turbulent motion, which mixes out the wake further downstream. The missing turbulence in the passage is the reason for the lower turbulent mixing of the wake in the SRS steady BC case. The vorticity contour plot of the URANS simulation and SRS with unsteady boundary conditions shows turbulent structures right from the inlet of the computational domain. Both simulations with unsteady inlet boundary conditions show similar vorticity contours in the area from the inlet to the leading edge of the vanes. However, these vortical structures are sharper in the SRS than in the URANS, where the contours are more diffuse. When moving through the passage between the vanes, in the URANS simulation, the fine vortex structures are suppressed, whereas in the SRS they remain intact and even new and smaller eddies arise. The SRS model is the only one capable of partly resolving the energy cascade of eddy decay. In contrast, the URANS model is based on averaged conservation equations and is not designed to resolve turbulent fluctuations. However, the averaging process (ensemble average) allows for large unsteady motions and the largest turbulent structures from the inlet to be transported through the passage before they dissipate. The turbulent eddies in the SRS migrate through the passage, interact with the boundary layers and wakes of

the vanes, and increase the turbulent mixing compared to the simulation with steady inlet boundary conditions. The mixing losses in the wake region of the two simulations with unsteady inlet BC are in the same range as when using the steady state RANS approach (see Fig. 5.14).

5.3.3. Secondary Flows

From the descriptions above, it is evident that the losses in the vane passage are primarily driven by the boundary layer. However, the radial distribution of the vane turning in Fig. 5.8e indicates the influence of the passage vortex. Therefore, the secondary flows that occur in the different simulations will be analysed and compared in the following section. A commonly used method of describing the rotational motion of fluid vortex structures is the vorticity

$$\vec{\omega} := \nabla \times \mathbf{u}. \tag{5.6}$$

It is defined by the curl of the velocity vector **u**. To visualize the above mentioned secondary flow features, the streamwise vorticity

$$\omega_{sw} = \omega_i \frac{u_i}{u_{mag}} \tag{5.7}$$

is used. It describes the velocity perpendicular to the main flow direction (Shouting and Ting [165]). In Fig. 5.17 a visualisation of secondary flows is shown by means of streamwise vorticity ω_{sw} (Eq. (5.7)). In the top row, a downstream view of the NGV passage is shown using iso-surface contours of positive and negative ω_{sw}. The threshold is set to $\pm 10000\ s^{-1}$. In the centre row the same iso-surfaces are shown looking upstream into the vane passage. The bottom row displays a contour of ω_{sw} at the exit of the NGV domain. For the sake of clarity, only the RANS and SRS unsteady BC results are shown and compared. The figure of the secondary flow structures of the SRS steady BC and the URANS unsteady BC case can be found in Appendix B, Fig. B.1. Please note that time-averaged values are used for transient simulation results. Following secondary flow features can be identified:

- Horse-Shoe Vortex:
  Starting from the leading edge of the vanes, the horse-shoe vortex forms at the corners of the vanes and the endwalls. It consists of a pair of counter-rotating vortices: clockwise rotating Ⓐ (indicated with +) and anticlockwise rotating Ⓑ (indicated with -). The horse-shoe vortices are more strongly developed in the simulations with unsteady BC. Both, the SRS unsteady BC case and the URANS unsteady BC case show stronger vorticities than in the RANS and SRS steady BC cases. The development of the horse-shoe vortex is highly dependent on the incoming boundary layer at the endwall. Fig. 5.15 shows similar boundary layer profiles in front of the vanes

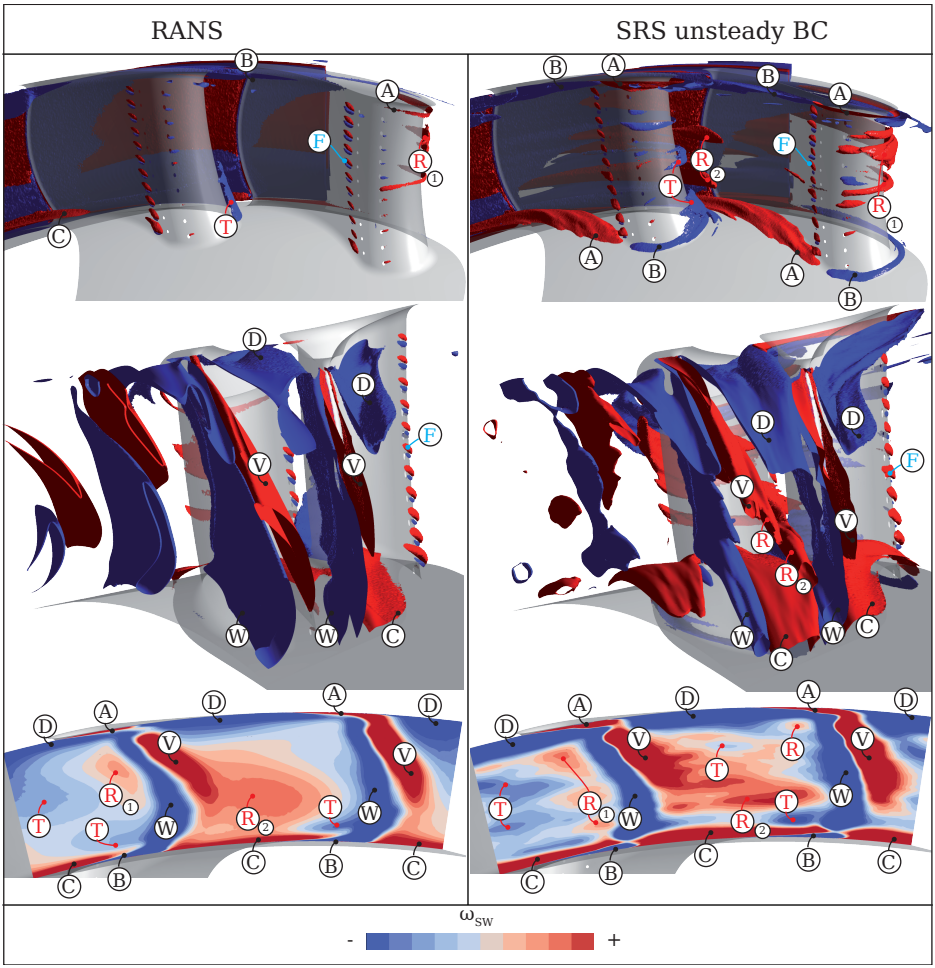

Figure 5.17.: Influence of inlet BC on secondary flow. RANS simulation with steady state inlet BC (left column). SRS with steady state inlet BC (centre column). SRS with unsteady inlet BC (right column)

($x_{rel} = 0.25$) when considering the time average. In transient simulations with unsteady inlet boundary conditions, turbulent fluctuations alter the boundary layer

over time, triggering the development of the horse-shoe vortex.

- Passage Vortex:
  The passage vortex arises from the streamline curvature in the passage and joins the pressure side leg of the horse-shoe vortex, which is transported towards the suction side of the neighboring vane by the pressure gradient in the passage. It is visible at the hub Ⓒ + and the shroud Ⓓ -, particularly towards the rear of the passage. This effect is again more pronounced in the simulations using unsteady BC than in the other two cases with steady BC.

- Trailing Shed Vortex:
  The circulation difference between the pressure and suction sides of the vanes generates a powerful vortex pair at the trailing edge. This vortex, also known as the trailing edge vortex, consists of a clockwise rotating leg towards the outer endwall Ⓥ+ and a counterclockwise rotating leg Ⓦ- that is more oriented towards the hub. The strength of the trailing shed vortices at the trailing edge is similar in all four simulations. However, they subside more quickly in the simulation with unsteady inlet boundary conditions and persist for a longer period in the two simulations that use steady-state inlet boundary conditions. This phenomenon is also demonstrated in Fig. 5.16 and can be explained by the increased mixing processes in the wake when resolving the combustor turbulence.

- Inlet related Vortices:
  In addition to the classical secondary flows mentioned above, there are additional vortex structures that can be identified. These are labelled in red with Ⓡ+ being clockwise rotating and Ⓣ- anticlockwise rotating. These vortices arise from inhomogeneities in the inlet traverse. When there are gradients in velocity and pressure at the leading edge of a vane, the flow rolls up and forms a pair of counter-rotating vortices. Similar to the horse-shoe vortex, one leg travels along the pressure side and the other leg travels along the suction side. The simulations show the presence of a strong vortex system along the suction side of vane one $Ⓡ_1$. Another source of inlet traverse related vortices is the flow of a total pressure deficit along a curved path, which occurs in the centre of the passage between both NGVs (refer to total pressure field in Fig. 5.2). This vortex is clearly visible at the exit of the domain between the trailing edge vortices of both vanes $Ⓡ_2$. The vortices related to the inlet are more pronounced in simulations that use unsteady inlet BC compared to those that use steady BC due to the unsteady triggering.

- Cooling Vortex:
  The escape of cooling air through a film cooling hole results in the formation of additional vortices Ⓕ±. The flow conditions within the cooling hole and the interaction of the cooling air with the boundary layer of the main flow lead to the development of a

pair of counter-rotating vortices, commonly referred to as ”kidney” vortices. These vortices are more prominent on the pressure side of the vanes and are strongest in the SRS steady BC case, due to the missing freestream turbulence and the less diffusive flow. The vortices in question play a pivotal role in the effectiveness of film cooling and the transfer of heat on the vane surface. (see Section 5.3.6)

From the examination of secondary flows in the NGV passage, it can be summarised that the simulation type and the method of prescribing inlet boundary conditions affect the characteristics of secondary flows. The use of unsteady inlet BC introduces unsteadiness to the flow, which triggers the development of stronger horse-shoe, passage, and inlet vortices than in simulations using steady BC. The trailing edge vortices exhibit contrasting behavior. They are more prominent in simulations that use steady BC than in those that use unsteady BC. In the SRS steady BC case, the absence of freestream turbulence and the resulting low diffusive flow lead to the development of cooling hole vortices that are exaggerated compared to the other simulations.In general, the steady RANS simulation and both simulations using unsteady inlet BC depict the same secondary flow characteristics with minor discrepancies in the strength of expression of the vortices.

5.3.4. Aerodynamic Performance

The primary aerodynamic parameters of turbine vanes are the vane loading (acceleration), vane turning and outlet mass distribution. Additionally the turbine capacity is a relevant system parameter for the integration of the HPT into the entire engine. In the following part, the effect of realistic inlet boundary condition on these aerodynamic parameters is examined. Fig. 5.18d illustrates the vane loading at 10%, 50%, and 90% span height utilising an isentropic Mach number (Eq. (5.5)). As previously shown, there is minimal variation in vane loading when the mesh resolution or turbulence model is altered. The same holds when examining the effect of inlet boundary conditions on vane loading. Switching the simulation type from steady RANS to unsteady SRS has no impact on the loading. Even using realistic turbulence conditions with unsteady boundary conditions has little effect. The vane loading curves exhibit only slight differences on the rear part of the suction side of the vanes. In this area the boundary layer profiles in Fig. 5.14 shows the highest deviations between the different simulations. Small disparities between the RANS and SRS results occur solely at the trailing edge at 10% span but the acceleration of the vanes is similar in all three simulations.

The NGV of a turbine is prescribing the inlet conditions for the following rotor blades. According to the *Euler turbine equation* (Eq. (2.3)), the amount of work extracted by the rotor depends, among other things, on the change in circumferential velocity and the mass flow. When evaluating this equation on infinitesimal sections of different blade heights,

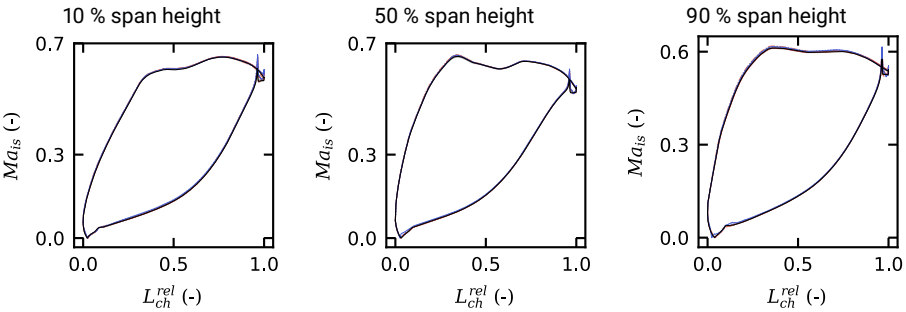

(d) Vane loading and turning: Isentropic Mach number Ma_{is} (Eq. (5.5)) distribution as a function of relative chord length L_{ch}^{rel}

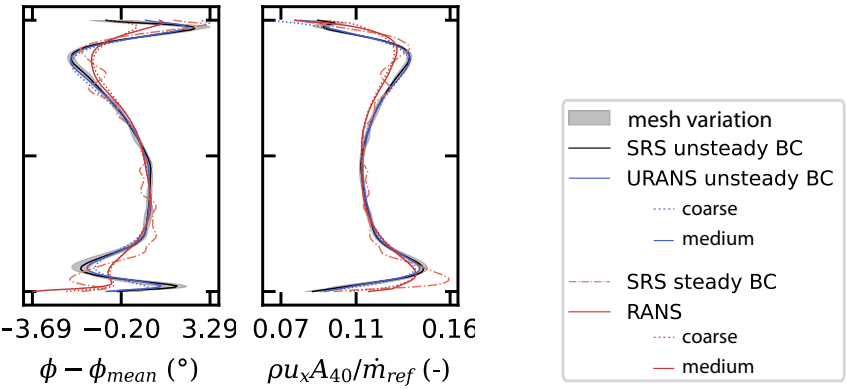

(e) Whirl angle: circumferential average at NGV outlet

(f) Mass flux: circumferential average at NGV outlet

Figure 5.18.: Aerodynamic parameters under variation of inlet boundary conditions

the power output of the rotor is directly affected by the radial distribution of the change in circumferential flow component ΔC_u and the outlet mass flow $\dot{m}$ of the NGV row. The NGV influences the change in circumferential flow component over the rotor by the outlet flow angle as it dictates the inflow angle to the rotor. In Fig. 5.18e the deflection to the mean value of the circumferential flow angle is plotted over the normalized span height. Two areas of reduced turning are visible at 15% and 85% relative span height. Moving closer to the endwalls, two peaks of increased turning are apparent. These changes of high and

low turning are more pronounced in the cases with unsteady BC, compared to the other two cases with steady inlet BC. The differences are due to the increased strength of the passage vortex in the URANS and SRS unsteady BC case, but are relatively small at $\pm 1°$. Nevertheless, this may affect the rotor flow at the hub and tip, and thus should be taken into account when evaluating the inflow conditions of the rotor. The change in secondary flows also alters the radial mass distribution. In the URANS and SRS unsteady BC case the mass is slightly shifted inwards in the regions of the passage vortex. The actual effects of these changes on the rotor need to be determined by simulations including the rotor flow.

The capacity of the turbine is a crucial design parameter and is defined by the reduced mass flow Eq. (2.9). It can be used to elaborate differences in mass throughput of the different simulations. Table 5.4 lists the capacity values for the different simulations and the percentage differences from the RANS simulation. The results in Table 5.4 indicate

Table 5.4.: Engine representative HPT: Turbine capacity

	Γ (-)	delta to RANS (%)
RANS steady BC	1.033	0.0
SRS steady BC	1.038	+0.5
URANS unsteady BC	1.031	-0.17
SRS unsteady BC	1.029	-0.4

that the turbine capacity increases by +0.5% when using SRS with steady BC compared to RANS simulation. However, the use of unsteady BC results in a slight decrease in capacity compared to the steady RANS simulation, with a maximum reduction of -0.4% observed in the SRS unsteady BC case compared to the RANS simulation. The decrease in capacity observed in simulations using unsteady BC can be attributed to the alteration in aerodynamic blockage within the passage. The simulations employing unsteady BC exhibit more pronounced secondary flow characteristics within the passage, which in turn reduce the throughput of the vane passage.

In conclusion, for LES-based scale-resolving turbine simulations to accurately predict turbulent mixing, it is necessary to have temporally resolved inlet boundary conditions. This was demonstrated by the SRS steady BC case, where no fluctuations were initialized at the inlet. The absence of freestream turbulence resulted in minimal turbulent diffusion in the NGV flow, leading to an overprediction of cooling hole vortices and profile wakes compared to the other simulations. When initializing turbulent fluctuations in the inlet boundary condition, they mix with the main passage flow and dampen the aforementioned flow features. In the RANS simulation, turbulent fluctuations are not resolved, but the additional turbulent viscosity leads to higher diffusion and a similar damping effect. It

is worth noting that the steady-state RANS simulation can predict the main aerodynamic features accurately. However, there are minor differences between the simulations. These differences are primarily due to the selection of inlet boundary conditions, which result in variations in vane turning and radial mass distribution. These variations are attributed to the differences in the predicted strength of the secondary flows, which are influenced by unsteady triggering when using unsteady inlet BC. The use of unsteady inlet boundary conditions leads to a more pronounced development of the horseshoe and passage vortex, which redistributes mass in the lower and upper 20% of the passage height. When considering aerodynamic parameters such as vane loading, losses, and flow angles, RANS simulations with time-averaged inlet boundary conditions accurately predict these parameters. Small changes in the results can be observed when using unsteady inlet boundary conditions. These changes are already apparent when using URANS simulations in combination with unsteady inlet boundary conditions, even on a coarser mesh. The additional effort of running scale-resolving simulations on very fine meshes may not be justified for aerodynamic investigations. It is yet to be evaluated how this changes when including the rotor and additional stages to the simulation.

5.3.5. Temperature Distribution and Thermal Mixing

The description of combustor turbulence as inlet BC, combined with the use of scale-resolving turbulence modelling, is anticipated to significantly impact the forecast of thermal performance of turbine simulations (Cubeda et al. [38], Duchaine et al. [46], Tomasello et al. [181]). As stated in Section 4.3, common steady state RANS simulations are incapable of predicting turbulent thermal diffusion in immensely turbulent situations. In a cooled CT setup, this leads to insufficient mixing between the cool air from the cooling features and the hot main flow. The thermal mixing in the flow through the NGV of a HPT is crucial as it determines the thermal load of the turbine materials. Two key aspects can be identified: firstly, the mixing of temperature non-uniformities originating from the combustion chamber. When simulating the turbine, the temperature profile is prescribed as the inlet boundary condition. As it is convected through the NGV passage, secondary flow features and turbulence redistribute the temperature pattern. The prediction of temperature redistribution in CFD simulations is impacted by the choice of turbulence model and the method used to describe inlet boundary conditions (steady or unsteady). Secondly, cooling within the NGV itself is another important aspect to consider. The first NGV of the HPT is massively cooled due to the very high temperatures. Once again, the operation of film cooling and its effectiveness may be affected by the choice of turbulence model and the way in which the inlet boundary conditions are described. This section will examine both of these factors, starting with the first.

The effect of the resolved thermal mixing and redistribution of the inlet temperature traverse

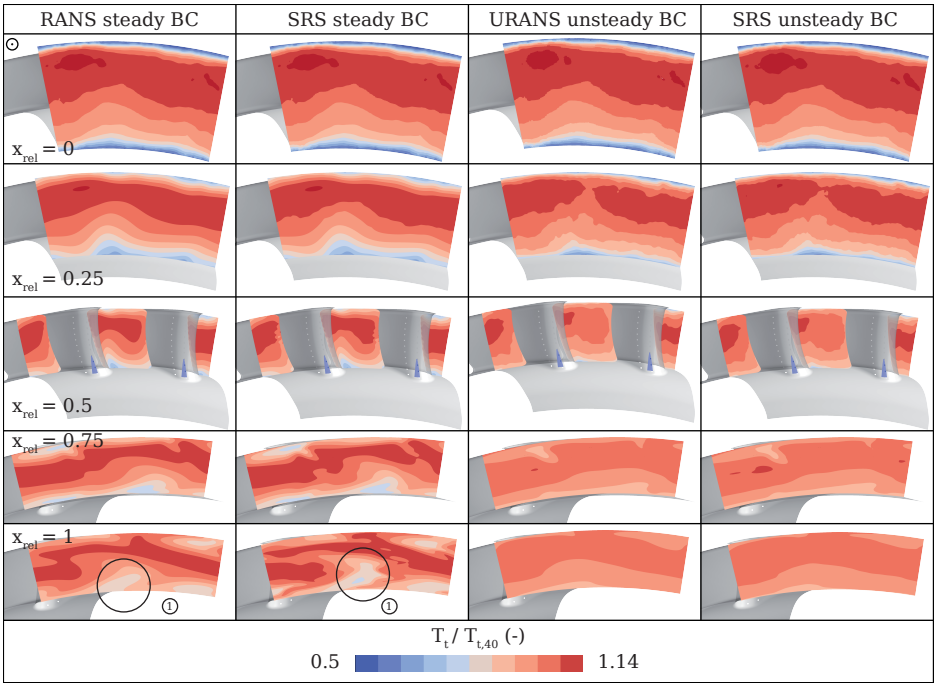

Figure 5.19.: Influence of inlet BC on development of total temperature distribution through NGV passage. Contour plots of relative total temperature on planes at different relative streamwise locations. RANS simulation with steady state inlet BC (left column), SRS with steady state inlet BC (centre left column), URANS with unsteady inlet BC (centre right column), SRS with unsteady inlet BC (right column)

is reflected in Fig. 5.19 which depicts the normalized total temperature on planes throughout the NGV domain, in Fig. 5.20 by radial temperature profiles at different streamwise positions and in Fig. 5.21 by contours of the total adiabatic wall temperature on the hub and shroud endwalls. At the inlet ($x_{rel} = 0$), all four simulation types exhibit analogous temperature distributions, as mandated by the applied inlet BC. The temperature traverse at the turbine inlet (Fig. 5.19) is distinguished by a hot region in the core, which is displaced towards the outer endwall, and colder regions proximal to the walls, resulting from the combustor liner cooling. The total temperature distribution around the circumference exhibits minor irregularities, with the highest values detected in front of the leading edge of the second vane. Likewise, the distribution of cooling air in the outer and inner regions of the inlet

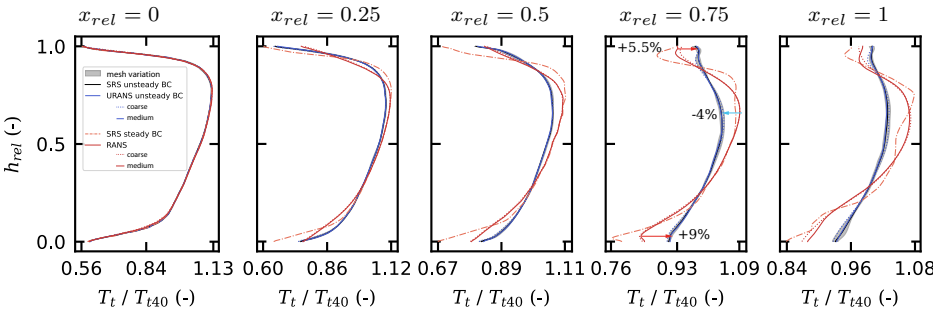

Figure 5.20.: Radial temperature distribution under variation of inlet boundary condition at multiple relative streamwise locations

plane is also non-uniform, leading to uneven temperatures on the hub and shroud caused by the inlet conditions (Fig. 5.21). The inhomogeneities are more noticeable in the RANS and SRS steady BC scenario than in the simulations utilizing an unsteady inlet BC. In the latter case, the distinctive cooling streaks are smoothed out, resulting in a more uniform temperature profile around the circumference. When moving downstream through the NGV passage, more evident differences arise between the unsteady BC cases and the other two simulations with steady inlet BC. The band of high temperature in the upper third of the channel is retained when flowing through the domain in the RANS and SRS steady BC case, whereas it mixes out more with the colder fluid around it in the URANS and SRS unsteady BC case. This phenomenon becomes evident in the radial temperature distribution (Fig. 5.20) from $x_{rel} = 0.25$ onwards. The unsteady BC cases demonstrate a gradual shift of hot gas from the central area to the outer regions. Upon reaching the outlet of the NGV domain, a notable difference in radial temperature distribution becomes apparent. The unsteady BC cases exhibit significantly lower temperatures in the central area of the flow path, while the hub and shroud endwalls register higher temperatures compared to the RANS and SRS steady BC cases. For this particular case, the radial total temperature profile at relative streamwise position $x_{rel} = 0.75$ (just behind the NGV trailing edge) is increased by 9% at the hub wall and 5.5% at the shroud wall, while the maximum temperature in the central part of the flow is decreased by 4% compared to the RANS steady BC approach.

The higher level of thermal mixing in the unsteady BC cases is leading to a more homogenous field when considering the 2D distribution of the temperature towards the outlet of the domain (Fig. 5.19). Distinct patches of hot and cold areas are visible in the RANS and SRS steady BC cases. These are imprints of the secondary flow features on the temperature field. The vortex system, originating from the trailing edge (Ⓥ and Ⓦ in Fig. 5.17) is

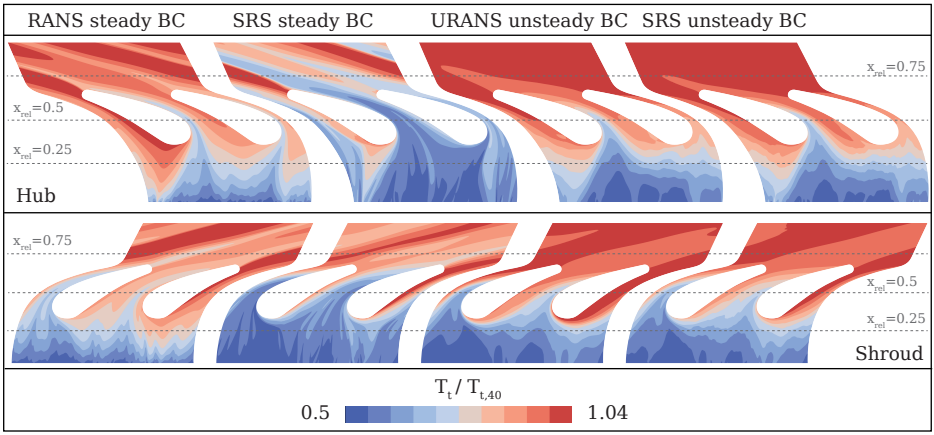

Figure 5.21.: Influence of inlet BC on the total temperature distribution on hub and shroud of NGV. Contour plots of relative total temperature. RANS simulation with steady state inlet BC (left column). SRS with steady state inlet BC (centre left column). URANS with unsteady inlet BC (centre right column) SRS with unsteady inlet BC (right column)

pulling cool endwall fluid towards the centre of the flow path ①. As was shown in section Section 5.3.4 these secondary flow features are less strongly pronounced when applying realistic combustor turbulence and the free-stream turbulence is mixing out the temperature field towards the outlet of the NGV domain.

The thermal mixing in turbulent conditions varies depending on how turbulence is treated in the simulation. In RANS simulations, this effect is fully modelled, while in SRS simulations, it is resolved to a large extent. A measure for the turbulent thermal mixing is the turbulent heat flux $-\rho c_p \overline{u_i' T'}$. In RANS turbulence models, it is modelled using the GDH (cf. Eq. (3.21)). In SRS, no modelling is required as it is directly resolved in the solution. To compare the turbulent heat flux between simulations, the magnitude $mag(\overline{u_i' T'})$ is calculated. The turbulent heat flux is compared between the steady state RANS simulation, the URANS and the SRS with unsteady inlet BC. The results of the SRS with steady BC are left out of this comparison, as the missing turbulence is leading to very little thermal mixing. Contours of the turbulent heat flux on 50% span are shown in Fig. 5.22a. Please note that the scale for the RANS result differs from that of the other two results. The development of the turbulent heat flux through the passage is presented as a mass average in Fig. 5.22b. The turbulent heat flux in the SRS unsteady BC case is significantly higher compared to the RANS simulation and exhibits a significantly different distribution. In both, the URANS and the SRS unsteady BC cases, the turbulent heat flux increases towards the outlet of the

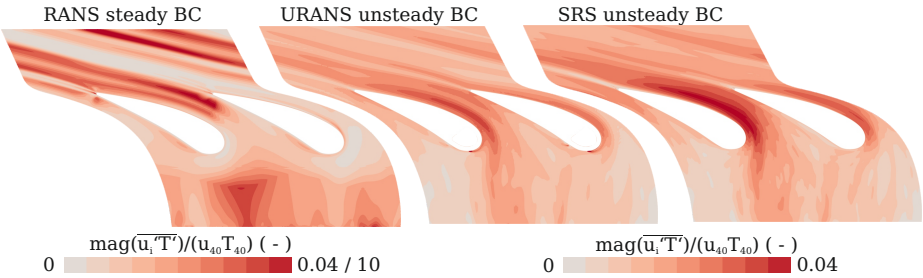

(a) Contour of correlation of velocity and temperature fluctuations on 50% span height. RANS simulation with steady state inlet BC (left). SRS with unsteady inlet BC (right)

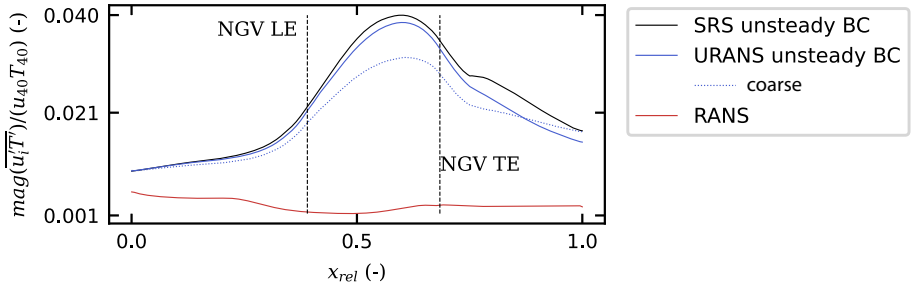

(b) correlation of velocity and temperature fluctuations: mass-flow average on surfaces of constant streamwise coordinate as a function of the relative streamwise coordinate.

Figure 5.22.: Turbulent thermal mixing in RANS and SRS. Contour plots of correlation of velocity and temperature fluctuations on 50% span height. RANS simulation with steady state inlet BC (left column). SRS with unsteady inlet BC (right column)

domain and the highest values are located near the suction side of the vanes, where the acceleration is the highest. In the RANS simulation, however, a different distribution of turbulent heat flux is present and the highest values are found at the edges of the vane wakes. Furthermore, on average, the turbulent heat flux is ten times higher in the unsteady BC cases. This highlights the limitations of using the turbulent heat flux modelling approach in RANS simulations, particularly in highly turbulent conditions such as those found in CT cases. One major difference between RANS and simulations with unsteady BC is the distribution of turbulent kinetic energy. This difference directly affects the modelling in the RANS formulation through the turbulent viscosity (cf. Eq. (3.22)). Furthermore, modelling with a constant turbulent Prandtl number introduces additional deviations. Although the

limitations of the GDH are well-known, they have mainly been evaluated for film cooling configurations in close proximity to the wall (Liu et al. [103], Ling et al. [102]). In the CT case, not only the velocity field but also the temperature field experiences high levels of turbulent fluctuations. This presents a challenge for RANS models that use GDH to model the response of the temperature field to the fluctuating velocity field. In technical applications with moderate temperature gradients and fluctuations, this approach may be valid. However, in the case of combustion-driven turbulence, the flow fields undergo high fluctuations due to the fluctuating heat release of the turbulent combustion. Therefore, when modelling the turbulent heat flux, it is necessary to consider the largest scale fluctuations. This hypothesis is supported by the fact that the URANS simulation with transient boundary conditions shows a similarly high turbulent heat flux as the SBES. The turbulence model in this case also employs the GDH. However, high temperature fluctuations are prescribed at the inlet and the majority of the turbulent heat transfer is resolved. Even when using a coarse mesh for URANS, high levels of turbulent heat flux are still observed. Although not as high as on a finer mesh, the levels are still in the same order and much higher than in the RANS simulation.

5.3.6. Surface Temperature and Vane Cooling

Applying combustor turbulence at the inlet of a turbine simulation alters the predicted thermal mixing and subsequently affects the thermal loads on the vane surfaces. Fig. 5.23 displays the radial distribution of area-averaged adiabatic temperature on the vane surfaces. Comparison of the two simulations with unsteady BC and the RANS simulation with steady inlet boundary conditions reveals a reduction of up to 6.7% in the central part of the vane and an increase of up to 9% at the hub when unsteady boundary conditions are used. The SRS steady BC case displays a distinct thermal load of the NGVs due to the absence of freestream turbulence and the results hardly present turbulent thermal mixing. Although the results of this simulation are shown, the comparison and analysis focuses on the other simulations. The contour plots of the adiabatic wall temperature are shown in Appendix B, Fig. B.2. Two effects can be attributed to the differences in adiabatic wall temperature resulting from the method of prescribing the inlet boundary conditions:

1. The above mentioned differences in the prediction of the turbulent thermal mixing is changing the adiabatic wall temperature on the surfaces of the NGVs.

2. When applying combustor unsteadiness at the inlet of the turbine simulation, turbulent fluctuations are transported through the NGV domain and interact with the cooling films. This is expected to change the film cooling effectiveness, which is affecting the wall temperature of the vane surfaces.

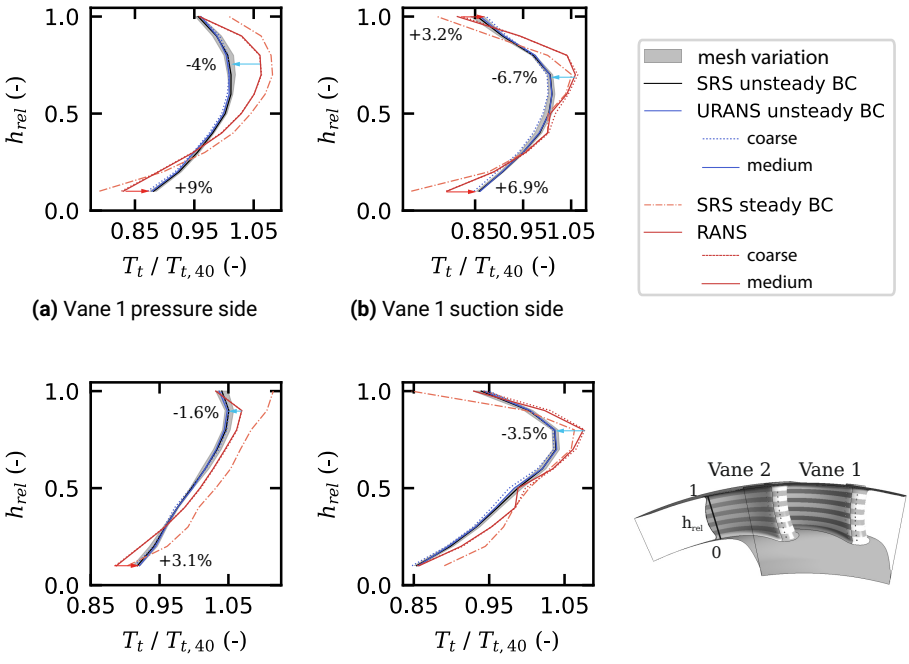

(a) Vane 1 pressure side

(b) Vane 1 suction side

(c) Vane 2 pressure side

(d) Vane 2 suction side

Figure 5.23.: Adiabatic wall temperature (normalized with T_{t40}) distribution on vane 1 and vane 2, pressure and suction side under variation of inlet BC. Area average on ten equally spaced patches

To distinguish between the two effects, an additional set of simulations was conducted with all cooling disabled. By comparing the uncooled simulations, it is possible to isolate the differences in the adiabatic wall temperature resulting from the calculation of the turbulent heat flux. Fig. 5.24a displays the uncooled adiabatic wall temperature of the four simulations, highlighting the differences between the steady and unsteady inlet boundary conditions. It is evident that the resolved velocity and temperature fluctuations in the inlet boundary conditions substantially alter the thermal loading of the NGV when comparing the two unsteady BC cases with the steady RANS simulation. In all four simulations, the hot band imprint from the inlet boundary conditions is visible on the upper third of both vanes ①. The peak temperatures are lower in the simulations with unsteady boundary conditions and the band of hot temperature is not as pronounced on the pressure side.

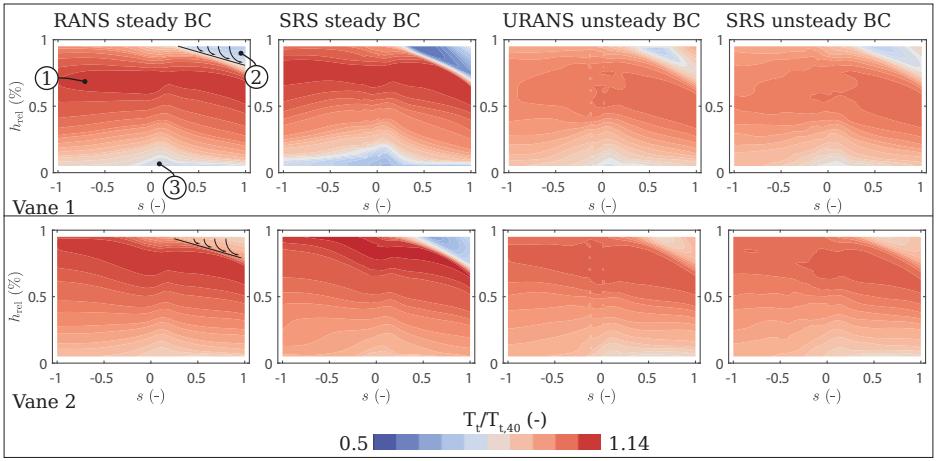

(a) Adiabatic wall temperature with cooling inactive

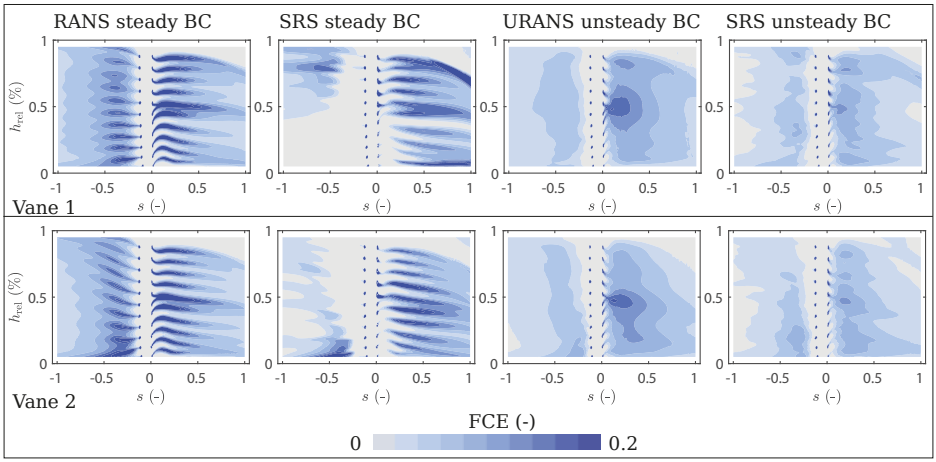

(b) Film cooling effectiveness

Figure 5.24.: Total temperature (normalized with T_{t40}) and film cooling effectiveness distribution on vanes pressure side (s<0) and vanes suction side (s>0) for simulations with different types of inlet boundary conditions

On the suction side of both vanes, the imprint of the casing passage vortex is visible by a downwash of cooler gas from the casing ②. A third area of interest is the leading edge of vane 1 where a zone of colder gas is located ③. It is again noticeable that the temperature lows are less pronounced in the simulations using unsteady BC than in the simulations with the steady mean BC. The usage of unsteady inlet BC increases the thermal mixing which leads to a smoothing out of the adiabatic wall temperature on the surfaces of the NGVs, resulting in less pronounced peak areas compared to the cases with steady inlet boundary conditions. The results for the URANS and SRS unsteady BC cases are very similar, which demonstrates the capability of URANS when combined with unsteady inlet boundary conditions in predicting turbulent thermal diffusion to a large extend.

To evaluate the effect of the inlet boundary conditions on the film cooling of the vanes, the adiabatic FCE (Eq. (2.18)) is considered. In Fig. 5.24b, the film cooling effectiveness is shown on the pressure and suction side of both vanes for all four simulations. Discrete streaks of film cooling are visible on the suction and pressure side for the RANS and the SRS with steady BC. The RANS simulation shows an evenly distributed pattern of films on the pressure side, with good coverage of cooling air over the entire area. The cooling air exits the holes and forms a smooth film that spreads laterally while moving downstream along the vane surface. On the suction side, the attached cooling films are more pronounced than on the pressure side due to the lower back pressure in the accelerating part of the flow. However, the lateral spread of the films is not as high as on the pressure side.

The largest differences between the RANS simulation and the SRS steady BC case occur on the pressure side of both vanes. In the SRS steady BC case, the cooling films become detached from the surface, particularly on the pressure side of the vanes, resulting in zero cooling effectiveness. The lack of free stream turbulence leads to low diffusivity in the flow and over-exaggerated vortexes exiting the cooling holes. This is evident in Fig. B.1 due to the increased strength of the kidney vortices. The film cooling pattern on the suction side in the SRS steady BC case is similar to the RANS result with the exception of a short detachment directly behind the cooling holes. A distinct cooling film pattern can be identified in both simulations using steady inlet boundary conditions.

A completely different situation can be observed when looking at the simulations with an unsteady BC. Here there are no distinct cooling streaks on the pressure side and the contour of the films is less pronounced on the suction side. On the pressure side, the cooling air lifts off the wall immediately after the holes before reattaching to the wall later. The turbulent eddies from the inlet boundary condition interfere with the development of a proper cooling film. The local pressure changes induced by the turbulent motion lift the cooling film away from the wall and push the cooling air back towards the hole at other times. A displacement of the cooling film in the spanwise direction can also be observed. The cooling films exhibit a highly unsteady behavior, as demonstrated by the instantaneous FCE contours in Fig. 5.25. The largest turbulent structures in the main flow are responsible for this destruction of

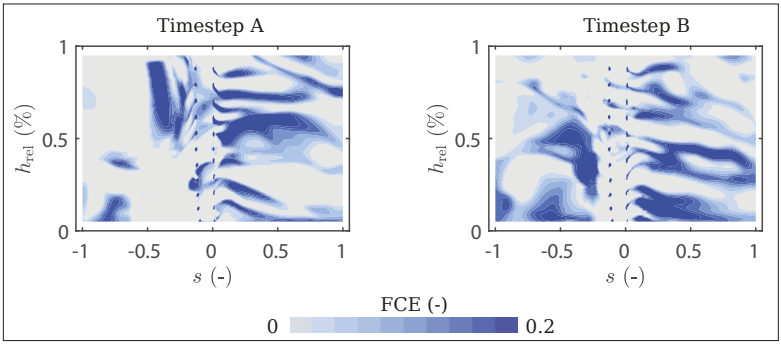

Figure 5.25.: Engine representative HPT: instantaneous η_{fc} for two time steps in the SRS unsteady BC case

the cooling films. Therefore, these effects are not only present in the SRS but also in the URANS simulation. However, there are small differences between the URANS and the SRS unsteady BC case due to the higher level of resolved turbulence in the SRS. In summary, it can be said that the resolution of the turbulence coming from the combustor changes the prediction of the film cooling significantly compared to the steady inlet BC. This reduces the time averaged cooling efficiency and consequently increases the wall temperature. A comparable pattern can be identified in the LSTR case. Fig. B.3 illustrates the film cooling effectiveness on the NGVs for the RANS simulation with a steady inlet BC and the SRS unsteady BC case.

The illustrations in Fig. 5.23, Fig. 5.24a and Fig. B.2 and the calculation of film cooling effectiveness are based on the adiabatic wall temperatures, which implies that there is no heat flux to the vane material. In reality, the solid material would act as a heat sink, reducing the actual temperature at the surface compared to the adiabatic temperature. Furthermore, the timescales of temperature changes in the solid are considerably greater than those in the fluid, which serves as a damping element and reduces temperature fluctuations in the solid. However, a coupled simulation of the aerodynamics of the flow around the vanes and the heat conduction in the solid turbine materials (CHT) was not feasible in this work due to limitations in computational capacity. To make a statement about heat transfer at the wall, the HTC is determined using the quadratic approximation described in Section 2.3.1. Fig. 5.26 displays the non-dimensional heat transfer coefficient using the Nusselt number distribution on the vanes for the RANS simulation, URANS unsteady BC, and SRS unsteady BC cases. The highest values of the Nusselt number are observed on the suction side near the leading edge and towards the trailing edge in areas where the flow is accelerated. This distribution is consistent with the literature (Bakhtiari [10]). As explained earlier,

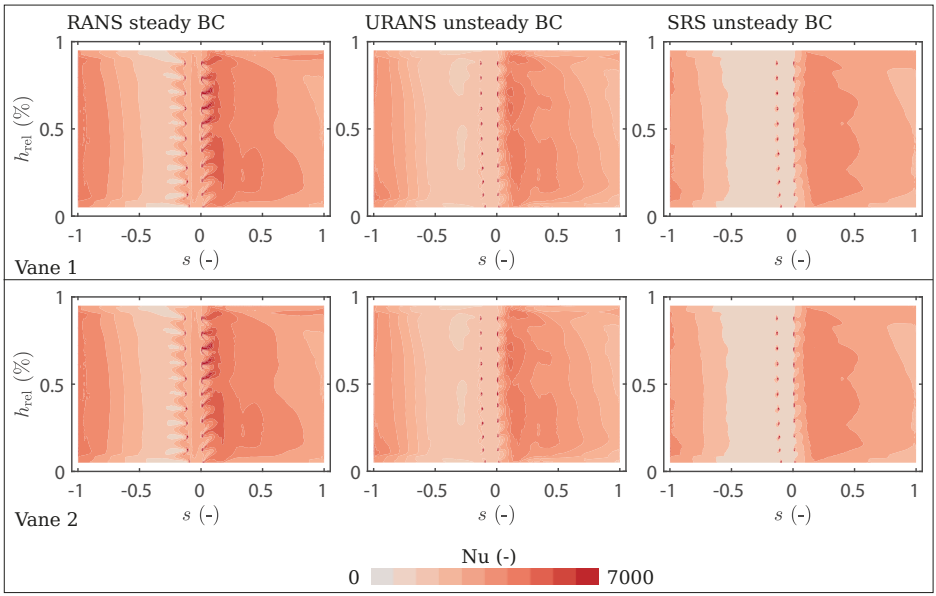

Figure 5.26.: Nusselt number distribution on vanes pressure side (s<0) and vanes suction side (s>0) for simulations with different types of inlet boundary conditions

film cooling is strongly influenced by the choice of inlet boundary conditions. This is also reflected in the imprint of the film cooling on the HTC. In the RANS simulation with steady inlet BC, a pattern of high and low Nu is visible in the area of the cooling films. The kidney vortices exiting the cooling holes drive the hot gas at the outer edge of the cooling films towards the wall, resulting in high Nu values there. The area where the actual cooling film overflows the wall is characterized by a relatively low HTC, as the cooling air protects the wall from high temperatures. These patterns of high and low Nu are less pronounced in the URANS and SRS with unsteady inlet BC as the cooling films are less strong developed there. Appart of the differences due to the film cooling, it is evident that the RANS simulation has slightly higher Nu values at the LE and TE. The overall distribution of Nu however is comparable between all three simulations. The choice of inlet boundary conditions and turbulence model has a limited impact on the HTC on the vanes. This can be expected as the HTC is primarily influenced by the boundary layer around the vanes. Section 5.3.4 demonstrates that the choice of inlet boundary conditions has little effect on the boundary layer profiles or other aerodynamic parameters, such as vane loading. This is to be expected, given that the SBES model operates in RANS mode in the area adjacent to the walls. A

different picture might be expected when the entire flow is fully resolved, all the way down to the wall, using LES.

As demonstrated in the previous sections, the variations in the adiabatic wall temperature between the simulations can be attributed to two phenomena. The first is the different calculation of the turbulent heat flux, which results in a significantly larger thermal mixing in the simulations using unsteady BC than when using stationary BC. The RANS simulation models turbulent heat flux using the GDH, but the approach is not suitable for the conditions of the CT case and predicts a significantly lower turbulent heat flux. In the SRS with steady BC, the turbulence from the combustion chamber is absent due to the lack of fluctuations at the inlet, resulting in an even bigger underestimation of the turbulent heat flux. The use of realistic combustion chamber turbulence in the URANS and SRS ensures a higher mixing of warm and cold fluid. This leads to a reduction in the wall temperature of the vanes while simultaneously increasing the endwall temperature. The second phenomenon is the change in film cooling effectiveness. The resolved combustion chamber turbulence in the URANS and SRS unsteady BC case, alters the effectiveness of the film cooling. Turbulent structures hinder the formation of stable cooling films, resulting in reduced film cooling effectiveness and increased vane wall temperature. Therefore, two opposing trends overlap.

To determine the proportion of temperature differences attributable to the two phenomena, in Fig. 5.27, a breakdown of the shares is provided. Similar to Fig. 5.23, temperature differences are evaluated as the area average on patches that are equally spaced over the span height for the pressure and suction sides of each vane individually. The RANS simulation with steady BC is used as the reference case, and differences are calculated by subtracting the RANS results from the other simulation results. The upper row shows the total temperature difference to the RANS results, $\Delta T_t = T_t - T_{t,RANS}$. The second row presents the contribution of thermal mixing to the total temperature difference. The temperature values of the uncooled simulations are used to calculate the temperature difference for this representation, $\Delta T_{t,mix} = T_{t,no\ cool} - T_{t,RANS,no\ cool}$. The bottom row displays the contribution of film cooling to the total temperature difference. It follows by deducting the mixing related difference from the total difference, $\Delta T_{t,FCE} = \Delta T_t - \Delta T_{t,mix}$.

Only the two simulations using unsteady inlet BC and the steady RANS simulation are included for this comparison. The SRS steady BC case has been excluded for clarity. From the previously shown results it is clear, that the missing freestream turbulence in that simulation is leading to a completely different flow and temperature field, which is not expected to be close to reality. The temperature difference to the RANS results (upper row) reflects the trends shown in Fig. 5.23. The use of unsteady inlet boundary conditions leads to a reduction in wall temperature in the central part of the vanes and an increase towards the hub and shroud endwalls. This general trend is present on both vanes and on the pressure and suction side. URANS and SRS show similar trends with only small local differences.

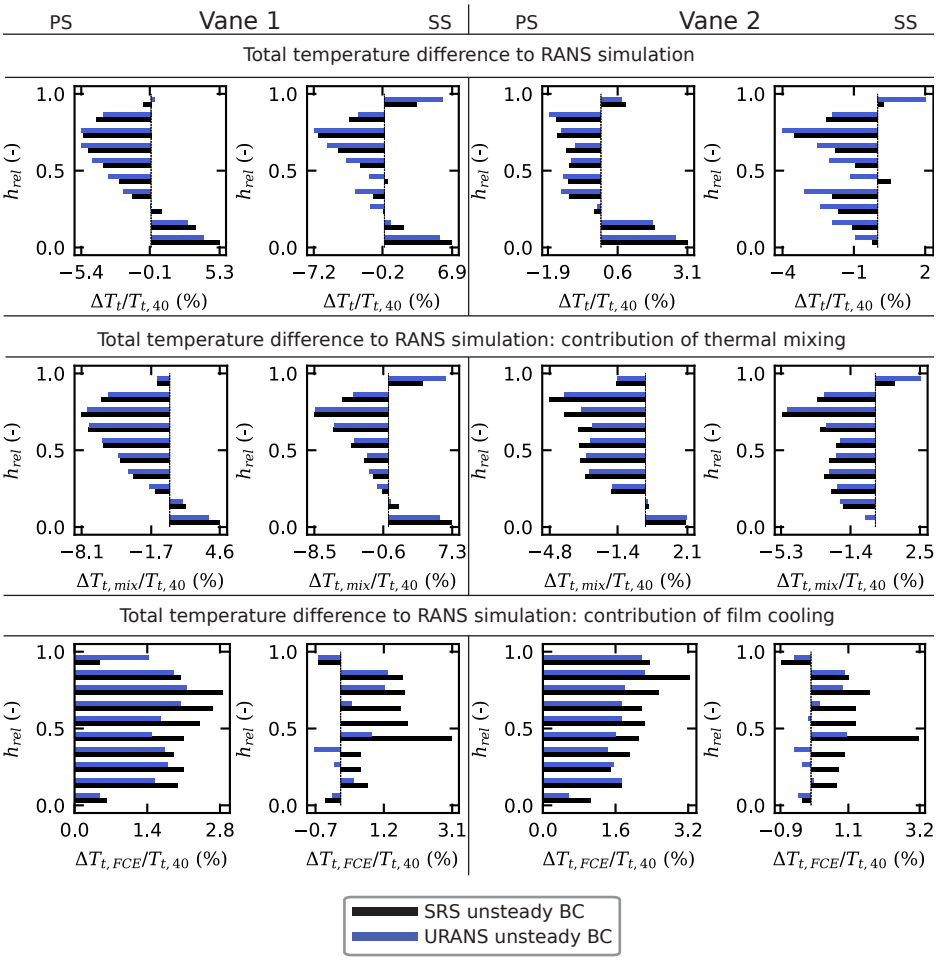

Figure 5.27.: Breakdown of total temperature difference on vane surface. Delta of total temperature (normalized with T_{t40}) to RANS simulation as radial distribution on vane 1 and vane 2, pressure and suction side with different types of inlet boundary conditions. Area average on ten equally spaced patches

The contribution of thermal mixing reduces the wall temperature in the inner 80% of the channel height for both simulations with unsteady BC. A tendency of increased temperature can be observed towards the hub and shroud endwall when resolving combustor turbulence in the inlet boundary condition. On vane 1, the temperature reduction in the central part is the largest, with approximately 8.5% of T_{t40}, and there is an increase in temperature towards the hub of around 7%. A similar trend can be observed on vane 2, but with smaller temperature differences. The increased turbulent heat flux causes a redistribution of temperature when the combustion chamber turbulence is resolved, resulting in a rise in temperature towards the endwalls and a decrease in temperature in the central part.

This trend is counteracted by the opposite behavior resulting from differences in film cooling effectiveness. The reduced effectiveness of film cooling in the simulations with unsteady BC is causing an increase in wall temperature at almost all vane heights, with only a small decrease in wall temperature observed on both suction sides in the last 10% towards the endwalls. On the pressure sides of the vanes, the film cooling is less effective, resulting in an increase in wall temperature of up to 3.2% of $T_{t,40}$ in the SRS unsteady BC case. On the suction side, the temperature increase is less pronounced. When considering the effect of film cooling, larger differences can be observed between the URANS simulation and the SRS. This supports the hypothesis that film cooling is more sensitive to the resolved part of the turbulence. The URANS simulation can resolve the largest structures but fails to predict the decay into smaller eddies. The ESD plots in Fig. 5.28 provide evidence to support this hypothesis. The energy spectrum is shown at four different monitor points for the SRS and the two URANS simulations, all of which use unsteady boundary conditions. The energy in the two URANS simulations drops off at lower frequencies than in the SRS, indicating a lower level of resolved turbulence. Coarsening the mesh in the URANS simulations strengthens this trend.

Although a reduction in film cooling effectiveness increases the total temperature, this effect is counteracted by a temperature decrease due to the higher thermal mixing. However, the film cooling related increase is smaller, resulting in a lower overall surface temperature in most areas of the vanes. This is observed when using scale-resolving turbulence modelling and accounting for combustor turbulence. The temperature at the NGV walls is influenced by a complex flow situation. The definition of boundary conditions influences the efficacy of the simulation in predicting the diverse mechanisms that contribute to the phenomenon under study. In the case presented in this work, turbulent thermal mixing has a greater impact than changes in film cooling effectiveness, resulting in a lower temperature in the central part of the vanes. However, in other cases, such as when more cooling rows are included, this trend may differ. To accurately predict metal temperatures and optimize cooling requirements, it is important to consider combustor-related unsteadiness when designing the HPT.

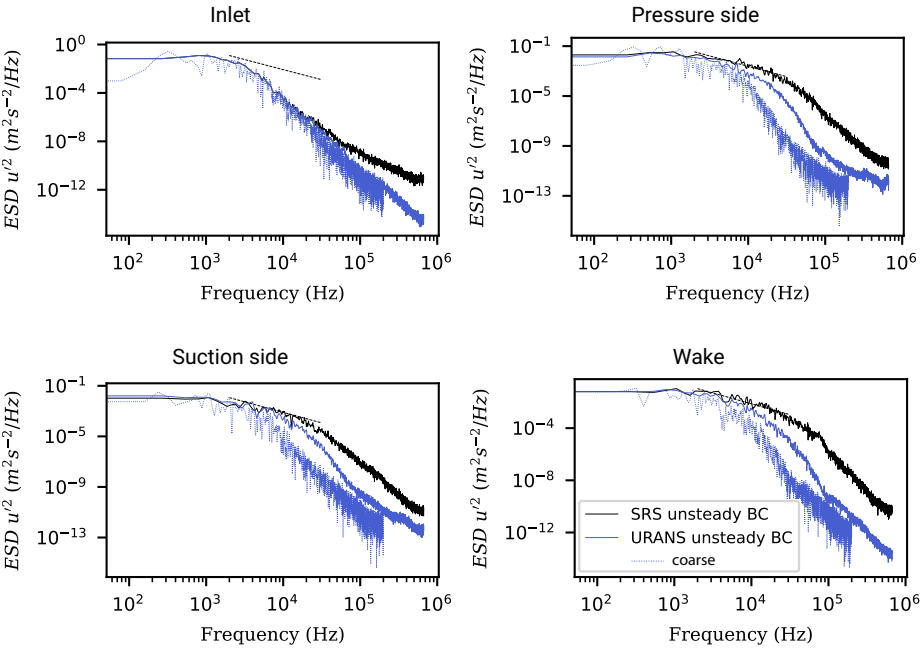

Figure 5.28.: ESD of four monitor points in NGV domain highlighting the differences between URANS and SRS

6. Conclusion and Outlook

This chapter presents a summary of the principal findings of this work, discusses their implications for the turbomachinery research and development community, and offers a prospective view of future work in the field of CTI.

6.1. Summary of Principal Findings

The principal findings in regard to the research objectives defined in Section 1.3 are as follows:

1. *Review of unsteady effects at the combustor outlet:* As part of a comprehensive literature review, the most relevant aspects of CTI have been collated. The focus of this study was on the numerical treatment of CTI and on unsteady effects. In addition to an inhomogeneous distribution of temperature, combustor swirl and crossflow components, unsteady effects and combustor turbulence represent the most significant factors to be considered when investigating the interaction between the combustor and turbine. Recent studies have highlighted the significance of resolving combustor turbulence in the inlet BC of a turbine simulation in order to accurately predict the aerothermal conditions within the turbine.
2. *Development of a method to efficiently collect and store unsteady field data:* This work presents an efficient method for collecting transient snapshot data from a precursor simulation. A combination of POD and Fourier series development in the PODFS method enables the derivation of a reduced-order model of the time series of field data (Section 4.1). The application of this methodology allows for the reduction of the original data size by a factor of 5 to 20, depending on the particular use case (Section 4.3). Furthermore, the time step size of the snapshot data is decoupled from that of the turbine simulation. This introduces temporal flexibility to the process of utilizing unsteady inlet BC.
3. *Integration of unsteady boundary condition reading routines into turbine CFD solvers:* The implementation of reading routines enables the PODFS representation of the time-resolved inlet boundary condition fields to be utilized in the two turbine CFD solvers, ANSYS® CFX® and HYDRA (Section 4.2).

4. *Validation of the entire workflow:* The workflow for collecting, compressing and reusing the interface data was validated using two test cases. First the capability of the method to reproduce the turbulent, time-accurate flow fields at the interface between two simulations was demonstrated on a generic channel test case. A comparison of the results of the baseline geometry simulation, which includes the turbulence-generating inlet section and the section of interest in one domain, with several simulations of the truncated domain of the section of interest, which use the PODFS boundary conditions at the inlet, demonstrated a high degree of agreement between the baseline results and the PODFS results. By varying the number of POD modes and the number of FCs, an optimal balance between compression rate and accuracy could be determined at 98% POD mode energy and 90% FC energy (Section 4.3).

   The PODFS method was further validated in a CT test case based on the LSTR research turbine. A comparison of the simulation results of the integrated combustor-turbine simulation with experimental data from rig tests demonstrates the capability of the numerical method used to accurately predict the flow in the HPT (Section 3.3.1). Furthermore, the results of the NGV simulation utilizing the PODFS boundary conditions were incorporated into the comparison, and demonstrated a satisfactory degree of concordance with the other results (Section 4.4).

5. *Application of the PODFS method on an engine representative CT case:* The snapshot data of an engine representative RQL combustor was employed in the PODFS method to generate a reduced order model of the time series of the field data at the combustor domain outlet. The most pertinent aspect of the signal could be represented by 709 POD modes (98%) and 3952 Fourier coefficients (90%). This represents a compression ratio of nine compared to the full snapshot data. The results of a SRS using PODFS data as inlet BC were compared to those of a steady-state RANS simulation, a SRS using steady inlet BC, and a URANS simulation with unsteady PODFS BC. (Section 5.1.2)

6. *Impact of combustor unsteadiness on the aerodynamics of turbine vanes*: The analysis of the simulations using different types of inlet boundary conditions revealed the following results: The utilization of unsteady inlet BC has a minimal impact on the aerodynamic characteristics of the turbine vanes. The highly unsteady flow in the NGV passage results in the formation of more pronounced horse-shoe and passage vortices. This results in a change in the turning of the vane in the regions close to the endwalls. The high free-stream turbulence in the passage flow interacts with the wakes behind the NGVs. This results in a greater degree of mixing between the wake and the passage flow compared to the simulations with steady BC. The vane loading by means of isentropic Mach number distribution remains unchanged, and the capacity of the vanes decreases by 0.4% when using an unsteady inlet BC. (Section 5.3.4)

7. *Impact of combustor unsteadiness on the turbine thermal loading and cooling of the*

vanes: A more pronounced impact of the unsteady inlet BC can be observed when considering the thermal effects in the NGV passage. Two phenomena can be attributed to this. Firstly, the utilization of unsteady inlet BC alters the thermal mixing within the flow. The turbulent fluctuations result in a convective transport of fluid with different temperatures, thereby reducing temperature gradients. In the case of the CT configuration, where the turbine inlet temperature field is characterised by cold areas at the endwalls and hot zones in the centre of the passage, this leads to a mixing of the hot and cold fluid. As the cold gas in the inner and outer endwall regions is mixed with the hot gas in the center of the passage, a flattened temperature profile is created, with higher temperatures at the endwalls and lower temperatures in the middle part of the domain. In the context of the aforementioned case, the reduction in the circumstantially averaged temperature at the TE of the vanes is 4% of T_{t40} in the channel center, while an increase is observed at the inner and outer endwall of 9% and 5.5% respectively. The NGV wall temperatures are similarly affected. The differences in the calculation of turbulent thermal mixing between steady RANS simulations and SRS with unsteady inlet BC is identified as the primary cause of this discrepancy. In RANS simulations, the turbulent thermal diffusion is entirely modeled using the GDH. In SRS, the turbulent heat flux is calculated as a solution of the conservation equations. In the context of highly turbulent flows, which are characteristic of the first stage of HPTs, the GDH is found to significantly underpredict the turbulent heat flux.

The second effect responsible for the differences in the thermal conditions is the alteration in the film cooling effectiveness. The turbulent motion in the freestream is interacting with the cooling films on the surface of the vanes. The formation of stable cooling films is impeded by turbulent structures, resulting in a reduction in film cooling effectiveness and an elevated vane wall temperature. Consequently, there is an opposing trend to the reduction of wall temperature due to the increased thermal mixing. In the given case, the increase in wall temperature due to the reduction in film cooling effectiveness is outweighed by the reduction in wall temperature due to the higher thermal mixing. (Section 5.3.5) It should be noted that the aforementioned may differ in other configurations, for example, when more cooling is used.

8. *Separation of effects caused by scale resolving turbulence models and scale resolving inlet boundary conditions:* The efficacy of enhancing the fidelity of the utilized CFD methodology by transitioning from RANS to a scale-resolving model in isolation has been found to be ineffective. In the absence of an appropriate set of inlet BC, the SRS is unable to predict the correct turbulent mixing. The utilization of unsteady inlet BC is the sole means of initiating turbulent fluctuations at the inlet and maintaining the correct level of mixture downstream within the passage. In the context of highly turbulent conditions, which are typical of the interface between the combustor and turbine, the use of SRS is only beneficial when prescribing the turbulent fluctuations

at the inlet. (Section 5.1)

9. *What is the relative performance of an URANS simulation in comparison to a real SRS?* The comparison of URANS simulation and SRS results indicates that URANS simulations are capable of resolving the largest unsteady structures when applying fluctuations at the inlet. The levels of turbulent kinetic energy in the URANS, and thus the turbulent mixing, lie slightly below those in the SRS. This leads to very similar aerodynamic results between the URANS and SRS unsteady BC cases. Small discrepancies occur in the thermal results. The thermal mixing in the URANS is not as strongly pronounced as in the SRS. However, it is above the levels of thermal mixing observed in the steady RANS simulation. In conclusion, it can be stated that the largest turbulent structures originating from the combustion chamber are the most significant in terms of the aerothermal behavior of the first NGV of the HPT. It can be proposed that URANS simulations may be sufficient when applying turbulent fluctuations at the inlet of the turbine domain. The utilization of SRS methods does, however, resolve additional turbulent structures, which slightly increase the turbulent thermal mixing. However, this comes at the cost of increased computational effort. The most critical aspect is the definition of realistic combustor turbulence at the inlet, which is necessary to calculate the correct level of turbulent thermal mixing. (Section 4.3, Section 5.1)

6.2. Impact of Results and Recommendations

The numerical studies presented in this work demonstrate the potential of employing unsteady inlet BC in conjunction with SRS to enhance the precision of thermal predictions for HPT vanes. For the investigated NGV case, the differences between SRS using unsteady inlet BC and a stationary RANS simulation are substantial. In this context, the inadequacy of RANS turbulence models in predicting elevated thermal mixing in the vane passage was identified as the primary reason for discrepancies between RANS simulations and the SRS. It should be noted that the temperatures compared in this work are adiabatic wall temperatures, and that due to the missing heat conduction in the solid material, the observed temperature differences are most likely to be overstated compared to the reality. In addition, the geometry under investigation is a vane with minimal cooling. In reality, NGV vanes of the first stage are significantly more intensely cooled, which is supposed to influence the effect of the inlet turbulence on the cooling and vane temperatures. Consequently, it is challenging to make a statement about the precise effect of unsteady inlet boundary conditions on the real metal temperatures and thus the service life of the turbine. Nevertheless, it could be demonstrated that the usage of unsteady inlet boundary conditions and SRS methods have a significant impact on the prediction of thermal mixing and film cooling in the simulation. Therefore, combustor unsteadiness should be included in the

design and investigation process of the first stage of the HPT. It can be argued that the use of ultra-fine mesh resolutions and highly sophisticated scale-resolving turbulence models is not always necessary, as even URANS simulations with unsteady inlet boundary conditions can effectively ”resolve” the most significant unsteady motions in the main passage flow, which are responsible for the majority of the turbulent mixing in the flow. However, in order to resolve the turbulent impact all the way down to the walls, it is necessary to employ fine resolution and real scale-resolving models.

In the context of a CT case, where highly turbulent conditions prevail, the utilization of SRS of the turbine without the application of turbulent fluctuations at the inlet is not beneficial. In order to simulate the turbulent mixing processes within the passage, it is necessary for the inlet boundary conditions to initialize the largest turbulent scales. In the absence of this, the simulation will be initialized with laminar inflow conditions, resulting in an underprediction of turbulent mixing and inaccurate results. Scale-resolving simulations can only be employed when an appropriate set of unsteady inlet boundary conditions is available.

6.3. Outlook

This section presents recommendations for the continuation of this work. These recommendations can be divided into two categories: those pertaining to further investigations of the impact of combustor unsteadiness on the HPT design and those concerning improvements to the presented method of creating unsteady inlet boundary conditions for HPT simulations.

Impact of Combustor Unsteadiness on the HPT

- The incorporation of additional cooling features, such as supplementary cooling rows on the endwalls and vanes, into the NGV setup would facilitate a more comprehensive understanding of the impact of combustor unsteadiness on the aerothermal behavior of the first NGV.
- Expansion of the scope of the analysis on the impact of combustor unsteadiness, conducted in this work, towards the detailed analysis of the flow through the rotor and further stages of the HPT by conducting SRS of the entire HPT including the rotating blades. Hereby, the impact of the combustor turbulence on the aerodynamics and the thermal behavior of the rotor and on the seal and purge flow between stages could be investigated.

- Investigation of the effect of wall resolution on the prediction of wall temperatures, HTC and film cooling. The SBES turbulence model employed in this research utilizes RANS in the wall-adjacent regions. This is anticipated to influence the turbulent mixing mechanisms at the wall. The outcomes of the SBES should be compared with those of a wall-resolving LES to assess the potential for further enhancements by resolving the wall region with LES.
- Integration of CHT techniques into the analysis of the impact of combustor turbulence on the HPT in order to obtain realistic wall temperatures by taking into account the heat conduction in the solid metal.

Improvements to the PODFS Method

- Enhancement of the flexibility of the PODFS method by incorporating operating point scaling functionality. This would permit the utilization of a single snapshot data set for multiple operating points without the necessity for multiple costly combustor LES. Special focus hereby must lie on the scalability of the turbulent fluctuations.
- The integration of a digital filter into the PODFS workflow enables the artificial creation of turbulent fluctuations based on mean fields and turbulent statistics. The primary challenge in this process is the generation of coupled velocity and pressure fluctuations, which are necessary to create the boundary conditions required for the turbine calculation. This approach would permit the generation of unsteady inlet BC without the necessity for a scale-resolving combustor simulation, thereby significantly reducing the computational effort within the design process.
- Investigation of the difference between realistic (derived from combustor simulation) and artificial (derived from digital filter) inlet boundary conditions.

A. Appendix to Methods

Fig. A.1 illustrates the velocity distribution in the baseline channel simulation for different turbulence models. The velocity field is comparable across all simulations in the region in front of the tabulators. It is evident that the velocity field exhibits differences in its distribution behind the turbulence-generating rods. In the RANS simulation, the wakes of the rods are discernible in the lateral velocity distribution. In the unsteady simulations, the wakes of the rods are less pronounced due to the unsteadiness, which allows for mixing. This phenomenon is most pronounced when the simulation resolves a greater proportion of the turbulent motion. As the channel outlet is approached, the results once again become more similar, as the differences between them diminish.

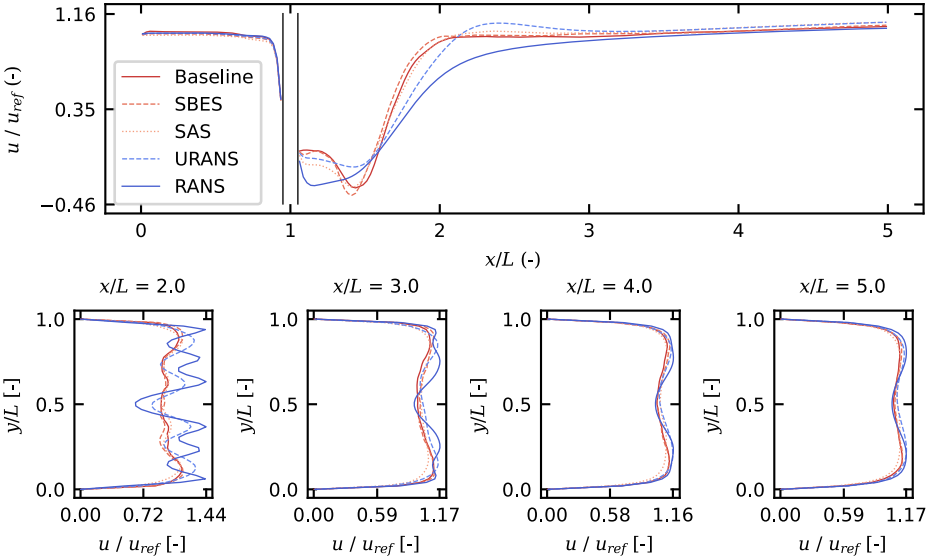

Figure A.1.: Centreline and lateral velocity in baseline channel for different turbulence models

Fig. A.2 depicts the velocity distribution in the baseline channel simulation and the truncated channel geometry simulation, employing the strong recycling and the PODFS method for inlet BC. The velocity field is comparable across all simulations within the entire channel. This illustrates the capacity of both methods to accurately prescribe the interface data as inlet BC.

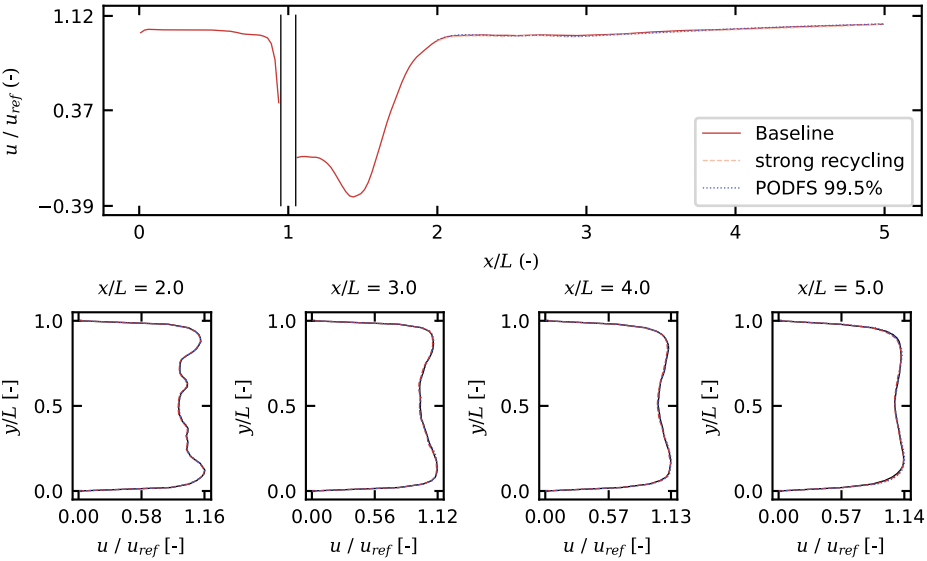

Figure A.2.: Centreline and lateral velocity in channel. Baseline simulation and two truncated domain simulation using different inlet boundary conditions

Fig. A.3 shows the velocity distribution in the baseline channel simulation and the truncated channel geometry simulation, employing the PODFS method for inlet BC and using different turbulence models. The velocity field is comparable across all simulations within the entire channel.

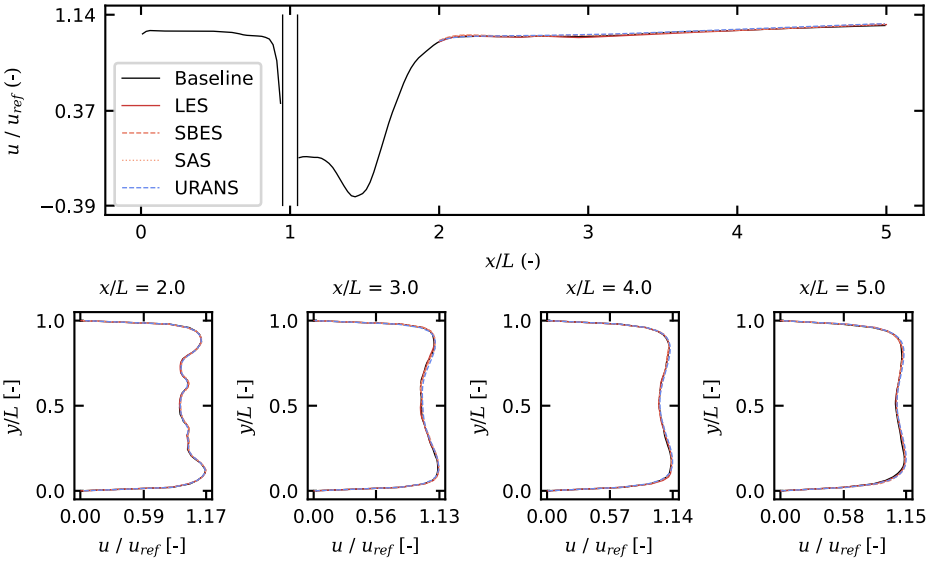

Figure A.3.: Centreline and lateral velocity in channel for different turbulence models on truncated domain

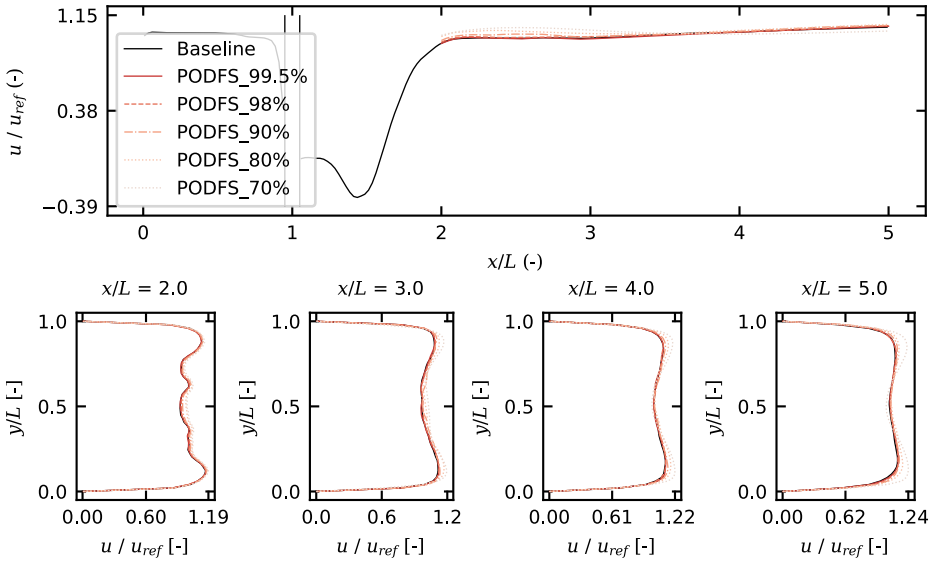

Figure A.4.: Centerline and lateral velocity in channel for different turbulence models

The impact of varying the number of POD modes on the velocity field is illustrated in Fig. A.4. The smaller the POD mode energy resolved, the greater the offset to the baseline simulation.

The impact of varying the number of POD modes on the total temperature distribution is illustrated in Fig. A.5 and Fig. A.6. The smaller the POD mode energy resolved, the greater the offset to the baseline simulation.

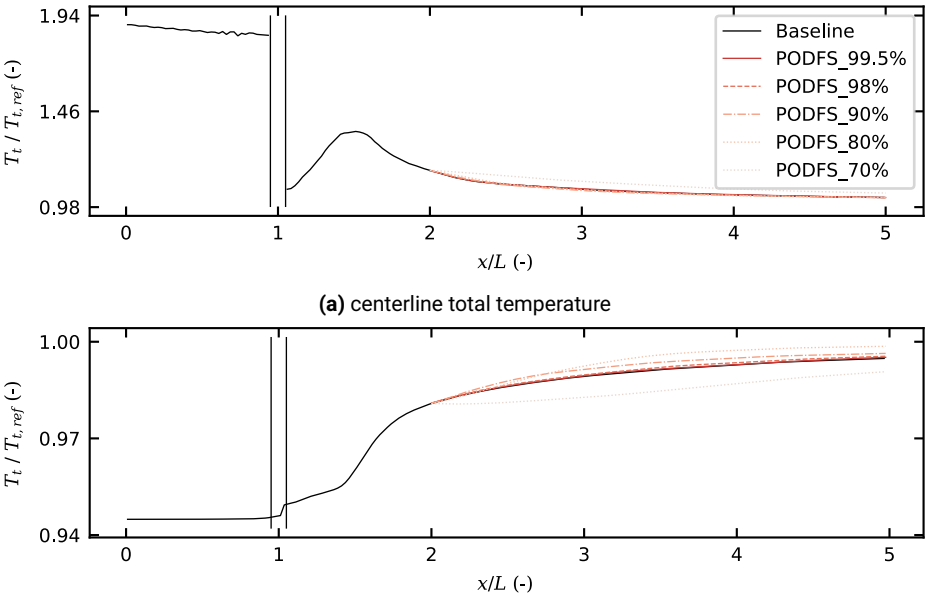

(a) centerline total temperature

(b) Averaged total temperature on cylindrical surface at channel walls

Figure A.5.: Total temperature distribution in truncated channel under variation of number of POD modes

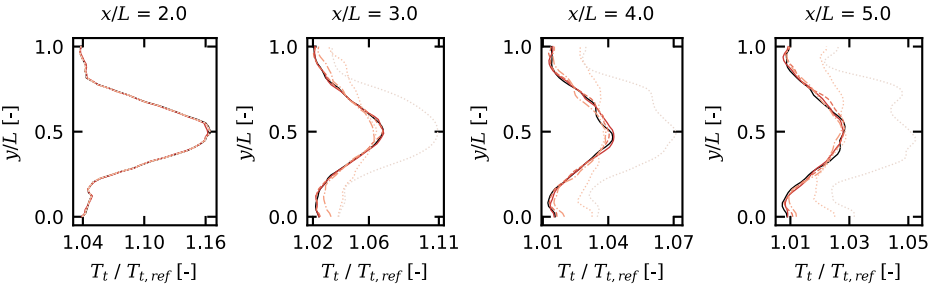

(a) Lateral total temperature distribution in y direction at different streamwise positions

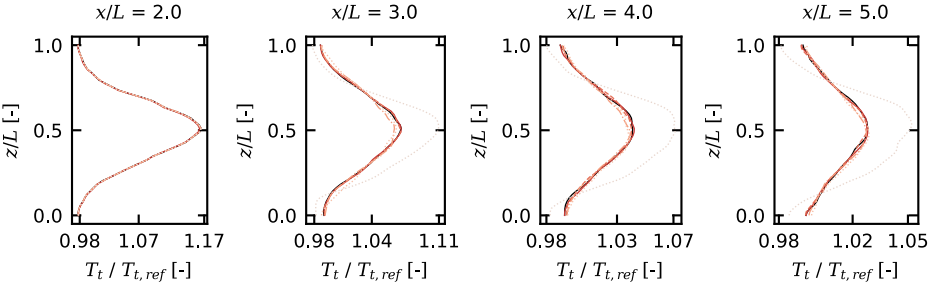

(b) Lateral total temperature distribution in z direction at different streamwise positions

Figure A.6.: Total temperature distribution in lateral direction in truncated channel under variation of number of POD modes

The impact of varying the number of FC on the velocity field is illustrated in Fig. A.7. The number of FC has a minimal effect on the resulting velocity field.

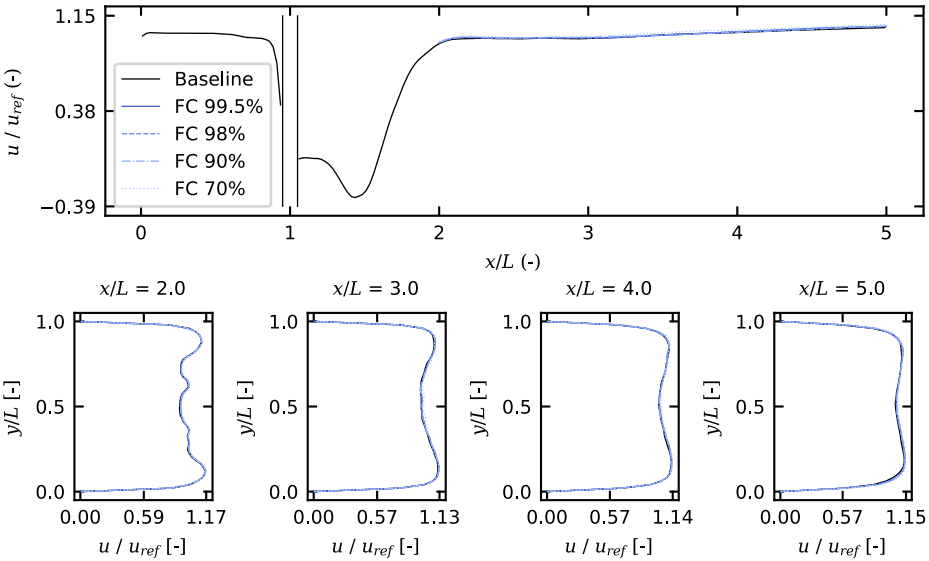

Figure A.7.: Centerline and lateral velocity in channel for different number of FC

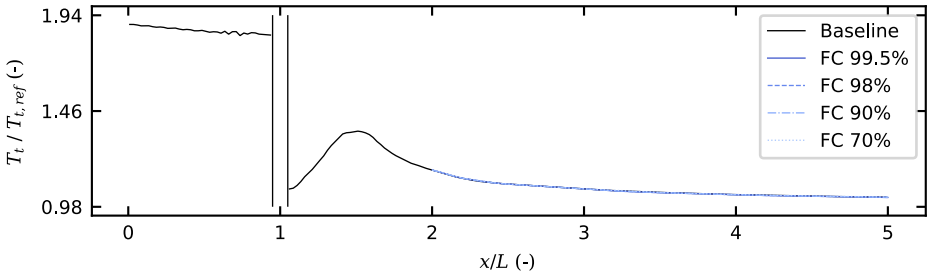

(a) Centerline total temperature

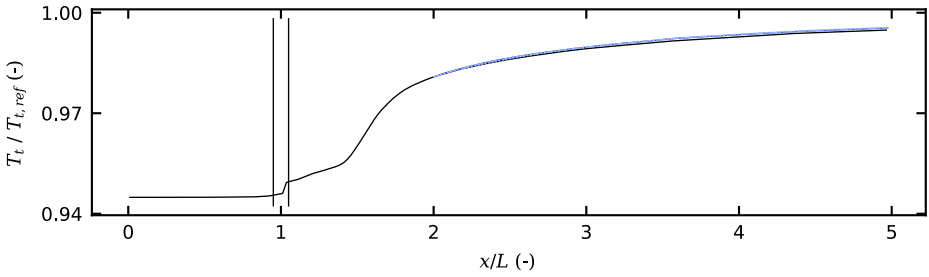

(b) Averaged total temperature on cylindrical surface at channel walls

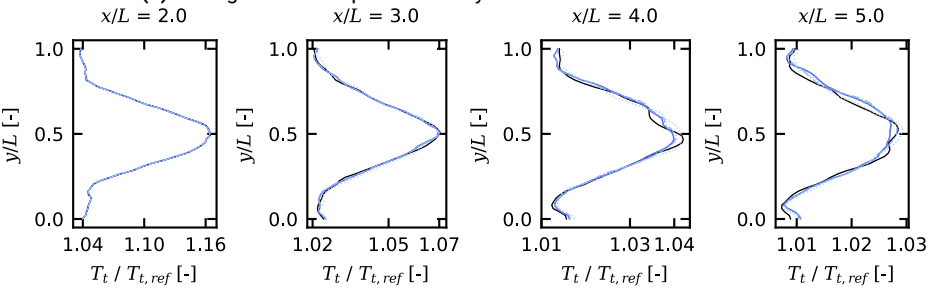

(c) Lateral total temperature distribution at different streamwise positions

Figure A.8.: Total temperature distribution in truncated channel under variation of number of FC

The impact of varying the number of FC on the total temperature distribution is illustrated in Fig. A.8. The number of FC has a minimal effect on the resulting temperature distribution in the channel.

B. Appendix to Results and Discussion

Fig. B.1 presents a comparison of the secondary flow structures for the SRS steady BC case and the URANS unsteady BC case. The URANS exhibits a remarkably similar secondary flow structure to that observed in the SRS unsteady BC case. A very disparate picture emerges in the SRS steady BC case. Here, the cooling and trailing edge vortices are markedly more pronounced than in the other simulations. The lack of free-stream turbulence in comparison to the simulations with unsteady inlet BC and the lower turbulent viscosity in comparison to the RANS simulation are responsible for the absence of turbulent mixture, resulting in the unphysical outcomes of this simulation.

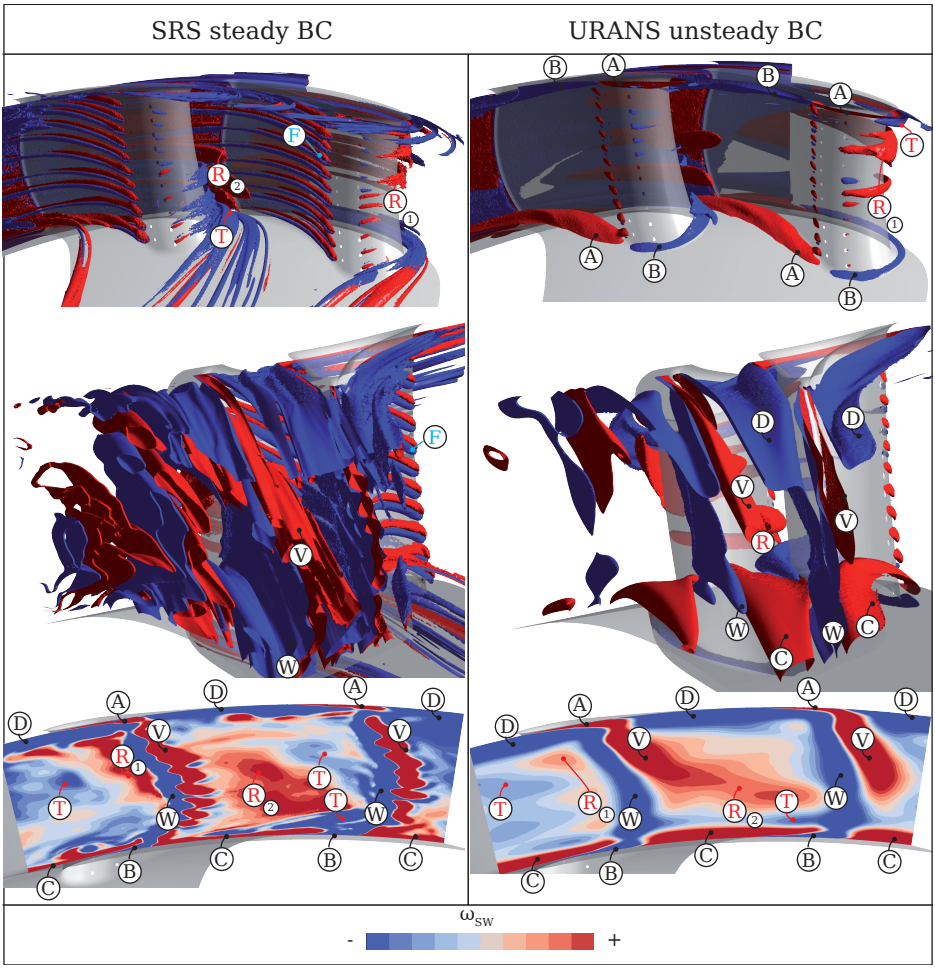

Figure B.1.: Streamwise vorticity SRS with steady state inlet BC and URANS unsteady BC

Fig. B.2 presents the adiabatic wall temperature of the cooled vane simulations for all four cases. It is noteworthy that the two simulations employing unsteady BC exhibit remarkably similar outcomes. The RANS simulation indicates the presence of overexhagurated cooling films and the SRS steady BC case very little thermal mixing.

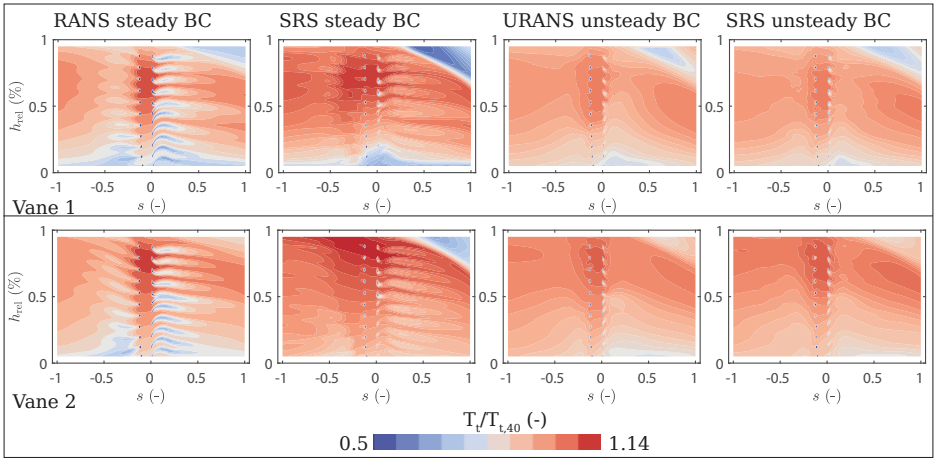

Figure B.2.: Total temperature (normalized with T_{t40}) distribution on vanes pressure side (s<0) and vanes suction side (s>0) for simulations with different types of inlet boundary conditions

Fig. B.3 illustrates the cooling effectiveness of the film on the vanes of the LSTR, by comparing the RANS simulation and the SRS unsteady BC results. This corroborates the findings of Section 4.4 and Section 5.3.6, which indicate that the cooling effectiveness is overestimated in the RANS simulation relative to the unsteady inlet BC case. This phenomenon was previously demonstrated on the LSTR platform and subsequently validated by experimental results. The results presented in Fig. B.3 also support this trend on the vanes.

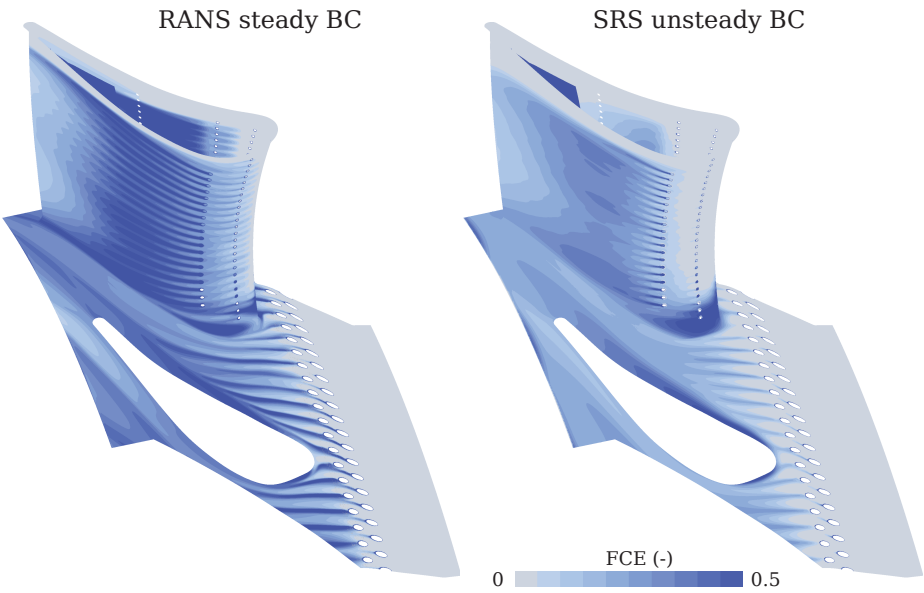

Figure B.3.: Film cooling effectiveness on vanes. Comparison between RANS and SRS unsteady BC

List of Figures

List of Tables

List of Symbols

The most commonly used symbols are listed here, alongside their location of first occurrence. Symbols used but not listed here are clarified in their respective contexts.

Symbols

Greek	Description	Unit
∇	nabla operator	m^{-1}
Γ	turbine capacity	$\mathrm{ms}\sqrt{\mathrm{K}}$
Δ	grid spacing	m
Δt	time step width	s
Π	pressure ratio	–
Θ	circumferential angle	$^\circ$
Φ	generic physical quantity	–
Φ	spatial modes	–
Ω	vorticity tensor	s^{-1}
α	general diffusion coefficient	–
α	bypass ratio	–
α	pitch angle	$^\circ$
γ	heat capacity ratio	–
δ	kronecker delta	–
δ_y	wall distance	m
ζ	model constant	–
η	efficiency	–
$\overline{\eta}$	isentropic efficiency	–
η	Kolmogorov length scale	m
η_{fc}	adiabatic film cooling effectiveness	–
κ	von Karman constant	–
λ	Eigenvalue	–
λ^*	material typical scalar value	–
λ	thermal conductivity	$\mathrm{W\,m^{-1}\,K^{-1}}$

(Symbols continued)

λ_2	Second positive Eigenvalue of the velocity field	–
μ	dynamic viscosity	$\mathrm{kg\,m^{-1}\,s^{-1}}$
ν	kinematic viscosity	$\mathrm{m^2\,s^{-1}}$
ρ	density	$\mathrm{kg\,m^{-3}}$
σ_k	model constant	–
τ	stress	–
τ	temporal distance	s
ψ	phase angle	$^\circ$
ω	specific dissipation rate	$\mathrm{s^{-1}}$
ω	rotational speed	$\mathrm{s^{-1}}$
$\vec{\omega}$	vorticity	$\mathrm{s^{-1}}$
ω	vorticity	$\mathrm{s^{-1}}$
ϵ	turbulent dissipation rate	$\mathrm{m^2\,s^{-2}}$
ϵ	sign function	–
ϕ	scaled spatial modes	–
ϕ	equivalence ration	–
ϕ	whirl angle	$^\circ$

Roman	**Description**	**Unit**
A	area	$\mathrm{m^2}$
A	temporal coefficients	–
a	cross correlation transformation	–
a	scaled temporal coefficients	–
b	filter coefficient	–
b	Fourier coefficient	–
C	velocity in absolute frame of reference	$\mathrm{m\,s^{-1}}$
C_{DES}	model constant	–
c_p	specific heat capacity under constant pressure	$\mathrm{J\,kg^{-1}\,K^{-1}}$
C_S	correlation matrix	–
C_W	model constant	–
C_μ	model constant	–
$\mathcal{D}$	dissipation term	–
$\tilde{d}$	model constant	m
D	diameter	m
E	energy	J
e	unity vector	–
e	Internal energy	$\mathrm{m^2\,s^{-2}}$
E_b	energy ratio Fourier Series	–
E_λ	energy ratio POD modes	–

(Symbols continued)

f	volume forces	N
f	shape function	–
f_S	shielding function	–
F_T	Engine trust	N
G	filter function	–
H	enthalpie	J
h	specific enthalpie	$\mathrm{m^2\,s^{-2}}$
h	span height	m
h	heat transfer coefficient	$\mathrm{W\,m^{-2}\,K^{-1}}$
I	turbulent intensity	–
k	turbulent kinetic energy	$\mathrm{m^2\,s^{-2}}$
$\mathbf{k}$	wave vector	$\mathrm{m^{-1}}$
k	wave number	$\mathrm{m^{-1}}$
$\tilde{\mathcal{L}}$	length scale DES	m
L	length	m
L	length	m
$\mathcal{L}$	turbulent length scale	m
l	ranking function	–
$\mathcal{L}_0$	largest turbulent length scale	m
L_{ref}	reference length	m
$\mathcal{L}_{vK}$	von Karman length scale	m
$\dot{m}$	mass flow	$\mathrm{kg\,s^{-1}}$
Ma	Mach number	–
N	number of	–
n	lenght scale in terms of grid spacing	–
n	normal vector	–
$\mathbf{n}$	normal vector	–
n	order of discretisation scheme	–
Nu	Nusselt number	–
P	power	W
P	tensor of friction forces	Pa
p	pressure	Pa
$\mathcal{P}_k$	production of turbulent kinetic energy	$\mathrm{kg\,m^{-1}\,s^{-3}}$
Pr	Prandtl number	–
Pr_t	turbulent Prandtl number	–
$\dot{q}$	specific heat flux	$\mathrm{W\,m^{-2}}$
R	two point correlation	–
R	radius	m
r	radius	m

(Symbols continued)

$\mathbf{r}$	distance between two points	m
r	random data	–
$\mathbf{r}$	random data vector	–
r	degree of reaction	–
r	recovery factor	–
R	specific gas constant	$\mathrm{J\,kg^{-1}\,K^{-1}}$
Re	Reynolds number	–
S	strain rate tensor	$\mathrm{s^{-1}}$
S	source term	–
S	swirl number	–
s	specific entropie	$\mathrm{J\,kg^{-1}\,K^{-1}}$
T	temperature	K
t	time	s
$\mathcal{T}$	turbulent time scale	s
U'	deformation velocity	$\mathrm{s^{-1}}$
U''	curvature of velocity field	$\mathrm{m^{-1}\,s^{-1}}$
$\mathbf{U}$	snapshot matrix	–
U	rotor wheel speed	$\mathrm{m\,s^{-1}}$
$\hat{u}$	velocity amplitude	$\mathrm{m\,s^{-1}}$
u	velocity	$\mathrm{m\,s^{-1}}$
$\tilde{u}$	filtered velocity	$\mathrm{m\,s^{-1}}$
$\mathbf{u}$	velocity vector	$\mathrm{m\,s^{-1}}$
$\tilde{\mathbf{u}}$	filtered velocity vector	$\mathrm{m\,s^{-1}}$
U_{mag}	velocity magnitude	$\mathrm{m\,s^{-1}}$
V	control volume	$\mathrm{m^2}$
v	velocity in y direction	$\mathrm{m\,s^{-1}}$
V_0	aircraft flight velocity	$\mathrm{m\,s^{-1}}$
w	velocity in z direction	$\mathrm{m\,s^{-1}}$
x	coordinate	–
$\mathbf{x}$	coordinate vector	–
Y	pressure loss coefficient	–
y	coordinate normal to wall	–
y^+	non-dimensional wall distance	–
z	coordinate	–

Sub- and Superscripts

Subscripts	Description
∞	free-stream
0	before turbine stator
1	behind turbine stator
2	behind turbine rotor
3	compressor outlet
30	plane 30, combustor inlet
40	plane 40, NGV inlet
ad	adiabatic
ax	axial direction
$bypass$	bypass
ch	chord
$cool$	cooling
$core$	core
eff	effective
F	Fourier coefficients
F	filter
f	fuel
i	ith coordinate
$ideal$	idealized process
in	inlet
is	isentropic
j	jth coordinate
k	kth coordinate
kin	kinetic
l	index
m	index
mag	magnitude
max	maximum
n	index
NGV	nozzle guide vane
o	overall
out	outlet
ox	oxidiser
P	POD modes
pr	propulsive
rad	radial direction
ref	reverence
rel	relative

(Subsuper continued)

res	resolved
S	surface
S	snapshots
sgs	subgrid-scales
sim	simulation
$stoic$	stoichiometric
sw	in streamwise direktion
t	total
t	turbulent
tan	tangential direction
th	thermal
tot	total
u	circumferential direction
V	volume
W	at the wall

Superscripts	**Description**
$circ$	circumferential
k	turbulent kinetic energy
rel	relative

Acronyms

Short	**Description**
2D	Two-Dimensional
3D	Three-Dimensional
5HP	Five-Hole Probe
AI	Artificial Intelligence
BC	Boundary Conditions
BSL	Baseline
CDS	Central Differencing Scheme
CERTS	Combustor Exit Radial Temperature Simulator
CFD	Computational Fluid Dynamics
CFL	Courant-Friedrichs-Lewy
CHT	Conjugate Heat Transfer
CNN	Convolutional Neural Network
CO	Carbon Monoxide

(Abbreviations continued)

Short	Description
CO_2	Carbon Dioxide
CPU	Central Processing Unit
CR	Compression Rate
CT	Combustor-Turbine
CTI	Combustor and Turbine aerothermal Interaction
CV	Control Volume
DDES	Delayed Detached-Eddy Simulation
DES	Detached-Eddy Simulation
DMD	Dynamic Mode Decomposition
DNS	Direct Numerical Simulation
DoR	Degree of Reaction
EAR	Element Aspect Ratio
ESD	Energy Spectral Density
EVR	Element Volume Ratio
FC	Fourier Coefficient
FCE	Film Cooling Effectiveness
FEA	Finite Element Analysis
FGM	Flamlet Generated Manifold
FS	Fourier Series
FVM	Finite Volume Method
GDH	Gradient Diffusion Hyphothesis
HPC	High Pressure Compressor
HPT	High Pressure Turbine
HTC	Heat Transfer Coefficient
HWA	Hot-Wire Anemometry
ILU	Incomplete Lower-Upper
LE	Leading Edge
LES	Large Eddy Simulation
LPC	Low Pressure Compressor
LPP	Lean Premixed Prevaporized
LPT	Low Pressure Turbine
LSRR	Large Scale Rotating Rig
LSTR	Large Scale Turbine Rig
ML	Machine Learning
MLP	Multilayer Perceptron
MMS	Memory Management System
NGV	Nozzle Guide Vane
NIF	Neural Implicit Flow

(Abbreviations continued)

Short	Description
NO	Nitrogen Oxide
NO_2	Nitrogen Dioxide
NO_X	Nitrogen Oxides
OTDF	Overal Temperature Distortion Factor
OTRF	Oxford Turbine Research Facility
PCA	Principle Component Analysis
PDF	Propability Density Function
PIV	Particle Image Velocimetry
POD	Proper Orthogonal Decomposition
PODFS	Proper Orthogonal Decomposition and Fourier Series
PS	Pressure Side
RANS	Reynolds-Averaged Navier-Stokes
RIDN	Rear Inner Discharge Nozzle
RMS	Root Mean Square
RODN	Rear Outer Discharge Nozzle
RQL	Rich-burn Quick-quench Lean-burn
RST	Reynolds Stress Tensor
RTDF	Radial Temperature Distortion Factor
SA	Spalart Allmaras
SAS	Scale-Adaptive-Simulation
SBES	Stress-Blended Eddy Simulation
SFC	Specific Fuel Consumption
SGS	Subgrid-Scale
SO_2	Sulfur Dioxide
SO_3	Sulfur Trioxide
SPOD	Spectral Proper Orthogonal Decomposition
SRS	Scale-Resolving Simulation
SS	Suction Side
SST	Shear-Stress-Transport
SWL	Swirl Leading edge clocking
SWP	Swirl Passage clocking
TAPS	Twin Annular Premixing Swirler
TBC	Thermal Barrier Coatings
TE	Trailing Edge
TET	Turbine Entry Temperature
TKE	Turbulent Kinetic Energy
TRF	Turbine Research Facility
UDS	Upwind Differencing Scheme

(Abbreviations continued)

Short	Description
UHC	Unburned Hydrocarbons
UQ	Uncertainty Quantification
URANS	Unsteady Reynolds-Averaged Navier-Stokes
UTC	University Technology Centre
WALE	Wall-Adapted Local Eddy-viscosity

Bibliography

[1] ACARE. *Strategic Research and Innovation Agenda: Delivering Europe's Vision vor Aviation*. 1 edition, 2017.

[2] F. E. Ames, C. Wang, and P. A. Barbot. Measurement and prediction of the influence of catalytic and dry low nox combustor turbulence on vane surface heat transfer. *Journal of Turbomachinery*, 125(2):221–231, 2003. ISSN 0889-504X. doi: 10.1115/1.1559898.

[3] M. S. Anand, R. Eggels, M. Staufer, M. Zedda, and J. Zhu. An advanced unstructured-grid finite-volume design system for gas turbine combustion analysis. In M. Jayaraman, editor, *Proceedings of the ASME Gas Turbine India Conference - 2013*, New York, NY, 2014. ASME. ISBN 978-0-7918-5616-1. doi: 10.1115/GTINDIA2013-3537.

[4] A. Andreini, T. Bacci, L. Mazzei, and S. Salvadori. Hybrid rans-les modelling of a hot streak generator oriented to the study of combustor-turbine-interaction. *Proceedings of ASME Turbo Expo 2015*, 2015.

[5] A. Andreini, T. Bacci, L. Mazzei, and S. Salvadori. Hybrid rans-les modelling of the aero-thermal field in an annular hot streak generator for the study of combustor-turbine-interaction. *Proceedings of ASME Turbo Expo 2016*, 2016.

[6] T. Auerswald, A. Probst, and J. Bange. An anisotropic synthetic turbulence method for large-eddy simulation. *International Journal of Heat and Fluid Flow*, 62:407–422, 2016. doi: 10.1016/j.ijheatfluidflow.2016.09.002.

[7] T. Bacci, C. Koupper, and J.-L. Champion. Turbulence field measurements at the exit of a combustor simulator dedicated to hot streak generation. *Proceedings of ASME Turbo Expo 2015*, 2015.

[8] T. Bacci, R. Becchi, A. Picchi, and B. Facchini. Adiabatic effectiveness on a high pressure turbine nozzle guide vanes under realistic swirling conditions. *Proceedings of ASME Turbo Expo 2018*, 2018.

[9] T. Bacci, T. Lenzi, A. Picchi, L. Mazzei, and B. Facchini. Flow field and hot streak migration through a high pressure cooled vanes with representative lean burn combustor outflow. *Journal of Engineering for Gas Turbines and Power*, 141(4): 041020, 2019. ISSN 07424795. doi: 10.1115/1.4040714.

[10] F. Bakhtiari. *Zum aerothermalen Verhalten konventioneller Hochdruckturbinen bei instationärer Zuströmung aufgrund neuer Brennkammerkonzepte*, volume 18 of *Forschungsberichte aus dem Institut für Gasturbinen, Luft- und Raumfahrtantriebe*. Shaker, Düren, 2022. ISBN 978-3-8440-8606-5.

[11] M. D. Barringer, K. A. Thole, and M. D. Polanka. Effects of combustor exit profiles on vane aerodynamic loading and heat transfer in a high pressure turbine. *Journal of Turbomachinery*, 131(2):021008, 2009. ISSN 0889-504X. doi: 10.1115/1.2950051.

[12] M. D. Barringer, K. A. Thole, and M. D. Polanka. An experimental study of combustor exit profile shapes on endwall heat transfer in high pressure turbine vanes. *Journal of Turbomachinery*, 131(2):021009–1, 2009. ISSN 0889504X. doi: 10.1115/1.2950072.

[13] M. D. Barringer, K. A. Thole, M. D. Polanka, and P. J. Koch. Migration of combustor exit profiles through high pressure turbine vanes. *Journal of Turbomachinery*, 131 (2):021010–021011, 2009. ISSN 0889-504X.

[14] A. M. Basol, P. Jenny, M. Ibrahim, A. I. Kalfas, and R. S. Abhari. Hot streak migration in a turbine stage: Integrated design to improve aerothermal performance. *Journal of Engineering for Gas Turbines and Power*, 133(6):061901, 2011. ISSN 0742-4795.

[15] P. F. Beard, T. Povey, and K. S. Chana. Turbine efficiency measurement system for the qinetiq turbine test facility. *Journal of Turbomachinery*, 132(1):011002, 2010. ISSN 0889504X. doi: 10.1115/1.3066271.

[16] P. F. Beard, A. Smith, and T. Povey. Impact of severe temperature distortion on turbine efficiency. *Journal of Turbomachinery*, 135(1):011018, 2013. ISSN 0889504X. doi: 10.1115/1.4006389.

[17] P. F. Beard, A. D. Smith, and T. Povey. Effect of combustor swirl on transonic high pressure turbine efficiency. *Journal of Turbomachinery*, 136(1):011002, 2014. ISSN 0889504X. doi: 10.1115/1.4024841.

[18] P. F. Beard, M. G. Adams, J. R. Nagawakar, M. R. Stokes, F. Wallin, D. N. Cardwell, T. Povey, and K. S. Chana. The lemcotec 1½ stage film-cooled hp turbine: Design, integration and testing in the oxford turbine research facility. In *13th European Conference on Turbomachinery Fluid Dynamics and Thermodynamics*, European Conference on Turbomachinery Fluid Dynamics and hermodynamics. European Turbomachinery Society, 2019. doi: 10.29008/ETC2019-216.

[19] W. Bechara, C. Bailly, P. Lafon, and S. M. Candel. Stochastic approach to noise modeling for free turbulent flows. *AIAA Journal*, 32(3):455–463, 1994. ISSN 0001-1452. doi: 10.2514/3.12008.

[20] T. Behr, A. I. Kalfas, and R. S. Abhari. Unsteady flow physics and performance of a one-and-1□2-stage unshrouded high work turbine. *Journal of Turbomachinery*, 129 (2):348–359, 2007. ISSN 0889-504X. doi: 10.1115/1.2447707.

[21] N. T. Birch. 2020 vision: the prospects for large civil aircraft propulsion. *The Aeronautical Journal*, 104(1038):347–352, 2000. ISSN 0001-9240. doi: 10.1017/S0001924000063971.

[22] R. B. Bird, W. E. Stewart, and E. N. Lighfoot. *Transport phenomena*. John Wiley, New York, 1960. ISBN 0-471-07392-X.

[23] D. G. Bogard. 4.2.2.1 airfoil film cooling. In U.S. Department of Energy, editor, *The Gas Turbine Handbook*, volume 4, pages 309–321. 2006. URL `https://netl.doe.gov/carbon-management/turbines/handbook`. Accessed: 10th June 2024.

[24] J. P. Bons. St and cf augmentation for real turbine roughness with elevated freestream turbulence. In *Proceedings of the ASME Turbo Expo 2002*, pages 349–363, New York, NY, 2002. American Society of Mechanical Engineers. ISBN 0-7918-3608-8. doi: 10.1115/GT2002-30198.

[25] J. Boudet and A. Giauque. Adaptation and evaluation of a weak recycling strategy for inflow boundary layers in large-eddy simulation. *Computers & Fluids*, 203:104489, 2020. ISSN 00457930. doi: 10.1016/j.compfluid.2020.104489.

[26] G. Boudier, L. Gicquel, T. Poinsot, D. Bissières, and C. Bérat. Comparison of les, rans and experiments in an aeronautical gas turbine combustion chamber. *Proceedings of the Combustion Institute*, 31(2):3075–3082, 2007. ISSN 15407489. doi: 10.1016/j.proci.2006.07.067.

[27] J. Boussinesq. *Essai sur la théorie des eaux courantes*. Impr. nationale, 1877.

[28] W. J. G. Bräunling. *Flugzeugtriebwerke: Grundlagen, Aero-Thermodynamik, ideale und reale Kreisprozesse, Thermische Turbomaschinen, Komponenten, Emissionen und Systeme*. Springer-Verlag Berlin Heidelberg, 2009.

[29] T. L. Butler, O. P. Sharma, H. D. Joslyn, and R. P. Dring. Redistribution of an inlet temperature distortion in an axial flow turbine stage. *Journal of Propulsion and Power*, 5(1):64–71, 1989. ISSN 0748-4658. doi: 10.2514/3.23116.

[30] I. B. Celik, Z. N. Cehreli, and I. Yavuz. Index of resolution quality for large eddy simulations. *Journal of Fluids Engineering*, 127(5):949–958, 2005. ISSN 0027-0644. doi: 10.1115/1.1990201.

[31] CFX. Ansys cfx-solver theory guide. 2021.

[32] C. M. Cha, S. Hong, P. T. Ireland, P. Denman, and V. Savarianandam. Experimental and numerical investigation of combustor-turbine interaction using an isothermal, nonreacting tracer. *Journal of Engineering for Gas Turbines and Power*, 134(8):193, 2012. ISSN 0742-4795. doi: 10.1115/1.4005815.

[33] C. M. Cha, S. Hong, P. T. Ireland, P. Denman, and V. Savarianandam. Experimental and numerical investigation of combustor-turbine interaction using an isothermal, nonreacting tracer. *Journal of Engineering for Gas Turbines and Power*, 134(8):081501, 2012. ISSN 0742-4795.

[34] C. M. Cha, P. T. Ireland, P. A. Denman, and V. Savarianandam. Turbulence levels are high at the combustor-turbine interface. *Proceedings of ASME Turbo Expo 2012*, 2012.

[35] K. Chana, D. Cardwell, and T. Jones. A review of the oxford turbine research facility. In *Volume 3C: Heat Transfer*. American Society of Mechanical Engineers, 2013. ISBN 978-0-7918-5516-4. doi: 10.1115/GT2013-95687.

[36] C. Clemen, J. Daehnert, B. Wurm, K. Lehmenn, and E. Janke. Full annular combustion rig testing with high-pressure turbine nozzle guide vanes. In Deutsche Gesellschaft für Luft- und Raumfahrt - Lilienthal-Oberth e.V., editor, *Deutscher Luft- und Raumfahrtkongress*, 2017.

[37] F. Cottier, P. Pinchaud, and G. Dumas. Aerothermal predictions of combustor/turbine interactions using advanced turbulence modeling. In *13th European Conference on Turbomachinery Fluid Dynamics and Thermodynamics*, European Conference on Turbomachinery Fluid Dynamics and hermodynamics. European Turbomachinery Society, 2019. doi: 10.29008/ETC2019-050.

[38] S. Cubeda, L. Mazzei, T. Bacci, and A. Andreini. Impact of predicted combustor outlet conditions on the aerothermal performance of film-cooled high pressure turbine vanes. *Journal of Engineering for Gas Turbines and Power*, 141(5):081501, 2019. ISSN 0742-4795. doi: 10.1115/1.4041038.

[39] J. Cuxart. When can a high-resolution simulation over complex terrain be called les? *Frontiers in Earth Science*, 3, 2015. doi: 10.3389/feart.2015.00087.

[40] L. Davidson. *Fluid mechanics, turbulent flow and turbulence modeling*. Course material, Chalmers University of Technology, SE-412 96 Göteborg, Sweden, 2014.

[41] J. D. Denton. Loss mechanisms in turbomachines. In *ASME 1993 International Gas Turbine and Aeroengine Congress and Exposition*, New York, N.Y., 1993. ASME. ISBN 978-0-7918-7889-7. doi: 10.1115/93-GT-435.

[42] L. Di Mare, M. Klein, W. P. Jones, and J. Janicka. Synthetic turbulence inflow conditions for large-eddy simulation. *Physics of Fluids*, 18(2), 2006. ISSN 1070-6631. doi: 10.1063/1.2130744.

[43] J. Dombard, F. Duchaine, L. Gicquel, N. Odier, K. Leroy, N. Buffaz, S. Le-Guyader, J. Démolis, S. Richard, and T. Grosnickel. Evaluation of the capacity of rans/urans/les in predicting the performance of a high-pressure turbine: Effect of load and off design condition. In *Proceedings of the ASME Turbo Expo 2020: Turbomachinery Technical Conference and Exposition - 2020*, New York, NY and Red Hook, NY, 2020. the American Society of Mechanical Engineers and Curran Associates Inc. ISBN 978-0-7918-8408-9. doi: 10.1115/GT2020-15447.

[44] D. J. Dorney and J. R. Schwab. Unsteady numerical simulations of radial temperature profile redistribution in a single-stage turbine. *Journal of Turbomachinery*, 118(4): 783–791, 1996. ISSN 0889-504X. doi: 10.1115/1.2840934.

[45] K. Dube. Emerging from the covid-19 pandemic: Aviation recovery, challenges and opportunities. *Aerospace*, 10(1):19, 2023. doi: 10.3390/aerospace10010019.

[46] F. Duchaine, J. Dombard, L. Gicquel, and C. Koupper. On the importance of inlet boundary conditions for aerothermal predictions of turbine stages with large eddy simulation. *Computers & Fluids*, 154(1):60–73, 2017. ISSN 00457930. doi: 10.1016/j.compfluid.2017.05.024.

[47] F. Ducros, F. Nicoud, and T. Poinsot. Wall-adapting local eddy-viscosity models for simulations in complex geometries. *Numerical Methods for Fluid Dynamics VI*, 1998.

[48] J. Faber. *Lower NOx at Higher Altitudes: Policies to Reduce the Climate Impact of Aviation NOx Emission*. 2008.

[49] S. Farokhi. *Aircraft Propulsion*. New York Academy of Sciences Series. John Wiley & Sons Incorporated, Newark, 1st ed. edition, 2014. ISBN 9781118806753.

[50] J. H. Ferziger and M. Perić. *Computational methods for fluid dynamics*. Springer, Berlin and Heidelberg and New York, 3rd, rev. ed. edition, 2002. ISBN 3-540-42074-6.

[51] M. Folk, R. J. Miller, and J. D. Coull. The impact of combustor turbulence on turbine loss mechanisms. *Journal of Turbomachinery*, 142(9), 2020. ISSN 0889-504X. doi: 10.1115/1.4047615.

[52] K. Fukami, Y. Nabae, K. Kawai, and K. Fukagata. Synthetic turbulent inflow generator using machine learning. *Physical Review Fluids*, 4(6), 2019. doi: 10.1103/PhysRevFluids.4.064603.

[53] A. Garai, S. M. Murman, and D. Ekelschot. A new recycling method to generate turbulent inflow profiles. In *AIAA Aviation 2019 Forum*, Reston, Virginia, 06172019. American Institute of Aeronautics and Astronautics. ISBN 978-1-62410-589-0. doi: 10.2514/6.2019-3420.

[54] German Aviation Association. Report on the first half year 2020: On the state of the german aviation industry (zur lage der deutschen luftverkehrswirtschaft). URL `https://www.bdl.aero/wp-content/uploads/2020/08/Halbjahreszahlen-2020.pdf`. Accessed: 10th June 2024.

[55] A. S. Ghate, A. Towne, and S. K. Lele. Broadband reconstruction of inhomogeneous turbulence using spectral proper orthogonal decomposition and gabor modes. *Journal of Fluid Mechanics*, 888, 2020. ISSN 0022-1120. doi: 10.1017/jfm.2020.78.

[56] L. Giller and H.-P. Schiffer. Interactions between the combustor swirl and the high pressure stator of a turbine. In *Proceedings of the ASME Turbo Expo 2012*, pages 1401–1415, New York, N.Y, 2012. ASME. ISBN 978-0-7918-4474-8. doi: 10.1115/GT2012-69157.

[57] R. J. Goldstein and R. A. Spores. Turbulent transport on the endwall in the region between adjacent turbine blades. *Journal of Heat Transfer*, 110(4a):862–869, 1988. ISSN 0022-1481. doi: 10.1115/1.3250586.

[58] D. Griffini, M. Insinna, S. Salvadori, and F. Martelli. Clocking effects of inlet nonuniformities in a fully cooled high-pressure vane: A conjugate heat transfer analysis. *Journal of Turbomachinery*, 138(2):021006, 2016. ISSN 0889504X. doi: 10.1115/1.4031864.

[59] M. S. Gritskevich, A. V. Garbaruk, J. Schütze, and F. R. Menter. Development of ddes and iddes formulations for the k-omega shear stress transport model. *Flow, Turbulence and Combustion*, 88(3):431–449, 2012. ISSN 1386-6184. doi: 10.1007/s10494-011-9378-4.

[60] J. Gründler, H.-P. Schiffer, and K. Lehmann. An efficient unsteady 1-way coupling method of combustor and turbine. *Proceedings of ASME Turbo Expo 2022*, 2022. doi: 10.1115/GT2022-78056.

[61] J. Gründler, K. Lehmann, and H.-P. Schiffer. The effect of unsteady inlet boundary conditions on the aero-thermal behavior of high-pressure turbine vanes – a numerical study using scale-resolving simulations. *Journal of Turbomachinery*, 147(1), 2024. ISSN 0889-504X. doi: 10.1115/1.4065858.

[62] K. Gundy-Burlet and D. Dorney. Three-dimensional simulations of hot streak clocking in a 1-1/2 stage turbine. In *32nd Joint Propulsion Conference and Exhibit*, Reston,

Virigina, 1996. American Institute of Aeronautics and Astronautics. doi: 10.2514/6.1996-2791.

[63] B. F. Hall and T. Povey. Experimental study of non-reacting low nox combustor simulator for scaled turbine experiments. In *Proceedings of the ASME Turbo Expo: Turbine Technical Conference and Exposition - 2015*, New York, NY, 2015. ASME. ISBN 978-0-7918-5669-7. doi: 10.1115/GT2015-43530.

[64] B. F. Hall, K. S. Chana, and T. Povey. Design of a nonreacting combustor simulator with swirl and temperature distortion with experimental validation. *Journal of Engineering for Gas Turbines and Power*, 136(8):031009, 2014. ISSN 0742-4795. doi: 10.1115/1.4026809.

[65] J.-C. Han, S. Dutta, and S. Ekkad. *Gas turbine heat transfer and cooling technology*. CRC Press, Boca Raton, Fla., 2nd ed. edition, 2013. ISBN 9781439855683.

[66] J. Hartsel. Prediction of effects of mass-transfer cooling on the blade-row efficiency of turbine airfoils. In *10th Aerospace Sciences Meeting*, Reston, Virigina, 1972. American Institute of Aeronautics and Astronautics. doi: 10.2514/6.1972-11.

[67] F. Haselbach, A. Newby, and R. Parker. Next generation of large civil aircraft engines-concepts & technologies. In *11th European Conference on Turbomachinery Fluid dynamics & Thermodynamics*, 2015.

[68] W. R. Hawthorne. Rotational flow through cascades part i. the components of vorticity. *The Quarterly Journal of Mechanics and Applied Mathematics*, 8(3):266–279, 1955. ISSN 0033-5614.

[69] L. He, V. Menshikova, and B. R. Haller. Influence of hot streak circumferential length-scale in transonic turbine stage. *Proceedings of ASME Turbo Expo 2004*, pages 1117–1126, 2004. doi: 10.1115/GT2004-53370.

[70] L. He, V. Menshikova, and B. R. Haller. Effect of hot-streak counts on turbine blade heat load and forcing. *Journal of Propulsion and Power*, 23(6):1235–1241, 2007. ISSN 0748-4658.

[71] J. Hilgert. *A pragmatic method for matching conjugate heat transfer predictions of high-pessure trbine blades with termal paint tests: Dissertation*, volume Band 16 of *Forschungsberichte aus dem Institut für Gasturbinen, Luft- und Raumfahrtantriebe*. Shaker, Düren, 2021. ISBN 978-3-8440-8098-8.

[72] J. Hilgert, M. Bruschewski, H. Werschnik, and H.-P. Schiffer. Numerical studies on combustor-turbine-interaction at the large scale turbine rig (lstr). *Proceedings of ASME Turbo Expo 2017*, 2017.

[73] C. Hirsch. *Numerical computation of internal and external flows*. Elsevier Butterworth-Heinemann, Amsterdam and Heidelberg, 2. ed., transferred to digit. print edition, 2010. ISBN 978-0-7506-6594-0.

[74] IATA. Industry statistics, 2023. URL https://www.iata.org/en/iata-repository/pressroom/fact-sheets/industry-statistics/. Accessed: 10th June 2024.

[75] IEA. World air passenger traffic evolution, 1980-2020, 2020. URL https://www.iea.org/data-and-statistics/charts/world-air-passenger-traffic-evolution-1980-2020. Accessed: 10th June 2024.

[76] M. Insinna, D. Griffini, S. Salvadori, and F. Martelli. Conjugate heat transfer analysis of a film cooled high-pressure turbine vane under realistic combustor exit flow conditions. In H. Hodson, editor, *Proceedings of the ASME Turbo Expo: Turbine Technical Conference and Exposition - 2014*, New York, NY, 2014. ASME. ISBN 978-0-7918-4571-4. doi: 10.1115/GT2014-25280.

[77] M. Insinna, D. Griffini, S. Salvadori, and F. Martelli. Effects of realistic inflow conditions on the aero-thermal performance of a film-cooled vane. In *11th European Conference on Turbomachinery Fluid dynamics & Thermodynamics*, 2015.

[78] S. Jacobi and B. Rosic. Development and aerothermal investigation of integrated combustor vane concept. *Journal of Turbomachinery*, 138(1), 2016. ISSN 0889-504X. doi: 10.1115/1.4031560.

[79] N. Jarrin, S. Benhamadouche, D. Laurence, and R. Prosser. A synthetic-eddy-method for generating inflow conditions for large-eddy simulations. *International Journal of Heat and Fluid Flow*, 27(4):585–593, 2006. doi: 10.1016/j.ijheatfluidflow.2006.02.006.

[80] S. Jenkins, K. Varadarajan, and D. G. Bogard. The effects of high mainstream turbulence and turbine vane film cooling on the dispersion of a simulated hot streak. *Journal of Turbomachinery*, 126(1):203, 2004. ISSN 0889504X. doi: 10.1115/1.1643911.

[81] S. C. Jenkins and D. G. Bogard. The effects of the vane and mainstream turbulence level on hot streak attenuation. *Journal of Turbomachinery*, 127(1):215, 2005. ISSN 0889504X. doi: 10.1115/1.1812777.

[82] G. Jiang, R. Yoshie, T. Shirasawa, and X. Jin. Inflow turbulence generation for large eddy simulation in non-isothermal boundary layers. *Journal of Wind Engineering and Industrial Aerodynamics*, 104-106:369–378, 2012. ISSN 01676105. doi: 10.1016/j.jweia.2012.02.030.

[83] F. Joos. *Technische Verbrennung: Verbrennungstechnik, Verbrennungsmodellierung, Emissionen*. SpringerLink Bücher. Springer Berlin Heidelberg, Berlin, Heidelberg, 2006. ISBN 9783540343349. doi: 10.1007/3-540-34334-2.

[84] S. Kallas, M. Geoghegan-Quinn, M. Darecki, C. Edelstenne, T. Enders, E. Fernandez, and P. Hartman. *Flightplan 2050: Europe's vision for aviation; maintaining global leadership and serving society's needs; report of the high-level group on aviation research*. policy. Publ. Off. of the Europ. Union, Luxembourg, 2011. ISBN 978-92-79-19724-6. doi: 10.2777/50266.

[85] B. Khanal, L. He, J. Northall, and P. Adami. Analysis of radial migration of hot-streak in swirling flow through high-pressure turbine stage. *Journal of Turbomachinery*, 135(4):041005, 2013. ISSN 0889-504X.

[86] E. V. Klapdor, S. Pyliouras, R. L. Eggels, and J. Janicka. Towards investigation of combustor turbine interaction in an integrated simulation. *ASME Turbo Expo 2010: Power for Land, Sea, and Air*, pages 2769–2780, 2010.

[87] M. Klein, A. Sadiki, and J. Janicka. A digital filter based generation of inflow data for spatially developing direct numerical or large eddy simulations. *Journal of Computational Physics*, 186(2):652–665, 2003. ISSN 00219991. doi: 10.1016/S0021-9991(03)00090-1.

[88] A. N. Kolmogorov. The local structure of turbulence in incompressible viscous fluid for very large reynolds numbers. *Proceedings of the Royal Society of London. Series A: Mathematical and Physical Sciences*, 434(1890):9–13, 1991. ISSN 0962-8444. doi: 10.1098/rspa.1991.0075.

[89] J. Kostas, J. Soria, and M. S. Chong. A comparison between snapshot pod analysis of piv velocity and vorticity data. *Experiments in Fluids*, 38(2):146–160, 2005. ISSN 0723-4864. doi: 10.1007/s00348-004-0873-4.

[90] C. Koupper, G. Caciolli, L. Gicquel, F. Duchaine, G. Bonneau, L. Tarchi, and B. Facchini. Development of an engine representative combustor simulator dedicated to hot streak generation. *Journal of Turbomachinery*, 136(11), 2014. ISSN 0889-504X. doi: 10.1115/1.4028175.

[91] C. Koupper, G. Bonneau, L. Gicquel, and F. Duchaine. Large eddy simulations of the combustor turbine interface: Study of the potential and clocking effects. In *Proceedings of the ASME Turbo Expo: Turbine Technical Conference and Exposition - 2016*, New York, N.Y., 2016. the American Society of Mechanical Engineers. ISBN 978-0-7918-4979-8. doi: 10.1115/GT2016-56443.

[92] R. H. Kraichnan. Diffusion by a random velocity field. *The Physics of Fluids*, 13(1): 22–31, 1970. ISSN 0031-9171. doi: 10.1063/1.1692799.

[93] A. Krichbaum, H. Werschnik, M. Wilhelm, H.-P. Schiffer, and K. Lehmann. A large scale turbine test rig for the investigation of high pressure turbine aerodynamics and heat transfer with variable inflow conditions. In *Volume 2A: Turbomachinery*. American Society of Mechanical Engineers, 2015. ISBN 978-0-7918-5663-5. doi: 10.1115/GT2015-43261.

[94] H. Kröger and N. Kornev. Generation of divergence free synthetic inflow turbulence with arbitrary anisotropy. *Computers & Fluids*, 165:78–88, 2018. ISSN 00457930. doi: 10.1016/j.compfluid.2018.01.018.

[95] B. Lakshminarayana. *Fluid dynamics and heat transfer of turbomachinery*. Wiley, New York, 1995. ISBN 0-471-85546-4.

[96] F. R. Larson and J. Miller. A time-temperature relationship for rupture and creep stresses. *Journal of Fluids Engineering*, 74(5):765–771, 1952. ISSN 0027-0644. doi: 10.1115/1.4015909.

[97] B. E. Launder and B. I. Sharma. Application of the energy-dissipation model of turbulence to the calculation of flow near a spinning disc. *Letters in Heat and Mass Transfer*, 1(2):131–137, 1974. ISSN 00944548. doi: 10.1016/0094-4548(74)90150-7.

[98] W. Lazik, T. Doerr, S. Bake, R. v. d. Bank, and L. Rackwitz. Development of lean-burn low-nox combustion technology at rolls-royce deutschland. *Proceedings of ASME Turbo Expo 2008*, pages 797–807, 2008. doi: 10.1115/GT2008-51115.

[99] C. Lechner and J. Seume, editors. *Stationäre Gasturbinen*. VDI-Buch. Springer Berlin Heidelberg, Berlin, Heidelberg, 3. aufl. 2019 edition, 2018. ISBN 978-3-662-56133-1.

[100] D. S. Lee, G. Pitari, V. Grewe, K. Gierens, J. E. Penner, A. Petzold, M. J. Prather, U. Schumann, A. Bais, T. Berntsen, D. Iachetti, L. L. Lim, and R. Sausen. Transport impacts on atmosphere and climate: Aviation. *Atmospheric environment (Oxford, England : 1994)*, 44(37):4678–4734, 2010. ISSN 1352-2310. doi: 10.1016/j.atmosenv.2009.06.005.

[101] S. Lee, S. K. Lele, and P. Moin. Simulation of spatially evolving turbulence and the applicability of taylor's hypothesis in compressible flow. *Physics of Fluids A: Fluid Dynamics*, 4(7):1521–1530, 1992. ISSN 0899-8213. doi: 10.1063/1.858425.

[102] J. Ling, K. J. Ryan, J. Bodart, and J. K. Eaton. Analysis of turbulent scalar flux models for a discrete hole film cooling flow. *Journal of Turbomachinery*, 138(1), 2016. ISSN 0889-504X. doi: 10.1115/1.4031698.

[103] C.-L. Liu, H.-R. Zhu, and J.-T. Bai. Effect of turbulent prandtl number on the computation of film-cooling effectiveness. *International Journal of Heat and Mass Transfer*, 51(25-26):6208–6218, 2008. ISSN 0017-9310. doi: 10.1016/j.ijheatmasstransfer.2008.04.039.

[104] J. L. Lumley. *Stochastic tools in turbulence*. Dover, Mineaola, NY, dover ed., republication edition, 2007. ISBN 978-0-486-46270-7.

[105] T. S. Lund, X. Wu, and K. D. Squires. Generation of turbulent inflow data for spatially-developing boundary layer simulations. *Journal of Computational Physics*, 140(2):233–258, 1998. ISSN 00219991. doi: 10.1006/jcph.1998.5882.

[106] R. Maffulli and L. He. Wall temperature effects on heat transfer coefficient for high-pressure turbines. *Journal of Propulsion and Power*, 30(4):1080–1090, 2014. ISSN 0748-4658. doi: 10.2514/1.B35126.

[107] S. Mank, L. Duerrwaechter, M. Hilfer, R. Williams, S. Hogg, and G. Ingram. Secondary flows and fillet radii in a linear turbine cascade. In H. Hodson, editor, *Proceedings of the ASME Turbo Expo: Turbine Technical Conference and Exposition - 2014*, New York, NY, 2014. ASME. ISBN 978-0-7918-4562-2. doi: 10.1115/GT2014-25458.

[108] B. Martin, F. Duchaine, L. Gicquel, and N. Odier. Generation of realistic boundary conditions at the combustion chamber/turbine interface using large-eddy simulation. *Energies*, 14(24):8206, 2021. doi: 10.3390/en14248206.

[109] B. Martin, F. Duchaine, L. Gicquel, N. Odier, and J. Dombard. Accurate inlet boundary conditions to capture combustion chamber and turbine coupling with large-eddy simulation. *Journal of Engineering for Gas Turbines and Power*, 144(2), 2022. ISSN 0742-4795. doi: 10.1115/1.4052099.

[110] M. Masiol and R. M. Harrison. Aircraft engine exhaust emissions and other airport-related contributions to ambient air pollution: A review. *Atmospheric environment (Oxford, England : 1994)*, 95:409–455, 2014. ISSN 1352-2310. doi: 10.1016/j.atmosenv.2014.05.070.

[111] R. M. Mathison, C. W. Haldeman, and M. G. Dunn. Aerodynamics and heat transfer for a cooled one and one-half stage high-pressure turbine—part i: Vane inlet temperature profile generation and migration. *Journal of Turbomachinery*, 134(1), 2012. ISSN 0889-504X. doi: 10.1115/1.4002994.

[112] J. J. McGuirk. The aerodynamic challenges of aeroengine gas-turbine combustion systems. *The Aeronautical Journal*, 118(1204):557–599, 2014. ISSN 0001-9240. doi: 10.1017/S0001924000009386.

[113] F. Menter. Zonal two equation k-w turbulence models for aerodynamic flows. In *23rd Fluid Dynamics, Plasmadynamics, and Lasers Conference*, Reston, Virigina, 1993. American Institute of Aeronautics and Astronautics. doi: 10.2514/6.1993-2906.

[114] F. Menter. Stress-blended eddy simulation (sbes)—a new paradigm in hybrid rans-les modeling. In Y. Hoarau, S.-H. Peng, D. Schwamborn, and A. Revell, editors, *Progress in Hybrid RANS-LES Modelling*, volume 137 of *Notes on Numerical Fluid Mechanics and Multidisciplinary Design*, pages 27–37. Springer International Publishing, Cham, 2018. ISBN 978-3-319-70030-4. doi: 10.1007/978-3-319-70031-1{\textunderscore}3.

[115] F. R. Menter. Two-equation eddy-viscosity turbulence models for engineering applications. *AIAA Journal*, 32(8):1598–1605, 1994. ISSN 0001-1452. doi: 10.2514/3.12149.

[116] F. R. Menter. Best practice: Scale-resolving simulations in ansys cfd: Version 2.00, 2015.

[117] F. R. Menter and Y. Egorov. Revisiting the turbulent scale equation. In G. E. A. Meier, K. R. Sreenivasan, and H.-J. Heinemann, editors, *IUTAM Symposium on One Hundred Years of Boundary Layer Research*, pages 279–290, Dordrecht, 2006. Springer Netherlands. ISBN 978-1-4020-4150-1.

[118] F. R. Menter and Y. Egorov. The scale-adaptive simulation method for unsteady turbulent flow predictions. part 1: Theory and model description. *Flow, Turbulence and Combustion*, 85(1):113–138, 2010. ISSN 1386-6184. doi: 10.1007/s10494-010-9264-5.

[119] F. R. Menter and M. Kuntz. Adaptation of eddy-viscosity turbulence models to unsteady separated flow behind vehicles. In F. Pfeiffer, P. Wriggers, R. McCallen, F. Browand, and J. Ross, editors, *The Aerodynamics of Heavy Vehicles: Trucks, Buses, and Trains*, volume 19 of *Lecture Notes in Applied and Computational Mechanics*, pages 339–352. Springer Berlin Heidelberg, Berlin, Heidelberg, 2004. ISBN 978-3-642-53586-4. doi: 10.1007/978-3-540-44419-0{\textunderscore}30.

[120] D. E. Metzger, H. J. Carper, and L. R. Swank. Heat transfer with film cooling near nontangential injection slots. *Journal of Engineering for Power*, 90(2):157–162, 1968. ISSN 0022-0825. doi: 10.1115/1.3609155.

[121] K. Miki, A. Ameri, T. Wey, J. P. Moder, and M. Celestina. Combustor-turbine interactions by using the open national combustion code (openncc) and the glenn-ht code. In *AIAA AVIATION 2023 Forum*, Reston, Virginia, 2023. American Institute of Aeronautics and Astronautics. ISBN 978-1-62410-704-7. doi: 10.2514/6.2023-3975.

[122] R. J. Moffat. What's new in convective heat transfer? *International Journal of Heat and Fluid Flow 19*, 1998.

[123] F. Montomoli, A. D'Ammaro, and S. Uchida. Uncertainty quantification and conjugate heat transfer: A stochastic analysis. *Journal of Turbomachinery*, 135(3), 2013. ISSN 0889-504X. doi: 10.1115/1.4007516.

[124] S. A. Mosier and R. M. Pierce. *Advanced combustion systems for stationary gas turbine engines: Vol. 1 – review and preliminary evaluation. Technical report*, volume Report No. EPA-600/7-80-0171. 1980.

[125] S. Nasir, J. S. Carullo, W.-F. Ng, K. A. Thole, H. Wu, L. J. Zhang, and H. K. Moon. Effects of large scale high freestream turbulence and exit reynolds number on turbine vane heat transfer in a transonic cascade. *Journal of Turbomachinery*, 131(2), 2009. ISSN 0889-504X. doi: 10.1115/1.2952381.

[126] G. C. Oates, editor. *Aerothermodynamics of aircraft engine components*, volume 3 of *AIAA Education Series*. New York, N. Y., 1985. ISBN 0-915928-97-3.

[127] J. Ong and R. J. Miller. Hot streak and vane coolant migration in a downstream rotor. *Journal of Turbomachinery*, 134(5):051002, 2012. ISSN 0889504X. doi: 10.1115/1.4003832.

[128] J. Ong, R. J. Miller, and J. D. Denton. The prediction of hot streak migration in a high pressure turbine. *The 12th International Symposium on Transport Phenomena and*, 2008.

[129] T. Ostrowski. *The Aero-Thermal Impact of Rim Seal Purge Flow in Axial Turbines*. PhD thesis, TU Darmstadt, 2023.

[130] M. Pamiès, P.-É. Weiss, E. Garnier, S. Deck, and P. Sagaut. Generation of synthetic turbulent inflow data for large eddy simulation of spatially evolving wall-bounded flows. *Physics of Fluids*, 21(4), 2009. ISSN 1070-6631. doi: 10.1063/1.3103881.

[131] S. Pan, S. L. Brunton, and J. N. Kutz. Neural implicit flow: a mesh-agnostic dimensionality reduction paradigm of spatio-temporal data. URL `http://arxiv.org/pdf/2204.03216.pdf`. Accessed: 10th June 2024.

[132] C. Picard and J. Delville. Pressure velocity coupling in a subsonic round jet. *International Journal of Heat and Fluid Flow*, 21(3):359–364, 2000. doi: 10.1016/S0142-727X(00)00021-7.

[133] T. Poehler, J. Niewoehner, P. Jeschke, and Y. Guendogdu. Investigation of nonaxisymmetric endwall contouring and three-dimensional airfoil design in a 1.5-stage axial turbine—part i: Design and novel numerical analysis method. *Journal of Turbomachinery*, 137(8), 2015. ISSN 0889-504X. doi: 10.1115/1.4029476.

[134] S. B. Pope. *Turbulent Flows*. Cambridge University Press, Cambridge, 1. edition, 2000.

[135] T. Povey and I. Qureshi. Developments in hot-streak simulators for turbine testing. *Journal of Turbomachinery*, 131(3), 2009. ISSN 0889-504X. doi: 10.1115/1.2987240.

[136] S. Pyliouras, H.-P. Schiffer, E. Janke, and L. Willer. Effects of non-uniform combustor exit flow on turbine aerodynamics. In *Proceedings of the ASME Turbo Expo 2012*, pages 1691–1701, New York, N.Y, 2012. ASME. ISBN 978-0-7918-4474-8. doi: 10.1115/GT2012-69327.

[137] I. Qureshi, A. Beretta, K. Chana, and T. Povey. Effect of aggressive inlet swirl on heat transfer and aerodynamics in an unshrouded transonic hp turbine. *Journal of Turbomachinery*, 134(6):061023, 2012. ISSN 0889504X. doi: 10.1115/1.4004876.

[138] I. Qureshi, A. D. Smith, K. S. Chana, and T. Povey. Effect of temperature nonuniformity on heat transfer in an unshrouded transonic hp turbine: An experimental and computational investigation. *Journal of Turbomachinery*, 134(1):011005, 2012. ISSN 0889504X. doi: 10.1115/1.4002987.

[139] I. Qureshi, A. D. Smith, and T. Povey. Hp vane aerodynamics and heat transfer in the presence of aggressive inlet swirl. *Journal of Turbomachinery*, 135(2):021040, 2013. ISSN 0889-504X. doi: 10.1115/1.4006610.

[140] R. W. Radomsky and K. A. Thole. Detailed boundary layer measurements on a turbine stator vane at elevated freestream turbulence levels. *Journal of Turbomachinery*, 124 (1):107–118, 2002. ISSN 0889-504X. doi: 10.1115/1.1424891.

[141] F. Raynaud, L. R. Eggels, M. Staufer, A. Sadiki, and J. Janicka. Towards unsteady simulation of combustor-turbine interaction using an integrated approach. *Proceedings of ASME Turbo Expo*, (GT2015-42110), 2015.

[142] H.-J. Rehder, A. Pahs, M. Bittner, and F. Kocian. Next generation turbine testing at dlr. In *Volume 2A: Turbomachinery*. American Society of Mechanical Engineers, 2017. ISBN 978-0-7918-5078-7. doi: 10.1115/GT2017-64409.

[143] H. Rick. *Gasturbinen und Flugantriebe*. Springer Berlin Heidelberg, Berlin, Heidelberg, 2013. ISBN 978-3-540-79445-5. doi: 10.1007/978-3-540-79446-2.

[144] J. C. Rotta. Über eine methode zur berechnung turbulenter scherströmungsfelder. *ZAMM - Journal of Applied Mathematics and Mechanics / Zeitschrift für Angewandte Mathematik und Mechanik*, 50(1-4):204–205, 1970. ISSN 00442267. doi: 10.1002/zamm.19700500199.

[145] P. Sagaut. *Large Eddy Simulation for Incompressible Flows: An Introduction*. Scientific Computation Ser. Springer Berlin / Heidelberg, Berlin, Heidelberg, 3rd ed. edition, 2006. ISBN 978-3-540-26344-9.

[146] P. Sagaut, E. Garnier, E. Tromeur, L. Larcheveque, and E. Labourasse. Turbulent inflow conditions for large-eddy-simulation of compressible wall-bounded flows. *AIAA Journal*, 42(3):469–477, 2004. ISSN 0001-1452. doi: 10.2514/1.3461.

[147] S. Salvadori, F. Montomoli, F. Martelli, P. Adami, K. S. Chana, and L. Castillon. Aerothermal study of the unsteady flow field in a transonic gas turbine with inlet temperature distortions. *Journal of Turbomachinery*, 133(3):031030, 2011. ISSN 0889504X. doi: 10.1115/1.4002421.

[148] N. D. Sandham, Y. F. Yao, and A. A. Lawal. Large-eddy simulation of transonic turbulent flow over a bump. *International Journal of Heat and Fluid Flow*, 24(4): 584–595, 2003. doi: 10.1016/S0142-727X(03)00052-3.

[149] M. Schäfer. *Computational Engineering – Introduction to Numerical Methods*. Springer-Verlag Berlin Heidelberg, Berlin, Heidelberg, 2006. ISBN 978-3-540-30685-6.

[150] H. Schlichting and K. Gersten. *Grenzschicht-Theorie*. Springer, Heidelberg, 10. überarbeitete auflage edition, 2006. ISBN 9783540329855.

[151] G. Schmid. *Effects of combustor exit flow on turbine performance and endwall heat transfer: Zugl.: Darmstadt, Techn. Univ., Diss., 2014*, volume 2 of *Forschungsberichte aus dem Institut für Gasturbinen, Luft- und Raumfahrtantriebe*. Shaker, Aachen, 2015. ISBN 384403773X.

[152] G. Schmid and H.-P. Schiffer. Numerical investigation of inlet swirl in a turbine cascade. In *Proceedings of the ASME Turbo Expo 2012*, pages 543–552, New York, N.Y, 2012. ASME. ISBN 978-0-7918-4470-0. doi: 10.1115/GT2012-69397.

[153] G. Schmid, A. Kirchbaum, H. Werschnik, and H.-P. Schiffer. The impact of realistic inlet swirl in a 1 1/2 stage axial turbine. *Proceedings of ASME Turbo Expo 2014*, 2014.

[154] P. J. Schmid. Dynamic mode decomposition of numerical and experimental data. *Journal of Fluid Mechanics*, 656:5–28, 2010. ISSN 0022-1120. doi: 10.1017/s0022112010001217.

[155] O. T. Schmidt and T. Colonius. Guide to spectral proper orthogonal decomposition. *AIAA Journal*, 58(3):1023–1033, 2020. ISSN 0001-1452. doi: 10.2514/1.J058809.

[156] S. Schmidt and M. Breuer. Source term based synthetic turbulence inflow generator for eddy-resolving predictions of an airfoil flow including a laminar separation bubble. *Computers & Fluids*, 146:1–22, 2017. ISSN 00457930. doi: 10.1016/j.compfluid.2016.12.023.

[157] F. G. Schmitt. About boussinesq's turbulent viscosity hypothesis: historical remarks and a direct evaluation of its validity. *Comptes Rendus Mécanique*, 335(9-10):617–627, 2007. ISSN 16310721. doi: 10.1016/j.crme.2007.08.004.

[158] M. Schneider. *Robust aero-thermal design of high pressure turbines at uncertain exit conditions of low-emission combustion systems: Dissertation*, volume 13 of *Forschungsberichte aus dem Institut für Gasturbinen, Luft- und Raumfahrtantriebe*. Shaker, Düren, 2019. ISBN 978-3-8440-6934-1.

[159] M. Schneider, H.-P. Schiffer, and K. Lehmann. Uncertainty propagation analyses of lean burn combustor exit conditions for a robust nozzle cooling design. *Journal of Turbomachinery*, 142(5):1, 2020. ISSN 0889-504X. doi: 10.1115/1.4046421.

[160] M. Schroll, U. Doll, G. Stockhausen, U. Meier, C. Willert, C. Hassa, and I. Bagchi. Flow field characterization at the outlet of a lean burn single-sector combustor by laser-optical methods. *Journal of Engineering for Gas Turbines and Power*, 139(1), 2017. ISSN 0742-4795. doi: 10.1115/1.4034040.

[161] S. Shahpar and S. Caloni. Aerodynamic optimisation of high pressure turbines for lean-burn combustion system. *Proceedings of ASME Turbo Expo 2012*, page 2173, 2012. doi: 10.1115/GT2012-69228.

[162] F. Shaikh and B. Rosic. Unsteady phenomena at the combustor-turbine interface. Proceedings of Global Power & Propulsion Society. GPPS, 2020. doi: 10.33737/gpps20-tc-150.

[163] T. Shang and A. H. Epstein. Analysis of hot streak effects on turbine rotor heat load. *Journal of Turbomachinery*, 119(3):544–553, 1997. ISSN 0889-504X. doi: 10.1115/1.2841156.

[164] T. I.-P. Shih and Y.-L. Lin. Controlling secondary-flow structure by leading-edge airfoil fillet and inlet swirl to reduce aerodynamic loss and surface heat transfer. *Journal of Turbomachinery*, 125(1):48–56, 2003. ISSN 0889-504X. doi: 10.1115/1.1518503.

[165] G. Shouting and L. Ting. Streamwise vorticity equation. *Advances in Atmospheric Sciences*, 17(3):339–347, 2000. ISSN 1861-9533. doi: 10.1007/s00376-000-0027-4.

[166] M. Sieber, C. O. Paschereit, and K. Oberleithner. Spectral proper orthogonal decomposition. *Journal of Fluid Mechanics*, 792:798–828, 2016. ISSN 0022-1120. doi: 10.1017/jfm.2016.103.

[167] C. H. Sieverding. Recent progress in the understanding of basic aspects of secondary flows in turbine blade passages. *Journal of Engineering for Gas Turbines and Power*, 107(2):248–257, 1985. ISSN 0742-4795. doi: 10.1115/1.3239704.

[168] L. Sirovich. Turbulence and dynamics of coherent structures. i. coherent structures. In *Quarterly of applied mathematics 1987*, volume 45 (3), pages 561–571.

[169] P. R. Spalart and S. Allmaras. A one-equation turbulence model for aerodynamic flows. In *30th Aerospace Sciences Meeting and Exhibit*, Reston, Virigina, 1992. American Institute of Aeronautics and Astronautics. doi: 10.2514/6.1992-439.

[170] P. R. Spalart and A. Leonard. Direct numerical simulation of equilibrium turbulent boundary layers. In *5th Symposium on Turbulent Shear Flows*, pages 9.35–9.40, 1985.

[171] P. R. Spalart, W.-H. Jou, M. Strelets, and S. R. Allmaras. Comments on the feasibility of les for wings, and on a hybrid rans/les approach. *Advances in DNS/LES, C. Liu & Z. Liu Eds.*, 1997.

[172] J. Spurk and N. Aksel. *Strömungslehre*. Springer Berlin Heidelberg, Berlin, Heidelberg, 2010. ISBN 978-3-642-13142-4. doi: 10.1007/978-3-642-13143-1.

[173] P. Stephan, L. Schaber, K. Stephan, and F. Mayinger. *Thermodynamik: Grundlagen und technische Anwendungen*. Springer-Lehrbuch. Springer, Berlin, 17. aufl. edition, 2007. ISBN 978-3-540-70813-1.

[174] R. Stickles. *TAPS II Technology Final Report – Technology Assessment Open Report*. FAA, 2013.

[175] M. Strelets. Detached eddy simulation of massively separated flows. In *39th Aerospace Sciences Meeting and Exhibit*, Reston, Virigina, 2001. American Institute of Aeronautics and Astronautics. doi: 10.2514/6.2001-879.

[176] P. Subbareddy, D. Peterson, G. Candler, and I. Marusic. A synthetic inflow generation method using the attached eddy hypothesis. In *24th AIAA Applied Aerodynamics Conference*, Reston, Virigina, 2006. American Institute of Aeronautics and Astronautics. ISBN 978-1-62410-028-4. doi: 10.2514/6.2006-3672.

[177] X. Sun, S. Wandelt, and A. Zhang. A data-driven analysis of the aviation recovery from the covid-19 pandemic. *Journal of air transport management*, 109:102401, 2023. doi: 10.1016/j.jairtraman.2023.102401.

[178] A. Suresh, D. C. Hofer, and V. E. Tangirala. Turbine efficiency for unsteady, periodic flows. *Journal of Turbomachinery*, 134(3), 2012. ISSN 0889-504X. doi: 10.1115/1.4003246.

[179] G. R. Tabor and M. H. Baba-Ahmadi. Inlet conditions for large eddy simulation: A review. *Computers & Fluids*, 39(4):553–567, 2010. ISSN 00457930. doi: 10.1016/j.compfluid.2009.10.007.

[180] J. A. Tallman. Unsteady half-annulus computational fluid dynamics calculations of thermal migration through a cooled 2.5 stage high-pressure turbine. *Journal of Turbomachinery*, 136(8), 2014. ISSN 0889-504X. doi: 10.1115/1.4026507.

[181] S. G. Tomasello, A. Andreini, R. Meloni, S. Cubeda, Andreini, L, A., and V. Michelassi. Numerical study of combustor-turbineinteraction by using hybrid rans-les approach. *Proceedings of ASME Turbo Expo 2022*, 2022. doi: 10.1115/GT2022-82139.

[182] S. G. Tomasello, A. Andreini, R. Meloni, S. Cubeda, L. Andrei, and V. Michelassi. Analysis of combustor-turbine interaction by using coupled and decoupled scale-resolving simulations under representative operating conditions. In *Proceedings of ASME Turbo Expo 2023: Turbomachinery Technical Conference and Exposition (GT 2023)*, New York, N.Y., 2023. the American Society of Mechanical Engineers. ISBN 978-0-7918-8700-4. doi: 10.1115/GT2023-103853.

[183] A. Towne, O. T. Schmidt, and T. Colonius. Spectral proper orthogonal decomposition and its relationship to dynamic mode decomposition and resolvent analysis. *Journal of Fluid Mechanics*, 847:821–867, 2018. ISSN 0022-1120. doi: 10.1017/jfm.2018.283.

[184] N. Treleaven, M. Staufer, A. Spencer, A. Garmory, and G. J. Page. Application of the podfs method to inlet turbulence generated using the digital filter technique. *Journal of Computational Physics*, 415:109541, 2020. ISSN 00219991. doi: 10.1016/j.jcp.2020.109541.

[185] N. C. W. Treleaven, J. Su, A. Garmory, and G. J. Page. An efficient method to reproduce the effects of acoustic forcing on gas turbine fuel injectors in incompressible simulations. *Flow, Turbulence and Combustion*, 103(2):417–437, 2019. ISSN 1386-6184. doi: 10.1007/s10494-019-00020-4.

[186] C. Tropea, A. L. Yarin, and J. F. Foss. *Springer handbook of experimental fluid mechanics: With ... 123 tables*. Springer handbooks. Springer, Berlin, 2007. ISBN 978-3-540-25141-5. doi: 10.1007/978-3-540-30299-5.

[187] J. Tyacke, N. R. Vadlamani, W. Trojak, R. Watson, Y. Ma, and P. G. Tucker. Turbomachinery simulation challenges and the future. *Progress in Aerospace Sciences*, 110: 100554, 2019. ISSN 03760421. doi: 10.1016/j.paerosci.2019.100554.

[188] S. Vagnoli and T. Verstraete. Numerical study of the combustor - turbine interaction using coupled unsteady solvers. *International Symposium on Air Breathing Engines*, 22, 2015.

[189] I. Veloudis, Z. Yang, J. J. McGuirk, G. J. Page, and A. Spencer. Novel implementation and assessment of a digital filter based approach for the generation of les inlet conditions. *Flow, Turbulence and Combustion*, 79(1):1–24, 2007. ISSN 1386-6184. doi: 10.1007/s10494-006-9058-y.

[190] I. Verma, L. Zori, J. Basani, and S. Rida. Modeling of combustor and turbine vane interaction. In *Volume 2C: Turbomachinery*. American Society of Mechanical Engineers, 2019. ISBN 978-0-7918-5857-8. doi: 10.1115/GT2019-90325.

[191] J. Weiss. A tutorial on the proper orthogonal decomposition. *AIAA Aviation 2019 Forum*, page 817, 2019. doi: 10.2514/6.2019-3333.

[192] H. Werschnik. *Aerodynamic impact of swirling Combustor Inflow on endwall heat transfer and the robustness of the film cooling design in an axial turbine*. Universitäts- und Landesbibliothek Darmstadt, Darmstadt, 2017. doi: 81453.

[193] H. Werschnik, J. Hilgert, M. Wilhelm, M. Bruschewski, and H.-P. Schiffer. Influence of combustor swirl on endwall heat transfer and film cooling effectiveness at the large scale turbine rig. *Journal of Turbomachinery*, 139(8), 2017. ISSN 0889-504X. doi: 10.1115/1.4035832.

[194] H. Werschnik, H.-P. Schiffer, and C. Steinhausen. Robustness of a turbine endwall film cooling design to swirling combustor inflow. *Journal of Turbomachinery*, 33(4): 917–926, 2017. ISSN 0889504X. doi: 10.2514/1.B36138.

[195] H. Werschnik, M. Schneider, J. Herrmann, D. Ivanov, H.-P. Schiffer, and C. Lyko. The influence of combustor swirl on pressure losses and the propagation of coolant flows at the large scale turbine rig (lstr): Experimental and numerical investigation. *International Journal of Turbomachinery, Propulsion and Power*, 2(3):12, 2017. doi: 10.3390/ijtpp2030012.

[196] D. C. Wilcox. *Turbulence modeling for CFD*. DCW Industries Inc, La Cañada, Calif., 1993. ISBN 0-9636051-0-0.

[197] M. Wilhelm. *Aerothermal Impact of Low Emission Combustion on the Turbine Blade Tip*, volume 15 of *Forschungsberichte aus dem Institut für Gasturbinen, Luft- und Raumfahrtantriebe*. Shaker, Düren, 1. auflage edition, 2020. ISBN 978-3-8440-7482-6.

[198] M. Wilhelm, M. Schmidt, F. Goertz, Schiffer Heinz-Peter, and C. Lyco. Influence of combustor swirl on turbulence at the large scale turbine rig (lstr). *ISABE-2017-21393*, 2017.

[199] T. Wolf, K. Lehmann, L. Willer, A. Pahs, M. Rößling, and L. Dorn. Interturb: High-pressure turbine rig for the investigation of combustor-turbine interaction. *Proceedings of ASME Turbo Expo 2017*, 2017. doi: 10.1115/GT2017-64153.

[200] X. Wu. Inflow turbulence generation methods. *Annual Review of Fluid Mechanics*, 49 (1):23–49, 2017. ISSN 0066-4189. doi: 10.1146/annurev-fluid-010816-060322.

[201] J. B. Young and J. H. Horlock. Defining the efficiency of a cooled turbine. *Journal of Turbomachinery*, 128(4):658–667, 2006. ISSN 0889-504X. doi: 10.1115/1.2218890.

[202] G. A. Zess and K. A. Thole. Computational design and experimental evaluation of using a leading edge fillet on a gas turbine vane. *Journal of Turbomachinery*, 124(2): 167–175, 2002. ISSN 0889-504X. doi: 10.1115/1.1460914.